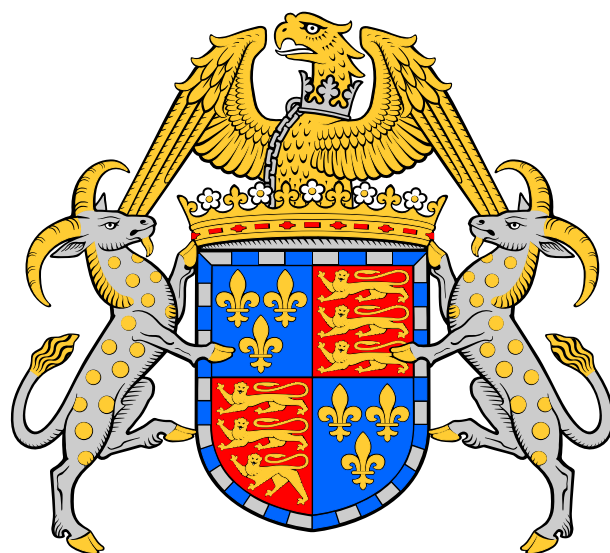


LUCKY EXPOSURES: DIFFRACTION LIMITED ASTRONOMICAL IMAGING THROUGH THE ATMOSPHERE

Robert Nigel Tubbs

Dissertation submitted in candidature for the degree of
Doctor of Philosophy in the University of Cambridge



St Johns College
Cambridge University

September 2003

Preface

This dissertation is the result of work I have undertaken between October 1999 and September 2003 as a research student in the Institute of Astronomy and Cavendish Astrophysics Group in the University of Cambridge.

This dissertation is my own work and contains nothing which is the outcome of work done in collaboration with others, except as specified in the text and Acknowledgements.

This dissertation is not substantially the same as any that has been submitted for a degree or diploma or other qualification at this or any other University.

This dissertation does not exceed 60 000 words.

Robert Nigel Tubbs

Originality

Chapter 1 is a review of recent developments in high resolution ground based optical imaging, and is mostly the work of other authors.

Chapter 2 includes some results from previous authors and some of my own work as indicated in the text.

Chapters 3-6 and Appendix A are my own work except where indicated in the text.

Summary

The resolution of astronomical imaging from large optical telescopes is usually limited by the blurring effects of refractive index fluctuations in the Earth’s atmosphere. By taking a large number of short exposure images through the atmosphere, and then selecting, re-centring and co-adding the best images this resolution limit can be overcome. This approach has significant benefits over other techniques for high-resolution optical imaging from the ground. In particular the reference stars used for our method (the *Lucky Exposures* technique) can generally be fainter than those required for the natural guide star adaptive optics approach or those required for other speckle imaging techniques. The low complexity and low instrumentation costs associated with the Lucky Exposures method make it appealing for medium-sized astronomical observatories.

The method can provide essentially diffraction-limited I-band imaging from well-figured ground-based telescopes as large as 2.5 m diameter. The faint limiting magnitude and large isoplanatic patch size for the Lucky Exposures technique at the Nordic Optical Telescope means that 25% of the night sky is within range of a suitable reference star for I-band imaging. Typically the 1%—10% of exposures with the highest Strehl ratios are selected. When these exposures are shifted and added together, field stars in the resulting images have Strehl ratios as high as 0.26 and full width at half maximum flux (FWHM) as small as 90 *milliarcseconds*. Within the selected exposures the isoplanatic patch is found to be up to 60 *arcseconds* in diameter at 810 nm wavelength. Images within globular clusters and of multiple stars from the Nordic Optical Telescope using reference stars as faint as $I \sim 16$ are presented.

A new generation of CCDs (*Marconi L3Vision CCDs*) were used in these observations, allowing extremely low noise high frame-rate imaging with both fine pixel sampling and a relatively wide field of view. The theoretical performance of these CCDs is compared with the experimental results obtained.

Acknowledgements

I would first like to acknowledge the people who made this project possible: Craig Mackay for building a low noise camera and knowing how to use it to its best advantage; and John Baldwin for developing the original concepts on which this work is based. Both John and Craig have guided me through this project, tactfully correcting my conceptual errors, providing a mathematical background for the work, building instrumentation and helping to turn exciting experiments into valuable science.

Current and former members of the COAST group in Cambridge provided essential input to this project. I would like to thank Dave Buscher for useful insights, many interesting conversations and for providing atmospheric modelling algorithms; Donald Wilson for helping to design and build our instrumentation; James Keen, Ali Bharmal and Ali Basden for many useful conversations and input to atmospheric modelling; and Peter Warner for getting me interested in interferometry in the first place, and then guiding me through the first few months. Thanks to Graham Cox for assisting with arrangements on La Palma, and to Richard Wilson and Peter Tuthill for useful conversations and data which helped in understanding the atmosphere. I am grateful to the whole COAST team for providing all the support I needed during my time in the group; to Chris Haniff for keeping things in perspective; to Natalie Thureau and John Young for providing various pieces of software useful for my COAST observing; and to Donald Wilson, Roger Boysen, Bodie Seneta, John Baldwin, John Young and Dave Buscher for keeping COAST running. Long nights observing at COAST would have been much duller without the humour of Josh Eisner, James Keen, Debbie Pearson and Bodie Seneta, and long days and nights at the NOT would have been much less bearable without the wit and insight of John Baldwin, Craig Mackay, Graham Cox and on the latest run Richard Wilson. I hope the COAST group continues to flourish in the coming years. Outside the COAST group, Dave Titterington, Helen Brimmer and Andrew Dean provided much software help.

I would like to give particular thanks to Helen for supporting me throughout this work, and in particular during the stressful writing-up period. Life would have been very difficult without you. I would also like to thank Ian for many relaxing evenings in The Castle, Neil, Andrew, Tim, Stian, Sarah R, Sarah B, Karen, Hannah, Dave, Dan, Lisa, and Andy for many enjoyable parties, Steve, Wendy and Haley for many fun trips to London, and Paula and Andy for always giving me somewhere pleasant to stay and doing my proof-reading.

I would like to acknowledge the support of a PPARC fellowship. This work is based on observations made with the Nordic Optical Telescope, operated on the island of La Palma jointly by Denmark, Finland, Iceland, Norway and Sweden, in the Spanish Observatorio del Roque de los Muchachos of the Instituto de Astrofísica de Canarias. The staff at the NOT provided much useful support, particularly Graham Cox, Peter Brandt, Johannes Andersen, Markku Verkkoniemi and Paco Armas. This project has been supported by the European Commission through the *Access to Research Infrastructures Action* of the *Improving Human Potential Programme*, awarded to the Instituto de Astrofísica de Canarias to fund European Astronomers' access to the European Northern Observatory, in the Canary Islands. This research has also made use of the SIMBAD database, operated at CDS, Strasbourg, France, and NASA's Astrophysics Data System.

This document was typeset by the author in L^AT_EX.

To all amateur and professional astronomers
with short exposure cameras. Good luck!

Contents

Front matter	a
1 Introduction	1
1.1 The need for high resolution optical imaging	1
1.2 Short exposure optical imaging through the atmosphere	3
1.2.1 The Kolmogorov model of turbulence	3
1.2.2 Example short exposure images	6
1.2.3 Exposure selection	8
1.3 Performance of ground-based high resolution imaging techniques	11
1.3.1 Limiting magnitude of reference source	12
1.3.2 Isoplanatic patch	18
1.3.3 Sensitivity to faint objects	18
1.3.4 Cost and complexity of implementation	19
1.3.5 Comparison of imaging techniques	19
1.4 Summary of thesis	19
2 Lucky Exposures	21
2.1 Introduction	21
2.2 Timescale measurements by previous authors	22
2.2.1 Normalising the short-timescale component of the autocorrelation .	22
2.2.2 The temporal power spectrum of intensity fluctuations	23
2.3 Timescale measurements for atmospheric simulations	24
2.3.1 Atmospheric models	27
2.3.2 Single Taylor screen model	28
2.3.3 Numerical simulations	29
2.4 Isoplanatic angle for atmospheric simulations	33
2.5 Exposure selection from simulated data	35
2.6 Conclusions	38
3 Observations of bright sources at the NOT	41
3.1 Introduction	41
3.2 Experimental method	41
3.2.1 Background	41

3.2.2	The effect of mirror aberrations	43
3.2.3	Observations	46
3.3	Data reduction method	50
3.3.1	Application to observational data	53
3.3.2	Exposure selection	56
3.4	Observational results with single stars	58
3.4.1	Exposure selection results	58
3.4.2	Temporal properties of the atmosphere	58
3.4.3	Timescales for exposure selection	63
3.5	Results with binary stars	65
3.5.1	Data taken on ζ Boötis	67
3.5.2	Varying the fraction of exposures selected	68
3.5.3	Strehl ratios obtained for ζ Boötis	70
3.5.4	Resolution and spatial frequency response	75
3.5.5	Weighting exposures	77
3.5.6	Anisoplanatism	80
3.5.7	Temporal and spatial cross correlation	83
3.5.8	Atmospheric dispersion and β Delphini	84
3.5.9	Dynamic range	85
3.5.10	Seeing conditions	85
3.6	Conclusions	86
4	Electron multiplying CCD performance	89
4.1	Introduction	89
4.2	Simple models of the L3Vision CCDs	90
4.2.1	L3Vision CCD architecture	90
4.2.2	Model descriptions	90
4.2.3	Statistics of a single gain stage	91
4.2.4	Statistical properties of registers with multiple stages	93
4.2.5	Signal-to-noise performance	94
4.2.6	Calculating the probability distribution for the output electrons	96
4.2.7	Results from numerical simulations	97
4.3	CCD measurements	102
4.3.1	Example data from observations at the NOT	103
4.3.2	Charge transfer efficiency problems with the camera	107
4.4	Conclusions	111
5	Observations with a low noise CCD at the NOT	113
5.1	Introduction	113
5.2	Aims	114
5.3	Observations	114
5.3.1	Filters and bandpasses	117

5.3.2	Observations in July 2001	118
5.3.3	Observations in July 2002	120
5.3.4	Observations in June-July 2003	121
5.4	Data reduction	122
5.4.1	Fourier filtering	123
5.4.2	Performance of the Fourier filtering	125
5.5	Results	128
5.5.1	Results of exposure selection	128
5.5.2	Isoplanatic angle	131
5.5.3	Limiting magnitude of reference star	133
5.5.4	Assessment of image quality	140
5.5.5	Dynamic range	143
5.6	Sky coverage	145
5.7	Conclusions	147
6	Conclusions	149
A	Simplified approximation to a single Taylor screen atmosphere	153
B	Observation log for June-July 2003	159
	Bibliography	165

Chapter 1

Introduction

1.1 The need for high resolution optical imaging

Ever since Galileo first pointed a simple refracting telescope at the heavens in 1609 and resolved the Jovian system, astronomers have wished for higher and higher resolution imaging instruments. Early telescopes were limited by the accuracy with which large lenses could be figured. The development of reflecting telescopes by James Gregory and Isaac Newton lead to a rapid increase in the resolution available to astronomers. With the work of Thomas Young in the 19th Century, astronomers realised that the resolution of their telescopes was limited by the finite diameter of the mirror used. This limit was set by the wave properties of light and meant that large, accurately figured mirrors would be required in order to obtain higher resolution. Well figured telescopes with larger aperture diameters were constructed, but the improvement in resolution was not as great as had been expected. The resolution which could be obtained varied with the atmospheric conditions, and it was soon realised that Earth's atmosphere was degrading the image quality obtained through these telescopes.

For much of the 20th Century, the blurring effect of the atmosphere (known as atmospheric "seeing") limited the resolution available to optical astronomers. This degradation in image quality results from fluctuations in the refractive index of air as a function of position above the telescope. The image of an unresolved (i.e. essentially point-like) star is turned into a dancing pattern of "speckles". An example short exposure image from such a pattern is shown in Figure 1.1. In order to obtain better atmospheric seeing conditions, telescopes were constructed at high altitudes on sites where the air above the telescope was particularly stable. Even at the best observatory sites the atmospheric seeing conditions typically limit the resolution which can be achieved with conventional astronomical imaging to about 0.5 *arcseconds* (0.5 *as*) at visible wavelengths.

Studies of short exposure images obtained through atmospheric seeing by Antoine Labeyrie

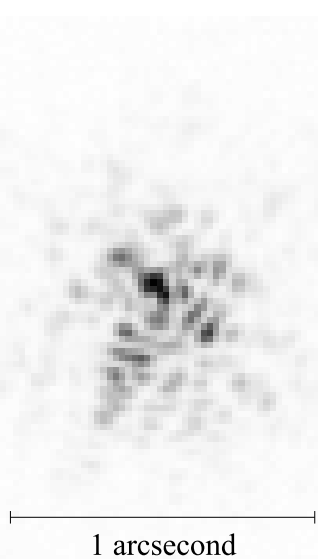


Figure 1.1: A K-band 140 *ms* exposure image obtained at the 10 *m* Keck I telescope showing a typical speckle pattern produced by atmospheric seeing. The image is plotted using a negative greyscale to highlight the fainter features. The pixel scale of $0.0206 \text{ as pixel}^{-1}$ was set by the Keck facility Near Infra-Red Camera (NIRC) instrument. This image is taken from data kindly provided by Peter Tuthill.

in 1970 (Labeyrie 1970) indicated that information about the high resolution structure of an astronomical object could be obtained from these short exposures despite the perturbing influence of the atmosphere. A number of imaging techniques were developed based on his approach, most involving fast frame-rate cameras (essentially high performance motion picture or video cameras) situated at the telescope focus. This thesis discusses one of these techniques in detail, that of Lucky Exposures. The Lucky Exposures method was first discussed in depth by David Fried in 1978 (Fried 1978), and the first experimental results followed in the 1980s. The optimum performance for the technique was not achieved during those observations, partly due to the camera equipment available at the time and partly due to the approach used for the data analysis. This thesis presents more recent results which demonstrate the enormous potential of the technique.

The effects of atmospheric seeing are qualitatively similar throughout the visible and near infra-red wavebands. At large telescopes the long exposure image resolution is generally slightly higher at longer wavelengths, and the timescale for the changes in the dancing speckle patterns is substantially lower. This would argue for the use of long wavelengths in experimental studies of these speckle patterns (although short wavelengths are of equal astronomical interest). The high cost of sensitive imaging detectors which operate at wavelengths longer than $\sim 1 \mu\text{m}$ makes them less appealing for studies of imaging performance, so the results presented in later chapters of this thesis will be restricted to wavelengths shorter than $\sim 1 \mu\text{m}$. The cameras used for my work are sufficiently fast to accurately

sample the atmosphere at the wavelengths used. The approaches developed in this thesis could equally be applied to longer wavelengths given suitable detectors and telescopes, broadening the astronomical potential of the method substantially.

1.2 Short exposure optical imaging through the atmosphere

It is first useful to give a brief overview of the basic theory of optical propagation through the atmosphere. In the standard classical theory, light is treated as an oscillation in a field ψ . For monochromatic plane waves arriving from a distant point source with wave-vector \mathbf{k} :

$$\psi_0(\mathbf{r}, t) = A e^{i(\phi_o + 2\pi\nu t + \mathbf{k} \cdot \mathbf{r})} \quad (1.1)$$

where ψ_0 is the complex field at position \mathbf{r} and time t , with real and imaginary parts corresponding to the electric and magnetic field components, ϕ_o represents a phase offset, ν is the frequency of the light determined by $\nu = c|\mathbf{k}|/(2\pi)$, and A is the amplitude of the light.

The photon flux in this case is proportional to the square of the amplitude A , and the optical phase corresponds to the complex argument of ψ_0 . As wavefronts pass through the Earth's atmosphere they may be perturbed by refractive index variations in the atmosphere. Figure 1.2 shows schematically a turbulent layer in the Earth's atmosphere perturbing planar wavefronts before they enter a telescope. The perturbed wavefront ψ_p may be related at any given instant to the original planar wavefront $\psi_0(\mathbf{r})$ in the following way:

$$\psi_p(\mathbf{r}) = \left(\chi_a(\mathbf{r}) e^{i\phi_a(\mathbf{r})} \right) \psi_0(\mathbf{r}) \quad (1.2)$$

where $\chi_a(\mathbf{r})$ represents the fractional change in wavefront amplitude and $\phi_a(\mathbf{r})$ is the change in wavefront phase introduced by the atmosphere. It is important to emphasise that $\chi_a(\mathbf{r})$ and $\phi_a(\mathbf{r})$ describe the effect of the Earth's atmosphere, and the timescales for any changes in these functions will be set by the speed of refractive index fluctuations in the atmosphere.

1.2.1 The Kolmogorov model of turbulence

A description of the nature of the wavefront perturbations introduced by the atmosphere is provided by the *Kolmogorov model* developed by Tatarski (1961), based partly on the studies of turbulence by the Russian mathematician Andreï Kolmogorov (Kolmogorov 1941a,b). This model is supported by a variety of experimental measurements (e.g. Buscher *et al.* (1995); Nightingale & Buscher (1991); O'Byrne (1988); Colavita *et al.* (1987)) and is widely used in simulations of astronomical imaging. The model assumes that the wavefront perturbations are brought about by variations in the refractive index

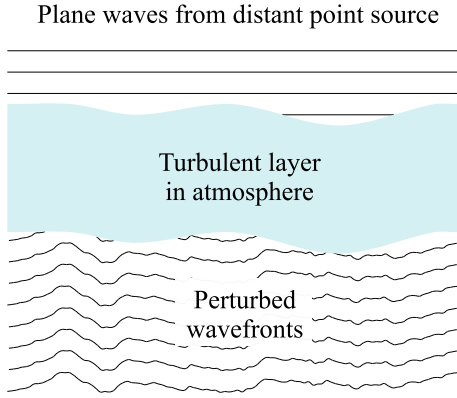


Figure 1.2: Schematic diagram illustrating how optical wavefronts from a distant star may be perturbed by a turbulent layer in the atmosphere. The vertical scale of the wavefronts plotted is highly exaggerated.

of the atmosphere. These refractive index variations lead directly to phase fluctuations described by $\phi_a(\mathbf{r})$, but any amplitude fluctuations are only brought about as a second-order effect while the perturbed wavefronts propagate from the perturbing atmospheric layer to the telescope. For all reasonable models of the Earth's atmosphere at optical and infra-red wavelengths the instantaneous imaging performance is dominated by the phase fluctuations $\phi_a(\mathbf{r})$. The amplitude fluctuations described by $\chi_a(\mathbf{r})$ have negligible effect on the structure of the images seen in the focus of a large telescope.

The phase fluctuations in Tatarski's model are usually assumed to have a Gaussian random distribution with the following second order structure function:

$$D_{\phi_a}(\rho) = \left\langle |\phi_a(\mathbf{r}) - \phi_a(\mathbf{r} + \rho)|^2 \right\rangle_{\mathbf{r}} \quad (1.3)$$

where $D_{\phi_a}(\rho)$ is the atmospherically induced variance between the phase at two parts of the wavefront separated by a distance ρ in the aperture plane, and $\langle \dots \rangle$ represents the ensemble average.

The structure function of Tatarski (1961) can be described in terms of a single parameter r_0 :

$$D_{\phi_a}(\rho) = 6.88 \left(\frac{|\rho|}{r_0} \right)^{5/3} \quad (1.4)$$

r_0 indicates the “strength” of the phase fluctuations as it corresponds to the diameter of a circular telescope aperture at which atmospheric phase perturbations begin to seriously limit the image resolution. Typical r_0 values for I band (900 nm wavelength) observations at good sites are 20—40 cm. Fried (1965) and Noll (1976) noted that r_0 also corresponds to the aperture diameter for which the variance σ^2 of the wavefront phase averaged over the aperture comes approximately to unity:

$$\sigma^2 = 1.0299 \left(\frac{d}{r_0} \right)^{5/3} \quad (1.5)$$

Equation 1.5 represents a commonly used definition for r_0 .

A number of authors (e.g. Kim & Jaggard (1988); Siggia (1978); Frisch *et al.* (1978); Mandelbrot (1974); Kuo & Corrsin (1972)) have suggested alternatives to this Gaussian random model designed to better describe the intermittency of turbulence discovered by Batchelor & Townsend (1949). Although variations in seeing conditions have been found on timescales of minutes and hours (Racine 1996; Vernin & Muñoz-Tuñón 1998; Wilson 2003), no significant experimental evidence has been put forward which strongly favours any one of the intermittency models for the turbulence involved in astronomical seeing. The Gaussian random model is still the most widely used, and will be the principal model discussed in this thesis.

The outer and inner scales of turbulence

In reality, phase fluctuations in the atmosphere are only expected to follow the structure function shown in Equation 1.4 over a finite range of length scales. The turbulent energy is injected at large scales by wind shear. The bulk of the wind shear is expected in discrete layers of the atmosphere, and the largest turbulent structures are expected to fit within one of these atmospheric layers. The length scale at which the structure function for Kolmogorov turbulence breaks down at large scales is called the *outer scale* of turbulence. Several attempts have been made at measuring the size of this outer scale using a variety of different methods (see e.g. Linfield *et al.* (2001); Martin *et al.* (2000); Wilson *et al.* (1999); Davis *et al.* (1995); Buscher *et al.* (1995); Ziad *et al.* (1994); Nightingale & Buscher (1991); Coulman *et al.* (1988)), but there has been substantial variation in the measured values. The Von Karman model (Ishimaru 1978) is expected to describe the form of the power spectrum for phase fluctuations on length scales larger than the outer scale. If the outer scale is larger than the telescope diameter, then most of the properties of short exposure astronomical images will not depend significantly on the precise size of the outer scale (although the amplitude of image motion is still weakly dependent on the outer scale size). The remaining uncertainty in the size of the outer scale has little impact on the work presented in this thesis.

At small scales ($< 1 \text{ cm}$) the turbulent energy in the atmosphere is dissipated through the viscosity of the air (Roddier 1981). The length scale at which this becomes significant is called the *inner scale* of turbulence. The steepness of the Kolmogorov turbulence spectrum means that any reduction in the power at such small length scales has relatively little effect on the imaging performance of optical and infra-red telescopes, and I will not discuss the inner scale any further in this thesis.

1.2.2 Example short exposure images

I will first investigate imaging performance in more detail using simulations of Kolmogorov atmospheres. For these simulations I have chosen to ignore amplitude fluctuations contained in the atmospheric term $\chi_a(\mathbf{r})$ entirely – this corresponds to the case where atmospheric refractive index perturbations are only found very close to the aperture plane of the telescope. This is achieved in the simulations simply by setting:

$$\forall \mathbf{r} : \chi_a(\mathbf{r}) = 1 \quad (1.6)$$

The effect of the finite aperture size of the telescope can be simulated by setting the wavefront amplitude to zero everywhere in the aperture plane except where the light path to the primary mirror is unobstructed. This can be achieved most easily by defining a function $\chi_t(\mathbf{r})$ which describes the effect of the telescope aperture plane coverage on the wavefronts in the same way that the effect of the atmosphere is described by $\chi_a(\mathbf{r})$. The value of $\chi_t(\mathbf{r})$ will be zero beyond the edge of the primary mirror and anywhere the primary is obstructed, but unity elsewhere. For the simple case of a circular primary mirror of radius r_p without secondary obstruction:

$$\chi_t(r) = \begin{cases} 1 & \text{if } |\mathbf{r}| \leq r_p \\ 0 & \text{if } |\mathbf{r}| > r_p \end{cases} \quad (1.7)$$

Phase perturbations introduced into the wavefronts by aberrations in the telescope can be described by a function $\phi_t(\mathbf{r})$ in similar way, resulting in wave-function ψ'_p given by:

$$\psi'_p(\mathbf{r}) = \left(\chi_a(\mathbf{r}) \chi_t(\mathbf{r}) e^{i[\phi_a(\mathbf{r}) + \phi_t(\mathbf{r})]} \right) \psi_0(\mathbf{r}) \quad (1.8)$$

I will begin with the simple case of a telescope which is free of optical aberrations observing in a narrow wavelength band. The perturbed wave-function reaching the telescope aperture for this case is given by setting $\phi_t(\mathbf{r}) \equiv 0$ in Equation 1.8. Combined with Equation 1.6 this gives:

$$\psi_p(\mathbf{r}) = \left(\chi_t(\mathbf{r}) e^{i\phi_a(\mathbf{r})} \right) \psi_0(\mathbf{r}) \quad (1.9)$$

For the simulations a long-period pseudo-random number generator was used to produce two-dimensional arrays containing discrete values of $\phi_a(\mathbf{r})$, having the second order structure function defined by Equation 1.4, using a standard algorithm provided by Keen (1999). The time evolution of $\phi_a(\mathbf{r})$ was ignored, as I was interested in the instantaneous imaging performance (the case for short exposures). Arrays of $\psi_p(\mathbf{r})$ were then generated corresponding to the wave-function provided by a distant point source after passing through the atmospheric phase perturbations and the telescope aperture using Equation 1.9. These arrays were Fourier transformed using a standard Fast Fourier Transform (FFT) routine to

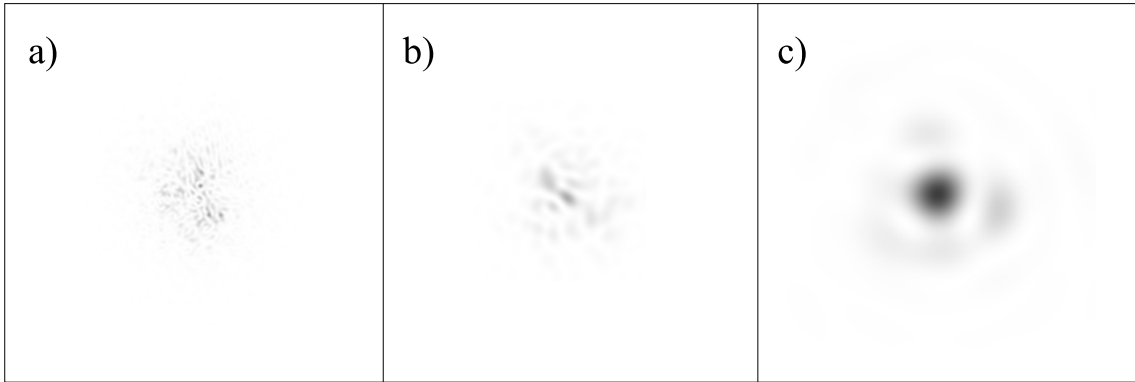


Figure 1.3: Typical short exposures through: a) a $20r_0$ aperture; b) a $7r_0$ aperture; and c) a $2r_0$ aperture. All three are plotted with the same image scale but have different greyscales.

provide images of the point source as seen through the atmosphere and telescope. The image of a point source through an optical system is called the point-spread-function (PSF) of the optical system. For our simple optical arrangement with phase perturbations very close to the aperture plane, the response of the system to extended sources of incoherent light is simply the convolution of the PSF with a perfect image of the extended source.

Figure 1.3 shows simulated PSFs for three atmospheric realisations having the same r_0 and image scales but with different telescope diameters. There are two distinct regimes for the cases of large (diameter $d \gg r_0$) and small ($d \sim r_0$) telescopes. Figure 1.3a is a typical PSF from a telescope of diameter $d = 20r_0$. The image is broken into a large number of speckles, which are randomly distributed over a circular region of the image with angular diameter $\sim \frac{\lambda}{r_0}$, where λ represents the wavelength. With the slightly smaller aperture shown in Figure 1.3b the individual speckles are larger – this is because the typical angular diameter for such speckles is $\sim 1.22\frac{\lambda}{d}$, equal to the diameter of the PSF in the absence of atmospheric phase perturbations for a telescope of the same diameter d (i.e. a *diffraction-limited* PSF). For the small aperture size shown in Figure 1.3c the shape of the instantaneous PSF deviates little from the diffraction-limited PSF given by a telescope of this diameter. The first Airy ring is partially visible around the central peak.

Real astronomical images of small fields obtained through the atmosphere will correspond to an image of the sky brightness distribution convolved with the PSF for the telescope and atmosphere. The perturbations introduced by the atmosphere change on timescales of a few milliseconds (known as the atmospheric coherence time). If the exposure time for imaging is shorter than the atmospheric coherence time, and the telescope is free of optical aberrations, then Figures 1.3a–c will be representative of the typical PSFs observed. The random distribution of speckles found in the short exposure PSFs of Figures 1.3a and 1.3b will have the effect of introducing random noise at high spatial frequencies into the images, making individual short exposures such as these of little direct use for high resolution astronomy. Figure 1.3c is dominated by a relatively uniform bright core, and

as such will provide images with relatively high signal-to-noise. Unfortunately the broad nature of the PSF core severely limits the image resolution which can be obtained with such a small aperture.

1.2.3 Exposure selection

The phase perturbations introduced by the atmosphere change on timescales of a few milliseconds, causing the speckle patterns in Figures 1.3a and 1.3b to vary randomly in both shape and overall position (the changes in the position of the PSF correspond to the image-motion commonly known to observational astronomers). For the small aperture shown in Figure 1.3c the overall position of the PSF still fluctuates with time, but the shape of the short exposure PSF changes very little. The most prominent effects of atmospheric phase perturbations on the shape in this case are small fluctuations in the Airy rings and in the intensity of the central peak.

It is useful at this stage to define a quantitative measure of image quality. One approach is to compare the PSF measured through the atmosphere with the diffraction-limited PSF expected in the absence of atmospheric aberrations. The ratio of the peak intensity in the PSF measured for an aberrated optical system to that expected for a diffraction-limited system is widely known as the *Strehl ratio*, after the work of Strehl (1895, 1902). In this case we treat the atmospheric perturbations as the optical aberration, with the telescope itself assumed to be aberration-free. In order to ensure that the images shown in Figure 1.3 were “typical”, several thousand random realisations of each PSF were generated, and the three with the median Strehl ratios were chosen for the figure. The Strehl ratios of the exposures picked were 0.024, 0.14 and 0.68 for Figures 1.3a, 1.3b and 1.3c respectively.

As the atmospheric fluctuations are random, one would occasionally expect these fluctuations to be arranged in such a way as to produce a diffraction-limited PSF, and hence good quality image. Fried (1978) coined the phrase “Lucky Exposures” to describe high quality short exposures which occur in such a fortuitous way. A perfectly diffraction-limited PSF will be extremely unlikely, but it is of interest to assess how good an image one would expect to occur relatively often during an observing run. If the speckle patterns change on timescales of a few milliseconds, and we are willing to wait a few seconds for our good image, then we can wait for a one-in-a-thousand Lucky Exposures. From several thousand random realisations I selected the PSFs with the highest 0.1% of Strehl ratios. Figures 1.4a—c show examples of these PSFs with the same atmospheric conditions and telescope diameters as were used for Figure 1.3a—c respectively.

Figure 1.4a has one speckle with unusually high intensity, resulting in an image Strehl ratio of 0.062 – significantly greater than the median Strehl of 0.024 for short exposure PSFs with this aperture size. If the brightest speckle is similar in shape to a diffraction-limited PSF, then the fraction of the light in the brightest speckle is approximately equal to the

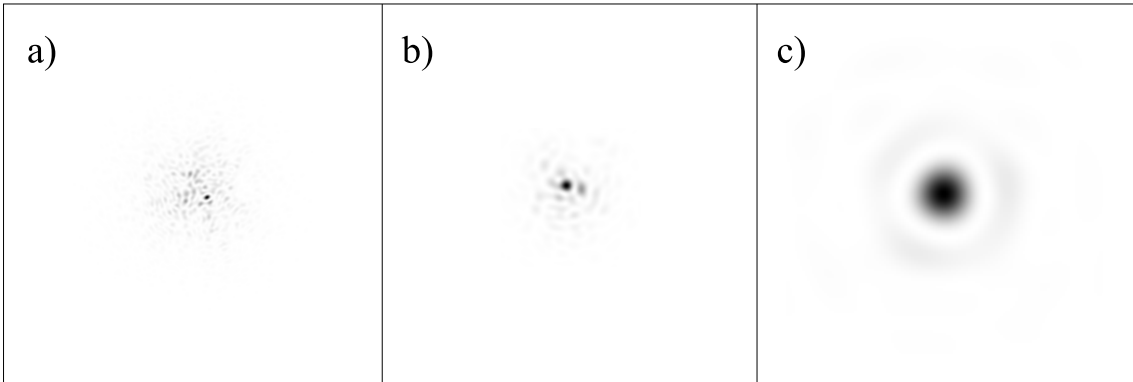


Figure 1.4: Short exposures through a $20r_0$, $7r_0$ and $2r_0$ aperture typical of those with the highest 0.1% of Strehl ratios. The Strehl ratios for a), b) and c) are 0.0619, 0.426 and 0.905 respectively.

Strehl ratio. In this case roughly 6% of the light resides in the brightest speckle. The vast majority of the light is distributed in a large number of fainter speckles. When imaging a complex source, each of the fainter speckles contributes noise to the image, resulting in poor image quality.

Figure 1.4b is dominated by a single speckle which contains a significant fraction of the total intensity in the image. If we take this speckle to be similar in size and shape to a diffraction-limited PSF, then the measured Strehl ratio of 43% implies that the speckle contains about 43% of the total light intensity. The remaining light is found in a large number of much fainter speckles. The surface brightness from these background speckles is relatively small and should not result in a very noisy image.

Figure 1.4c is very similar to the typical exposure shown in Figure 1.3c. With this aperture size the PSF of a lucky exposure shows little improvement over that for a typical exposure. The broad core of the PSF is dominated by diffraction through the small aperture, giving very poor angular resolution.

Fried (1978) suggested that for an aperture of diameter $7r_0$ or $8r_0$, roughly 0.1% of the short exposures should be of very good quality (with the RMS variation in wavefront phase over the aperture less than one radian). This is borne out by the compact core and high Strehl ratio for the PSF shown in Figure 1.4b, which should mean that this case provides better high-resolution imaging performance than Figures 1.4a and 1.4c.

In order to compare the imaging performance of the PSFs qualitatively, each of the PSFs in Figures 1.4a—c was convolved with a simulated astronomical image; the results are shown in Figures 1.5a—c respectively. For comparison, an image on the same scale was generated using an ideal PSF (a delta-function), and this is displayed in Figures 1.5d and 1.5e. Both the galaxy-like structure and the point sources are clearly evident in Figure 1.5b, whereas these structures are much more difficult to make out in Figures 1.5a and 1.5c.

Even under high light level conditions the signal to noise for imaging using short exposures

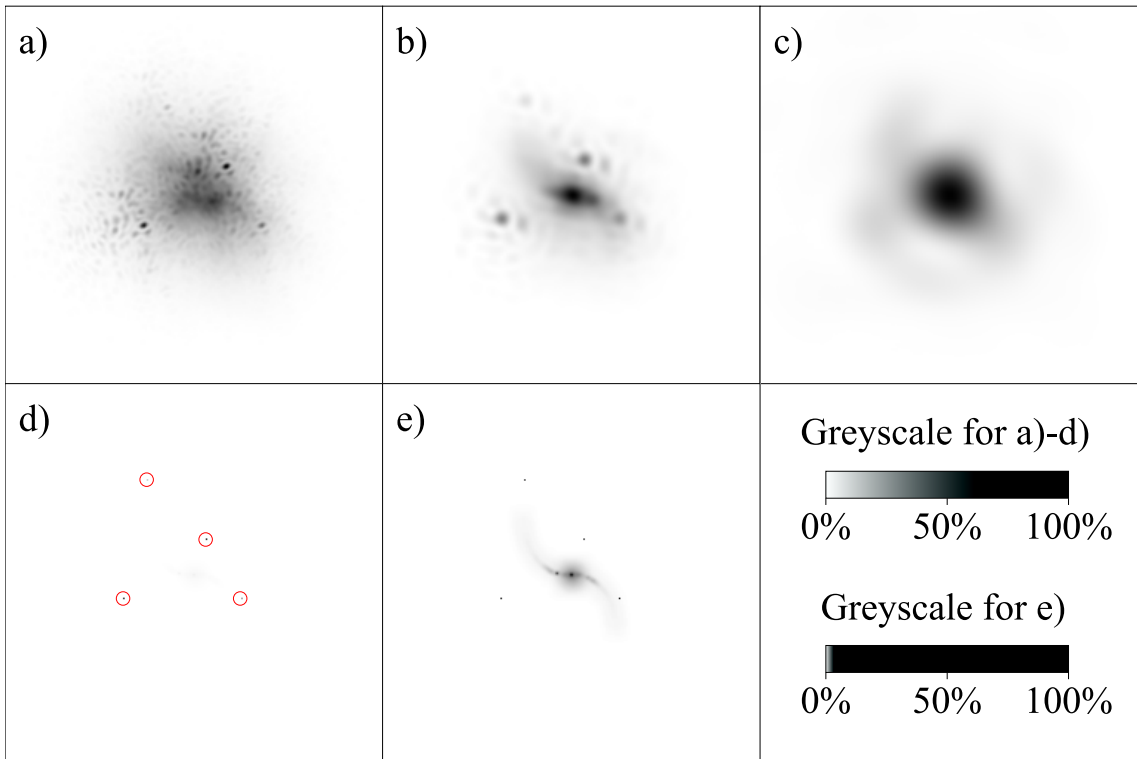


Figure 1.5: a)—c) show the short exposure PSFs from Figure 1.4 convolved with a simulated sky brightness distribution. The sky brightness distribution used is shown with two different greyscales in d) and e). Four point sources of differing brightness are circled in red in d). In panels a)—c) the blurring effect of the PSFs re-distributes the flux from the point sources over a wider area of the image leading to a substantial reduction in the peak pixel values in the images.

can be improved by combining large numbers of short exposures taken at different times. For PSFs having a bright core such as Figure 1.4b, the location of this core within the image is randomly determined by the atmosphere. To maximise the image quality, the images must be shifted so that the contribution from the bright core of each PSF is brought to a common location. If the short exposures are then co-added, the contribution from the bright core of each PSF will add coherently, while the contributions from the randomly varying speckles will combine incoherently. In practice the PSF must be determined from the short exposure images themselves – this is most easily achieved if there is an unresolved star within the field of view. The image of such a star obtained through the atmosphere accurately maps the PSF due to the telescope and atmosphere. The re-centring and co-adding of short exposures in this way has been widely discussed by other authors (e.g. Christou (1991)).

Determination of the instantaneous PSF from short exposure images of a reference star, and the use of such PSF measurements to select the exposures with the highest Strehl ratio and to then re-centre and co-add these exposures forms the basis for most of the work described in this thesis. I will refer to this method as the *Lucky Exposures* technique. A number of other authors have published results using very similar methods, particularly

for solar and planetary observations. Observations of fainter astronomical targets have typically used exposure times which are too long to freeze the atmosphere, but these have often produced valuable astronomical science results nevertheless (Nieto *et al.* 1987, 1988, 1990; Lelievre *et al.* 1988; Crampton *et al.* 1989; Nieto & Thouvenot 1991). Dramatic improvements in CCD technology have allowed recent observations to be performed at much higher frame rates (Dantowitz *et al.* 2000; Baldwin *et al.* 2001; Davis & North 2001), providing new insights into the characteristics of the atmosphere, and demonstrating the potential of high frame-rate imaging using low noise detectors.

To help provide some background material in the field of high resolution imaging, I will now introduce some alternative methods for high resolution imaging. This will hopefully clarify the advantages and disadvantages of Lucky Exposures.

1.3 Performance of ground-based high resolution imaging techniques

Ground-based high resolution imaging techniques can be broadly classified into two types:

1. Passive observations – techniques which make astronomical measurements on time-scales comparable to the atmospheric coherence time. Measurements are usually repeated many times in order to increase the signal to noise ratio. Typical examples include speckle interferometry, the shift-and-add method, Lucky Exposures and observations of visibilities and closure phases at long baseline interferometers such as COAST and SUSI.
2. Active correction – designed to remove atmospheric perturbations in optical wavefronts in real time before they enter an imaging instrument. Adaptive optics (including tip-tilt correction) and fringe tracking at long baseline interferometers such as NPOI represent active correction.

The Lucky Exposures method is passive, relying on a high frame-rate camera in the image plane of a telescope to record the speckle patterns. In the past the poor signal-to-noise performance of high frame-rate cameras has often limited observations like this to relatively bright targets. It should be noted that the recent development of high frame-rate CCD cameras with extremely low readout noise will allow many of the active and passive imaging methods to be used on much fainter astronomical sources.

All of the techniques require measurements of the perturbations introduced by the atmosphere using light from a reference source. This reference source may either be a component of the astronomical target (e.g. the bright core of an active galaxy) or another source nearby in the sky such as a star. For most of the methods described here the reference source must be small enough that it is not significantly resolved by the observations.

For adaptive optics slightly larger reference sources may be used. The abundance of stars in the night sky mean that they are the most common form of reference source used for high-resolution imaging through the atmosphere.

Each of the imaging techniques can only be applied in a small field around each reference source – this field is usually called the *isoplanatic patch*. Only those astronomical objects which are close enough to a suitably bright reference source can be imaged. Under the same observing conditions passive imaging approaches can typically use fainter reference stars than active techniques, which require a servo-loop operating at a fast rate.

The range of astronomical sources to which each technique can be applied is thus dependent on how faint a reference source can be used. The fraction of the sky which is within range of a suitable reference star is termed the *sky coverage* of the imaging technique. For most of the techniques described here the sky coverage is relatively small, seriously limiting their applicability in scientific observations. This thesis will concentrate on imaging at wavelengths shorter than $1\mu m$. For these wavelengths the small sky coverage available is the principle limitation on the scientific output of all these techniques, making this the most important issue to address here. Some aspects of the discussion presented below would be less relevant for observations at longer wavelengths.

In comparing the methods I will discuss four aspects of the techniques:

1. The limiting magnitude of reference star which can be used;
2. The isoplanatic patch;
3. The sensitivity to faint objects; and
4. The cost and complexity of implementation.

1.3.1 Limiting magnitude of reference source

At optical and near infra-red wavelengths the brightness of stars is defined using the stellar magnitude scale of Pogson (1856). The apparent magnitude m at a given wavelength λ is defined in terms of the amplitude A of the electromagnetic waves:

$$m = -5 \log_{10} (A) + k(\lambda) \quad (1.10)$$

where a number of definitions for the wavelength dependent constants $k(\lambda)$ exist such as the Johnson magnitude system (Aller *et al.* 1982).

For observations in a given waveband the apparent magnitude of the faintest reference source which can be used for a high-resolution imaging technique is called the reference source limiting magnitude m_l . The applicability of the imaging technique depends on the

density $\rho(m < m_l)$ of stars brighter than this limiting magnitude on the night sky. For the range of limiting magnitudes appropriate to most of the imaging techniques described here this density is relatively well fit over the majority of the night sky by $\rho(m < m_l) \propto 10^{0.35m_l}$ (see e.g. Cox (2000); Bahcall & Soneira (1984)). Improving the limiting magnitude for any one of the imaging techniques by only one magnitude typically *doubles* the sky coverage of the technique, dramatically improving the range of astronomical studies which can be undertaken by that technique.

Limiting magnitude of reference source for Lucky Exposures

In order for the Lucky Exposures method to be successful, each short exposure must be re-centred based on an unresolved feature in a reference source which provides a measure of the PSF. If the imaging detector is limited by photon noise, the unresolved reference source must provide a few photons within the brightest speckle during one atmospheric coherence time in order for this method to be successful. This sets a limit on the faintest reference sources which can be used, which in turn limits the range of astronomical targets which can be observed. For I-band observations under good astronomical seeing conditions the limiting magnitude for high resolution observations with a $\sim 2.5\text{ m}$ diameter telescope is in the range $I = 17$ to $I = 18$.

Limiting magnitude of reference source for shift-and-add

The shift-and-add method described by e.g. Christou (1991) bears the greatest similarity to the Lucky Exposures method, the principle difference being that all the short exposures are used rather than just those exposures with the highest Strehl ratio. In order for the re-centring to be successful using exposures which have a lower Strehl ratio, a correspondingly brighter reference source is required in order provide the same number of photons within the brightest speckle. The limiting magnitude of reference source for this technique is thus one or two magnitudes poorer than that for Lucky Exposures.

Limiting magnitude of reference source for speckle interferometry

A number of high resolution imaging techniques exist which involve Fourier analysis of individual short exposure images taken at a large telescope (see e.g. Roddier (1988)). Only those methods which preserve some Fourier phase information from the source can be used to produce true astronomical images, and the techniques which preserve Fourier phase information require higher light levels than the Lucky Exposures and shift-and-add methods (see e.g. Chelli (1987); Roddier (1988)). These methods are thus limited to a smaller range of astronomical targets. The bispectral analysis (speckle masking) method has often been applied to data taken through masked apertures, where most of the aperture

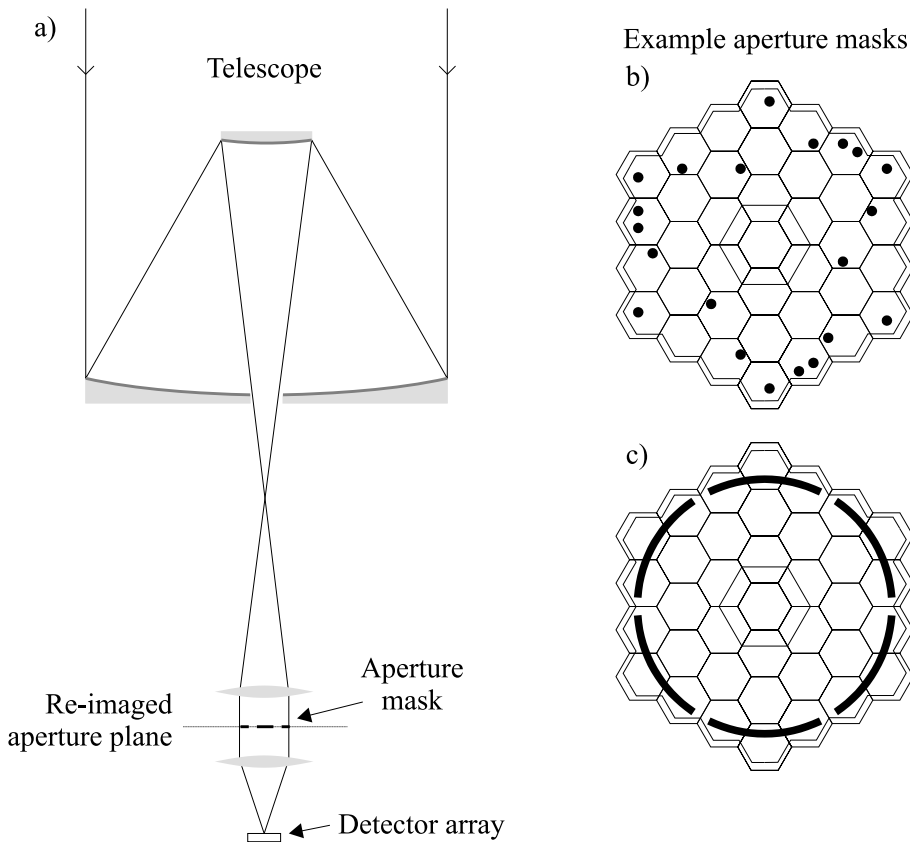


Figure 1.6: a) shows a simple experiment using an aperture mask in a re-imaged aperture plane. b) and c) show diagrams of aperture masks which were placed in front of the secondary mirror of the Keck telescope by Peter Tuthill and collaborators. The solid black shapes represent the subapertures (holes in the mask). A projection of the layout of the Keck primary mirror segments is overlaid.

is blocked off and light can only pass through a series of small holes (subapertures). For simplicity these aperture masks are usually either placed in front of the secondary (e.g. Tuthill *et al.* (2000)) or placed in a re-imaged aperture plane as shown in Figure 1.6a (e.g. Baldwin *et al.* (1986); Haniff *et al.* (1987); Young *et al.* (2000)). The masks are usually categorised either as non-redundant or partially redundant. Non-redundant masks consist of arrays of small holes where no two pairs of holes have the same separation vector. Each pair of holes provides a set of fringes at a unique spatial frequency in the image plane. Partially redundant masks are usually designed to provide a compromise between minimising the redundancy of spacings and maximising both the throughput and the range of spatial frequencies investigated (Haniff & Buscher 1992; Haniff *et al.* 1989). Figures 1.6b and 1.6c show examples of aperture masks used in front of the secondary at the Keck telescope by Peter Tuthill and collaborators; Figure 1.6b is a non-redundant mask while Figure 1.6c is partially redundant. Although the signal-to-noise at high light level can be improved with aperture masks, the limiting magnitude cannot be significantly improved for photon-noise limited detectors (see Buscher & Haniff (1993)).

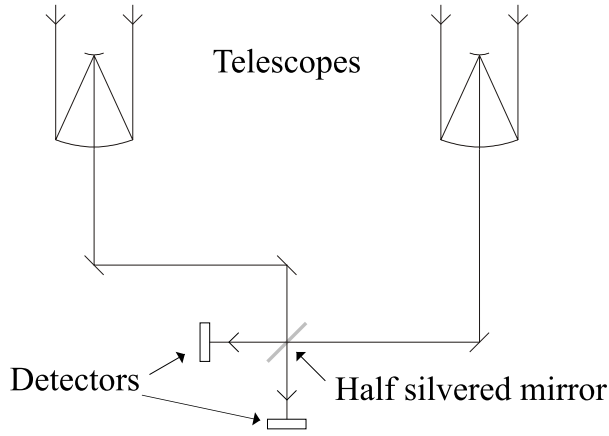


Figure 1.7: Schematic showing pupil-plane beam combination in a two-telescope optical interferometer.

Limiting magnitude of reference source for separate element interferometry

Astronomical imaging from Michelson interferometers with separated elements has been demonstrated by a number of authors (e.g. Baldwin *et al.* (1996); Monnier (2003); Burns *et al.* (1997); Young *et al.* (2003)). The principles of the technique are the same as bispectral analysis of images taken through non-redundant aperture masks at a single telescope as described above. Each telescope in a separate element interferometer array is equivalent to one subaperture of the aperture mask. In separate element interferometers the light is often combined using half-silvered mirrors in a pupil-plane as shown in Figure 1.7, rather than in an image plane. With no active wavefront correction on the individual telescopes and photon-counting detectors the limiting magnitude for this method is similar to that of bispectrum imaging at single telescopes. All existing and planned separate-element interferometers have some form of adaptive optics correction (often only the image position or *tip-tilt* component). The limiting magnitude of reference source required for adaptive optics correction sets an upper limit on the limiting magnitude for these arrays, and this is discussed in the next section.

Limiting magnitude of reference source for adaptive optics

Active correction of wavefront perturbations introduced by the atmosphere is known as adaptive optics. The simplest form of adaptive optics system is a mechanical tip-tilt corrector which removes the average gradient in wavefront phase across a telescope aperture. With this level of correction, diffraction-limited long exposure imaging can only be performed for aperture diameters up to $3.4r_0$ diameter (Noll 1976). To obtain diffraction-limited images from larger telescopes, the shape of the perturbations in the wavefront across the telescope aperture must be measured and actively corrected. Deformable mirrors in a re-imaged pupil-plane are most often used to introduce additional optical path

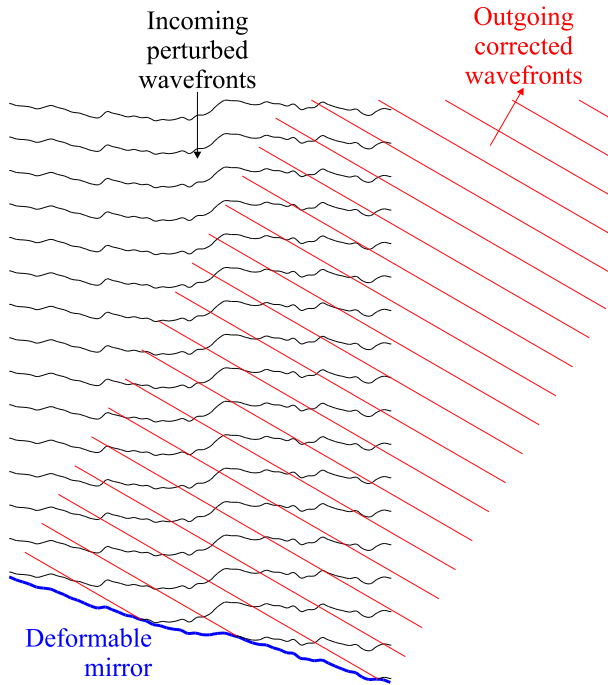


Figure 1.8: Adaptive optics correction of atmospherically perturbed wavefronts using a deformable mirror.

which corrects the perturbations introduced by the atmosphere as shown schematically in Figure 1.8. One of the simplest systems for measuring the shape of the wavefront is a Shack-Hartmann array (see Figure 1.9). This consists of a series of subapertures typically of $\sim r_0$ diameter, positioned across a telescope pupil-plane. The wavefront sensor accepts light from the reference star, while light from the science object (or light at a science imaging wavelength) is directed to a separate imaging camera. Each subaperture contains a focusing element which generates an image of the reference source, and the position offset of these images is used to calculate the mean gradient of the wavefront phase over each subaperture. The gradient measurements can then be pieced together to provide a model for the shape of the wavefront perturbations. This model is then fed into the wavefront corrector. In order to accurately correct the rapidly fluctuating atmosphere using a stable servo-feedback loop, the process must typically be repeated ten times per atmospheric coherence time (see e.g. Hardy (1998); Karr (1991)). The atmospheric coherence time itself is usually found to be shorter for measurements through small subapertures than for imaging through the full telescope aperture, as will be discussed further in Chapter 2 (see also Roddier *et al.* (1982a)).

Comparison of limiting magnitudes

The limiting magnitude of reference source which can be used for adaptive optics is set by the need to measure the reference source image position in each of the $\sim r_0$ diameter

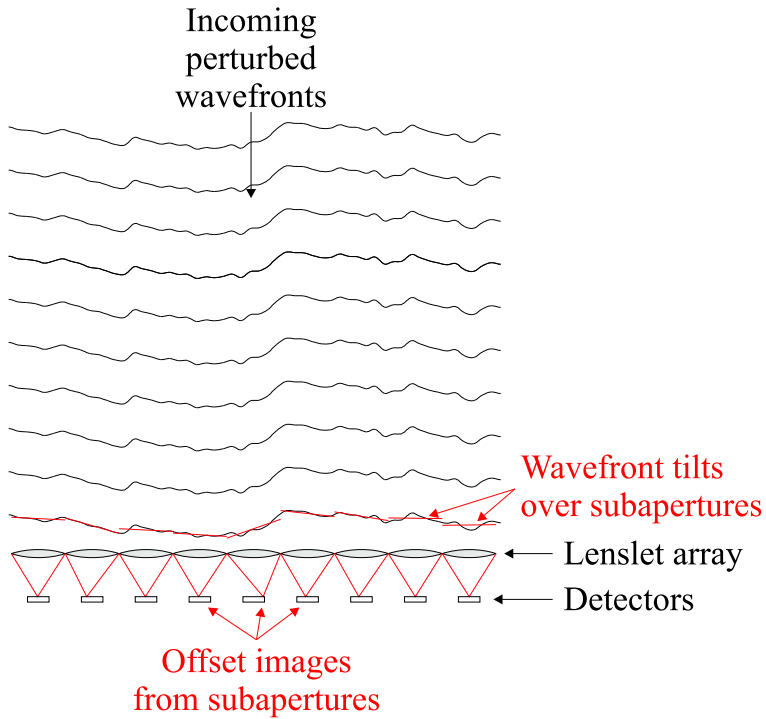


Figure 1.9: Schematic of a Shack-Hartmann wavefront sensor positioned in a telescope pupil-plane. An array of lenslets act as subapertures, and the position of the image centroid measured using each subaperture is used to calculate the wavefront tilt over this subaperture. These wavefront tilts are then used to construct a model of the wavefront shape over the full telescope aperture.

subapertures in about one tenth of the atmospheric coherence time for the subapertures. This is a similar problem to the correction of image position for Lucky Exposures, and I will now compare the two limiting magnitudes directly.

In the simplest approximation, the limiting magnitude for measurement of image position is set by the requirement for a minimum number of photons in the image core. The number of photons in the image core is proportional to the photon flux density I from the star at the observing wavelength, the collecting area of the aperture A , the exposure time T and the Strehl ratio of the image \mathcal{S} . If the number of photons required in the image core is the same in both cases, and the losses in the optics and the detector are the same, then from Equation 1.10 the limiting magnitude for adaptive optics will be poorer by:

$$\Delta m = 2.5 \log \left(\frac{A_{AO} T_{AO} \mathcal{S}_{AO}}{A_{LE} T_{LE} \mathcal{S}_{LE}} \right) \quad (1.11)$$

where the subscripts AO and LE refer to the adaptive optics and Lucky Exposures cases respectively. For the case described in Figure 1.4b the telescope diameter for the Lucky Exposures case is seven times the adaptive optics subaperture diameter. Passive Lucky Exposures observations can have ten times longer exposure times than adaptive optics wavefront sensors, but the Strehl ratio in the subapertures of an adaptive optics wavefront

sensor is typically twice that in a Lucky Exposure. This means that Lucky Exposures should be able to use stars which are about seven magnitudes fainter than would be required for near diffraction-limited imaging with adaptive optics. The faintest reference stars which provide good adaptive optics correction at I-band are $I \sim 10$ (Graves *et al.* 1998), in broad agreement with the arguments here.

Recent studies (e.g. Ragazzoni & Farinato (1999)) have shown that novel wavefront sensors such as Pyramid sensors can improve the reference star limiting magnitude for adaptive optics by several magnitudes at extremely large telescopes, but the gains for moderate sized telescopes such as those described in this thesis are relatively small. The limiting reference star magnitude is still not competitive with Lucky Exposures.

One approach which may overcome the problems with the reference source limiting magnitude for adaptive optics is the use of artificial reference stars, typically provided by light scattered from a high power laser pointing along the line of sight of the telescope. A number of observatories are currently developing such laser systems.

1.3.2 Isoplanatic patch

The area of sky around a reference star over which high-resolution imaging is possible is called the isoplanatic patch (this will be discussed in more detail in Chapter 2). If the sky coverage of an imaging technique is substantially less than 100%, it will generally vary in proportion with the area of the isoplanatic patch. The diameter of the isoplanatic patch for an imaging technique thus has a very substantial impact on the applicability of that technique to astronomical imaging. A number of authors including Roddier *et al.* (1982b) have shown that the isoplanatic patch of fast frame-rate imaging techniques such as shift-and-add is expected to be substantially larger than that for adaptive optics. If the Lucky Exposures method selects exposures at times when the atmospheric conditions are particularly good, then this method would give an even larger isoplanatic patch than the shift-and-add method. In Chapter 5.5.2 I present results which demonstrate that the isoplanatic angle for Lucky Exposures observations can sometimes be as large as 30 as for I-band observations, a substantial improvement over typical values of 2–15 as predicted for speckle imaging and non-conjugate adaptive optics at wavelengths shorter than 1 μm (Vernin & Muñoz-Tuñón 1994; Roddier *et al.* 1982a, 1990; Marks *et al.* 1999).

1.3.3 Sensitivity to faint objects

The recent development of CCDs with negligible readout noise (see e.g. Mackay *et al.* (2001); Robbins & Hadwen (2003)) has almost eliminated the noise penalty for high frame-rate imaging at CCD wavelengths. For the first time this has made shift-and-add imaging competitive with adaptive optics for the imaging of very faint objects at I band.

For unresolved sources, the high resolution in Lucky Exposures images can help to reduce the effect of the sky background contribution on images. However, if a large fraction of the observation data is discarded, this necessarily has an impact on the sensitivity of the technique to faint objects in a fixed period of observing time. Astronomers using the Lucky Exposures method have to make a trade-off between high resolution (obtained using a very small fraction of the exposures) and high sensitivity (the fraction of exposures which should be selected to obtain the maximum sensitivity to a faint source depends on the source geometry and observing conditions, but is typically a large fraction of the total number of exposures).

1.3.4 Cost and complexity of implementation

Fast frame-rate imaging techniques such as Lucky Exposures are extremely easy and cheap to implement at existing ground-based telescopes. In contrast the installation of an adaptive optics system at a ground based telescope is generally a complex and expensive process. There are even greater technical difficulties associated with laser guide star adaptive optics systems, and it will probably be a number of years before they are widely available to the astronomical community.

1.3.5 Comparison of imaging techniques

The Lucky Exposures method is expected to have the highest sky coverage of all the natural guide star techniques discussed here, utilising fainter reference stars and providing an isoplanatic patch at least as large as the shift-and-add method. The method is also much cheaper and simpler to implement at observatories than adaptive optics systems.

The sensitivity of the Lucky Exposures method to faint objects is likely to be reduced due to the rejection of a significant fraction of the observational data. However, it is worth noting that for R-band (600—800nm wavelength) and I-band (800—1000nm wavelength) observations, scattered light from the bright reference stars required for high order adaptive optics correction may also limit the sensitivity to faint objects. At these wavelengths the higher limiting magnitude for Lucky Exposures and a potential increase in the isoplanatic patch size are likely to give sky coverage at least one hundredfold greater than that of adaptive optics at the same wavelength. At longer wavelengths the sky coverage will saturate at close to 100%, and the relative benefit over adaptive optics will be smaller.

1.4 Summary of thesis

Chapter 2 will start with a discussion of the timescales for speckle imaging techniques such as the Lucky Exposures method. A number of numerical models for the atmosphere

will be introduced, and the results of these models will be compared to previous experimental measurements. The isoplanatic angle expected for speckle imaging techniques will be calculated for the simulations and compared with data available from astronomical observatories. Simulations will then be used to determine the effect that varying the aperture size has on the quality of short exposure images which can be obtained through atmospheric seeing.

Chapter 3 will present high frame-rate observations of bright stars taken using a conventional CCD camera at the Nordic Optical Telescope (NOT). The impact that the properties of the camera and telescope have on the expected performance of the Lucky Exposures method will be discussed. The data analysis method will be introduced and applied to the observational data. The atmospheric timescales measured at the NOT will be discussed, and the performance of the Lucky Exposures technique will be studied and compared to that of the shift-and-add approach.

Chapter 4 will introduce low noise L3Vision CCD detectors which have recently been developed by E2V Technologies¹. Using simple models for the operation of these devices, the theoretical performance of the detectors will be calculated. These calculations will then be compared with measurements made using real L3Vision CCDs.

Chapter 5 will present high frame-rate observations using the low noise CCDs discussed in Chapter 4. The performance of the Lucky Exposures method using these detectors will be studied in detail, and will be used to demonstrate the applicability of the Lucky Exposures technique to various astronomical programs.

¹E2V Technologies, 106 Waterhouse Lane, Chelmsford, Essex. <http://e2vtechnologies.com/>

Chapter 2

Lucky Exposures

2.1 Introduction

The simulations discussed in Chapter 1.2.2 provided a very simple model for the effect of the atmosphere at a single instant in time. In order to determine the best observational approach for the Lucky Exposures technique, it is important to develop more realistic simulations which also address the time evolution and spatial distribution of atmospheric perturbations above the telescope. The principle model atmospheres investigated here consist of a number of thin moving layers above the telescope, each introducing perturbations following the Kolmogorov model described in Chapter 1.2.1. Each layer is blown at a characteristic wind velocity. These layers introduce position-dependent path length variations into the incoming wavefronts, and are intended to simulate turbulent atmospheric layers with variable refractive index.

In order to apply the Lucky Exposures method to an astronomical target which is too faint or too resolved for accurate measurement of the Strehl ratio of the PSF, an unresolved source must be found which is sufficiently bright to allow Strehl ratio measurements, and which lies within the isoplanatic patch surrounding the target of interest (the isoplanatic patch is the area of sky enclosed by a circle of radius equal to the isoplanatic angle, and will be discussed in more detail in the chapter). The size of the isoplanatic patch which prevails at the times of the selected exposures thus affects the range of astronomical targets for which a suitable reference star can be found for the Lucky Exposures approach. In this chapter the size of the isoplanatic patch around a reference star is calculated for the layered models under different atmospheric conditions. The timescales for changes in the speckle pattern and the isoplanatic angle are found to be determined by similar geometrical effects for these models, which helps to simplify the analysis.

In the last part of the chapter, Monte Carlo simulations of the atmosphere are used to investigate the range of short exposure Strehl ratios which are obtained with a variety

of different telescope diameters and atmospheric conditions. This will be important in determining the applicability of the Lucky Exposures technique at various observatory sites.

I start this chapter with an introduction to measurements of the timescale for changes to speckle patterns in the image plane of a telescope. This will be useful in comparing results from my own simulations with previous observational results.

2.2 Timescale measurements by previous authors

At a number of astronomical observatories in the late 1970s and early 1980s experiments were undertaken which were designed to investigate the timescales for changes in the image plane speckle patterns seen when observing unresolved point sources through large telescopes. Scaddan & Walker (1978); Parry *et al.* (1979); Dainty *et al.* (1981) found that there were two dominant timescales – a slow timescale corresponding to motion of the centroid of the speckle pattern, and a fast timescale corresponding to changes within the speckle pattern. The faster timescale is most relevant to high resolution imaging, and they developed a method for accurately measuring this timescale from the temporal autocorrelation of time-resolved photometric observations at a point in the image plane of the telescope. It will be of interest to compare my results to previous work in the field, so I will give a brief description of their method here.

2.2.1 Normalising the short-timescale component of the autocorrelation

Early investigations of atmospheric timescales typically involved a single high-speed photometer positioned at a single point in the image plane of a telescope. The temporal autocorrelation of a time series of measurements from such a device (i.e. the convolution of the time series with itself) provides a useful time-domain representation of the variance of the photometric flux with time. The long-timescale component of the measured temporal autocorrelation is assumed by Scaddan & Walker (1978) to be separable from the short-timescale component. The long-timescale (low frequency) component varies essentially linearly over the region of the autocorrelation which is of interest to speckle imaging. The solid line in Figure 2.1 shows a schematic representation of a typical temporal autocorrelation curve. The long-timescale component is indicated by the dashed line. In order to remove the effect of the long-timescale component, a linear fit to this component is calculated over the region of the temporal autocorrelation which is of interest for speckle imaging. The measured autocorrelation is then divided by this linear function to remove the long timescale component. The result can then be rescaled so that it ranges from zero to unity, to give the normalised high frequency component of the temporal autocorrelation as shown in Figure 2.2. The atmospheric timescale is the time delay over which this

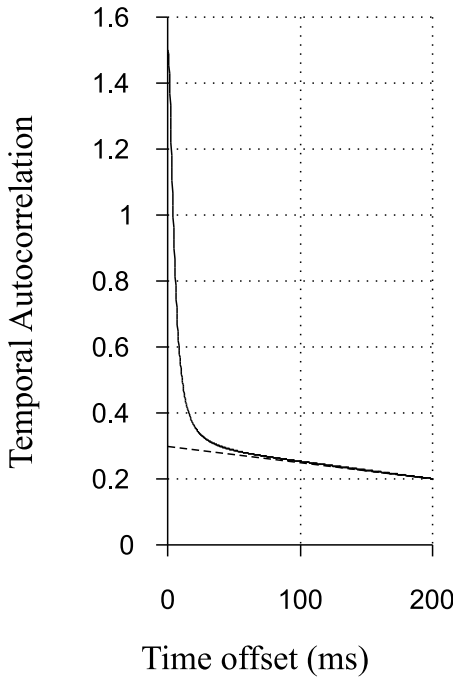


Figure 2.1: Temporal autocorrelation for photometric measurements at a fixed point (solid curve). The dashed line shows a linear fit to the long-timescale fluctuations brought about by motion of the image centroid.

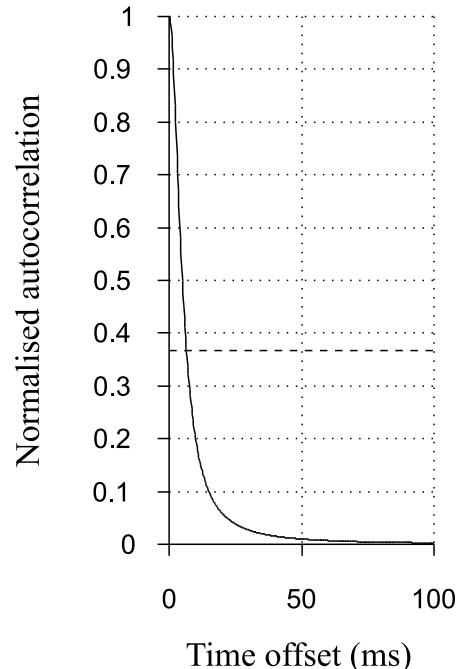


Figure 2.2: Normalised temporal autocorrelation for photometric measurements at a fixed point (solid curve). The dashed line marks a value of $\frac{1}{e}$. The timescale τ_e is 7 ms in this example.

function decays to $1/e$, defined by Roddier *et al.* (1982a); Vernin *et al.* (1991) as τ_e (but known as $\tau_{1/e}^B$ in Scaddan & Walker (1978)). In Figure 2.2, τ_e is marked by the crossing point between the solid curve and dashed horizontal line.

2.2.2 The temporal power spectrum of intensity fluctuations

Aime *et al.* (1986) showed that experimentally measured temporal power spectra of photometric measurements in the image plane of a telescope can be well fitted at high frequencies by negative exponential functions of the form:

$$P(f) = Ae^{(-a|f|)} \quad (2.1)$$

In many of their observations there is excess power at low frequencies, attributed to long-timescale motion of the image centroid (this excess power in the power spectrum is sometimes fitted empirically by adding another exponential term to Equation 2.1).

Equation 2.1 can be used to predict the form of the high frequency component of the

temporal autocorrelation of stellar speckle patterns. After normalisation as described in Chapter 2.2.1, the temporal autocorrelation $C(t)$ corresponding to Equation 2.1 has the form:

$$C(t) = \frac{a^2}{a^2 + t^2} \quad (2.2)$$

The coherence timescale τ_e for the case described by Equation 2.1 will be:

$$\tau_e = a\sqrt{e - 1} \quad (2.3)$$

Many measurements of the atmospheric coherence time τ_e for speckle imaging have been made at a variety of observatory sites. At 500 nm wavelength the measured timescales are usually found to be a few milliseconds or tens of milliseconds (Roddier *et al.* 1990; Vernin & Muñoz-Tuñón 1994; Karo & Schneiderman 1978; Scaddan & Walker 1978; Parry *et al.* 1979; Lohmann & Weigelt 1979; Dainty *et al.* 1981; Marks *et al.* 1999) although Aime *et al.* (1981) report timescales as long as a few hundred milliseconds under good conditions.

It will now be of interest to compare these experimental results and empirical analysis with atmospheric simulations.

2.3 Timescale measurements for atmospheric simulations

In this section I will develop a number of models for the effect of the Earth's atmosphere on astronomical observations. Refractive index fluctuations in the Earth's atmosphere will be included in a number of thin horizontal layers in the model atmospheres. These layers will remain unchanged, but will move at a constant horizontal velocity intended to represent the local wind velocity, as shown schematically in Figure 2.3. Most previous authors (e.g. Conan *et al.* (1995)) have also assumed that the structure of these layers remains unchanged as they are blown past the telescope by the wind. This assumption is based upon the work of Taylor (1938) which argues that if the turbulent velocity within eddies in a turbulent layer is much lower than the bulk wind velocity then one can assume that the changes at a fixed point in space are dominated by the bulk motion of the layer past that point. The wind-blown, unchanging turbulent layers used for simulations are often called *Taylor phase screens*. It should perhaps be noted that Taylor's original argument applied to atmospheric measurements at a single fixed point, and may not be strictly true for the case of a telescope with large diameter. The Earth's curvature can be ignored for such simulations, and the perturbing layers are taken to be parallel planes above the ground surface.

The layered model of atmospheric turbulence used for my simulations is supported by a number of experimental studies at Roque de los Muchachos observatory, La Palma (Vernin

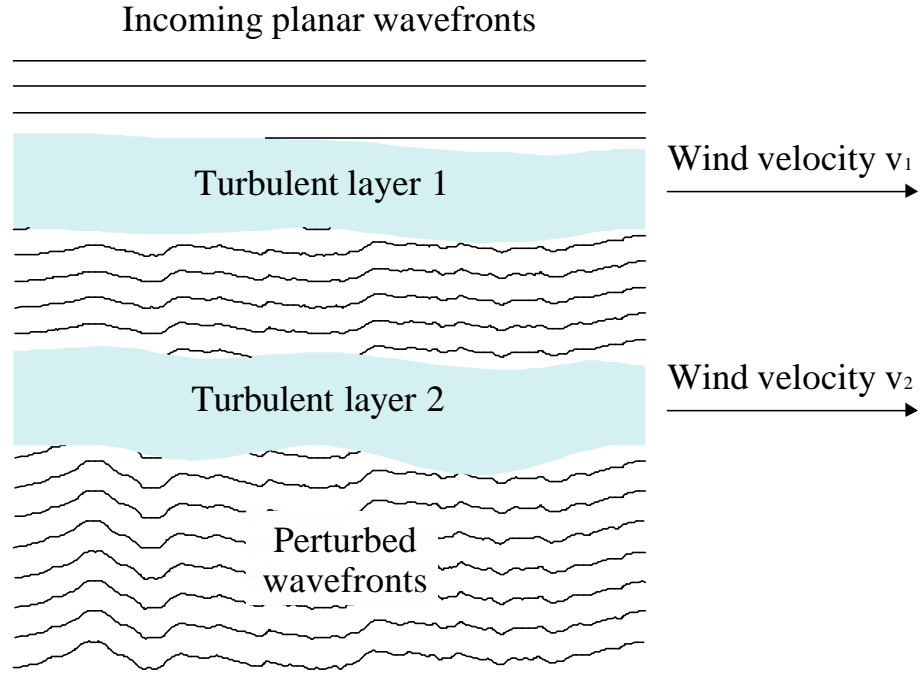


Figure 2.3: When turbulent mixing of air with different refractive indices occurs in the atmosphere, phase perturbations are introduced into starlight passing through it. Experimental measurements at a number of astronomical observatories have indicated that these refractive index fluctuations are usually concentrated in a few thin layers in the atmosphere. Two layers are shown in the above figure, each expected to travel at the local wind velocity.

& Muñoz-Tuñón (1994); Avila *et al.* (1997); Wilson & Saunter (2003)); the model would also provide realistic results for many other good observatory sites.

Following the work of Tatarski (1961), the refractive index fluctuations within a given layer in the simulations can be described by their second order structure function:

$$D_N(\rho) = \left\langle |N(\mathbf{r}) - N(\mathbf{r} + \rho)|^2 \right\rangle_{\mathbf{r}} \quad (2.4)$$

where $N(\mathbf{r})$ is the refractive index at position \mathbf{r} and $D_N(\rho)$ is the statistical variance in refractive index between two parts of the wavefront separated by a distance ρ in an atmospheric layer. For the case of an isotropic turbulent layer following the Kolmogorov model, this structure function D_N depends only on the strength of the turbulence:

$$D_N(\rho) = C_N^2 |\rho|^{2/3} \quad (2.5)$$

where C_N^2 is simply a constant of proportionality which describes the strength of the turbulence. For the case of an atmosphere stratified into a series of horizontal layers, $C_N^2(h)$ can be taken as a function of the height h above ground level. Under these conditions Equation 2.5 will only be valid within a layer of constant C_N^2 .

The phase perturbations introduced into wavefronts by this layered atmosphere can be described by the second order structure function for the phase perturbations (Equation 1.3). This function is dependent on the integral of $C_N^2(h)$ along the light path z and the wavenumber k as follows:

$$D_{\phi_a}(\rho) = 2.91k^2 |\rho|^{5/3} \int_0^\infty dz C_N^2(h) \quad (2.6)$$

($D_{\phi_a}(\rho)$ here is equivalent to $D_S(\rho)$ in Tatarski (1961)).

Equation 2.6 can be more conveniently described in terms of wavelength λ and the angular distance of the source from the zenith γ :

$$D_{\phi_a}(\rho) = \left(115\lambda^{-2} (\cos \gamma)^{-1} \int_0^\infty dh C_N^2(h) \right) |\rho|^{5/3} \quad (2.7)$$

Using Equations 1.4 and 2.7 we can also write r_0 in terms of $C_N^2(h)$:

$$r_0 = \left(16.7\lambda^{-2} (\cos \gamma)^{-1} \int_0^\infty dh C_N^2(h) \right)^{-3/5} \quad (2.8)$$

The amplitude of the refractive index fluctuations described by $C_N^2(h)$ varies only weakly with wavelength λ at red and infra-red wavelengths, so the variation of r_0 with wavelength can be approximated by:

$$r_0 \propto \lambda^{6/5} \quad (2.9)$$

For observations in different wavebands, this relationship determines the physical diameter of telescope which would be suitable for the Lucky Exposures method. The work presented in this thesis was carried out between 0.7 and 1.0 μm . Under good seeing conditions, the $7r_0$ apertures discussed in Chapter 1.2.3 would correspond to between 2 and 3 m diameter telescopes at these wavelengths. For observations in the near infra-red K-band $7r_0$ would correspond to 8 m , while at B-band $7r_0$ telescopes would have 1 or 1.5 m diameter.

Saint-Jacques & Baldwin (2000) undertook detailed atmospheric seeing measurements with the *Joint Observatory Seeing Experiment* (JOSE – Saint-Jacques *et al.* (1997); Wilson *et al.* (1999)) at the William Herschel Telescope, located at the same observatory as the NOT. The experimental setup consisted of an array of Shack-Hartmann sensors capable of measuring the wavefront tilt as a function of position and time in the aperture plane (see Figure 1.9). They found experimentally that the dominant atmospheric phase fluctuations at the William Herschel Telescope (WHT) are frequently associated with a single wind velocity, but also found evidence for gradual change in the phase perturbations applied to wavefronts as the perturbations progressed downwind. This can be explained either by turbulent boiling taking place within an atmospheric layer as it is blown past the telescope, or by the turbulence associated experimentally with one layer actually being distributed in several separate screens, with a narrow range of different wind velocities for the each

of the screens (distributed about the measured mean wind velocity). This evolution of the turbulent structure for an atmospheric layer is consistent with the decorrelation with time of turbulent layers found by Caccia *et al.* (1987), although unlike Roque de los Muchachos observatory they found the typical atmosphere above Haute-Provence to have several such turbulent layers travelling at distinctly different wind velocities. Similar experiments were undertaken using binary stars at the WHT by Wilson (2003). The SLODAR technique (Wilson 2002) was applied to these binary observations to obtain the heights of the turbulent layers as well as their wind velocities. Preliminary results provided by Wilson (2003) indicated that several turbulent layers with very different wind velocities were present on some of the nights. On at least one night, most of the turbulence was found at very low altitude above the WHT, and it is not necessarily certain that the same conditions would be present at the NOT further up the mountain.

For my numerical simulations I have ignored the possibility of turbulent boiling taking place within individual atmospheric layers because of the lack of a suitable mathematical model for the boiling process. Models which are free of boiling but which have multiple Taylor screens with a scatter of wind velocities describing each individual atmospheric layer can adequately fit existing experimental results, and these are the most widely used models for atmospheric simulations. This form of multiple Taylor screen model is usually known as a *wind-scatter* model.

Each of the atmospheric layers has a characteristic velocity for bulk motion (v_1 and v_2 for the two layers in Figure 2.3) corresponding to the mean local wind velocity at the altitude of the layer.

2.3.1 Atmospheric models

The temporal statistics of the wind-scatter models introduced in Chapter 2.3 are discussed in some detail by Roddier *et al.* (1982a); Aime *et al.* (1986). They highlight the fact that the timescale for speckle imaging at a large well-figured telescope is expected to be rather different to the timescale for Shack-Hartmann sensing or for adaptive optics correction. This is an important point, and I will introduce a simplified model to help explain it in Chapter 2.3.2 and Appendix A. An essentially identical argument can be used to explain the differing isoplanatic angles provided by speckle imaging techniques and non-conjugate adaptive optics.

For large telescopes and significant dispersion in the bulk velocities for the turbulent screens, the coherence time τ_e of speckle patterns is shown by Roddier *et al.* (1982a); Aime *et al.* (1986) to depend on Δv , the standard deviation of the distribution of wind

velocities $v(h)$ weighted by the turbulence $C_N^2(h)$ profile:

$$\Delta v = \left[\frac{\int_0^\infty |v(h)|^2 C_N^2(h) dh}{\int_0^\infty C_N^2(h) dh} - \left| \frac{\int_0^\infty v(h) C_N^2(h) dh}{\int_0^\infty C_N^2(h) dh} \right|^2 \right]^{1/2} \quad (2.10)$$

The precise relationship between Δv and τ_e depends on the model for the temporal correlation. Roddier *et al.* (1982a) use a Gaussian model, predicting that τ_e will be given by:

$$\tau_e = 0.36 \frac{r_0}{\Delta v} \quad (2.11)$$

While Aime *et al.* (1986); Vernin *et al.* (1991) use a Lagrangian model to give:

$$\tau_e = 0.47 \frac{r_0}{\Delta v} \quad (2.12)$$

For smaller telescopes (but still with aperture diameter $d \gg r_0$) or for a case with little dispersion in the wind velocities, the wind crossing time of the aperture may be shorter than the timescales of Equations 2.11 and 2.12. In this case the timescale τ_e will be set by the wind crossing time, as discussed for large apertures in the next section. The timescale for the motion of the image centroid in a Shack-Hartmann sensor will usually be set by the wind-crossing time of the Shack-Hartmann subaperture. If the outputs of different Shack-Hartmann sensors in an array are cross-correlated the decorrelation timescale for the atmospheric phase perturbations relevant for speckle imaging can be calculated (see e.g. Saint-Jacques & Baldwin (2000)).

2.3.2 Single Taylor screen model

One of the simplest temporally varying models for the atmosphere is that of a single Taylor screen moving at a constant wind velocity. The simplicity of this model has made it appealing to a number of previous authors. Roddier *et al.* (1982a); Lopez & Sarazin (1993) note that for speckle imaging at large apertures this model can provide quite different temporal characteristics to models with multiple Taylor screens having a scatter of different wind velocities. For this reason I will introduce a simplified model for a single wind-blown Taylor screen atmosphere which will help in highlighting the unusual properties of these atmospheres.

As discussed above and in Roddier *et al.* (1982a); Aime *et al.* (1986), if the scatter Δv is small the timescale for changes in the image plane will be related to the wind crossing time of the telescope aperture. This will certainly apply for the case of a single Taylor screen atmosphere as in this case Δv is zero. A demonstration of this relationship is given for a simplified approximation to a single Taylor screen atmosphere in Appendix A. The timescale τ_e for changes to the speckle pattern in a telescope aperture of diameter d for

Model	Layer velocities	Δv
1	Single layer of turbulence moving at a speed of $0.15r_0$ per timestep	0
2	Two layers with equal turbulent strength, moving at $0.12r_0$ per timestep and $0.18r_0$ per timestep respectively	$0.03r_0$ per timestep

Table 2.1: A brief summary of the two model atmospheres investigated. The third column shows the scatter in the wind velocities calculated using Equation 2.10.

this simplified model is found to be:

$$\tau_e = \frac{0.31d}{|\mathbf{v}|} \quad (2.13)$$

for a constant wind velocity \mathbf{v} (Equation A.16).

It is interesting to note that τ_e is independent of the atmospheric coherence length r_0 with the simple model used for a single layer of atmospheric turbulence.

2.3.3 Numerical simulations

A number of numerical simulations were undertaken to investigate the temporal properties of Taylor screen models more rigorously. Initially, two models were investigated, the first with a single Taylor screen moving at a constant wind speed as discussed in Chapter 2.3.2, the second having two equal Taylor screens with slightly different wind speeds but the same wind direction. The properties of the two models are summarised in Table 2.1. The Taylor phase screens used had Kolmogorov turbulence extending to an outer scale of $683r_0$, with no power on spatial frequencies larger than this. The size of the outer scale was determined by the available computer memory. Both simulations produced wavefront perturbations with the same coherence length r_0 . Images from filled circular apertures with diameters between $3r_0$ and $10r_0$ were generated at a large number of discrete time points.

Photometric measurements were made at a fixed point in the image plane corresponding to each of the simulated apertures at each time point, and the temporal autocorrelation of this data was calculated. Figure 2.4 shows two example autocorrelations for an aperture diameter of $7r_0$. There is relatively good agreement between the model of Aime *et al.* (1986) (Equation 2.2) and the normalised autocorrelation data from numerical simulations up to time differences corresponding to the coherence timescale τ_e . For larger time differences Equation 2.2 tends quickly to zero, while the simulation data usually drifted either side of zero somewhat. This may be due to the limited timescale of the simulations (a few hundred times τ_e , which is not long enough to average very many realisations of the longer timescale changes in the speckle pattern). Similar results were found for all of

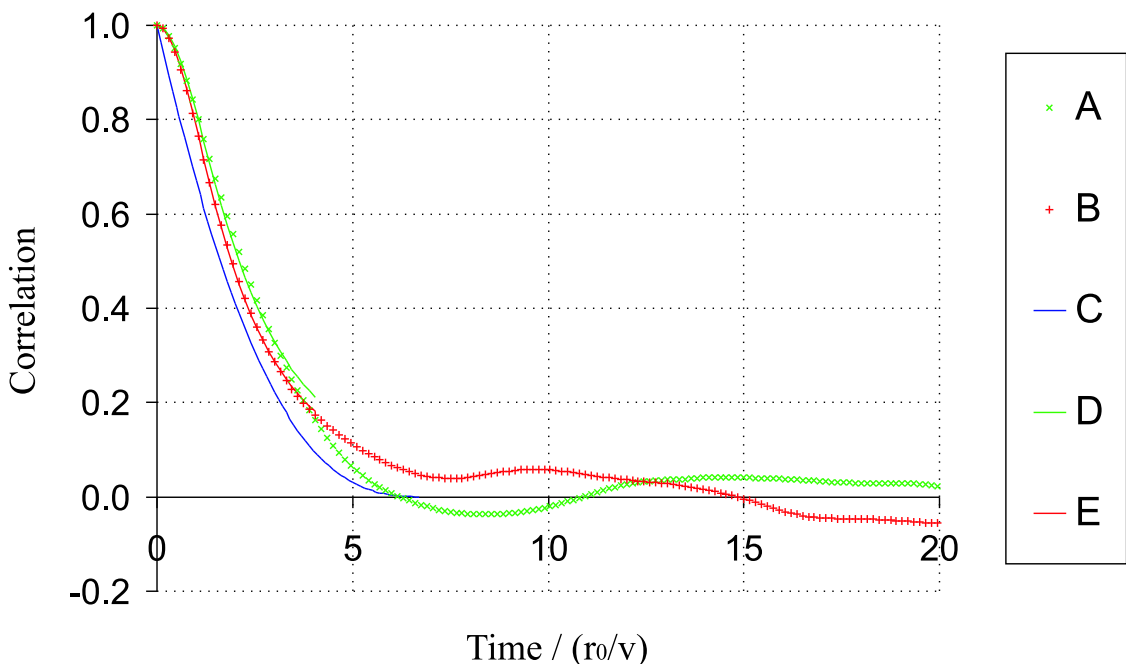


Figure 2.4: Two examples of the temporal autocorrelation curves generated from numerical simulations (and used to produce Figure 2.5). The curves have been normalised using the method described in Chapter 2.2.1. **A** shows the result for a single layer atmosphere and **B** for a two-layer atmosphere (models 1 and 2 from Table 2.1 respectively). **C** shows the predicted decorrelation using the highly simplified model for a single layer atmosphere described in Appendix A. **D** and **E** show least-squared fits of the form of Equation 2.2 to the early parts of curves **A** and **B** respectively.

the aperture diameters simulated, and the temporal power spectra were found to agree with the model of Aime *et al.* (1986).

The coherence timescale τ_e was then calculated from each simulation using the method described in Chapter 2.2.1. A plot of the variation of the coherence timescale with telescope aperture diameter is shown in Figure 2.5.

The red line in Figure 2.5 is a linear regression fit to the measured timescale τ_e for simulations with a single Taylor screen. The equation for this best fit line is:

$$\tau_e = \frac{0.33(d + 2.0r_0)}{|v|} \quad (2.14)$$

The timescale appears to depend approximately linearly on the aperture diameter d , as predicted in Appendix A. The value of τ_e was found to be larger than predicted by my simplified model by a constant amount $\sim 2r_0/|v|$. This is consistent with a small region of the atmospheric layers extending $\sim r_0$ into areas *A* and *C* in Figure A.3 being correlated with the phase perturbations in area *B*. The same hypothesis would explain why the measured temporal autocorrelations shown in Figure 2.4 as curves **A** and **B** lie to the

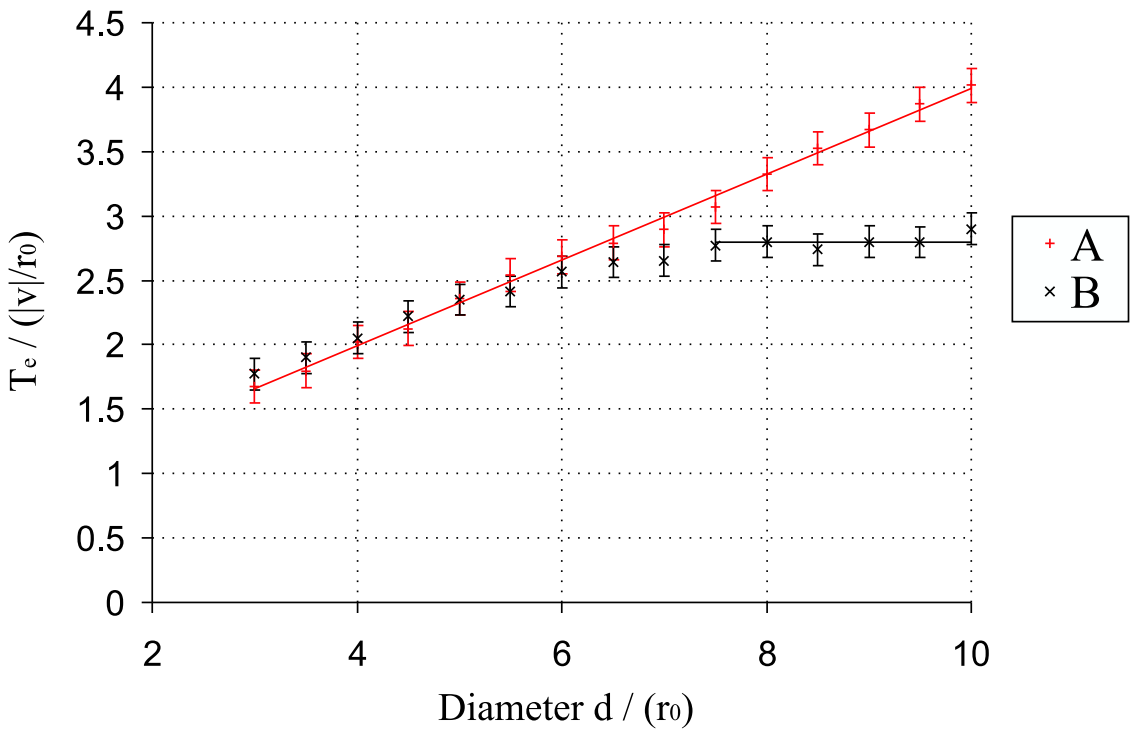


Figure 2.5: Timescale τ_e for a range of aperture diameters, for the two atmospheric models. Curve **A** shows the result for a single Taylor screen of frozen Kolmogorov turbulence. **B** is a similar plot for the two layer atmosphere listed as model 2 in Table 2.1. The error bars simply indicate the standard error of the mean calculated from the scatter in results from a number of repeated Monte Carlo simulations. Errors in the measurements at different aperture diameters are partially correlated as the same realisations of the model atmospheres were used for all the aperture diameters shown. The red line is described by Equation 2.14 and the black horizontal line is at the value given in Equation 2.15.

right of the prediction corresponding to my simplified model (curve **C**) over the left-hand part of the graph.

For small aperture diameters, the simulations with a two-layer atmosphere have very similar timescales to those with a single atmospheric layer. However there is a knee at $D \simeq 6r_0$, and at diameters larger than this the timescale τ_e appears to be constant at:

$$\tau_e \sim 2.8 \frac{r_0}{|v|} \quad (2.15)$$

where $|v|$ is the average wind velocity for the two layers. It is of interest to compare this timescale with that predicted by Equations 2.11 and 2.12. For this atmospheric model, the wind scatter Δv is equal to:

$$\Delta v = 0.2 |v| \quad (2.16)$$

The timescale τ_e can be written in terms of Δv :

$$\tau_e \sim 0.56 \frac{r_0}{\Delta v} \quad (2.17)$$

This is larger than the timescales predicted by both Equation 2.11 (from Roddier *et al.* (1982a)) and Equation 2.12 (from Aime *et al.* (1986)). The result of Aime *et al.* (1986) is within 3σ of these simulations however (remembering that the errors in the simulations are correlated for different aperture diameters).

Figure 2.5 implies that the timescale for changes in the speckle pattern found at the focus of a well figured astronomical telescope may increase somewhat with aperture diameter if the atmospheric turbulence is moving with a common wind velocity. This would not be the case if there is a substantial scatter in the wind velocities, as the timescale saturates at a level close to that predicted by Equation 2.12. Vernin & Muñoz-Tuñón (1994) found that the scatter in the velocities of the turbulent layers above the NOT is small enough that the timescale for speckle patterns using the full aperture of the NOT should be twice the timescale which would be found with small apertures, or that for standard adaptive optics correction. This is consistent with measurements by Saint-Jacques & Baldwin (2000) which indicated that a single wind velocity (or narrow range of wind velocities) dominates above La Palma. This contrasts with results at a number of other observatories (e.g. Roddier *et al.* (1993); Caccia *et al.* (1987); Parry *et al.* (1979); Vernin & Roddier (1973)) where either strong turbulence is found in several layers with differing wind velocities, or there is little evidence for any bulk motion of the atmospheric perturbations across the telescope aperture. Wilson (2003) also found evidence for significant dispersion in the wind velocities above the WHT on some nights.

2.4 Isoplanatic angle for atmospheric simulations

The light from two astronomical objects which are separated on the sky by a small angle will travel on slightly different paths through the Earth's atmosphere, as shown schematically in Figure 2.6. If layers of turbulence exist within the atmosphere, the light from the two objects will travel through slightly different parts of each turbulent layer. For two objects separated by a small angle $\Delta\theta$, the offset x in the position of the light paths as they intersect a layer at a height h is given by:

$$x = h\Delta\theta \quad (2.18)$$

as demonstrated in Figure 2.6. If the offset x between the paths is sufficiently large, the atmospheric perturbations applied to light from the two astronomical targets will differ. This variation in the atmospheric perturbations with angle is closely analogous to the change in the atmospheric perturbations as time elapses and the atmospheric layers move past the telescope in the wind scatter model described in Chapter 2.3.3. Whereas the motion of the atmospheric layers as a function of time was determined by the wind velocities for the wind-scatter case, the relative motion of the atmospheric layers as a function of angular separation from the reference star is determined by the heights of the layers above the telescope.

The angular separation at which the atmospheric perturbations applied to the light from the two stars becomes uncorrelated is called the *isoplanatic angle*. For a wind scatter model consisting of thin Taylor screens, the calculation of the isoplanatic angle is undertaken in an identical manner to the calculation of the timescale for decorrelation of the speckle pattern described above. The numerical simulations investigating the effect of relative motions of atmospheric layers on the image plane speckle pattern in Chapter 2.3.3 would be equally applicable to the study of isoplanatic angle, and the results can be used here directly. The similarity between the temporal properties and isoplanatic angle for wind-scatter models has been noted by a number of previous authors including Roddier *et al.* (1982a).

The calculation of the isoplanatic angle for atmospheres consisting of a number of layers of Kolmogorov turbulence is described in Roddier *et al.* (1982b), following a similar argument to that for atmospheric coherence time calculations described in Roddier *et al.* (1982a). The isoplanatic angle is inversely proportional to the weighted scatter Δh of the turbulent layer heights:

$$\Delta h = \left[\frac{\int h^2 C_N^2(h) dh}{\int C_N^2(h) dh} - \left(\frac{\int h C_N^2(h) dh}{\int C_N^2(h) dh} \right)^2 \right]^{1/2} \quad (2.19)$$

If the atmospheric turbulence is concentrated in a narrow altitude range, then the isoplanatic angle for short exposure imaging will increase with telescope diameter in a fashion

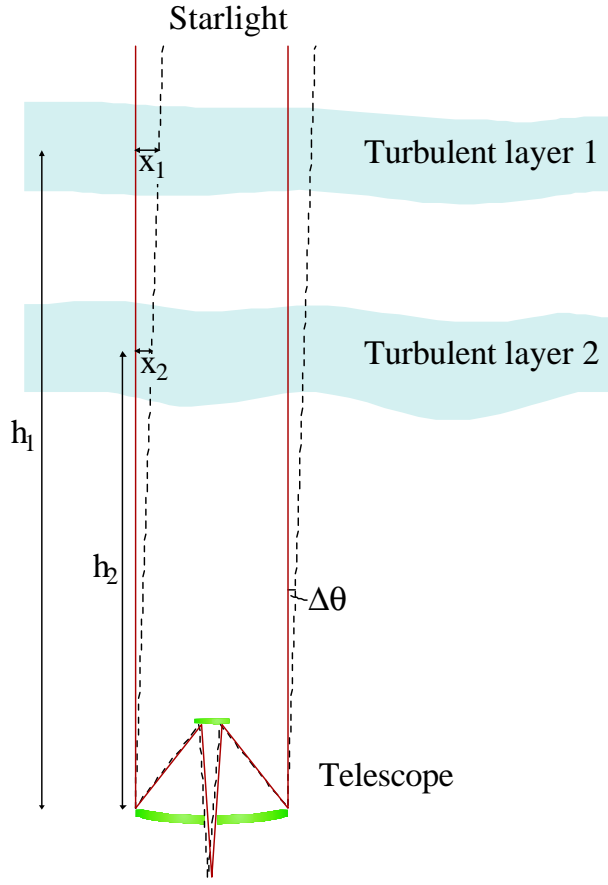


Figure 2.6: Schematic showing off-axis observations through an atmosphere with two turbulent layers. The off-axis beam passes through the turbulent layers at a position which is offset by an amount proportional to the height of the layer above the telescope (and indicated by x_1 and x_2 in the figure).

exactly analogous to the dependence of the speckle timescale τ_e on telescope diameter for the wind scatter model described in Chapter 2.3.3.

The decorrelation of the speckle pattern for a target with increasing angular distance θ from a reference star is expected to follow a similar relationship to that for the temporal decorrelation of a speckle pattern (Equation 2.2). The cross-correlation of the speckle patterns $C(\theta)$ should thus obey the relationship:

$$C(\theta) = \frac{a^2}{a^2 + \theta^2} \quad (2.20)$$

where a depends on the relative separations of the atmospheric layers.

I have not repeated the numerical simulations here for the case of isoplanatism as the new simulations would be computationally identical to those performed for the measurements of the timescale τ_e – the only difference would be in the units used. The vertical axis in Figure 2.5 is labelled τ_e , but it could equally have been labelled isoplanatic angle θ_e . The plot would then correspond to the variation in isoplanatic angle as a function of telescope

diameter for two models of the atmosphere. The model corresponding to curve **A** would be an atmosphere with a single layer at an altitude of h , with the isoplanatic angle θ_e on the vertical axis plotted in units of $\frac{r_0}{h}$ radians. The model corresponding to curve **B** would have two layers each with half the value of C_N^2 and at altitudes of $0.8h$ and $1.2h$.

A number of different measures of the isoplanatic angle have been suggested in the literature. In order to provide consistency with the discussion of atmospheric timescales in Chapters 2.2 and 2.3, I will take the isoplanatic angle θ_e for speckle imaging to be that at which the correlation of the speckle pattern for two objects drops to $\frac{1}{e}$ of the value obtained near the reference star. For an atmosphere consisting of Taylor screens, the value of θ_e will be dependent on the relative motions of the Taylor screens with angle in same way as τ_e depends on the relative motions with time. For the model described by Equation 2.20, θ_e will be:

$$\theta_e = (\sqrt{e - 1}) a \quad (2.21)$$

Vernin & Muñoz-Tuñón (1994) suggest the isoplanatic angle for short exposure imaging with the full aperture of the NOT will be significantly larger than the isoplanatic angle expected for non-conjugate adaptive optics (or for interferometric techniques involving small apertures). This is due to the turbulent layers being distributed over a narrow range of heights above the telescope. With non-conjugate adaptive optics the isoplanatic angle is determined by the typical height of the turbulence (whereas with large telescope apertures the isoplanatic angle for speckle imaging techniques such as Lucky Exposures is related to the scatter of different altitudes Δh over which the turbulence is distributed rather than the absolute height). In calculating the isoplanatic angle for non-conjugate adaptive optics, the deformable mirror (typically positioned in a re-imaged pupil plane) can be treated like an additional layer of atmospheric turbulence which cancels out the phase perturbations along one line of sight, but contributes additional perturbation for objects significantly off-axis.

Measurements of the isoplanatic angle for speckle imaging at a number of observatories have typical given values in the range 1.5 as to 5 as for observations at 500 nm wavelength (see e.g. Roddier *et al.* (1982a); Vernin & Muñoz-Tuñón (1994)). The isoplanatic angle for speckle observations is expected to be about 70% larger than that for adaptive optics, based on measurements by Vernin & Muñoz-Tuñón (1994). The isoplanatic angle for observations at I-band should be a further factor of two larger due to the relationship between the coherence length r_0 and the wavelength (Equation 2.9).

2.5 Exposure selection from simulated data

In order to determine the performance of the Lucky Exposures technique under a variety of different conditions, the simulations described in Chapter 2.3.3 were used to generate

a large number of short exposure images for each of the aperture diameters. The Strehl ratio of the short exposure images describes the fraction of the light which resides in a diffraction-limited core of the PSF. It is a very good indicator of how useful the exposures are for high-resolution imaging, as the light in the core of the PSF maps out the sky brightness distribution at high resolution, while the remaining light is distributed in the wings of the PSF and contributes largely to the noise in the image. In a speckled image the PSF core corresponds to the location of the brightest speckle. The offset in position of the PSF core and the distribution of light in the wings vary with the coherence timescale of the atmosphere. If a large number of short exposures are re-centred with respect to the core of the PSF and co-added, the contribution from the wings of the PSF will be averaged into a smooth halo, while the diffraction-limited information from the compact core of each PSF will remain (see e.g. Christou (1991)).

Figure 2.7 shows histograms of the measured Strehl ratios for the short exposures simulated with a variety of different aperture diameters (where the aperture diameter is described in terms of the atmospheric coherence length r_0). It is clear that the probability of obtaining a high Strehl ratio short exposure diminishes rapidly with increasing aperture size. If the investigator chooses to select the best 1% of exposures of an unresolved source using an aperture of diameter $d = 7r_0$, and to re-centred and co-add these exposures, the final image will have a Strehl ratio of 30%—35%. There will be approximately twice as much light in a diffuse halo as is found in the core of the PSF. If the aperture diameter is increased slightly to $d = 10r_0$, the PSF core in the selected exposures will be reduced slightly in diameter, but the diffuse halo will contain five times as much flux as the image core. For most imaging applications, the marginal gain in resolution is more than offset by the increased flux in the wings of the PSF, confirming that a $d \sim 7r_0$ aperture represents the largest which will provide high quality imaging using 1% of the short exposures. If larger fractions of exposures are selected, it may be beneficial to use a slightly smaller aperture diameter.

It is of interest to compare these results to the model of Fried (1978). He described the wavefronts entering a circular aperture in terms of the phase variance σ_ϕ^2 from a best-fitted planar wavefront. Using Monte Carlo simulations, Fried calculated the probability that this variance σ_ϕ^2 would be less than 1 radian². From these results he produced the following model for the probability P of good exposures:

$$P \simeq 5.6 \exp \left(-0.1557 \left(\frac{d}{r_0} \right)^2 \right) \quad (2.22)$$

given an aperture size d greater than $3.5r_0$. Englander *et al.* (1983) compared the fraction of good images predicted by this model with the fraction of Lucky Exposures observed in ground-based imaging experiments and found agreement within the accuracy of the experimental measurements.

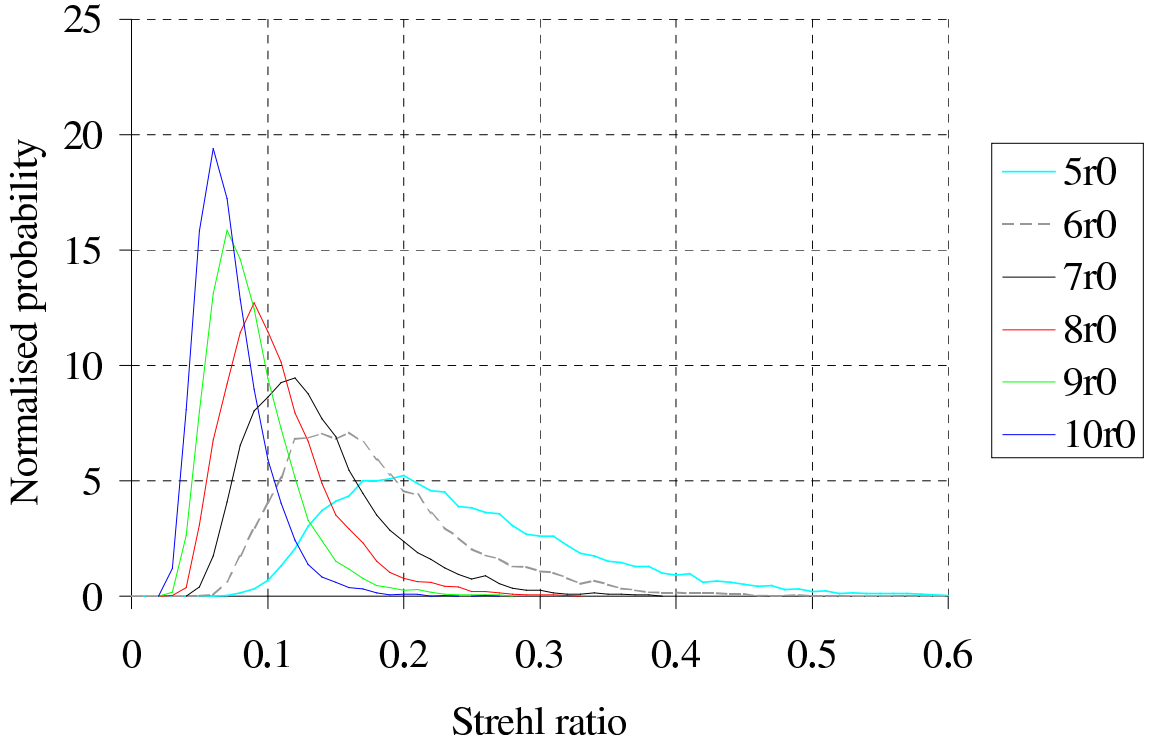


Figure 2.7: Strehl ratios obtained from simulated short exposures with a range of different aperture diameters. The two atmospheric models gave similar distributions of Strehl ratios.

The instantaneous Strehl ratio on axis S_a obtained in the image plane of a simple imaging system can be determined by integrating the probability distribution for the wavefront phase variance across the aperture plane to give:

$$S_a \sim \exp(-\sigma_\phi^2) \quad (2.23)$$

For small values of σ_ϕ^2 this on-axis Strehl ratio will be approximately equal to the image Strehl ratio S which we are interested in.

The criteria of selecting exposures when the phase variance $\sigma_\phi^2 \leq 1$, Equation 2.23 would imply an image Strehl ratio $S \gtrsim 0.37$ (taking the approximation that the on-axis Strehl ratio represents the true Strehl ratio for the image). Figure 2.8 shows the fraction of exposures having a Strehl ratio greater than 0.37 in my simulations plotted against Fried's model. There is excellent agreement for aperture diameters greater than $4r_0$.

One measure of image quality which incorporates both the Strehl ratio S and the diffraction-limited resolution of the telescope diameter d is the Strehl resolution \mathcal{R} , defined as:

$$\mathcal{R} = \frac{\pi S}{4} \left(\frac{d}{\lambda} \right)^2 \quad (2.24)$$

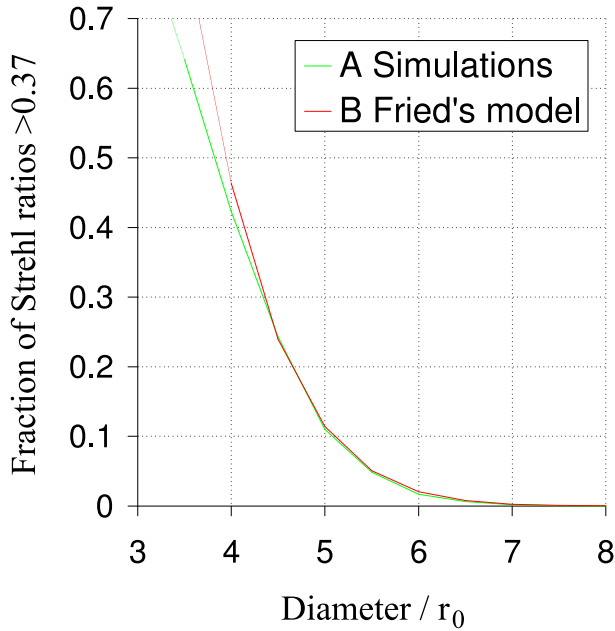


Figure 2.8: Curve **A** shows the fraction of the exposures with a Strehl ratio greater than 0.37 in each simulation, plotted against the aperture diameter measured in terms of the atmospheric coherence length r_0 . Equation 2.22 is plotted as curve **B**. This is the model of Fried (1978) for the fraction of exposures where the wavefronts deviate by less than 1 radian RMS from a flat plane, and are expected to have Strehl ratios greater than 0.37.

If the best 1% of exposures are selected, Hecquet & Coupinot (1985) showed that the Strehl resolution achieved is greatest for apertures with diameters between $4r_0$ and $7r_0$. The Strehl resolution decreases relatively quickly for apertures larger than $7r_0$. The Strehl resolution does not represent a true measure of the image *resolution* in this application as the FWHM of the PSF core continues to get smaller with increasing aperture diameter beyond $d = 7r_0$. The Strehl ratio and image FWHM separately provide a more useful description of the short exposure images, and I will generally use these parameters in describing the quality of the PSF.

2.6 Conclusions

In this chapter I have discussed the timescales for high resolution imaging found both in experimental work by other authors and in my own simulations. The temporal properties at a point in the telescope image plane for simulated observations are compared with experimental measurements and found to agree qualitatively. For atmospheres with a small scatter in the wind velocities the coherence timescale for speckle observations is found to be proportional to the telescope diameter, as predicted by Roddier *et al.* (1982a); Aime *et al.* (1986). This coherence timescale is expected to be significantly longer than the coherence time applicable to current designs for adaptive optics systems. Measurements made at the

NOT by Vernin & Muñoz-Tuñón (1994) suggest that a factor of two increase in coherence timescale would be expected for speckle imaging at this telescope. The dependence of the atmospheric coherence time on the C_N^2 profile and telescope aperture diameter is found to agree with the predictions of Aime *et al.* (1986) for the two atmospheric models tested, apart from a small difference in the constant multiplying factor for one of the atmospheric models.

A direct analogy can be drawn between the calculation of the coherence time for speckle imaging and the isoplanatic angle. The agreement between the timescales measured for simulations and previous theoretical predictions thus also indicates agreement between the isoplanatic angle measured in simulations and theoretical predictions. Measurements by Vernin & Muñoz-Tuñón (1994) suggest that the isoplanatic angle for speckle observations should be approximately 70% larger than that which would be obtained for adaptive optics at the NOT site. The isoplanatic angle at I-band is predicted to be between 3 and 5 *as* from the results of Vernin & Muñoz-Tuñón (1994).

The fraction of short exposures with a Strehl ratio greater than 0.37 in numerical simulations is found to be consistent with the Monte Carlo simulations of wavefront perturbations by Fried (1978). The maximum aperture diameter for which exposures with a high Strehl ratio (> 0.3) are frequently obtained is shown to be approximately $7r_0$. The probability of obtaining good exposures decreases very rapidly for larger aperture diameters.

Chapter 3

Observations of bright sources at the NOT

3.1 Introduction

On 2000 May 12 and 13, high frame-rate observations of bright stars were undertaken at the NOT in order to obtain experimental verification of the Lucky Exposures method and test its applicability to astronomical observations. These observations were designed to investigate the timescales appropriate for Lucky Exposures and the image quality which could be obtained using the technique. Results from the observations are presented in this chapter. Some of the results presented here were previously published by the author and collaborators in Baldwin *et al.* (2001).

The short exposure Strehl ratios obtained at the NOT will be compared with theoretical predictions, and the image quality obtained using different exposure selection criteria for the Lucky Exposures method will be investigated.

The chapter will begin with a discussion of the background to the experimental measurements, and the practical implementation of the Lucky Exposures method to the experimental data taken at the NOT.

3.2 Experimental method

3.2.1 Background

During the 1990s the COAST group in Cambridge developed a high frame-rate CCD camera for use in the JOSE seeing monitor based at the William Herschel Telescope on La Palma. The high sensitivity of this camera, and the possibility of adjusting the frame



Figure 3.1: During the summer months the NOT telescope is usually above the thermal inversion layer(s). An inversion layer is typically found at the height of the cloud deck, seen here below the telescope.

rate and the area of the CCD to be read out made it an ideal choice for experimental observations using the Lucky Exposures method. The unthinned CCD within the camera had a peak sensitivity between $\sim 500\text{ nm}$ and $\sim 900\text{ nm}$ (around the R and I astronomical wavebands).

The optimum aperture size to use for the Lucky Exposures method depends on a compromise between the probability of obtaining a short exposure with a high Strehl ratio and the limiting magnitude of reference star that can be used. The numerical simulations presented in Chapter 2.3.3 suggested that this compromise would be met for telescopes with diameter d seven or eight times greater than the atmospheric coherence length r_0 . The value of r_0 depends both on the atmospheric conditions and the wavelength at which the observations are undertaken, as described by Equations 2.8 and 2.9. r_0 is estimated to be 35 cm at I-band under the median summer seeing conditions at the NOT site (Muñoz-Tuñón *et al.* 1997; Vernin & Muñoz-Tuñón 1994), making the 2.56 m aperture of this telescope ideally suited to Lucky Exposures experiments in this waveband at this time of year. The exceptionally good astronomical conditions at this site in the summer can be partially attributed to the thermal inversion layer(s) usually being at a lower altitude than the observatory (Figure 3.1).

In May 2000 high frame-rate imaging observations were undertaken by John Baldwin, Craig Mackay and Graham Cox at the NOT using the JOSE camera. In order to accurately

characterise the temporal characteristics of the atmosphere, the observations were made with high frame rates with no autoguider in operation. All of the stars observed were relatively bright (with $I < 6$) allowing the shape of the stellar PSF to be recorded with high signal-to-noise in each short exposure.

3.2.2 The effect of mirror aberrations

Adjustments to the primary mirror supports of the NOT by Michael Anderson and Anton Sørensen (Andersen & Sørensen 1996; Sørensen 2002) are understood to have given the NOT an extremely good mirror figure for zenith angles less than $\sim 50^\circ$. After the adjustments had been made the small residual errors were found to vary with telescope pointing, but a detailed description of these variations is not available to me at the time of writing.

In order to investigate the possible impact of any remaining aberrations, I undertook simulations with various different levels of mirror aberration. In the absence of direct measurements of the mirror shape after the adjustment to the actuators had been made I have suggested two models for the mirror aberrations as follows:

Model 1 represents a “worst-case scenario”, with no improvement to the mirror aberrations after adjustment of the mirror supports. The mirror aberrations are taken directly from measurements of wavefront curvature made *before* the mirror actuators were adjusted (these measurements were provided by Sørensen (2002)). There is no defocus component in the model. The wavefront errors are shown as a function of position in the aperture plane in Figure 3.2.

Model 2 is identical to model 1 except that mirror aberrations on scales larger than the mean separation between adjacent mirror supports have been strongly suppressed. It is intended to represent a “best-case scenario”, with near-optimal corrections to the mirror supports. The wavefront errors for model 2 are shown in Figure 3.3. It is understood that the residual wavefront errors at the NOT were small after the mirror actuators had been adjusted, hence the real shape of the primary mirror was probably similar to that shown in model 2.

Models 1 and 2 are intended to represent the two extremes of negligible improvement and near-optimal improvement. A third model investigated for purposes of comparison was that of a diffraction-limited mirror. The three models are summarised in Table 3.1

For each of the models the telescope PSF in the absence of the atmosphere was generated using an FFT (as described in Chapter 1.2.2). The PSF Strehl ratios obtained were 0.23, 0.87 and 1.00 for models 1, 2 and 3 respectively.

For the numerical simulations based upon these models, the secondary supports were ignored, and the telescope aperture was modelled as an annulus with inner radius r_s equal

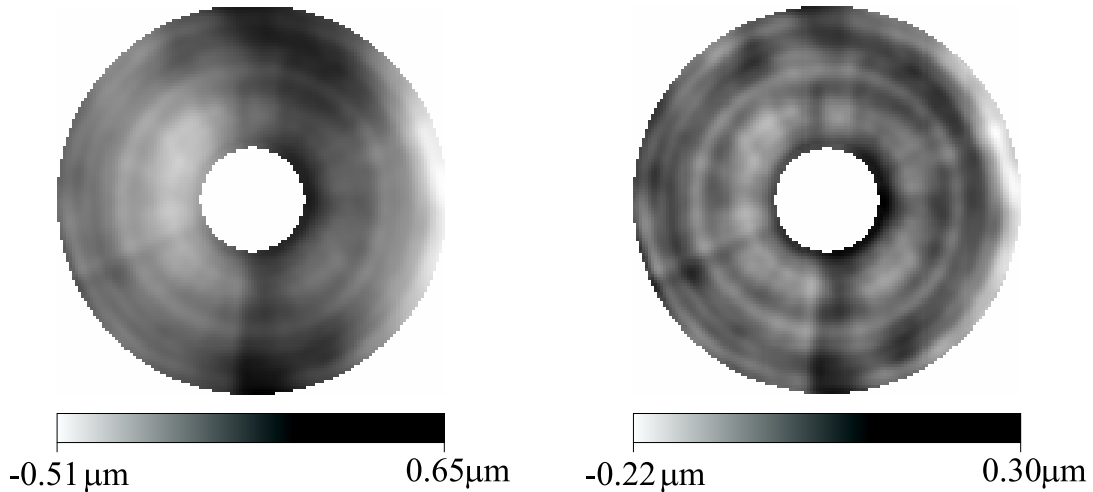


Figure 3.2: Greyscale map of the phase aberrations in the NOT aperture provided by Sørensen (2002).

Figure 3.3: Phase map of the NOT aberrations with structure on large spatial scales subtracted. Note that the greyscale is different to Figure 3.2.

Model	Description of phase aberrations
1	as measured before adjustment of mirror supports
2	estimated aberrations after adjustment
3	a diffraction-limited mirror

Table 3.1: A brief summary of the three models used for the NOT mirror aberrations.

to that of the secondary obscuration, and outer radius r_p determined by the radius of the primary mirror (as shown in Figure 3.4). The shape of the aperture used in the simulations can be described mathematically in terms of the throughput $\chi_t(r)$ as a function of radius r (in the same way as for Equation 1.7):

$$\chi_t(r) = \begin{cases} 0 & \text{if } |\mathbf{r}| < r_s \\ 1 & \text{if } r_s \leq |\mathbf{r}| \leq r_p \\ 0 & \text{if } |\mathbf{r}| > r_p \end{cases} \quad (3.1)$$

For the NOT, $r_p = 2.56\text{ m}$ and $r_s = 0.70\text{ m}$.

For each model, many realisations of atmospheric phase fluctuations that had a Kolmogorov distribution with r_0 seven times smaller than telescope diameter were calculated. These Kolmogorov distributions had a large outer scale (approximately thirty times the telescope diameter). The phase perturbations from the telescope mirror for each model were added to the simulated atmospheric phase distribution, and short exposure images

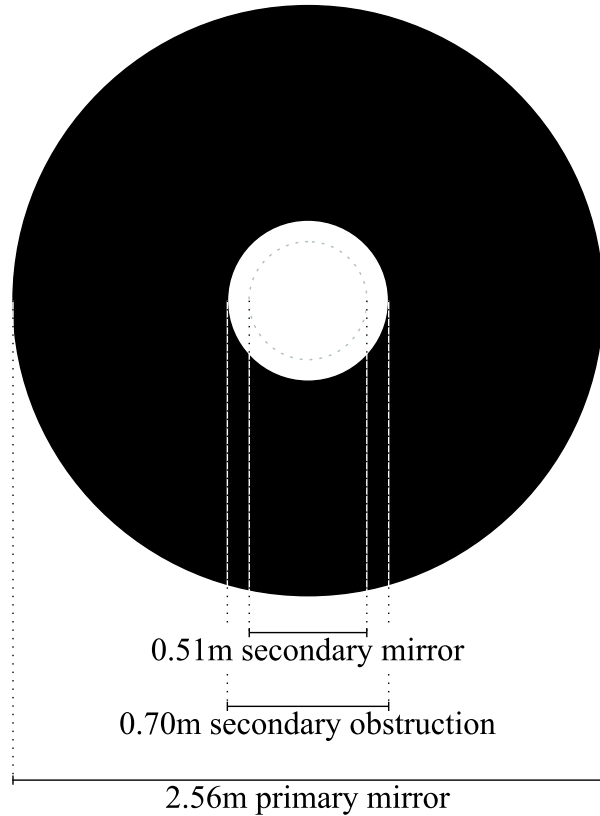


Figure 3.4: The geometry of the NOT aperture

were generated using the aperture shape described by Equation 3.1. The mirror aberrations in models 1 and 2 produce a reduction in the typical Strehl ratios for the short exposure images when compared with the diffraction-limited case. Histograms showing the frequency distribution of Strehl ratios measured for the short exposures from each of the models are shown in Figure 3.5.

It is interesting to note that with model 1 (the worst-case scenario) some of the short exposures through the atmosphere have higher Strehl ratios than would be obtained in the absence of the atmosphere. In these exposures the atmospheric phase perturbations are compensating for the errors in the figure of the telescope mirror. This effect is even more noticeable under slightly better astronomical seeing conditions. One example of an exposure with very high Strehl ratio which appeared by chance in such a simulation is shown in Figures 3.6a—f. r_0 for this simulation was five times smaller than the telescope diameter. Figure 3.6a shows the selected exposure with a Strehl ratio of 0.32. The PSF of the telescope (in the absence of atmospheric perturbations) is shown in Figure 3.6b, with a Strehl ratio of 0.23. Figure 3.6c shows the PSF that would be obtained through the same atmosphere using a diffraction-limited telescope (i.e. the PSF for the atmospheric perturbations alone). The shape of this PSF is almost a mirror-image of Figure 3.6b, suggesting that the wavefront errors from the atmosphere are approximately equal and opposite to the aberrations introduced by the telescope. This is also apparent in Figures 3.6d, 3.6e

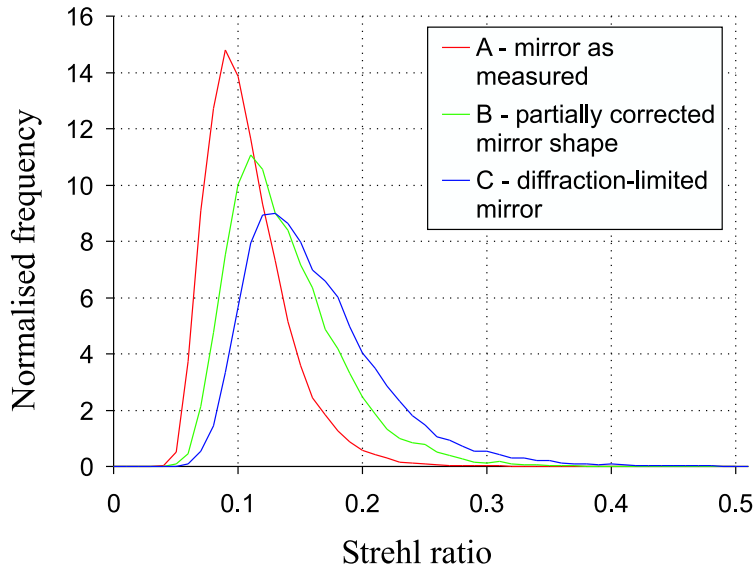


Figure 3.5: Histograms of the Strehl ratios obtained in simulated short exposure images using each of the three models for the NOT mirror aberrations. Incoming wavefronts were simulated with a Kolmogorov spectrum of phase fluctuations, with coherence length r_0 seven times smaller than the telescope aperture diameter. The aperture geometry shown in Figure 3.4 was used for the simulations. Curve **A** corresponds to model 1, using the mirror aberrations measured by Andersen & Sørensen (1996); Sørensen (2002). Curve **B** corresponds to model 2, where the large scale fluctuations have been subtracted. Curve **C** corresponds to the case of a diffraction-limited telescope with the same aperture geometry.

and 3.6f which show greyscale maps of the wavefront error for the PSFs in Figures 3.6a, 3.6b and 3.6c respectively.

The atmosphere is much less likely to correct those phase perturbations which have small spatial scales across the telescope mirror, because the Kolmogorov wavefront perturbations have very little power on small spatial scales. The perturbations in model 2 are restricted to small spatial scales so little correction is expected, but the phase perturbations in the model are sufficiently small in amplitude that they only have a small impact on the distribution of the measured Strehl ratios, as shown in Figure 3.5.

It is clear from the tails of the distributions in Figure 3.5 that we can expect the best short exposure images taken at the NOT to have reasonably high Strehl ratios under good atmospheric seeing conditions. Even with model 1, representing something of a worst-case scenario, Strehl ratios higher than 0.22 are expected 1% of the time.

3.2.3 Observations

In order to assess the short exposure PSF experimentally, observations of individual unresolved stars were undertaken at the NOT. These observations were made at the Cassegrain

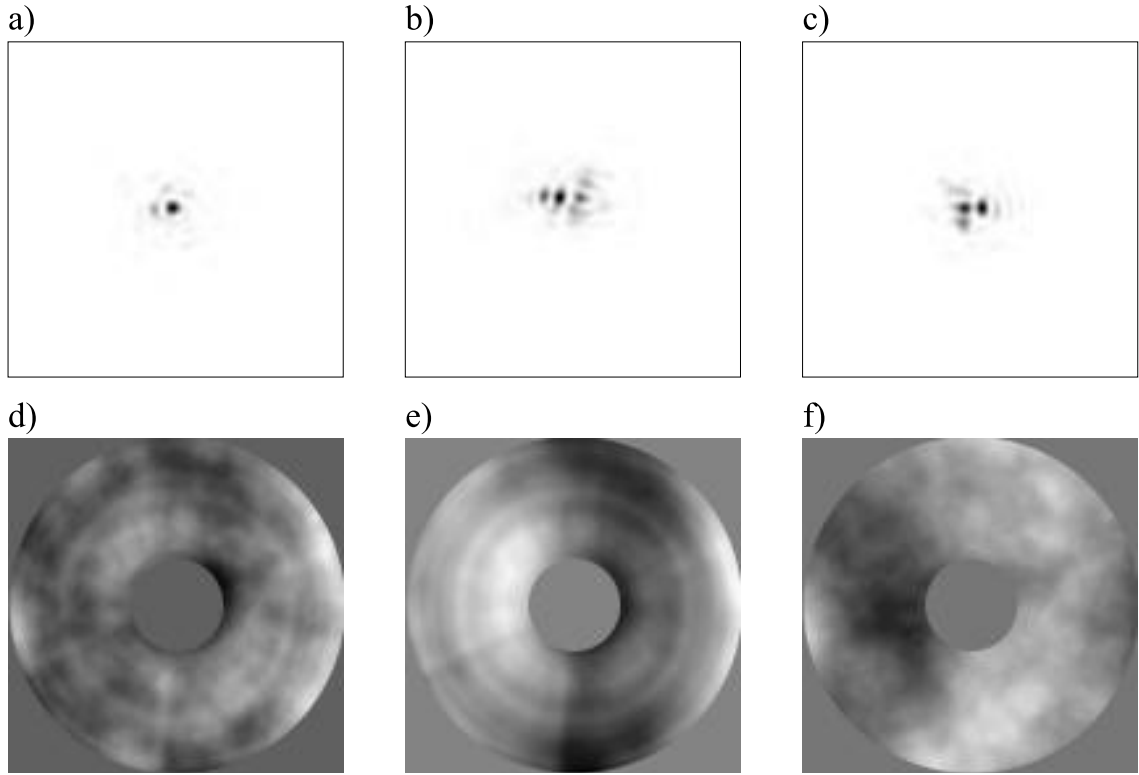


Figure 3.6: Atmospheric correction of the shape of the NOT mirror: **a)** shows a selected exposure; **b)** shows the PSF of the telescope; and **c)** shows the PSF for a diffraction limited telescope through the same atmosphere as in **a)**. The compensation of the telescope aberrations by the atmosphere can also be seen in the wavefront error maps plotted as greyscale in **d)**, **e)** and **f)**, and corresponding to the PSFs shown in **a)**, **b)** and **c)** respectively.

focus of the telescope during technical time at the very end of the night of 2000 May 12 and on the night of 2000 May 13 by Craig Mackay, John Baldwin and Graham Cox. The JOSE camera used for the observations comprised a 512×512 front-illuminated frame-transfer CCD with $15 \mu\text{m}$ square pixels run by an AstroCam 4100 controller. The controller allowed windowing of the area of readout and variable pixel readout rates up to 5.5 MHz . The detector read noise was typically 50–60 electrons for these observations. The $f/11$ beam at the focus was converted to $f/30$ using a single achromat to give an image scale of $41 \text{ mas pixel}^{-1}$ ($25 \text{ pixels mas}^{-1}$).

The observations were taken through the I-band filter from the HiRac instrument at the NOT. The bandpass of this filter is similar to a top-hat in shape, with a centre wavelength of 810 nm and a bandwidth of 125 nm . All of the short exposures were taken at frame rates higher than 150 Hz and without autoguiding to ensure that the temporal behaviour of the periods of good seeing was adequately characterised.

The diffraction-limited PSF of the 2.56 m telescope with 0.70 m secondary obstruction has a FWHM of 64 mas at the observing wavelength of 810 nm . The pixel scale of $41 \text{ mas pixel}^{-1}$ was a compromise between the area of sky which could be observed at high

Target	Frame rate / Hz	Number of ex- posures	Seeing FWHM / as	Strehl ratio for best 1% of exposures
ϵ Aquilae	185	6000	0.38	0.26
V656 Herculis	185	6000	0.49	0.21

Table 3.2: High frame-rate observations performed at the end of the first night of NOT technical time in May 2000.

frame rate and the degradation of the image FWHM due to the finite pixel size.

Four stars were observed at the end of the first night of technical time at the NOT in May 2000. Two of these stars (α Aquilae and γ Aquilae) were sufficiently bright that the CCD camera reached saturation in the best exposures, and these runs have been excluded from further analyses. A small number of frames (less than 1%) in all the runs were mis-recorded by the camera, and these frames have also been excluded from further analysis. Table 3.2 describes the two usable observing runs from the first night.

The seeing was good and the short exposure images clearly showed a single bright speckle at some instants. In order to assess the atmospheric conditions, the individual short exposures were summed without re-centring to produce an *average image*, equivalent to a conventional long exposure with duration equal to the total time for the run. The FWHM of the star in this image represents a measure of the atmospheric seeing conditions, and is listed in column 4 of Table 3.2. The FWHM measurements are consistent with an r_0 of 0.34–0.44 m at the 810 nm observing wavelength for Kolmogorov turbulence with an infinite outer scale. The telescope diameter would then equal 6 or 7 times r_0 . Previous atmospheric measurements at La Palma have typically favoured an outer scale of a few metres (see e.g. Wilson *et al.* (1999); Nightingale & Buscher (1991)), and under these conditions a slightly smaller value of r_0 would be consistent with the long exposure FWHM.

A list of the observations on the second night is given in Table 3.3. Each run typically comprised between 5000 and 24000 frames over a period of 30–160 s. Target stars, both single stars and binaries, were chosen principally lying in the declination range 10°–20° and close to the meridian, so that most of the data was taken at zenith angles $< 20^\circ$. Zenith angles up to 50° were explored later in the night, and the effects of atmospheric dispersion became significant, since no corrective optics were employed. As on the first night, a small number of short exposures in each run were mis-recorded, and these exposures were excluded from further analysis.

Figure 3.7 shows the wind speed during the observations at the NOT in May 2000. These measurements were taken at the top of the NOT weather mast situated at the right hand side of Figure 3.1, a few tens of metres from the telescope.

Target	Frame rate / Hz	Number of exposures	Seeing FWHM / as	Strehl ratio for best 1% of exposures
α Leonis	185	6000	0.71	0.079
γ Leonis	159	5000	0.65	0.092
γ Leonis	182	5000	0.54	0.099
ζ Boötis	152	24000	0.58 ^a	0.20
ζ Boötis	152	24000	0.64 ^a	0.17
CN Boötis	152	2000	0.58	0.084
α Herculis	191	6000	0.42	0.21
α Herculis	191	6000	0.38	0.21
β Delphini	373	10000	0.52	0.20 ^b
β Delphini	257	10000	0.40	0.18 ^b
β Delphini	190	10000	0.60	0.16 ^b
α Delphini	180	10000	0.47	0.18 ^b
α Delphini	180	10000	0.57	0.20 ^b

^a Approximate value after accounting for tracking error

^b The Strehl ratio was reduced by atmospheric dispersion at high zenith angle

Table 3.3: Observations on the second night of NOT technical time in May 2000.

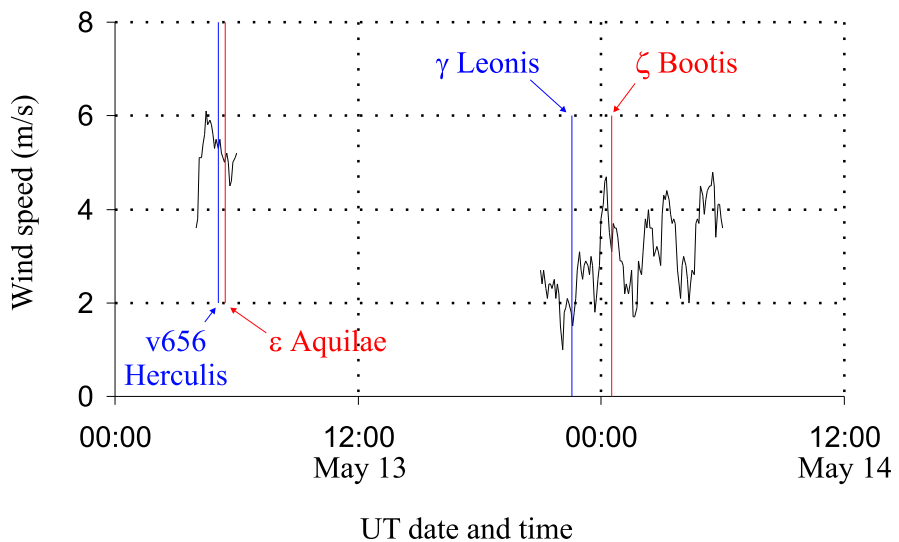


Figure 3.7: The wind speed measured at the NOT weather station during the observations in May 2000. The times that four runs were taken are indicated by the star names on the graph. The wind speed was typically in the range $1\text{---}6 \text{ m s}^{-1}$ for these observations.

3.3 Data reduction method

In order to obtain a quantitative measure of the image quality, the Strehl ratio of the PSF in each short exposure was estimated from the flux in the brightest pixel in that exposure. Our estimate of the Strehl ratio of a short exposure was linearly related to the peak flux density F_p in the image measured per steradian on the sky (calculated from the flux in the brightest pixel). This was divided by the total flux from the star in that exposure (integrated over the whole image: $\int_{-\infty}^{\infty} F(\theta, \phi) d\theta d\phi$). This gave an estimate S of the Strehl ratio:

$$S = C \frac{F_p}{\int_{-\infty}^{\infty} F(\theta, \phi) d\theta d\phi} \quad (3.2)$$

The constant of proportionality C represents a measure of the area of the PSF in steradians on the sky. In order to calculate the value of C required to normalise the Strehl ratios for the case of diffraction-limited PSFs, it was necessary to generate a number of simulated PSFs.

Simulated diffraction-limited PSFs were generated for the observing wavelength of 810 nm with flat incoming wavefronts at various tilt angles, using the aperture geometry described by Equation 3.1. An example is shown in Figure 3.8a. These were then binned into 41 mas pixels to match the camera resolution. The pixellated shape of the PSF was found to depend slightly on the tilt of the incoming wavefronts (i.e. the position of the PSF in relation to the pixel grid) as shown for three example PSFs in Figures 3.8b—d. This led to a variation of $\sim 15\%$ in the flux in the brightest pixel. Our estimate for the peak flux density was taken as the flux in the brightest pixel divided by the area of the pixel (1681 mas² for 41 × 41 mas pixels). By setting the Strehl ratio of these diffraction-limited images to unity, values of C were calculated from Equation 3.2. The mean value of C for a grid of 32 × 32 different wavefront tilts was calculated as 2.015×10^{-13} steradians² (8573 mas²).

In order to investigate the accuracy of Strehl ratio measurements on realistic PSFs, numerical simulations of observations were undertaken using Kolmogorov atmospheres where the incident flux in the image plane was integrated over individual 41 × 41 mas pixels in a square array, again resembling the optical layout for the camera and CCD detector at the NOT. Strehl ratios for the individual short exposures were calculated from the flux in the brightest pixel as described above. The flux in the brightest pixel was found to vary at the $\sim 15\%$ level depending on sub-pixel variations in the position of the brightest speckle relative to the grid of pixels, in a similar manner to the case of the diffraction-limited PSF shown in Figures 3.8b—d. This implied a position dependent error in the measured Strehl ratio at the 15% level (similar to the case for a diffraction-limited PSF).

So as to reduce the dependence of the measured Strehl ratio on the position of the stellar image on the CCD pixel array, the simulated short exposure images of the star were sinc-

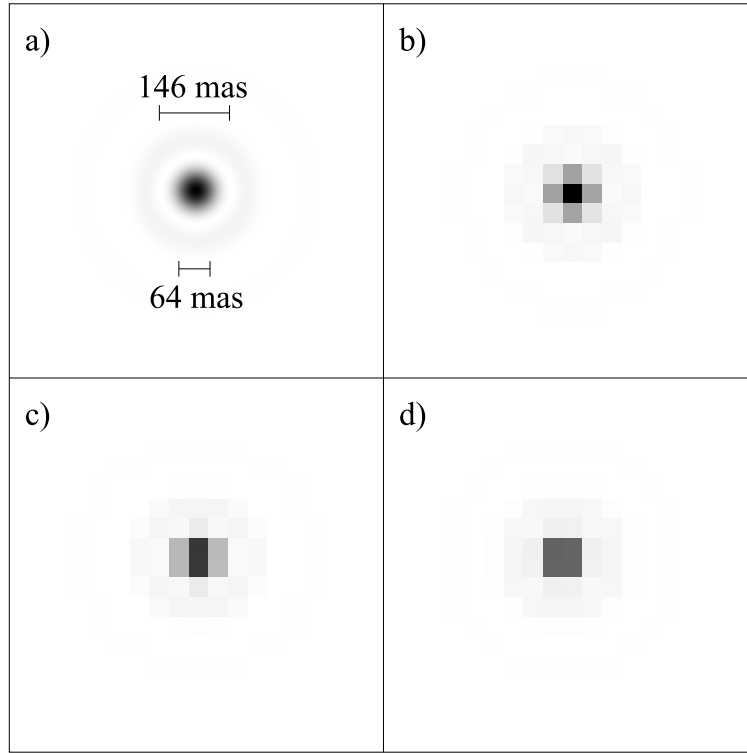


Figure 3.8: **a)** Simulation of a diffraction-limited PSF for an aperture similar to that of the NOT (the precise aperture geometry used for the simulation is described by Figure 3.4). **b)—d)** demonstrate the pixel sampling of the PSF by our camera. The three images correspond to three different positions of the PSF with respect to the detector pixel grid. The pixels corresponded to 41 mas squares on the sky. The peak pixel in **b)—d)** typically contains 20% of the light in the image.

resampled to give four times finer pixel sampling in each coordinate. This was performed in the Fourier domain – the dimensions of the discrete Fourier domain were increased by padding it with zeros, and the power at Nyquist Fourier components was distributed equally at both positive and negative frequencies. The sinc-resampling process preserves the Fourier components with spatial frequencies below the Nyquist cutoff, and does not introduce any power at spatial frequencies above this cutoff. The Nyquist cutoff for the pixel sampling of the CCD in the horizontal and vertical directions of 12 cycles as^{-1} is only slightly lower than highest spatial frequency components in the PSF of around $\frac{d}{\lambda} = 15$ cycles as^{-1} (in other words only a small range of spatial frequencies are not adequately sampled by the CCD). Spatial frequency components of the PSF above the Nyquist cutoff for the CCD pixel sampling are expected to contain little power, making the sinc-resampled short exposures a reasonably good approximation to the original PSF before the pixellation process (although spatial frequencies just below the Nyquist cutoff of the CCD array will be suppressed due to the finite pixel size). The four-fold sinc-resampling process successfully reduced the variation in Strehl ratio with image position to 1% or less. Further resampling with even finer pixel spacing had little effect on the

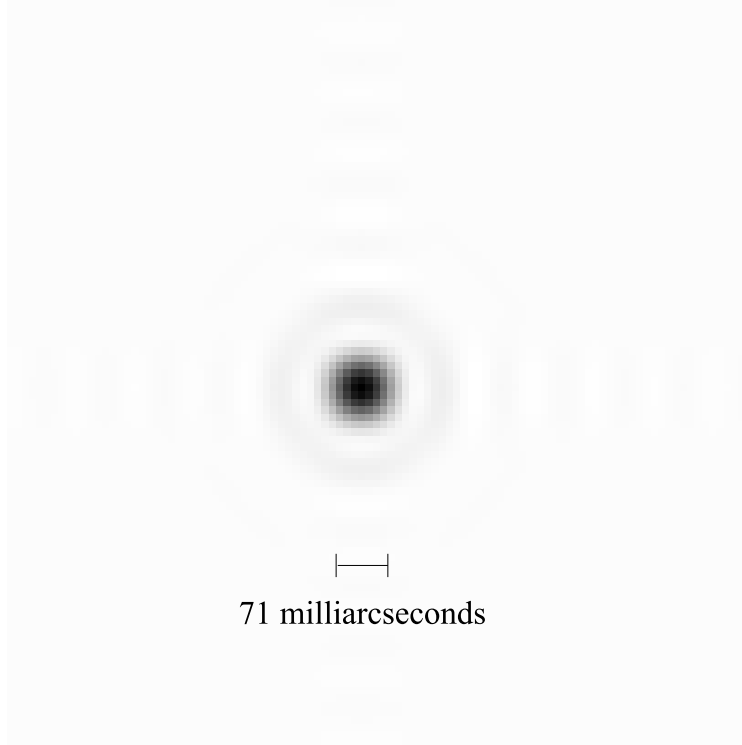


Figure 3.9: A PSF reconstructed from pixellated exposures using sinc-resampling and image re-centring. The NOT PSF was sampled with 41 *mas* square pixels at a grid of 32×32 different sub-pixel positions similar to (and including) those shown in Figure 3.8. The resulting images were sinc-resampled to have four times as many pixels in each dimension, and shifted and added together using the location brightest pixel in the resampled image for re-centring.

measured Strehl ratios.

The ability of the sinc-resampling process to recreate the original PSF is demonstrated in Figure 3.9. In this Figure, diffraction-limited PSFs with a range of different position offsets were pixellated in the same way as was shown in Figures 3.8b—d. The pixellated images were then sinc-resampled with four times as many pixels in both dimensions, and the resulting images were shifted to a common centre and co-added to form Figure 3.9. The Airy pattern is clearly reproduced, and the FWHM of the image core is only slightly larger than that for the true diffraction-limited PSF shown in Figure 3.8a. The sinusoidal ripples extending in both the horizontal and vertical directions from the core of Figure 3.9 are a result of aliasing (Gibb's phenomenon), as the Nyquist cutoff for the CCD pixel sampling in the horizontal and vertical directions is slightly less than the highest spatial frequency $\frac{d}{\lambda}$ (the Nyquist cutoff frequency is sufficiently high along the image diagonal that aliasing does not occur).

3.3.1 Application to observational data

Two stars were observed without saturation at the end of the first night of technical time at the NOT in May 2000, as listed in Table 3.2. The individual short exposures were sinc-resampled to have four times finer pixel sampling, and Strehl ratios for each of the exposures were calculated from the flux in the peak pixel of the resampled images using Equation 3.2. The value of the normalisation constant C used was 8573 mas^2 calculated from the peak pixel value in simulations of diffraction-limited PSFs pixellated in the same way as the CCD observations. A summary of the results of this analysis including a histogram of the Strehl ratios for the run on ϵ Aquilae was included in Baldwin *et al.* (2001).

The Strehl ratios calculated in this way provide a direct comparison between the peak flux in the sinc-resampled short exposures with the peak flux which would be expected in a diffraction-limited exposure taken with the same camera. The sinc-resampling process produces a small change in the peak pixel flux in the short exposure images (typically 10%) which leads to the slightly unsatisfactory situation that simulated short exposures under diffraction-limited atmospheric conditions processed in the same way give Strehl ratios greater than unity (the sinc-resampled images have a higher peak flux than the non-resampled images). This was resolved by recalculating the constant C based upon the peak flux in diffraction-limited PSFs which had been sinc-resampled in the same way as the observational data. The value of C is reduced from 8573 mas^2 to 7060 mas^2 in this case, causing a proportionate decrease in the estimated Strehl ratios. The Strehl ratios presented in this thesis were all calculated using the reduced value of C , giving values which are slightly smaller than those quoted in Baldwin *et al.* (2001).

The Strehl ratios calculated for the individual short exposures of ϵ Aquilae were binned into a histogram, and this is plotted alongside similar histograms calculated for a number of numerical simulations in Figure 3.10. It was possible to select atmospheric seeing conditions for each model which led to good agreement between the model Strehl histograms and those for the run on ϵ Aquilae. The four curves in the figure show:

- A. a numerical simulation with mirror perturbations described by model 1 (those measured by Sørensen (2002)) and an atmosphere having r_0 five times smaller than the telescope diameter;
- B. a simulation using the mirror perturbations described by model 2 (with large scale structure removed) with an atmosphere having r_0 seven times smaller than the telescope diameter;
- C. a simulation using model 3, a diffraction-limited telescope with an atmosphere having r_0 eight times smaller than the telescope diameter; and
- D. the observations of ϵ Aquilae.

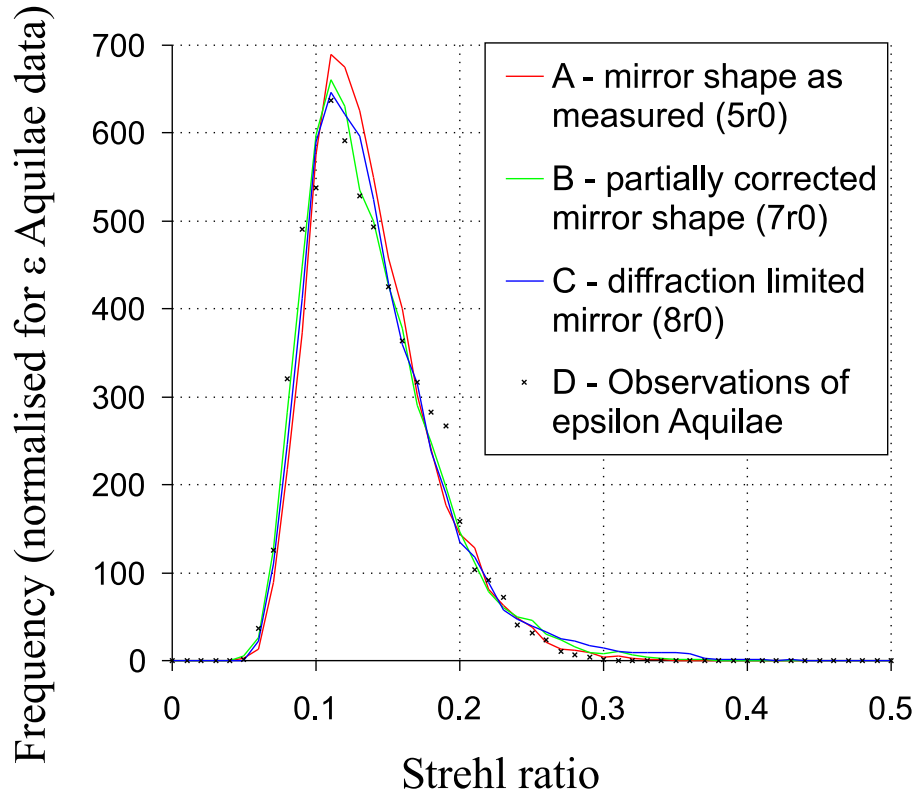


Figure 3.10: Simulated Strehl ratio histograms and measured data from the star ϵ Aquilae. Curves **A**, **B** and **C** correspond to models 1, 2 and 3 respectively (see Table 3.1). Atmospherically degraded short exposures were generated by combining Kolmogorov-like phase perturbations with those in the model used for the telescope aperture. The coherence length r_0 used for the Kolmogorov turbulence was 5 times, 7 times and 8 times smaller than the telescope diameter for Curves **A**, **B** and **C** respectively. Curve **D** corresponds to a histogram of the measured Strehl ratios from short exposure images of ϵ Aquilae. Curves **A**, **B** and **C** have been re-scaled vertically to account for the difference between the number of simulated short exposures and the number of exposures taken on ϵ Aquilae (so the area under the four curves is the same).

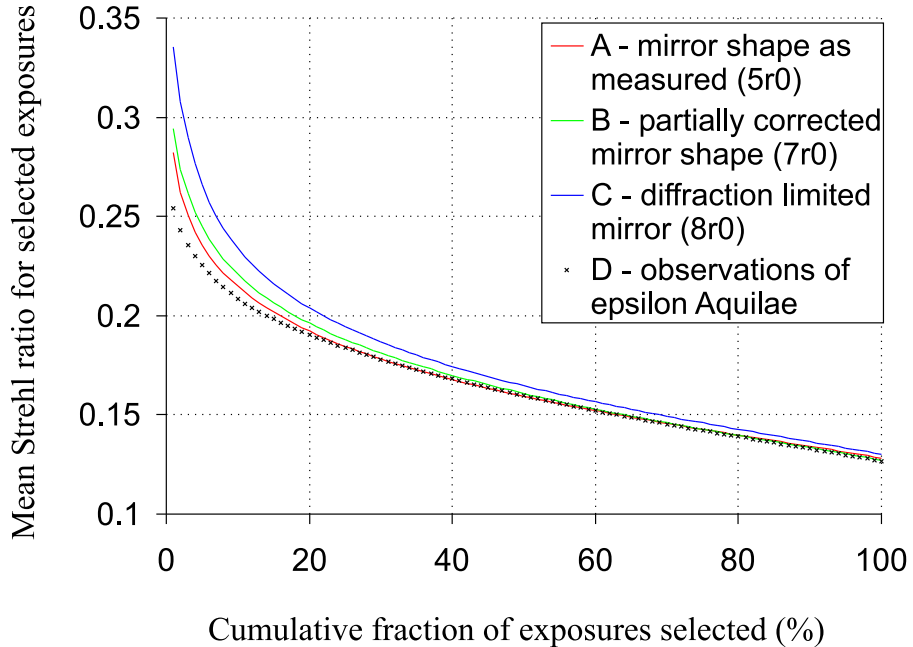


Figure 3.11: Cumulative Strehl ratio plots for the data presented in Figure 3.10. Curves **A**, **B** and **C** correspond to models 1, 2 and 3 respectively (as for Figure 3.10). The exposures having the highest Strehl ratios were selected from each dataset, and the mean of the Strehl ratios for the selected exposures is plotted against the total fraction of exposures selected (ranging from the best 1% to 100% of the exposures). Curve **D** shows the same plot for the measured Strehl ratios from short exposure images of ϵ Aquilae.

The mirror perturbations on the NOT primary mirror are likely to have similar magnitude to those described by model 2, implying that the most likely value for the atmospheric coherence length r_0 is $\frac{d}{7}$ or about 0.37 m.

Figure 3.11 shows cumulative plots of the Strehl ratio datasets used in Figure 3.10. The exposures in each dataset were first sorted by descending Strehl ratio. Plotted in the figure for each dataset is the mean of the highest 1% of Strehl ratios, the mean of the highest 2% of Strehl ratios, and so on up to the mean of all the Strehl ratios in the dataset. These mean Strehl ratios give an indication of the image quality which would be obtained if a given fraction of exposures was selected for use in the Lucky Exposures method.

Strehl ratios were calculated in the same way for data taken on the star V656 Herculis, and Curve **A** in Figure 3.12 shows a histogram of the Strehl ratios obtained. Also shown in the figure are Strehl ratio histograms for simulations with a diffraction-limited telescope and atmospheric seeing conditions corresponding to $\frac{d}{r_0} = 10$ (labelled **B**) and $\frac{d}{r_0} = 11$ (labelled **C**). Again there is close correspondence between the simulated curves and the observational results. The lower Strehl ratios as compared to the run on ϵ Aquilae may result from slightly poorer seeing conditions, as highlighted by the long exposure FWHM in Table 3.2.

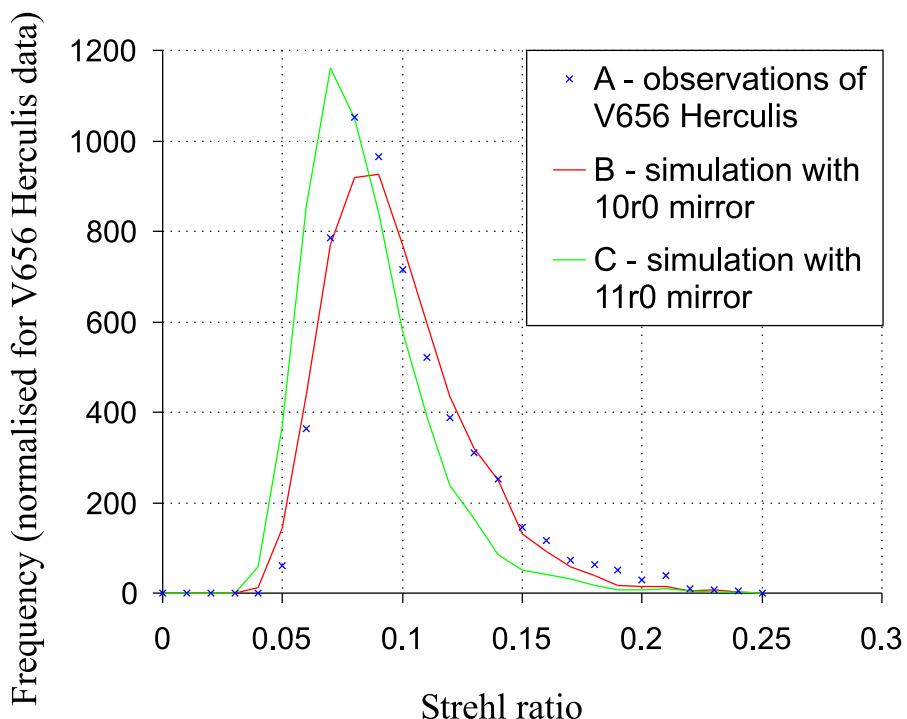


Figure 3.12: Strehl ratio histograms for the observation of V656 Herculis alongside two simulations. Curve **A** shows the Strehl ratios measured for V656 Herculis, curve **B** shows the Strehl ratio histogram for a simulation with a diffraction-limited mirror of $10r_0$ diameter, and curve **C** shows results of a simulation with an $11r_0$ diffraction-limited mirror. Curves **B** and **C** have been re-scaled vertically to account for the difference between the number of simulated short exposures and the number of exposures taken on V656 Herculis (so the area under the three curves is the same).

3.3.2 Exposure selection

In order to apply the Lucky Exposures image selection procedure to observational data taken on astronomical sources, one star in the field can be selected to act as a reference for measurement of the Strehl ratio and position of the brightest speckle. The data reduction software written by the author selected a small rectangular region in each short exposure which surrounded the reference star, but did not include a significant flux contribution from any other sources in the field. This region of each short exposure was then sinc-resampled to have four times as many pixels in each dimension. The Strehl ratio and position of the brightest speckle were then calculated from the resampled image region. The exposures having the highest Strehl ratios were then selected for further processing. A summary of this approach to the data reduction is given in Figure 3.13.

The sinc-resampling process described in panel **c**) of Figure 3.13 is one of the most computationally intensive parts of the data reduction as it involves two Fast Fourier Transforms (FFTs). By limiting the area of the image which is resampled to a small region around

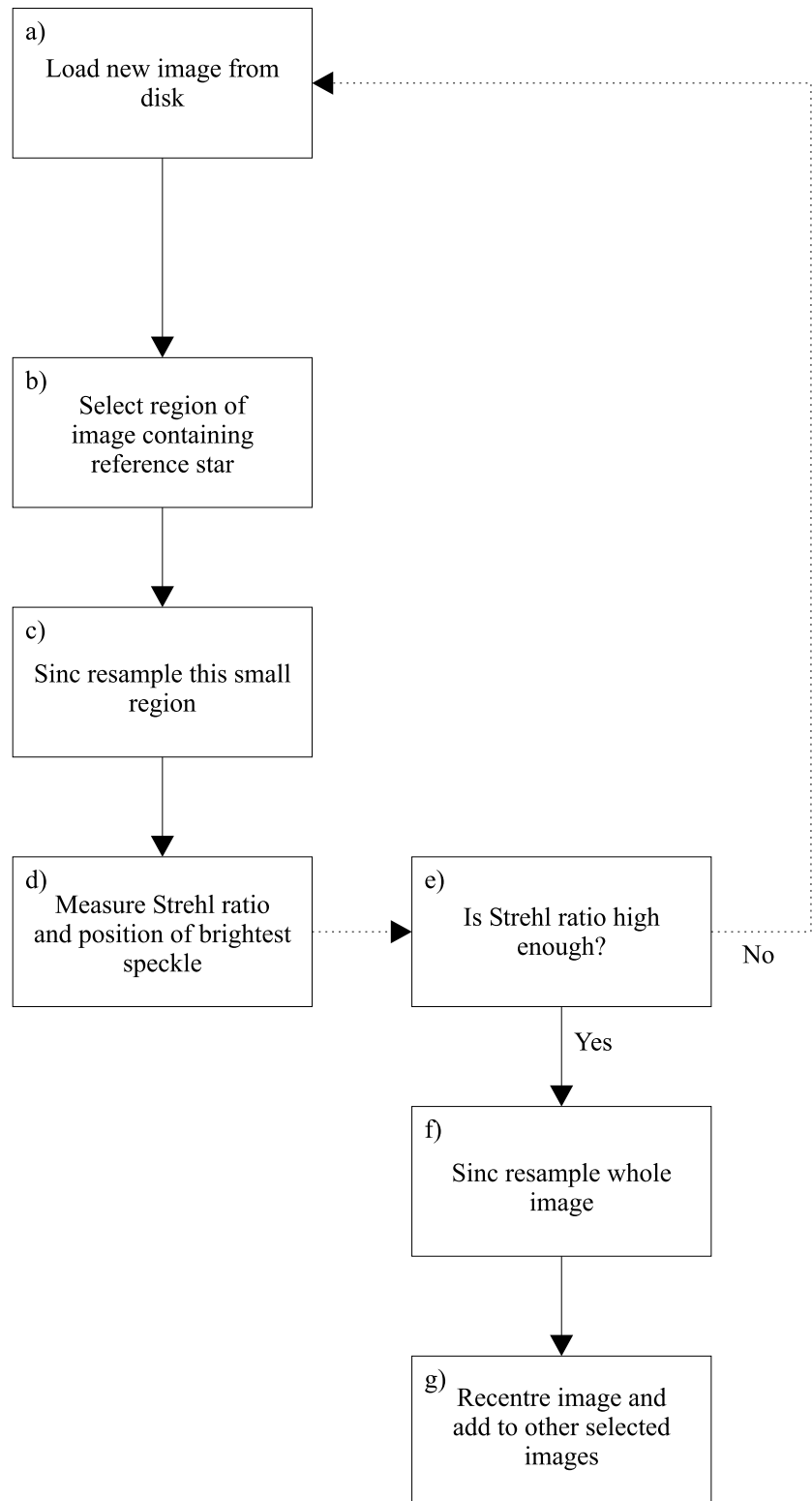


Figure 3.13: Flow chart describing the data reduction method for Lucky Exposures imaging of astronomical targets.

the reference star, the speed of the data reduction process is dramatically improved, allowing near real-time data-reduction while observing using a year 2000 vintage PC. The time-saving became even more significant in later runs using larger image dimensions.

After the position of the brightest speckle and Strehl ratio for each short exposure had been calculated in panel d) of Figure 3.13, the short exposures with the highest Strehl ratios were selected for further processing. The full frame image for each of these short exposures was sinc-resampled, and then re-centred and co-added based on the location of the brightest pixel in the reference star image as calculated in panel d). The process of sinc resampling the full short exposure image was computationally intensive, but this was only applied to the selected exposures (typically 1–10% of the total number of exposures).

3.4 Observational results with single stars

3.4.1 Exposure selection results

In order to assess the imaging performance of the Strehl selection method, the data on V656 Herculis and ϵ Aquilae listed in Table 3.2 were analysed using the approach described in Figure 3.13. The best 1% of exposures were selected and co-added – the resulting images for V656 Herculis and ϵ Aquilae are shown in Figures 3.14a and 3.14b. Shown beneath are the average (seeing-limited) images from the same data in Figures 3.14c and 3.14d, representing conventional long exposures. It is possible that telescope tracking errors might have contributed to the asymmetry in the long exposure image of V656 Herculis, but it is difficult to distinguish these errors from the random motion due to the atmosphere.

The image selection method provides images with FWHM of 80×94 mas for V656 Herculis and 79×94 mas for ϵ Aquilae, a very substantial improvement over the FWHM of the conventional astronomical images (490×600 mas and 380 mas respectively). In the Lucky Exposures images the first Airy ring is visible (although it is not uniform around the stars). In both images the total flux beyond the first Airy ring is relatively small. If these PSF were available for imaging complex fields, extremely high image resolution and quality would be obtained.

3.4.2 Temporal properties of the atmosphere

In order to investigate the temporal properties of the atmosphere during these observations and help determine the optimum exposure time for the Lucky Exposures method it is of interest to look at the typical variation in the flux at a point in the image plane speckle pattern from one short exposure to the next. The statistics of the temporal fluctuations at one fixed point in the image plane should be representative of the fluctuations at any other point in the image plane.

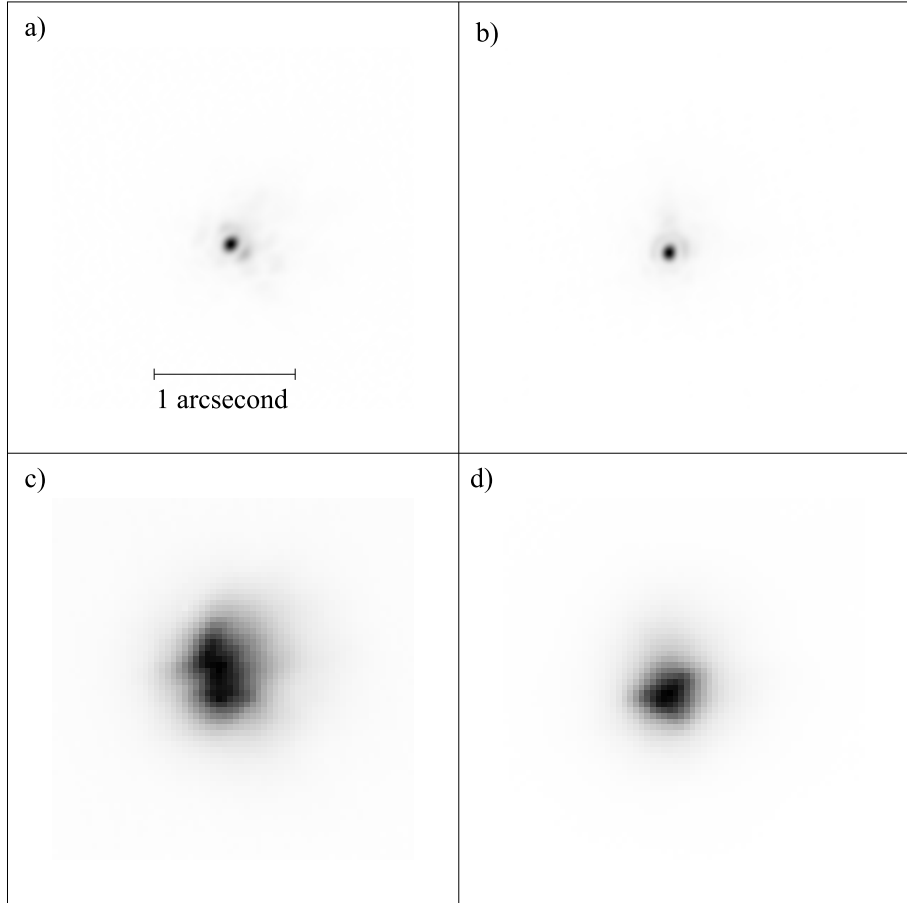


Figure 3.14: Two stars were observed on the first night at the NOT without saturation – V656 Herculis and ϵ Aquilae. Panels **a)** and **b)** show the best 1% of exposures shifted and added for V656 Herculis and ϵ Aquilae respectively, processed using the method described in the text. Beneath these panels are the respective averaged images in panels **c)** and **d)**. These were generated by summing all of the short exposures without re-centring, and represent the conventional astronomical seeing disks at the times of the observations. The Strehl ratios and FWHM for the four images are: **a)** 0.21 and 80×94 mas, **b)** 0.26 and 79×94 mas **c)** 0.018 and 490×600 mas, **d)** 0.033 and 380 mas.

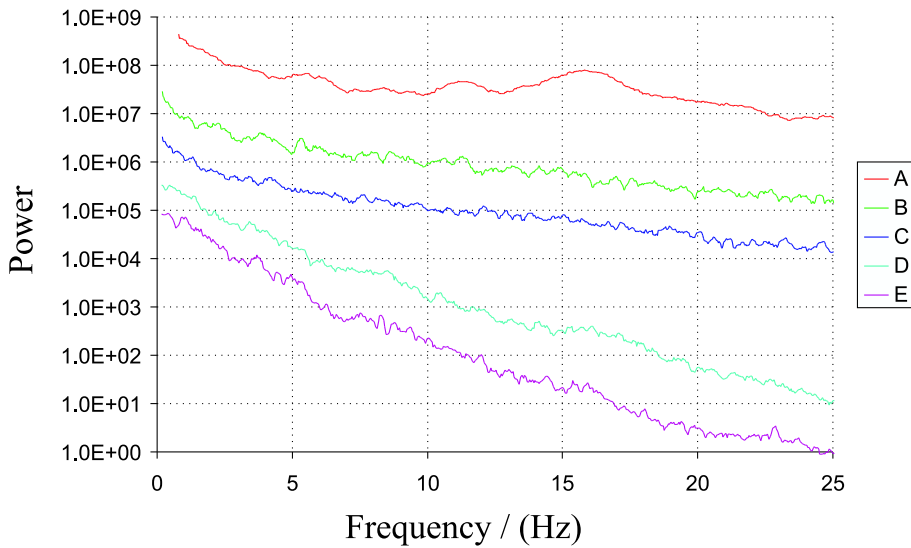


Figure 3.15: Temporal power spectra generated from flux measurements at a fixed point in the image plane. The curves have been smoothed by binning together adjacent spatial frequencies. **A** shows the result for data taken on the star ϵ Aquilae at the NOT. **B** shows results from an example atmospheric simulation, in this case with two wind blown Taylor screens, one having 75% of the turbulence strength and taking 420 ms to cross the telescope diameter, and one having 25% of the turbulence strength and taking 63 ms to cross the aperture. Model 2 was used for the mirror aberrations. The simulation used for curve **C** was the same as that for **B** but with a diffraction-limited mirror (model 3). For curve **D** all the turbulence was in a single layer taking 420 ms to cross the telescope mirror with model 2 for the aberrations in the mirror. Curve **E** is for the same case as **D** but with a diffraction-limited mirror. The lines are offset vertically for clarity.

In order to minimise the effects of long-timescale drift in the location of the stellar PSF on the measurements, the pixel located at the centroid of the long exposure average image of the run on ϵ Aquilae was selected (i.e. the centroid of Figure 3.14d). The average image for this run had an unusually compact PSF, showing no evidence for substantial drift in the location of the speckle pattern during the 30 s run. The stellar flux from the selected pixel was recorded in each short exposure, producing a one-dimensional dataset characterising the temporal fluctuations in the PSF. The temporal power spectrum of this dataset is shown as curve **A** in Figure 3.15. The power spectrum shows a peak at a frequency of 16 Hz. This is in close agreement with the first harmonic of mechanical oscillation for the telescope structure, and movies made from the raw speckle images clearly show motion consistent with such oscillations. The frequency was confirmed to be 16 Hz by measuring the position of the brightest speckle in each short exposure and then looking at the temporal power spectrum of this time series.

The effect of telescope oscillation on the temporal fluctuations at a fixed point in the image plane can be seen by splitting into partial derivatives the derivative of the flux I with respect to time at a fixed point in the telescope image plane. It is simplest to work

in a coordinate frame which is fixed with respect to the speckle pattern, and study the effect of moving the optical detector at a velocity \mathbf{v} relative to the speckle pattern. In these coordinates, the time derivative of the flux is:

$$\frac{dI}{dt} = \frac{\partial I}{\partial t}\Big|_r + \mathbf{v} \cdot \frac{\partial I}{\partial \mathbf{r}}\Big|_t \quad (3.3)$$

where \mathbf{r} is the position of the optical detector in the speckle pattern, and \mathbf{v} is the velocity of the detector with respect to the speckle pattern. The motion of the detector with respect to the speckle pattern resulting from telescope oscillation thus produces a coupling between the spatial variations of the flux in the speckle pattern and temporal fluctuations measured at a fixed point in the image plane.

It is the total differential from Equation 3.3 which limits the exposure time we can use during observations at the NOT. For our data it is the telescope oscillation which provides the dominant contribution on short timescales. If the amplitude of the telescope oscillation could somehow be reduced however, the ultimate limit to the exposure time would be set by the partial derivative $\frac{\partial I}{\partial t}\Big|_r$. This term represents the component of the time variation in the flux which is introduced directly by changes in the speckle pattern. It is of interest to try to measure the timescale associated with this, as it would be applicable to other telescopes operating under similar atmospheric conditions.

Curve **A** in Figure 3.16 shows the temporal autocorrelation of the same dataset from ϵ Aquilae as Figure 3.15 (it represents the Fourier transform of curve **A** in Figure 3.15). The curve has been normalised so that it ranges from unity at zero time difference to a mean value of zero for time differences between ~ 200 ms and ~ 2000 ms. The 16 Hz oscillatory component is clearly visible. This oscillation is largely responsible for the initial decorrelation in the measured flux as a function of time. The telescope oscillation will only reduce the temporal correlation, so the true autocorrelation function corresponding to the atmosphere would lie above curve **A** for all time differences. The effect of photon-shot noise was negligible in these observations due to the high flux in each individual exposure. The frame rate (185 Hz) was sufficiently high that the sharp peak in curve **A** around zero time difference is relatively well sampled in this dataset (the peak does not simply correspond to a single high value at zero time difference, but contains several data points).

Curve **B** in this Figure is a function extrapolated from the measured curve by dividing it by a decaying sinusoid having the same period as the telescope oscillation. The amplitude and decay time of the sinusoid were chosen so as to minimise the residual component at 16 Hz. This curve is intended to represent a possible shape for the temporal autocorrelation in the absence of telescope oscillation.

Curve C shows a fit to curve **B** of the form of Equation 2.2 (based on the model of temporal fluctuations by Aime *et al.* (1986)). The broad peak produced by this model does not

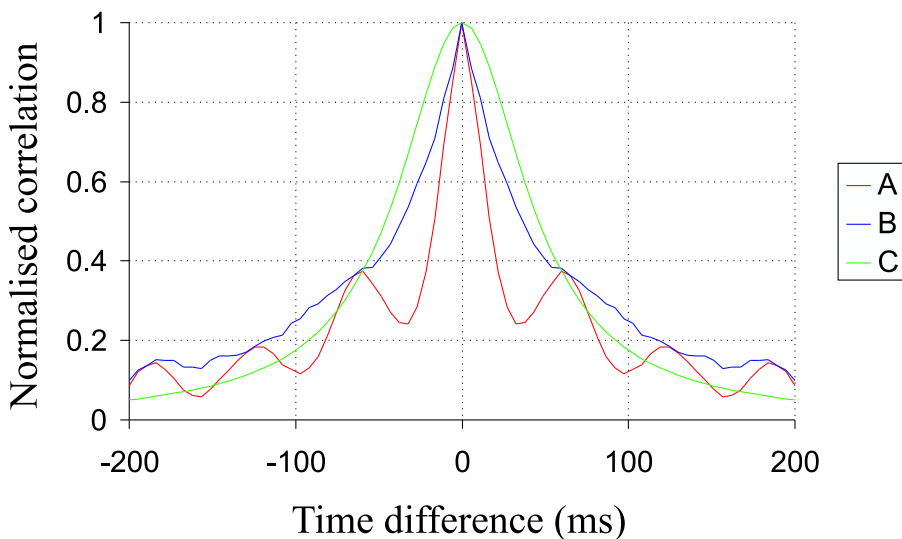


Figure 3.16: Curve **A**) shows the temporal autocorrelation of the flux at a fixed point in the image plane for the ϵ Aquilae data. Curve **B** is based on the same data, but the oscillation in the curve has been artificially suppressed as described in the text. **C** is a fit to curve **B** based on Equation 2.2 (the model of Aime *et al.* (1986)).

seem consistent with the sharp peak seen in the experimental data.

The sharp peak seen in curves **A** and **B** of Figure 3.16 could be reproduced qualitatively in numerical simulations if multiple Taylor screens were used with a scatter of different wind velocities. One example of a simulation which gave a better fit to the shape of the experimentally measured temporal autocorrelation is shown as curve **C** in Figure 3.17. The atmospheric model for this simulation consisted of two Taylor screens moving at constant velocities. Both layers moved in the same direction but with different speeds. One layer, containing 75% of the the turbulence took 420 ms to cross the diameter of the telescope aperture. The other contained 25% of the turbulence, but took only 63 ms to cross the telescope aperture. Curves **A** and **B** from Figure 3.16 are also reproduced as curves **A** and **B** in Figure 3.17 for comparison. Temporal power spectra generated using this model of the atmosphere are plotted as curves **B** and **C** in Figure 3.15. It is clear that they provide a much better fit to the experimentally measured data in curve **A** than the single layer atmospheric models shown in curves **D** and **E**.

It is clear from the temporal autocorrelation plots of Figures 3.16 and 3.17 that there are (at least) two timescales associated with the decorrelation of the speckle pattern: the half-period of the telescope oscillation and the timescale for the decorrelation of the atmosphere. The decorrelation timescale τ_e (as defined in Chapter 2.2.1) which results from the combination of these two effects is 22 ms. Using a simple fit to the oscillatory component (used to produce curve **B** in both Figures) the decorrelation timescale for the atmosphere alone was calculated to be 65 ms.

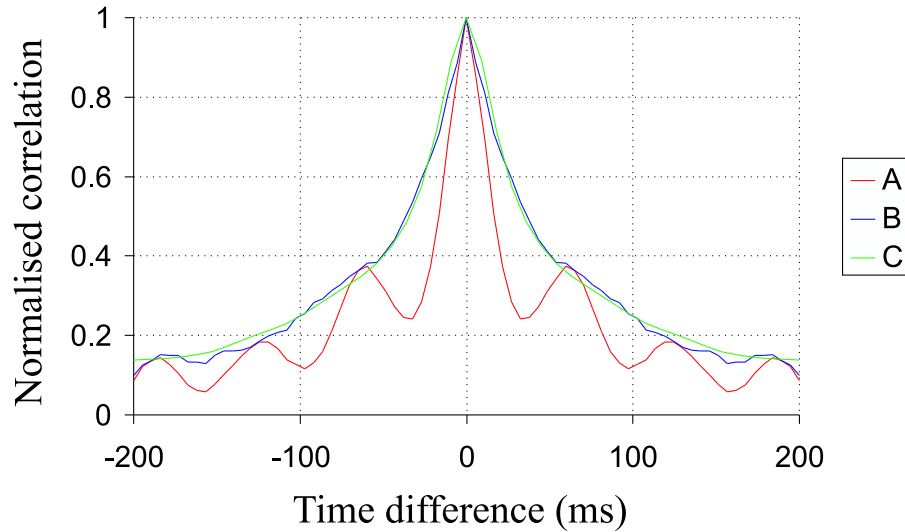


Figure 3.17: Curve **A**) shows the temporal autocorrelation of ϵ Aquilae data and **B** shows the same data with the oscillation artificially suppressed, as in Figure 3.16. Curve **C** shows an example of one simulation which fitted the data of curve **B**. The model atmosphere had two layers: one with 75% of the turbulence strength taking 420 ms to move across the diameter of the aperture, and one with 25% of the turbulence taking 63 ms to move across the aperture. This curve is the Fourier transform of the power spectrum shown in curve **B** of Figure 3.15

If the atmosphere had a single, boiling-free layer then Equation 2.14 could be used to obtain the wind velocity. Taking $r_0 = 0.37\text{ m}$ (consistent with the seeing disk, and with the Strehl ratios in Figure 3.10), a wind velocity of 17 m s^{-1} is obtained. This is significantly larger than the wind velocity near ground level of 5 m s^{-1} (from Figure 3.7), but would not be implausible if the turbulence were situated at high altitude.

If the atmosphere had multiple layers travelling at different velocities, and the timescale for decorrelation of the wavefronts was shorter than the wind crossing timescale of the telescope aperture, then the dispersion in the wind velocities Δv could be calculated using Equation 2.12. The value obtained for $\tau_e = 65\text{ ms}$ is $\Delta v = 5.7\text{ m s}^{-1}$ (again taking $r_0 = 0.37\text{ m}$). This level of dispersion in wind velocities between atmospheric layers seems consistent with the wind velocity of 5 m s^{-1} measured near to the ground.

Both of these atmospheric configurations are plausible. The second is perhaps more likely given that the strongest turbulence is most commonly found at relatively low altitudes, where small wind speeds were observed.

3.4.3 Timescales for exposure selection

A variation to the exposure selection method was developed in order to measure the timescale associated with the decorrelation of the brightest speckle in each exposure. The

image selection and position corrections calculated for each exposure were actually applied to an earlier or later exposure. The exposure which was selected always came a fixed number of exposures before or after the exposure used for calculations of the Strehl ratio and position of the brightest speckle. For these analyses there thus exists a time difference between the measurement of the properties of the speckle pattern, and the response of the algorithm which selects and then co-adds the exposures. The analysis was repeated many times, varying the time difference used. No correction was made for the oscillation of the telescope, leaving an oscillation in the Strehl ratio as a function of the time difference used.

The Strehl ratio for the shift-and-add image using all the exposures is plotted as a function of this time difference in curve **B** of Figure 3.18, alongside curve **A**, the temporal autocorrelation of the speckle pattern previously shown in Figures 3.16 and 3.17. Qualitatively the curves appear similar suggesting that the decorrelation process is not substantially different for the brightest speckle than for the fixed point chosen in the image plane. Both curves are almost equally affected by the telescope oscillation as would be expected. If we ignore the effects of the telescope oscillation, the brightest speckle does appear to decorrelate slightly more quickly at first than the autocorrelation curve for the measurements taken at a fixed location in the image. Also shown in the Figure are the Strehl ratios obtained in the final image when the best 1% of exposures are used, based upon the Strehl ratio and position of the brightest speckle measured in a different short exposure in the same run (i.e. taken at a slightly different time). If we ignore the effects of the telescope oscillation, this appears to decay slightly more slowly than the other timescales, perhaps indicating that the atmospheric coherence time is slightly extended during the times of the best exposures. This is a small effect, and it is clear that the timescales for the decay of the brightest speckle are very close to the coherence timescale of the speckle pattern.

Figure 3.18 shows that the timescale for the decay of the brightest speckle is 10–20 ms brought about predominantly by the 16 Hz telescope oscillation. If exposure times greater than this are used, one would expect the typical Strehl ratios of the exposures to be reduced. This was tested experimentally by splitting the dataset on ϵ Aquilae into groups of five consecutive exposures. The five exposures in each group were added together without re-centring to form a single exposure with five times the duration. The best 1% of these 27 ms exposures is shown as a contour plot in Figure 3.19b alongside the shift-and-add image from the best 1% of the original 5.4 ms exposures in Figure 3.19a. The increase in exposure time from 5.4 ms to 27 ms brings about a reduction in the Strehl ratio of the best 1% from 0.26 for Figure 3.19a to 0.22 for Figure 3.19b. The image FWHM is increased from 79×94 mas to 81×96 mas. It is clear that the amplitude of the telescope oscillation is small enough that relative good image quality can still be obtained with exposure times as long as 27 ms using the Lucky Exposures method.

Figure 3.19c shows the single best 108 ms exposure formed by summing together without re-centring 20 consecutive short exposures from the run on ϵ Aquilae. The Strehl ratio

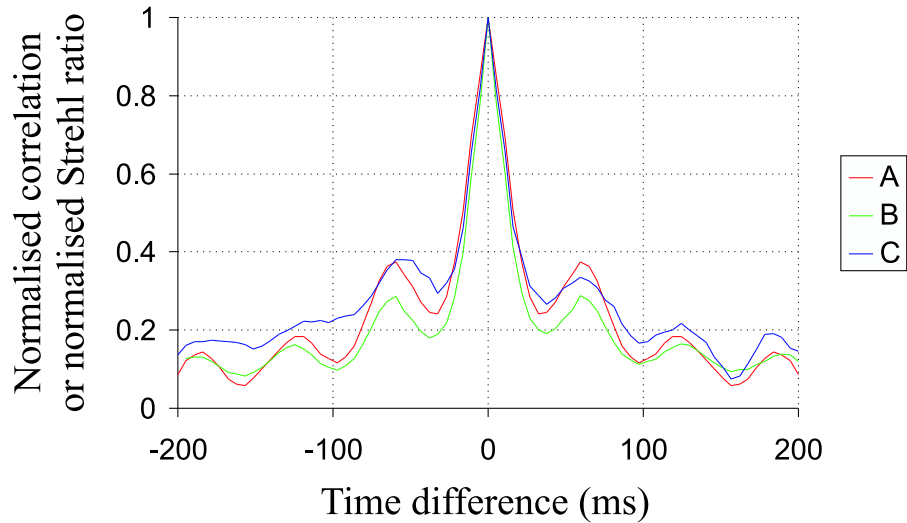


Figure 3.18: Curve **A** shows the temporal autocorrelation of flux measurements at a single point in the image plane for the ϵ Aquilae data. Curves **B** and **C** show normalised plots of the Strehl ratio obtained when individual exposures are re-centred based on the measured position of the brightest speckle in a different exposure (with the time difference between the position measurement and the re-centring process indicated on the horizontal axis). All of the exposures in the run on ϵ Aquilae were used for curve **B**. For curve **C**, exposure selection and re-centring was based on the Strehl ratio and position of the brightest speckle in a different exposure, with only 1% of the exposures selected.

for this image is 0.24. The small amplitude of the telescope oscillation seen in movies generated from the raw short exposures around the moment that the 20 constituent short exposures were taken may partly explain the high Strehl ratio obtained. It is clear that the atmospheric timescale must have been quite long at the time this exposure was taken. Although the Strehl ratios are comparable, the shift-and-add images shown in Figures 3.19a and 3.19b show much less structure in the wings of the PSF than the single exposure of Figure 3.19c. This is probably due to the shift-and-add images being the average of many atmospheric realisations, which helps to smooth out the fluctuations in the wings of the PSF. To demonstrate that this is not simply an integration-time effect, Figure 3.19d shows a shift-and-add image with the same total integration time and similar Strehl ratio (0.25) to Figure 3.19c, but using individual short exposures taken at widely separated times. The wings of the PSF are substantially smoother than for the 108 ms single exposure of Figure 3.19c. This suggests that a significant fraction of the noise in these images results from the limited number of atmospheric realisations used in generating them.

3.5 Results with binary stars

On the night of 2000 May 13, a number of binary stars were observed, as listed in Table 3.3. These were used to give an indication of the imaging performance of the Lucky Exposures

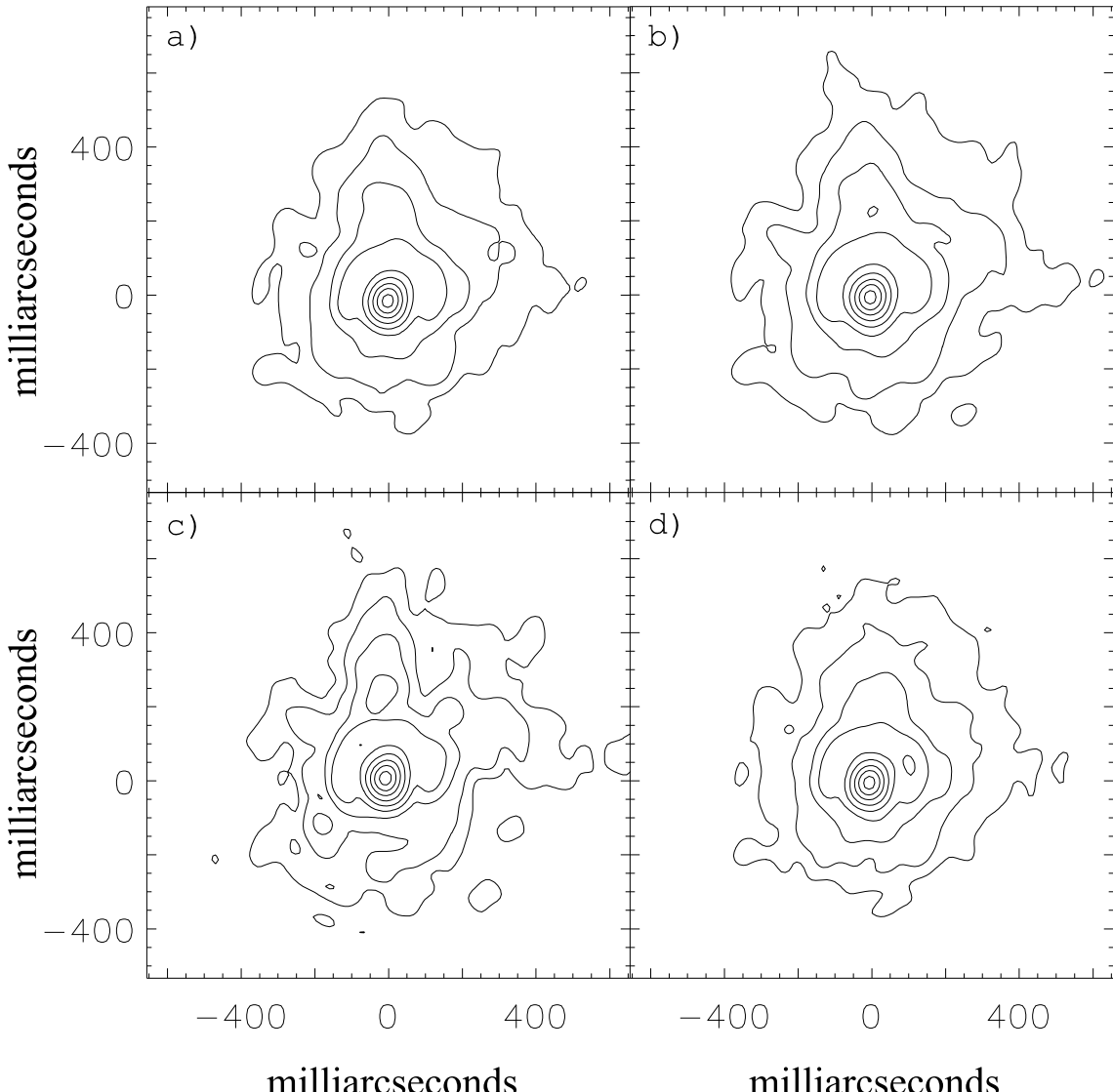


Figure 3.19: **a)—d)** Image quality of ϵ Aquilae using differing criteria for exposure selection from a 32 s run. Contour levels are at 1, 2, 4, 8, 16, 30, 50, 70, 90% peak intensity.

- a)** The 60 individual 5.4 ms exposures of ϵ Aquilae with the highest Strehl ratios, shifted and added together. The Strehl ratio of this image is 0.26.
- b)** 12 exposures of 27 ms duration selected, re-centred and combined. The Strehl ratio of this image is 0.22.
- c)** The single best 108 ms exposure. The Strehl ratio of the image is 0.24.
- d)** 20 individual 5.4 ms exposures from ϵ Aquilae taken from widely separated time periods were re-centred and combined to give a Strehl ratio of 0.25.

method for astronomical targets where an off-axis reference star is required for exposure selection and re-centring. One of the stars in the binary is used as the reference star for measurements of the Strehl ratio and relative position of the brightest speckle. After exposure selection, re-centring and co-adding, the image of the binary companion then provides a measure of the imaging PSF.

The correlation between the Strehl ratios measured on one binary component with those measured on the other binary component in individual exposures can provide lower limits on both the atmospheric isoplanatism and the signal-to-noise ratio for the Strehl ratio measurements, as the dominant sources of noise (photon shot noise, stochastic detector readout noise) will not be correlated for the two stellar images. Analyses of this sort will also be presented in this section. If the detector “pattern noise” was strongly correlated for large distances across the short exposures this might have given a correlated error to the measured Strehl ratios for the two stars. Measurements of the summed Fourier power spectrum for the short exposure images indicate that the pattern noise should not have made a significant contribution to the Strehl ratios for these observations of ζ Boötis, however.

3.5.1 Data taken on ζ Boötis

Two runs were taken on the 0.8 *as* binary ζ Boötis, each comprising 24000 short exposures. During both of these runs the binary drifted slightly across the detector due to telescope tracking problems. The parts of each of the two runs were identified where both binary components were well within the readout region of the CCD (more than 16 pixels from the edge), and only these short exposures were used in the following analysis.

Two example short exposures of ζ Boötis are shown in Figures 3.20a and 3.20b. Figure 3.20a is typical of the data set (with a Strehl ratio close to the median) while Figure 3.20b has an unusually high Strehl ratio of 0.26. In both of these exposures there is strong similarity between the shapes of the speckle patterns around each binary component, suggesting that the PSF due to the atmosphere is the same for both stars. The small differences which are visible between the images of the two binary companions can partly be explained by the different alignment of the stellar images with respect to the pixel grid of the CCD. Figure 3.20c shows the effect of sinc-resampling the image shown in Figure 3.20b to have four times as many pixels in each dimension, revealing a hint of the first Airy ring. The similarities between the stellar images of the two binary companions is even more pronounced in this resampled image.

The Lucky Exposures image selection procedure was applied to the data using the approach described in Chapter 3.3.2. The left-hand brighter component of ζ Boötis was initially used as the reference star.

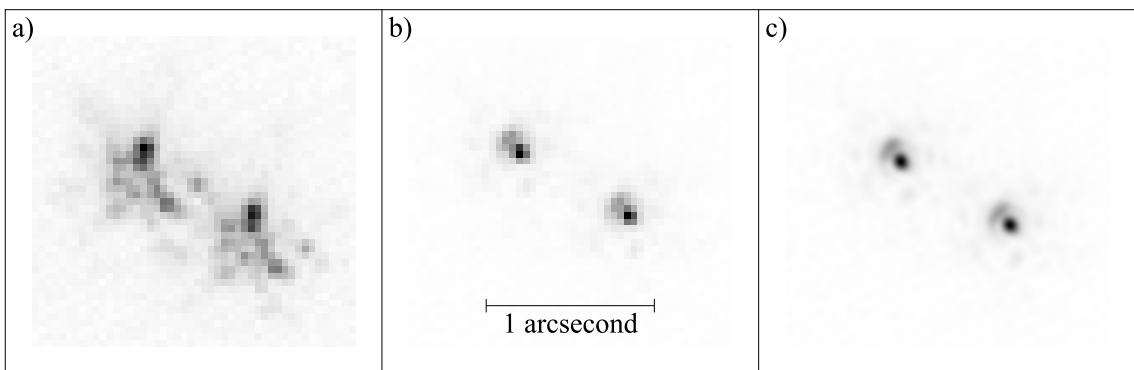


Figure 3.20: Example short exposure images of ζ Boötis: **a)** a typical exposure, having Strehl ratio of 0.074 (close to median); **b)** a good exposure with Strehl ratio of 0.26; and **c)** the same exposure as shown in **b)** but sinc-resampled to have four times as many pixels in each dimension.

3.5.2 Varying the fraction of exposures selected

In order to assess the performance of the Lucky Exposures method with different exposure selection parameters, I analysed the ζ Boötis data several times. In each case the images of the two binary components appear very similar, suggesting that the field is isoplanatic with little variation in the imaging PSF as a function of position.

Some of the results from the ζ Boötis data are summarised in Figure 3.21. Figure 3.21a shows an image generated from the short exposures have the highest 1% of Strehl ratios as measured on the left-hand component of ζ Boötis. The stellar images appear almost diffraction limited, with the first Airy ring clearly visible. The diffuse halo surrounding the stars is very faint and barely visible in the image. Figure 3.21b shows the result when the process is repeated using the right-hand star as the reference for measuring Strehl ratio and the position of the brightest speckle. Figures 3.21a and 3.21b are almost indistinguishable to the eye, emphasising the high degree of isoplanatism and the good signal-to-noise in the images. The Strehl ratio for the reference star in each case is 0.19.

Figures 3.21c and 3.21d show images generated in a similar way but using the short exposures which have the highest 10% of Strehl ratios. A diffuse halo is clearly visible around both stars slightly reducing the Strehl ratio for the reference star images to 0.14.

Figures 3.21e and 3.21f show images generated in a similar way but using all of the short exposures regardless of Strehl ratio. The diffuse halos are much more prominent around the stars reducing the Strehl ratio for the reference star images to 0.078. These represent the conventional shift-and-add images from the same data.

For all six images shown in Figure 3.21, the Strehl ratio for the binary companion was found to be only $98.5\% \pm 0.5\%$ as high as that of the reference star. This indicates a small level of decorrelation between the shapes of the stellar images for the two binary

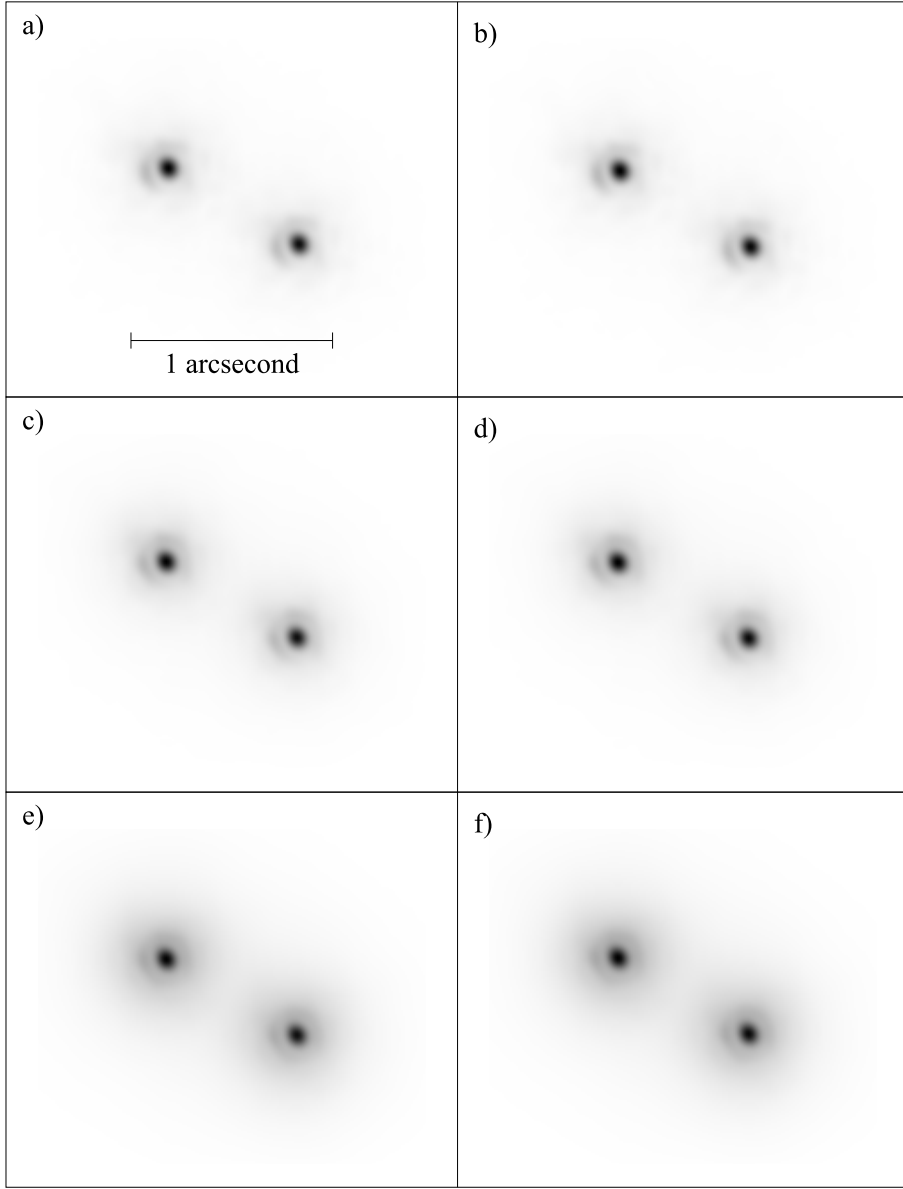


Figure 3.21: Comparison of images generated using different exposure selection approaches in ζ Boötis. In the three left-hand panels (**a**, **c**, **e**), the left-hand binary component has been used as the reference star, while the right-hand component was used for the images in the right-hand panels. The properties of the six images are as follows: **a**) & **b**) best 1% of exposures selected, Strehl ratio of reference star is 0.190 in both images; **c**) & **d**) best 10% of exposures selected, Strehl ratio of reference star is 0.136 in both images; **e**) all exposures shifted and added, Strehl ratio of reference star is 0.0782; and **f**) all exposures shifted and added, Strehl ratio of reference star is 0.0783. In each case the Strehl ratio for the binary companion star is found to be a factor of 0.985 ± 0.005 times lower than for the reference star.

components as recorded on the detector. It is likely that the decorrelation comes partially from noise sources such as detector readout noise, photon shot noise, and in particular the pixellation of the stellar image on the detector. Both the exposure selection step and the image re-centring have a tendency to coherently add the noise components in the image of the reference star to give an artificially high Strehl ratio for this binary component. This effect is described in detail by Nieto & Thouvenot (1991) for the photon-shot noise component. The noise contribution is not expected to show strong correlation between the separate binary components, so the Strehl ratio for the binary companion should not be systematically affected in this way.

It is clear from Figures 3.21a to 3.21f that the imaging PSF degrades gradually as the fraction of exposures selected is increased. The gradual nature of this change may be extremely useful in astronomical programs as the performance of the Lucky Exposures method can be adjusted according to the scientific needs. If an astronomical target is too faint to give good signal to noise using only the best 1% of exposures, the astronomer can choose to use a larger fraction of exposures at the expense of a small degradation in the image quality. If the observational data are stored in a suitable manner, the fraction of exposures selected can be adjusted after the observations have been completed (during the data reduction) in order to give the highest quality science results.

3.5.3 Strehl ratios obtained for ζ Boötis

Figure 3.22 shows a scatter diagram comparing the Strehl ratios for each binary companion in the individual short exposures. There is a strong linear correlation between the Strehl ratios measured for the two stars, with a linear regression correlation coefficient of $r^2 = 0.975$ for a straight line through the origin. The gradient of 1.001 for the best fit line gives a good consistency check on the magnitude difference between the two binary companions (calculated as $\delta m_{(810nm)} = 0.045 \pm 0.03$ from the images in Figure 3.21, and used for calculating the Strehl ratios). The scatter in the points about the best fit line indicates the error in the Strehl ratio measurements from individual short exposures. The RMS difference between the Strehl ratios measured for the two stars was 0.0043. If the random error component of the Strehl ratio measurements is equal for each of the stars, this would imply an RMS random error of 0.003 on each Strehl ratio measurement.

Figure 3.22 compares the Strehl ratios of the brightest speckle in the PSF obtained from each of the stars in individual exposures. This comparison is not sensitive to variations in the relative positions of the brightest speckles for the two stars. In observations of distant ground-based artificial light sources through a turbulent medium, Englander *et al.* (1983) found relative motions in the position of the brightest speckle in Lucky Exposures for light sources which were separated in the object plane but within the isoplanatic patch. A qualitative discussion of this effect for astronomical observations is also found in Dantowitz *et al.* (2000); Dantowitz (1998). If such a variation occurs in the relative positions of the

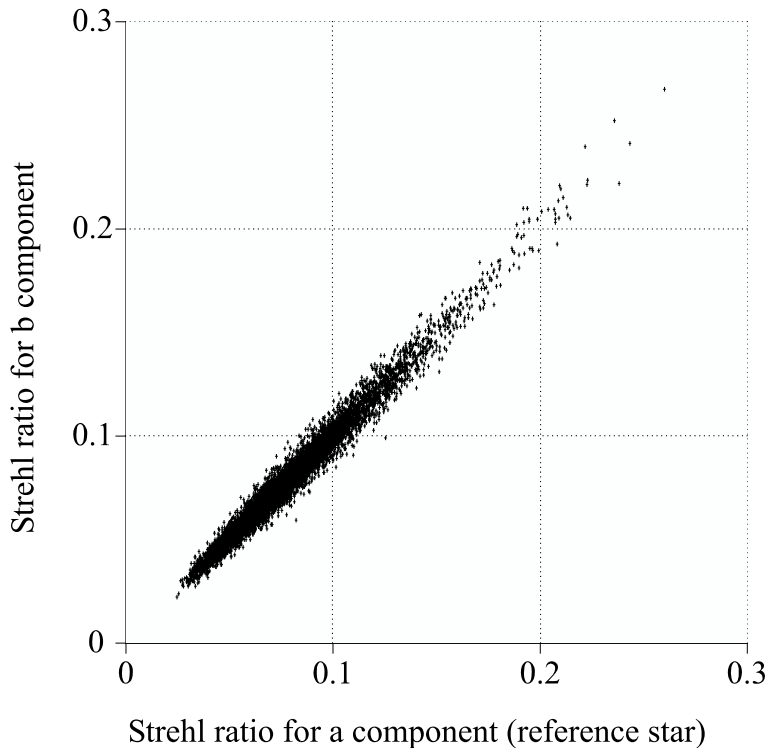


Figure 3.22: Comparison of measured Strehl ratios for the two components in ζ Boötis. The regression coefficient for a straight line through origin is $r^2 = 0.975$. Only exposures of ζ Boötis where both stars are more than 16 pixels from edge of usable detector area were utilised, using data from both runs on this target.

brightest speckles for the two components of ζ Boötis, this will lead to blurring of the image of the companion star when the short exposures are re-centred and co-added based on measurements of the reference star.

In order to investigate the magnitude of this effect, the short exposures were sorted by Strehl ratio into groups which each contained 1% of the total number of exposures. The exposures in each group were then re-centred and co-added based on the measured positions of the brightest speckle for the reference star. This gave a single averaged PSF for the exposures in that group. The Strehl ratios for binary component b are plotted against the Strehl ratios for the reference star (component a) in Figure 3.23 for each of the summed images generated in this way. There is extremely good correlation between the Strehl ratios for the two stars, as emphasised by Figure 3.24. In this Figure, the Strehl ratio for component b has been divided by the Strehl ratio for component a for each of the summed images. The Strehl ratios for component b are typically only 0.5% lower than those for the reference star although there is a more significant difference for the poorest exposures. It is clear from these Figures that there must be very good correlation between the positions of the brightest speckle for the two stars, and that measurements of the position of the brightest speckle using a reference star can reliably be used for re-centring images of another object in the field.

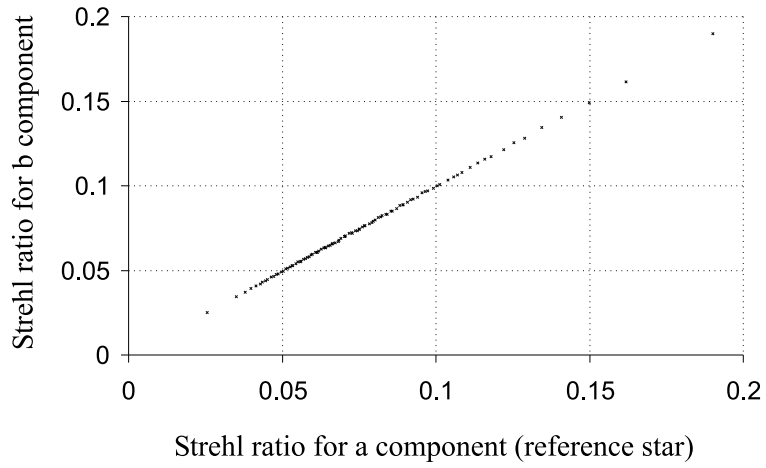


Figure 3.23: Exposures of ζ Boötis were binned into 100 equal groups according to the Strehl ratio measured for binary component *a* (the reference star). The exposures in each group were then re-centred and co-added according to the position of the brightest speckle in the image of the reference star. The Strehl ratios measured in the shift-and-add images for the two binary components are plotted in the figure. The regression coefficient for a straight line through the origin is $r^2 = 0.99985$. Only exposures from both runs on ζ Boötis where both stars are more than 8 pixels from edge of usable detector area were used for this analysis.

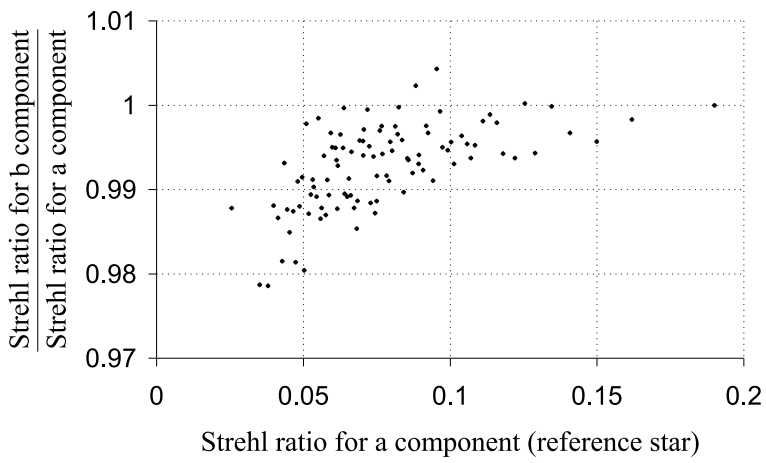


Figure 3.24: The same data as for Figure 3.23, but the Strehl ratios measured for component *b* have been divided by the Strehl ratio for component *a* in each of the summed images.

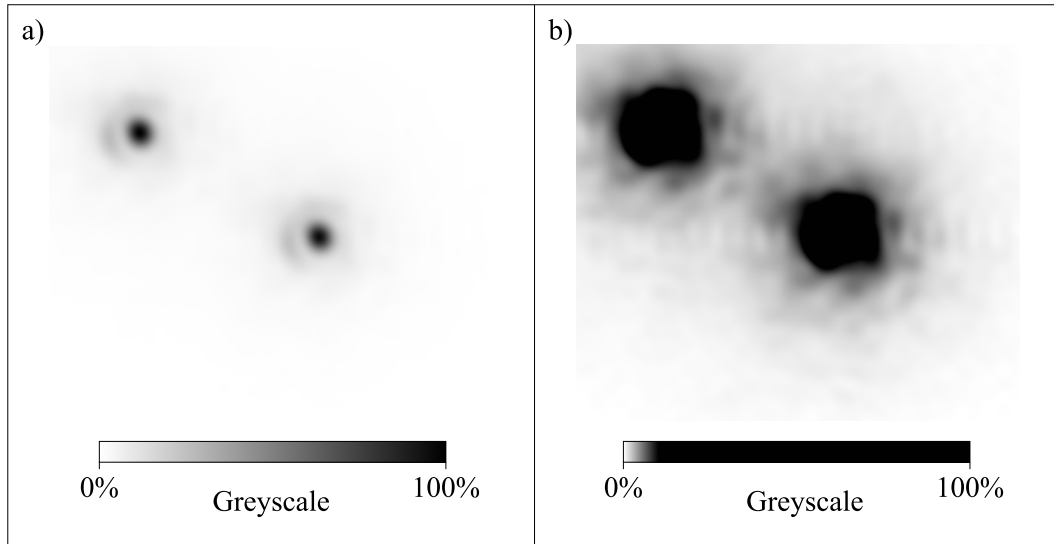


Figure 3.25: The best 1% of exposures of ζ Boötis processed using the Lucky Exposures method and plotted with two different greyscales. Both greyscales are linear below saturation. The upper left star (component *a*) was used as the reference star.

The precise shape of the PSF obtained for the reference star and also that for other objects in the vicinity of a reference star is of interest in determining the applicability of the Lucky Exposures method for astronomical programs. The extent of the wings of the PSF determines the area of sky around bright stars which will be “polluted” by photon shot noise from starlight. If the image of the reference star is sufficiently similar to the PSF obtained for other objects in the field it can be used for deconvolving the astronomical image. For this reason I undertook an investigation of the faint wings of the PSF, and the differences between the PSF obtained for the reference star and that for the binary companion.

Figure 3.25 shows the best 1% of exposures of ζ Boötis using the brighter (left-hand) component as a reference for Strehl ratio measurements. Figure 3.25a shows a linear greyscale ranging from zero to the maximum flux in the image. Figure 3.25b shows the same image with a stretched linear greyscale ranging from zero to one-tenth of the maximum flux. In order to investigate the level of similarity between the PSFs for the two binary companions, I subtracted the image of the right-hand star from the image of the left-hand star. A copy of the image shown in Figure 3.25 was multiplied by the intensity difference between the two stars, shifted by the separation of the stars and subtracted from the original image. This eliminated most of the flux from the left-hand star, as shown in Figure 3.26. The small residual component visible in the greyscale-stretched version of this image shown in Figure 3.26b is largely due to a small error in the measured separation of the stars due to the finite pixel size used. There is no clear evidence for anisoplanatism between the two binary components.

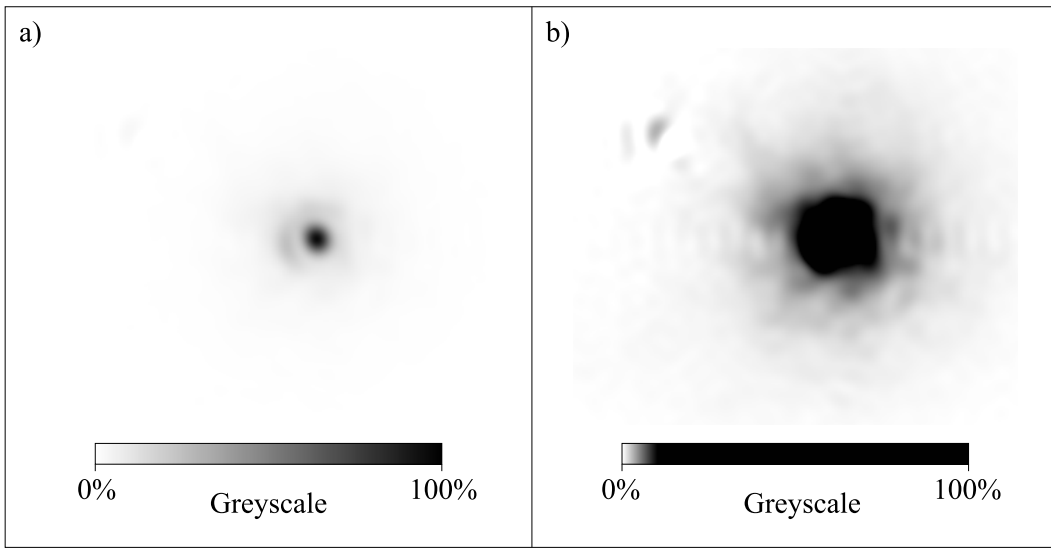


Figure 3.26: The reference star was suppressed from the image shown in Figure 3.25 by subtracting the image of binary component *b* from the reference star image (component *a*). This was done by taking a copy of the image shown in Figure 3.25, scaling it by the magnitude difference for the binary, shifting it by the binary separation, and subtracting it from the original image. Both greyscales are linear below saturation.

The remaining binary component in Figure 3.26 represents a good measure of the PSF for imaging in the vicinity of a reference star using the Lucky Exposures method. The compact image core and steeply decaying wings around the star in this figure indicate that high resolution, high dynamic range imaging will be possible using the Lucky Exposures technique.

The subtracted image in Figure 3.26 allowed investigation of the faint wings of the PSF for component *b* without strong effects from the contribution of the reference star (component *a*). Figure 3.27 shows profiles through the image in Figure 3.26. Curve **X** in Figure 3.27a shows a single cross-section along a line perpendicular to the separation vector between the two stars, passing through binary component *b*. Curve **Y** shows the flux averaged around the circumference of a circle centred on the star, plotted as a function of the circle radius (i.e. a radial profile). At large distances from the core, the flux in the PSF drops off exponentially in both of these curves (with an *e*-folding distance of 0.17 *as*). This is highlighted in the logarithmic plots of the same curves shown in Figure 3.27b. The kink at ~ 0.78 *as* in the radial profile plot corresponds to the location of the reference star, indicating that it was not fully subtracted from the images. For comparison the profile of a diffraction-limited PSF sampled with the same pixel scale is shown in both figures as curve **Z**.

If a large number of selected exposures are co-added, the speckle patterns in the wings of the PSF will average out to give a smooth halo. If the flux in this halo follows the exponentially decaying radial distribution shown by curves **X** and **Y** of Figure 3.27, then the

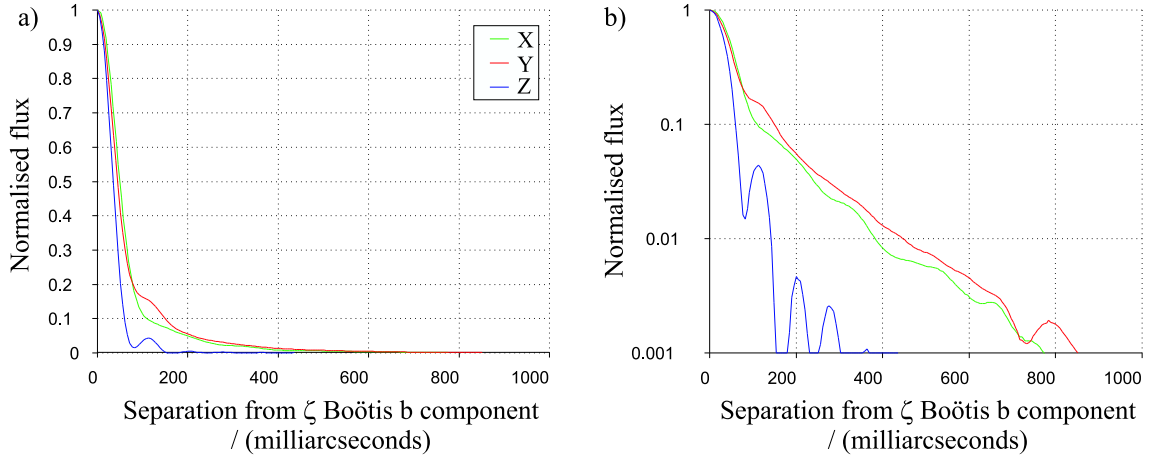


Figure 3.27: Cross sections through the b component of ζ Boötis plotted on a linear scale in the left-hand panel and on a logarithmic scale in the right-hand panel. Curve **X** shows the variation of flux along a line perpendicular to the separation between the binary components in Figure 3.25. Curve **Y** shows a radially averaged profile of the b component after subtraction of the a component (based on Figure 3.26). Curve **Z** shows the simulated profile in the absence of atmospheric turbulence (but with the same pixel sampling and a 32×32 grid of sub-pixel position offsets for star, resampled, re-centred and co-added in the usual way).

halo flux could be removed using deconvolution with a simple axisymmetric, exponentially decaying model for the PSF. This would only leave a small residual component from the photon shot noise and small deviations of the PSF halo from the model. It is clear from the rapid decay of the curves in Figure 3.27 that very high dynamic range imaging should be possible, even within relatively crowded fields.

3.5.4 Resolution and spatial frequency response

Both the Lucky Exposures method and the conventional approach of shifting and co-adding all the exposures preserve the Fourier phase information in the images very effectively. For both methods the Fourier amplitudes are reduced (by the modulation transfer function). In order to compare the high resolution imaging performance of the Lucky Exposures and shift-and-add methods, I computed a number of Fourier autocorrelations using some of the data taken on ζ Boötis, and have displayed them in Figure 3.28. These Fourier autocorrelations preserve the Fourier amplitude information, although all phase information is lost. The Fourier autocorrelation provides a more intuitive representation of the high resolution performance than the modulation transfer function, as the structures in the image autocorrelation can be related directly to structure in the images.

Figure 3.28a shows the summation of the autocorrelations for all the short exposures used in the analysis. This image essentially represents the method of Labeyrie (1970) as applied

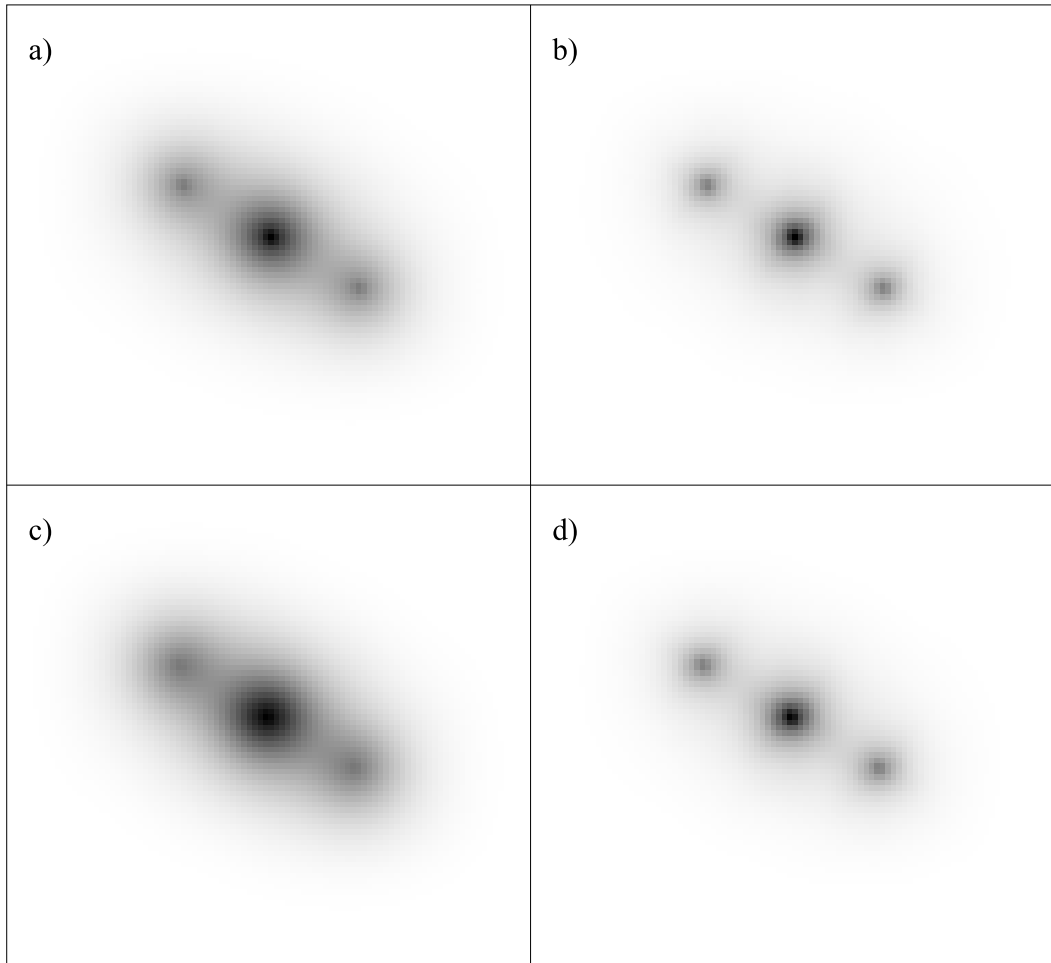


Figure 3.28: Spatial autocorrelations calculated from exposures of ζ Boötis from the first of the two runs on 2000 May 13. Exposures where the binary components are less than 16 pixels from edge of the usable region of the CCD have been excluded. **a)** shows the summed autocorrelation of all the raw exposures; **b)** shows the summed autocorrelation of the exposures with the highest 1% of Strehl ratios; **c)** shows the autocorrelation of the shift-and-add image generated from the raw data; and **d)** shows the autocorrelation of the shift-and-add image of the exposures with the highest 1% of Strehl ratios. The FWHM of these autocorrelations are: **a)** 0.44 as ; **b)** 0.22 as ; **c)** 0.61 as ; and **d)** 0.24 as .

to our data on ζ Boötis. Figure 3.28b shows the summation of the autocorrelations for only those exposures having the highest 1% of Strehl ratios. This autocorrelation has a much more compact core and a fainter halo, indicating that the best 1% of exposures preserve significantly more high spatial frequency information.

It is now of interest to compare the autocorrelations of Figure 3.28a and 3.28b (generated directly from the raw data) with the autocorrelations obtained after the short exposures have been processed using either the conventional shift-and-add approach or using the Lucky Exposures method. Figure 3.28c shows the autocorrelation generated from the conventional shift-and-add image based on the same exposures as were used in Figure 3.28a. The shift-and-add process has produced a substantial reduction in the sharpness of the final autocorrelation, which indicates that the shift-and-add image itself is somewhat degraded in resolution. On the other hand, the autocorrelation of the shift-and-add image generated using the selected exposures (Figure 3.28d) is almost as sharp as that generated directly from the original exposures (Figure 3.28b). It is clear that with the Lucky Exposures method, one benefits not only from the higher resolution of the selected exposures themselves, but also from a substantial improvement in the performance of the shift-and-add process when it is applied to these high Strehl ratio exposures.

3.5.5 Weighting exposures

Instead of selecting or rejecting individual exposures, measurements of the image quality could be used to weight the exposures in the final re-centred and summed image. In this section I will compare the performance of one formula for exposure weighting with the exposure selection method. In order to determine the best approach for the exposure weighting, it is necessary to define a more quantitative measure of the signal to noise for high resolution imaging. In order to allow rapid measurements on large datasets I chose a rather simple three step approach:

1. The Fourier power at high spatial frequencies in the core of the PSF was summed, to represent a measure of the signal at high spatial frequencies;
2. The Fourier power at high spatial frequencies in a region of the wings of the PSF was summed, to represent a measure of the noise at high spatial frequencies; and
3. My estimate of the signal-to-noise R was taken simply as a ratio of the two numbers calculated in steps 1 and 2.

In order to ensure that the measurements of the signal were not significantly contaminated by noise, these signal-to-noise measurement were applied to images obtained after shifting and co-adding a number of exposures.

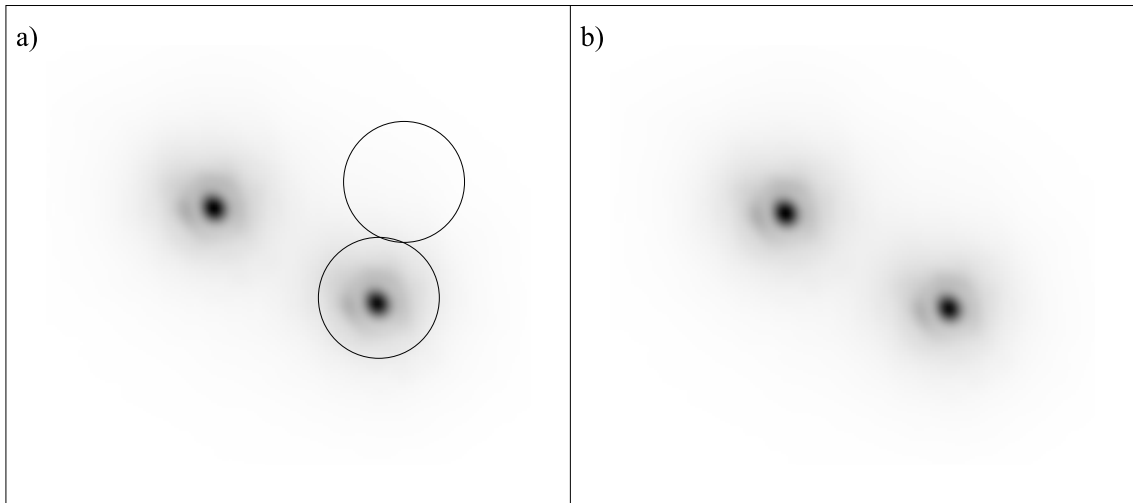


Figure 3.29: **a)** shows the Lucky Exposures image generated using the best 41% of exposures with circles overlaid to indicate regions used for signal and noise measurements at high spatial frequencies. **b)** shows an image where each exposure is weighted by Strehl ratio to the power of 2.416. The left-hand star was used as the reference, and the Strehl ratio for the companion star in both these images is 0.11. For simplicity only data from the first run on ζ Boötis was used for this analysis.

The short exposure images of ζ Boötis in the first run were first sorted in order of the Strehl ratio measured on the brighter component. The exposures were then binned into groups of exposures with similar Strehl ratios, each group containing 1% of the total exposures. The exposures in each group were then shifted and co-added, reducing the dataset to 100 images, each representing one of the groups.

The signal-to-noise measurement described above was applied to these 100 images using the *b* component of ζ Boötis (the *a* component had been used as the reference star). The region around the *b* component used for the “signal” measurements was limited to the circle around the star shown in Figure 3.29a. A circular flat-topped window which dropped smoothly to zero at the edges (similar to a Hanning window) was used to extract a finite region of the image data without introducing high frequency noise components at the boundaries of the circle. A similar section of the image away from the stars was used for noise measurements (shown by the upper circle in the image). The range of spatial frequencies used to represent *high resolution* in the image was initially chosen (rather arbitrarily) as those ranging between 6.25 *cycles/as* and 12.5 *cycles/as*, and the image power spectrum was summed in two dimensions over these spatial frequencies. The effect of varying this range of spatial frequencies will be discussed later.

The signal-to-noise ratio R for high spatial frequencies calculated in this way is plotted against the Strehl ratio S for the reference star in the images in Figure 3.30a. Also shown

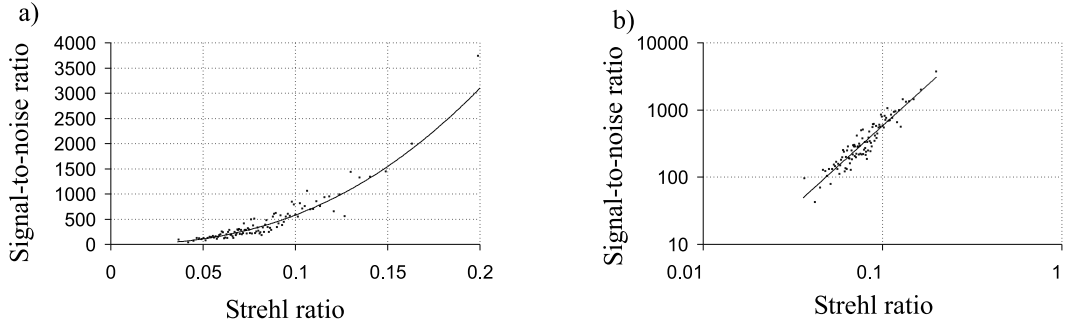


Figure 3.30: Panel **a)** shows an estimator for the signal-to-noise of the high spatial frequency components in the image of binary component *b* when component *a* is used as the reference star, as described in the text. Panel **b)** shows the same data on a logarithmic scale. The first run of ζ Boötis was used for this analysis.

is the best fitting function of the form:

$$R = AS^b \quad (3.4)$$

where the values of A and b were determined by least-squares fit. For the best fit line shown in Figure 3.30a, $b = 2.4$. Figure 3.30b shows the same data plotted on logarithmic scales.

Now that we have a relationship between the Strehl ratio of the short exposures and R , our measure of the signal-to-noise ratio, we can make a concerted effort to produce the image with the maximum signal-to-noise ratio using the data on ζ Boötis. If the individual exposures are treated as independent, uncorrelated measurements, then the signal-to-noise ratio should be maximised if all the exposures are selected, but the individual exposures are weighted according to their Strehl ratios.

The data from the first run on ζ Boötis were processed in this way, with the individual exposures weighted by a value W proportional to our signal-to-noise estimate:

$$W = AS^b \quad (3.5)$$

The exposures were then re-centred and co-added to give the image in Figure 3.29b. This image has a Strehl ratio of 0.11 and a signal-to-noise ratio of $R = 936$. Alongside this in Figure 3.29a is the image generated from simple exposure selection (without weighting of the exposures) which has the same Strehl ratio. The fraction of exposures required to give this Strehl ratio was 41% (determined by trial and error in a semi-automated procedure). The signal-to-noise ratio R for the image in Figure 3.29a is 935, essentially identical to that provided by the weighted exposures approach in Figure 3.29b. The conventional shift-and-add approach performs less favourably, with a signal-to-noise ratio of 479.

If the signal-to-noise criteria R used to determine the signal-to-noise ratio for high resolution imaging is modified, and the same analysis is followed through, then the Strehl ratio

of the final image from the weighted exposures approach will be different. A number of different measures of signal-to-noise were tested, either utilising different ranges of spatial frequencies, or weighted proportionately with the image Strehl ratio. For all the weighting models tested, I also generated images with similar Strehl ratios using the simple exposure selection method without weighting. The images generated using exposure selection always gave similar signal-to-noise ratios to the images generated using exposure weighting. With faint reference stars the accuracy of the Strehl ratio measurements is dependent on the Strehl ratio itself, and the choice of optimum weighting function becomes very complex. The complexity of the various weighting models, their dependence on the numerous aspects of the observations which affect the accuracy of Strehl ratio measurements, and the increased computational requirements make this approach less favourable than simple exposure selection. The analyses in the remainder of this thesis will be restricted to exposure selection without weighting of the exposures.

3.5.6 Anisoplanatism

Short exposure images of the two components in the 4.4 *as* binary γ Leonis provide measurements of the atmospheric perturbations along two paths through atmosphere. The difference in the speckle pattern observed for the two binary components gives a measure of the isoplanatism in the atmosphere. For the purposes of this analysis I will consider the isoplanatic angle θ_e to be the separation from a reference star which causes a reduction by a factor of $\frac{1}{e}$ in the Strehl ratio of an unresolved target.

The isoplanatic angle for the Lucky Exposures technique θ_e should be very similar to the angle at which the speckle patterns for the two stars have decorrelated by a factor of $\frac{1}{e}$. The argument for this is based on the direct parallels between the decorrelation of the speckle pattern as a function of angle and the decorrelation of the speckle pattern as a function of time discussed in Chapter 2.4. Measurements in Chapter 3.4.3 indicated that the decrease in the Strehl ratio with time followed the decorrelation occurring at another (arbitrary) point in the speckle pattern with time, and the same relationship would be expected as a function of angle between the reference star and an off-axis target. The isoplanatic angle θ_e is thus expected to be analogous to the timescale τ_e for changes in the speckle pattern.

Measurements of θ_e would ideally be obtained from simultaneous observations of a target very close to the reference star, and another target at a separation which produced a Strehl ratio lower by a factor of $\frac{1}{e}$. As appropriate data is not available here, a model of the effect of atmosphere is required in order to extrapolate the results, leading to some uncertainty in the accuracy of the result.

In order to obtain the best possible temporal sampling, the second run on γ Leonis with the higher frame rate of 182 Hz was used in this analysis (as described in Table 3.3).



Figure 3.31: Lucky Exposures observation of γ Leo using the left-hand star as the reference and selecting the best 1% of exposures. The Strehl ratio for the reference star is 0.099, which compares favourably with the Strehl ratio for the average image (generated without selection or re-centring) of 0.015. The Strehl ratio for the right hand star is only 65% as high as that for the left hand star, and the separation of the stars is 4.4 as .

The left-hand (fainter) star was used as a reference for selecting the best 1% of exposures, and the resulting image is shown in Figure 3.31. The reference star Strehl ratio is 0.099, unusually low for observations in this period of NOT technical time. This suggests that the seeing may have been poorer for this run.

We cannot tell exactly what Strehl ratio could be obtained in the vicinity of the reference star. However, the high signal-to-noise for these observations, and the high level of correlation between the stars in the close binary ζ Boötis suggest that the Strehl ratio for the reference star gives us a reasonable approximation for the Strehl ratio which would be obtained on a nearby target. The right-hand star in Figure 3.31 has a Strehl ratio only 65% as high as that for the reference star. The lower Strehl ratio implies that the images of the two stars are partially decorrelated in the short exposures. This decorrelation probably results from anisoplanatism related to the separation of the binary. In order to calculate the separation from the reference star which would give a Strehl ratio of $\frac{1}{e}$ it would be necessary to know the detailed structure of the atmosphere at the time of the observations. Fitting models of the form of Equation 2.20 or similar to those of Roddier *et al.* (1982b) give values between 7 as and 8 as . Much better constraints could be put on this if wider binaries were observed – the observations in 2000 were somewhat limited by the maximum pixel rates at which the camera could operate, and hence the field of view which could be used for high frame-rate imaging. It is possible that better seeing conditions present for the runs on other targets might have also given a different (presumably larger) isoplanatic angle.

Figure 3.32 shows a shift-and-add image utilising all of the short exposures. The faint halo around the stars is more obvious in this image, but it is also much smoother in appearance. The smoothness is probably a result of the larger number of different short exposures involved, each representing a different atmospheric realisation. The Strehl ratio of the left hand star in this case is 0.048. The Strehl ratio for the right-hand star is 0.033, only a factor of two higher than the Strehl ratio of the long exposure seeing disk. The



Figure 3.32: γ Leo using left hand star as reference, all the exposures. The Strehl ratio for the left hand star is 0.048. The Strehl ratio for the right hand star is 68% as high as that for the left hand star.

Strehl ratio of this star is 68% as high as that for the left hand star, again suggesting significant anisoplanatism.

The reduction in the Strehl ratio brought about by anisoplanatism was measured using different criteria for exposure selection. The exposures of γ Leonis were binned into one hundred equal groups each containing exposures with similar reference star Strehl ratios, as had been performed for data on ζ Boötis in Figure 3.23. The exposures in each group were shifted and co-added, resulting in a set of 100 images. The Strehl ratios for the reference star and the binary companion were calculated for each of these images. The high signal-to-noise ratio for these observations mean that the ratio of the binary companion Strehl to the reference star Strehl is a good measure of the reduction factor for the off-axis Strehl ratio brought about by atmospheric anisoplanatism. Figure 3.33 shows such measurements, plotted against the reference star Strehl ratio. It is clear that the fractional reduction in Strehl ratio brought about by atmospheric anisoplanatism for this data is not strongly dependent on the reference star Strehl ratio if the Strehl ratio is greater than 0.03.

It should be noted that the fractional reduction in Strehl ratio brought about by atmospheric anisoplanatism does not provide a direct measure of the size of the isoplanatic patch. The long exposure image constructed from the same data has a Strehl ratio of 0.015, and it will be unlikely that the Strehl ratios for short exposures would fall substantially below this value however small the isoplanatic patch. For low reference star Strehl ratios there will be a lower limit on the companion star Strehl ratio set by the finite size of the seeing disk into which most of the light from the companion star will fall (regardless of the anisoplanatism). This will tend to bias the companion star Strehl ratios obtained for low reference star Strehl ratios, and may explain why the Strehl ratios of the two stars are more similar under these conditions.

Given the lack of a model for the stratification of the atmosphere at the time of the observation, it is not possible to determine how the Strehl ratio should vary as a function of binary separation, and so we cannot say with any certainty that the isoplanatic patch is larger or smaller in the Lucky Exposures than it is in typical exposures.

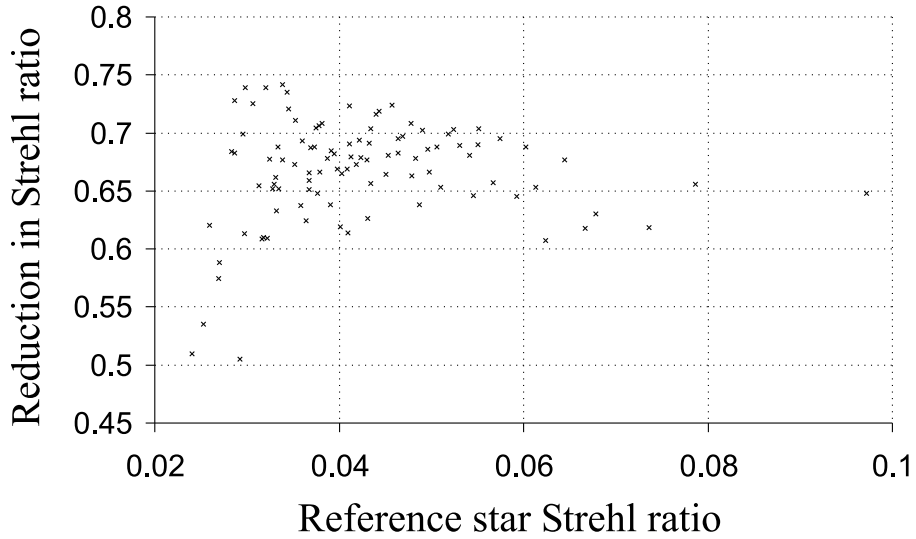


Figure 3.33: The fractional decrease in Strehl ratio for off-axis stars as measured for γ Leonis. This plot is of the same type as Figure 3.24 but for the data on γ Leonis. The left hand binary component was used as a reference star for measurements of the Strehl ratio and position of the brightest speckle. The exposures were then put into groups according to reference star Strehl ratio, with each group containing 1% of the exposures. The fractional difference between the Strehl ratios of the two binary components is plotted against the reference star Strehl ratio in the figure.

3.5.7 Temporal and spatial cross correlation

In order to investigate the temporal properties of the correlation between the left-hand star Strehl ratio and the Strehl ratio of the right-hand star, a temporal cross correlation of the measured Strehl ratios was performed. The peak of this function occurs when the Strehl ratio of the left-hand star is correlated with the Strehl ratio obtained one or two frames later for the right-hand star (5–11 ms later), as shown in Figure 3.34a.

Figure 3.34b shows the effect of finding the highest 1% of reference star Strehl ratios, but actually selecting exposures an integer number of frames before or after the frame with the high reference star Strehl ratio. The image re-centring was also based on measurements of the reference star in the exposure with the high reference star Strehl ratio, and not the exposure actually used. The Strehl ratio obtained on the binary companion in the final image is plotted against the delay between the Strehl ratio and reference star position measurements and the application of these measurements to the data. The peak Strehl ratio for the companion star is obtained if the delay is 5 ms. The curve has the same general shape as that for self referencing with ϵ Aquilae, shown in Figure 3.18, except for the time delay.

The observed delay in the response of the binary companion image to fluctuations in the reference star image suggests the presence of an intermediate or high altitude layer

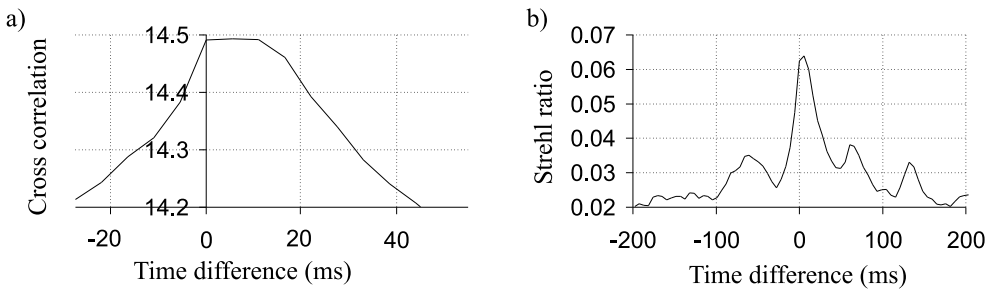


Figure 3.34: **a)** The cross correlation of Strehl ratio for the left-hand binary component in the γ Leo data with the Strehl ratio for right-hand star in a different exposure. The difference in the exposures used is indicated by the time difference between the acquisition times of the exposures, shown along the horizontal axis. The peak correlation is after a delay of one frame ($\simeq 5.5$ ms), suggesting that the wind was blowing refractive index fluctuations from the left-hand side to the right-hand side of the light path through the atmosphere. **b)** The Strehl ratio obtained for the right hand star using the Lucky Exposures method selecting 1% of the exposures using the left-hand star as the reference. The Strehl ratio and position of the brightest pixel were used to select and re-centre different short exposures to see how the final image was affected – the difference in exposure number used is indicated as a time difference on the horizontal axis.

of seeing moving with a velocity which has a component along the axis of the binary separation in the plane of the sky. Phase perturbations experienced by the reference star are thus blown into the beam of light from the binary companion between 5 and 11 ms later, producing the observed cross-correlation.

3.5.8 Atmospheric dispersion and β Delphini

Fig. 3.35 shows the result of a selection of the 1% of images with the best Strehl ratios from a dataset of 7000 short-exposure CCD images of the binary β Delphini. In this case the zenith angle of the observation was 50° and the images are blurred by 100 mas due to atmospheric dispersion over the 125 nm bandpass of the filter, reducing the Strehl ratio of the final image to 0.20. This dispersion results from the variation in the refractive index of air with wavelength, which causes a change in the atmospheric refraction angle as a function of wavelength. It can be corrected using glass prisms with an appropriate wedge angle.

The magnitude difference between the components is $\Delta m = 1.070 \pm 0.005$. This value is in good agreement with those of Barnaby *et al.* (2000) of 1.071 ± 0.004 at 798 nm and 1.052 ± 0.010 at 884 nm made using a 1.5 m telescope.

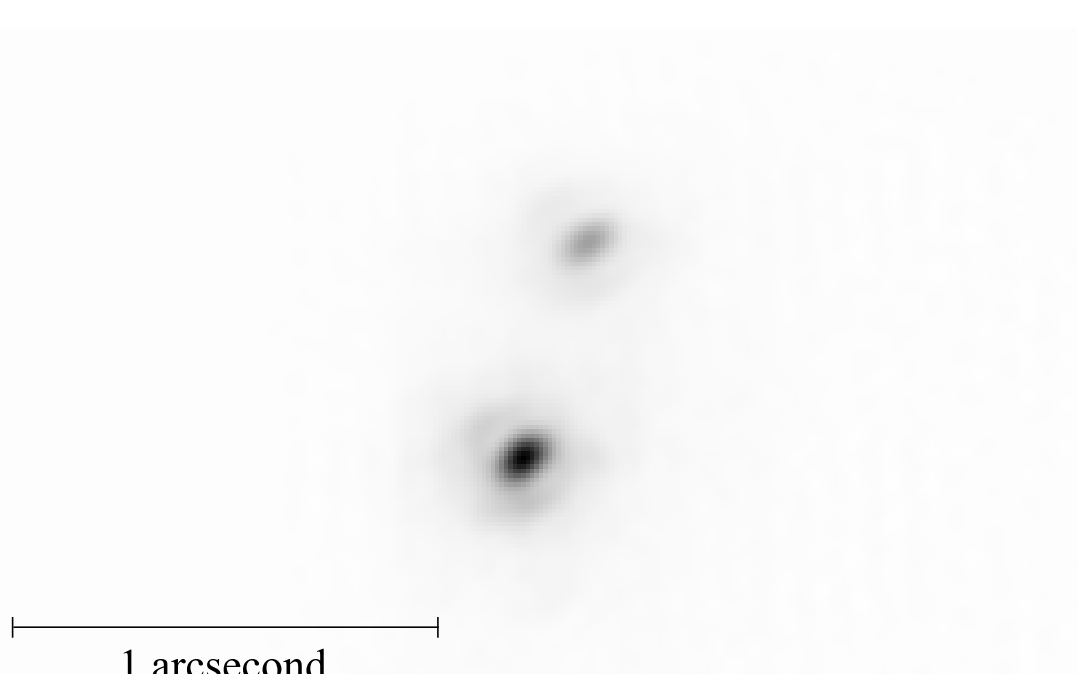


Figure 3.35: The Lucky Exposures method as applied to the spectroscopic binary β Delphini. The best 1% of exposures of β Delphini were selected, shifted and added to produce this image. The blurring evident in the image is thought to result from atmospheric refraction.

3.5.9 Dynamic range

Observations of the binary α Herculis were also obtained on the night of 2003 May 13. The brighter primary component saturated the detector, but it was possible to perform exposure selection on the faint companion (typically three magnitudes fainter, depending on the variable brightness of the primary component), as shown in Figure 3.36. The absence of significant scattered light from the bright companion emphasises the potential to perform high-dynamic range imaging given suitable camera performance. There is no evidence that the primary component is a 190 mas binary as suggested by McAlister *et al.* (1989), but this cannot be ruled out due to the detector saturation.

3.5.10 Seeing conditions

In order to investigate the relationship between the FWHM of the seeing disk for observations with the performance of the Lucky Exposures method, all the observations in Tables 3.2 and 3.3 were analysed using the Lucky Exposures approach. The best 1% of exposures were selected in each case, and the Strehl ratio for the image obtained in this way is plotted against the FWHM of the seeing disk in Figure 3.37. There is a clear relationship between these two parameters, indicating (as expected) that the highest image quality is obtained under conditions where the conventional seeing disk is small. The scat-

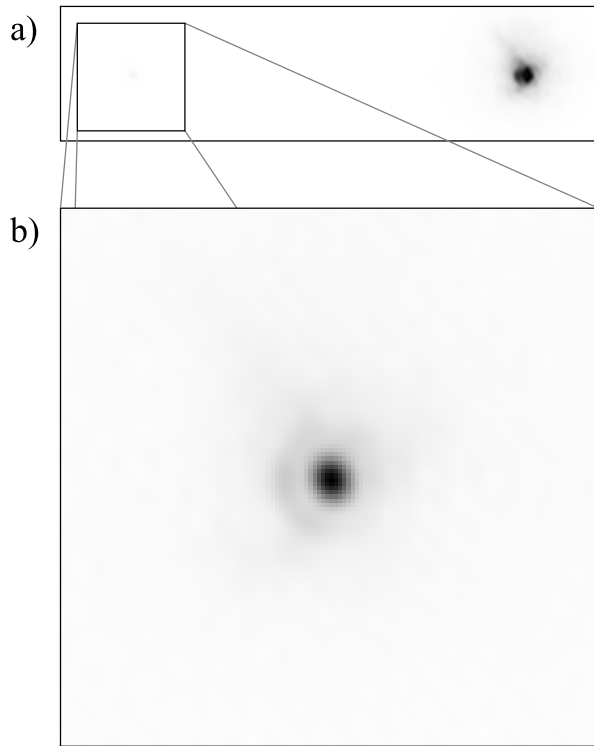


Figure 3.36: Lucky Exposures image of α Her using the faint component as the reference star. The best 1% of exposures were selected, giving a Strehl of ratio of 0.24 for the reference star. The bright component was saturated in the individual short exposures.

ter in the results may be due to the strong dependence of seeing FWHM on the low-order tip-tilt components in the wavefront perturbations, which have insignificant effect on the Lucky Exposures image quality. The regression coefficient for the fitted line is $r^2 = 0.44$.

3.6 Conclusions

The analyses presented here indicate that high resolution images can be obtained using the Lucky Exposures method even if the telescope used for the observations is not diffraction-limited. Mirror figuring errors which only vary slowly with position in the aperture plane can be corrected by the atmosphere during a Lucky Exposure as long as the figuring errors are sufficient small in amplitude. However, the probability of obtaining exposures with high Strehl ratios is reduced by such aberrations.

Using numerical simulations I found that accurate Strehl ratios could be calculated from pixellated short exposure images by sinc-resampling the images and then using the flux in the brightest pixel of the resampled image as an indication of the peak flux in the original speckle pattern. The images generated from the resampled, simulated exposures clearly showed a first Airy ring indicating that the pixel sampling was adequate for high

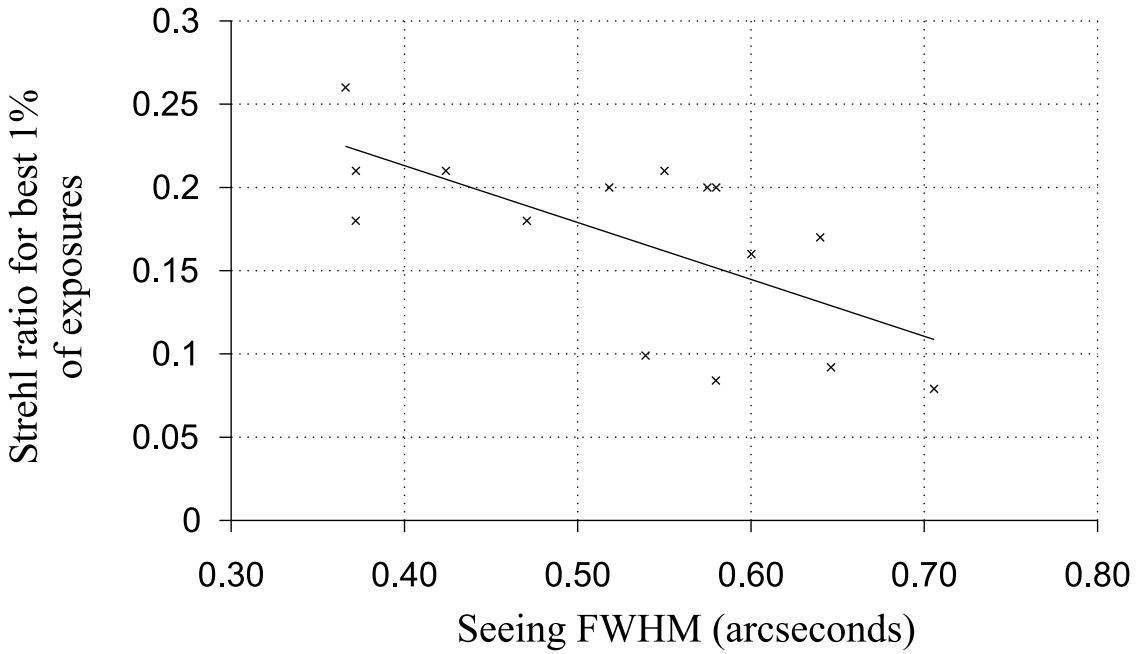


Figure 3.37: Strehl ratio for the Lucky Exposures image generated using best 1% of exposures plotted against the seeing FWHM for each of the runs.

resolution imaging. The calculated Strehl ratios were normalised using simulated data.

High frame-rate imaging data taken at the NOT in May 2000 were analysed in this chapter. The Strehl ratios measured for the short exposure images were found to be consistent with the atmospheric models presented in Chapters 1 and 2.

The temporal properties of the high frame-rate imaging data were investigated. The initial decorrelation in the recorded datasets was found to be determined by the telescope oscillation. Aside from the effects of telescope oscillation, the speckle patterns appeared to remain correlated for $\sim 65\text{ ms}$ for the data analysed on ϵ Aquilae (this was also consistent with the observations of γ Leonis). This implies that exposure times of at least 30 ms should be adequate for high resolution imaging under atmospheric conditions similar to those experienced during our observing run. The brightest speckle was found to decay on similar timescales. The timescale relevant for the best 1% of exposures appeared very slightly larger (but of a very similar magnitude).

Short exposures of ϵ Aquilae were binned together without re-centring in order to simulate longer camera exposure times. With effective exposure times of 27 ms , the Strehl ratio for the Lucky Exposures image generated from the best 1% of exposures is only 15% lower than that obtained using 5.4 ms exposures. This reduction in Strehl ratio is probably predominantly due to the telescope oscillation. One 108 ms exposure generated from data taken when the telescope oscillation appeared to be at a minimum had a very high Strehl ratio of 0.24. This implies that the atmospheric coherence timescale may have been longer than 65 ms at this instant. Studies of data from ϵ Aquilae suggest that much of the

structure in the wings of the PSF for our imaging method results from the limited number of atmospheric realisations sampled. For deeper observations utilising longer periods of observing time (and using more selected exposures and hence more realisations of the atmosphere) the PSF should be much smoother. This is supported by results from ζ Boötis using a larger number of short exposures.

Observations of the binary star ζ Boötis showed a high degree of isoplanatism over the small separation of the binary ($0.8\text{ }as$). When one star was used as the reference for image selection, the imaging PSF for that star was not substantially different than that obtained for the companion. Profiles through one component of ζ Boötis indicated that the flux in the PSF dropped exponentially towards zero with increasing radial distance from the PSF core, with an *e*-folding distance of approximately $0.17\text{ }as$. This implies that high dynamic range observations should be possible using the Lucky Exposures method, as highlighted by the observations of α Herculis.

When larger fractions of exposures were selected, the image Strehl ratio decreased in a gradual way. When all the exposures are used, a conventional shift-and-add image is obtained.

The Strehl ratios measured for the two different components in ζ Boötis were found to agree in individual exposures to within 0.3% RMS. No evidence was found for differential motion of the two stars in the short exposure imaging data.

Spatial autocorrelations of the individual short exposures and of the images generated using the Lucky Exposures method indicate that re-centring and co-adding the best 1% of exposures does not produce a significant loss of high spatial frequency information. In contrast, re-centring and co-adding all the exposures does appear to produce a significant reduction in the highest spatial frequencies. Combined with the poorer intrinsic quality of typical exposures, this leads to substantially poorer image resolution.

Observations of the $4.4\text{ }as$ binary γ Leonis showed evidence of atmospheric anisoplanatism, implying an isoplanatic angle of less than $10\text{ }as$. Simultaneous observations of objects separated by a larger angle on the sky are required in order to measure the isoplanatic angle accurately. The Strehl ratio obtained for one component of γ Leonis was found to be most strongly correlated with the Strehl ratio for the other component 5—11 ms later, suggesting that the temporal decorrelation was at least partly related to an intermediate or high altitude layer which had a velocity component in the direction separating the stars in the plane of the sky.

Chapter 4

Electron multiplying CCD performance

4.1 Introduction

The observations described in Chapter 3 were of relatively bright stars using a conventional high frame rate CCD camera. The readout noise present at these high frame rates would have led to poor signal-to-noise ratios for observations of faint sources.

CCDs recently developed by both E2V Technologies (Jerram *et al.* 2001; Harris *et al.* 2000) and Texas Instruments (Hynecek & Nishiwaki 2002) with essentially zero readout noise at low light levels seem particularly well suited to high frame rate imaging techniques like the Lucky Exposures method. Craig Mackay acquired a number of these devices at the Institute of Astronomy, and developed a camera designed to operate them at fast readout rates. This seemed an excellent instrument for testing the performance of the Lucky Exposures technique for imaging faint astronomical targets.

Before undertaking any astronomical observations with this camera, an assessment was made of the expected signal-to-noise performance at low light levels. Two simple numerical models of the output register from one of the E2V *L3Vision* CCDs were developed by the author in order to make estimates of the signal-to-noise. Detailed descriptions of the statistical properties of these models are presented in this chapter.

The astronomical observations undertaken using the camera will be introduced in Chapter 5. However, a small section of example data from one of the observing runs is introduced in the current chapter, in order that I can compare the statistical properties of the data with the properties of my theoretical models.

In this chapter I will develop models for the expected distributions of output electrons from these CCDs. These models will be of use to future researchers wishing to simulate

the performance of the devices. These models are also used to estimate the performance of photon-counting approaches with one run of data taken at the NOT.

In this chapter I also briefly discuss measurements of the charge transfer efficiency of the camera at low signal levels which were undertaken in the laboratory after the first observations at the NOT. These results will be of use in discussions of observational data in later chapters.

4.2 Simple models of the L3Vision CCDs

4.2.1 L3Vision CCD architecture

L3Vision CCDs have a relatively standard frame-transfer CCD structure but have an output register which has been extended with an additional section called the “multiplication register”, as shown in Figure 4.1. In the multiplication register one of the three phases is clocked with a much higher voltage than is needed purely for charge transfer (typically 30–40 V). The large electric fields which are established within the semiconductor material accelerate charge-carrier electrons to sufficiently high velocities that additional carriers can be generated by impact ionisation, as described in Burt & Bell (1998); Jerram *et al.* (2001). This generates a small level of charge multiplication (signal gain) in each stage of the high-voltage multiplication register. The large number of gain stages in the register can lead to a substantial overall gain in signal level. The output of the multiplication register is read out using a conventional CCD amplifier. Measurements in the laboratory did not show any signs of non-linearity in the multiplication register when the CCDs were operated at signal levels well below saturation (Mackay *et al.* 2001).

4.2.2 Model descriptions

Two simple mathematical models were developed for the multiplication register gain stages of the L3Vision CCDs. In both cases the number of additional charge carriers generated from each input electron through impact ionisation was treated as an independent random variable with a probability distribution which remained fixed for the duration of each simulation. The gain stages were assumed to have perfect charge transfer efficiency, so the input electrons were always passed to the output of the gain stage regardless of whether or not impact ionisation took place. The two linear models of a single gain stage which were considered can be summarised as follows:

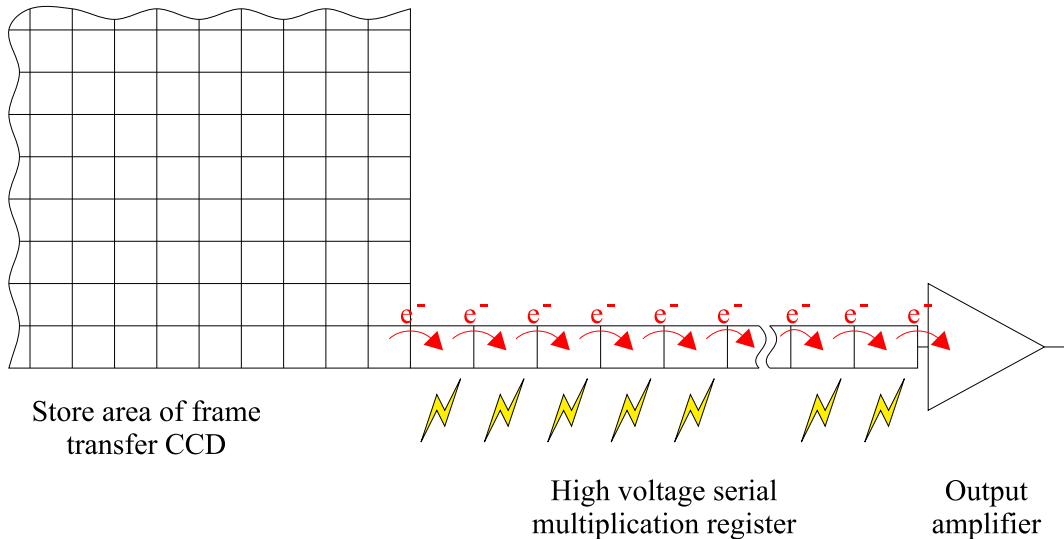


Figure 4.1: Electrons are transferred serially through the gain stages making up the multiplication register of an L3Vision CCD. The high voltages used in these serial transfers induce the creation of additional charge carriers through impact ionisation.

- Model 1 For the first model, for each input electron the number of additional electrons generated by impact ionisation within the gain stage was selected from a Poisson distribution. This corresponds to the case where impact ionisation is an instantaneous process, and an input electron can generate multiple charge carriers within a single gain stage. Impact ionisation events triggered by secondary electrons generated within that gain stage were not considered.
- Model 2 For the second model, a maximum of one additional electron could be generated through impact ionisation within one gain stage. This corresponds to the case where the generation of additional electrons by impact ionisation cannot occur twice within the time taken to transfer the charge from one gain stage to the next.

It is unlikely that either model perfectly describes the real operation of a gain stage, but the models considered here cover a reasonably broad spectrum of possible properties.

4.2.3 Statistics of a single gain stage

The statistics of each of these models can be calculated straightforwardly for the case of a single input electron.

Model 1

For model 1, the probability distribution for the number x of electrons generated by impact ionisation from a gain stage when one electron is input is defined by a Poisson distribution:

$$P(x) = \frac{\alpha^x e^{-\alpha}}{x!} \quad (4.1)$$

where $P(x)$ is the probability distribution for the number x of additional charge carriers generated and α is the expectation value for the number of additional charge carriers generated. The variance of the Poisson distribution is equal to the expectation value α .

It is perhaps more useful to describe Equation 4.1 in terms of the total number of output electrons $n = x + 1$ (i.e. including the single input electron):

$$P_{1e}(n) = \frac{(\mu - 1)^{(n-1)} e^{(1-\mu)}}{(n-1)!} \quad (4.2)$$

where $P_{1e}(n)$ is the probability distribution for the total number of output electrons and μ is the expectation value for the total number of output electrons (equal to the gain of the stage; $\mu = \alpha + 1$). As the charge transfer efficiency is perfect, μ is always greater than or equal to one. The variance in the total number of output electrons is equal to the gain minus one:

$$\sigma_{out}^2 = \mu - 1 \quad (4.3)$$

As the model is linear and the electrons are treated independently, the variance in the number of output electrons for a fixed number of input electrons m_{in} is just:

$$\sigma_{out}^2 = m_{in} (\mu - 1) \quad (4.4)$$

If there is a variance σ_{in}^2 in the number $\langle m_{in} \rangle$ of input electrons, the total variance in the number of output electrons σ_{out}^2 is just:

$$\sigma_{out}^2 = \langle m_{in} \rangle (\mu - 1) + \mu^2 \sigma_{in}^2 \quad (4.5)$$

Model 2

For model 2 the probability distribution for the output electrons from one gain stage given one input electron is described by:

$$P_{1e}(n) = \begin{cases} 2 - \mu & \text{for } n = 1 \\ \mu - 1 & \text{for } n = 2 \\ 0 & \text{for other values of } n \end{cases} \quad (4.6)$$

The expectation value of the gain μ is limited to the range $1 \leq \mu \leq 2$ by the assumptions in model 2.

The variance in the number of output electrons given precisely m_{in} input electrons with model 2 is given by:

$$\begin{aligned}\sigma_{out}^2 &= m_{in} \left(\sum_n P_{1e}(n) n^2 - (\sum_n P_{1e}(n) n)^2 \right) \\ &= m_{in} \left((\mu - 1) - (\mu - 1)^2 \right)\end{aligned}\quad (4.7)$$

If there is a variance σ_{in}^2 in the number of input electrons m_{in} , the total variance in the number of output electrons σ_{out}^2 is just:

$$\sigma_{out}^2 = \langle m_{in} \rangle \left((\mu - 1) - (\mu - 1)^2 \right) + \mu^2 \sigma_{in}^2 \quad (4.8)$$

where $\langle m_{in} \rangle$ is the expectation value of m_{in} .

For gain μ close to unity this approaches the value from Equation 4.5 appropriate for model 1.

Gain variance

If there is a variance σ_μ^2 in the gain μ itself, this will also contribute to the variance in the number of output electrons. If this variance is much smaller than the $(\mu - 1)^2$ (and also smaller than $(2 - \mu)^2$ for model 2) as seems likely for a real electronic device, the contribution this makes to the output variance from an individual gain stage is negligible for both of the models when combined with the statistical noise described above.

4.2.4 Statistical properties of registers with multiple stages

Equations 4.5 and 4.8 can be extended to registers with multiple gain stages as a geometric series. For a register of s gain stages described by model 1, summing the series for Equation 4.5 gives:

$$\sigma_{out}^2 = \mu^{2s} \sigma_{in}^2 + \mu^{s-1} \langle m_{in} \rangle (\mu^s - 1) \quad (4.9)$$

For a register of s gain stages described by model 2, Equation 4.8 gives:

$$\sigma_{out}^2 = \mu^{2s} \sigma_{in}^2 + \mu^{s-1} \langle m_{in} \rangle (\mu^s - 1) (2 - \mu) \quad (4.10)$$

If the inputs are Poisson-noise limited, $\sigma_{in}^2 = \langle m_{in} \rangle$ so for model 1 we have:

$$\begin{aligned}\sigma_{out}^2 &= \mu^{2s} \langle m_{in} \rangle + \mu^{s-1} \langle m_{in} \rangle (\mu^s - 1) \\ &= \mu^{s-1} \langle m_{in} \rangle (\mu^{s+1} + \mu^s - 1)\end{aligned}\quad (4.11)$$

For a register of s gain stages described by model 2, we have:

$$\begin{aligned}\sigma_{out}^2 &= \mu^{2s} \langle m_{in} \rangle + \mu^{s-1} \langle m_{in} \rangle (\mu^s - 1) (2 - \mu) \\ &= \mu^{s-1} \langle m_{in} \rangle (2\mu^s + \mu - 2)\end{aligned}\quad (4.12)$$

If we remember that the gain $\mu = \alpha + 1$ then Equation 4.12 is clearly consistent with Robbins & Hadwen (2003).

If the stage gain $\mu(t)$ varies as a function of time (e.g. due to voltage fluctuations), then the overall gain applied to the signal from one pixel in the imaging array will be the product of the $\mu(t)$ values at each stage while the signal is passed along the serial multiplication register. The large number of gain stages will suppress the effects of high frequency fluctuations in the gain voltage, and only long term drifts in the gain would be expected to affect the output signal.

4.2.5 Signal-to-noise performance

In the absence of the multiplication register, the signal to noise for imaging with the CCD is determined by the photon-shot noise and the readout noise of the analogue CCD amplifier. For an expectation value of $\langle m_{in} \rangle$ detected photons, the RMS photon shot noise is equal to $\sqrt{\langle m_{in} \rangle}$. At fast readout rates, the readout noise r typically has an RMS of a few tens of electrons and is not correlated with the photon shot noise. The RMS noise σ in determining the detected flux in a CCD pixel thus comes to:

$$\sigma = \sqrt{\langle m_{in} \rangle + r^2} \quad (4.13)$$

The signal-to-noise ratio R for conventional imaging is equal to:

$$R = \frac{\langle m_{in} \rangle}{\sqrt{\langle m_{in} \rangle + r^2}} \quad (4.14)$$

At low light levels the detector readout noise dominates Equation 4.13.

If the multiplication register is enabled, then the expectation value for the number of output electrons will be increased by a factor equal to the total multiplication register gain. The variance in the number of output electrons will also be increased, as described by Equations 4.11 and 4.12 for models 1 and 2 respectively. If the output of the multiplication register is treated in an analogue fashion (in the same way as for a conventional CCD), then this variance acts as a source of additional noise.

The signal-to-noise ratio for a register containing s stages each giving a gain of μ is:

$$R = \frac{\mu^s \langle m_{in} \rangle}{\sqrt{\langle m_{in} \rangle \mu^{s-1} (\mu^{s+1} + \mu^s - 1) + r^2}} \quad (4.15)$$

if the gain stages are described by model 1 and

$$R = \frac{\mu^s \langle m_{in} \rangle}{\sqrt{\langle m_{in} \rangle \mu^{s-1} (2\mu^s + \mu - 2) + r^2}} \quad (4.16)$$

if the stages are described by model 2. For both models, if the number of stages s is large and the gain per stage μ is close to unity then the signal-to-noise is well approximated by:

$$R = \frac{g \langle m_{in} \rangle}{\sqrt{2g^2 \langle m_{in} \rangle + r^2}} \quad (4.17)$$

$$= \frac{\langle m_{in} \rangle}{\sqrt{2 \langle m_{in} \rangle + \frac{r^2}{g^2}}} \quad (4.18)$$

where $g = \mu^s$ is the total gain of the multiplication register.

For large multiplication register gains ($g \gg r/\sqrt{\langle m_{in} \rangle}$) the readout noise of the CCD becomes negligible giving:

$$R = \frac{\langle m_{in} \rangle}{\sqrt{2 \langle m_{in} \rangle}} \quad (4.19)$$

$$= \sqrt{\frac{\langle m_{in} \rangle}{2}} \quad (4.20)$$

It is interesting to compare the signal-to-noise in Equation 4.20 with the signal-to-noise R_{ideal} for an ideal readout-noise free detector (limited only by photon shot noise):

$$R_{ideal} = \sqrt{\langle m_{in} \rangle} \quad (4.21)$$

The ratio of the signal-to-noise of a device with a multiplication register to that of an ideal readout-noise free detector is called the noise factor F . For the L3Vision CCDs operated at high gain this noise factor will be $F \simeq \sqrt{2}$.

In an ideal readout-noise free detector a reduction by a factor of $\sqrt{2}$ in signal-to-noise would be brought about if the quantum efficiency of the detector was halved. The noise performance of the L3Vision devices is thus similar to the performance of a readout-noise free device with half the quantum efficiency (see also Mackay *et al.* (2001)).

If the photon flux per pixel read out is very low, electron multiplying CCDs operated at high gain can be used as photon-counting devices (rather like an array of avalanche photodiodes). In this mode of operation, it should be possible to detect individual photons with high quantum efficiency. The performance of the devices for photon counting under these conditions will depend on the probability distribution for the output electrons.

4.2.6 Calculating the probability distribution for the output electrons

So far I have only investigated the variance in the number of output electrons. The precise form of the probability distribution for the number of output electrons is also of interest in describing the performance of these multiplication registers.

For the case of high multiplication-register gain, the large number of electrons involved in the latter stages of the register make Monte Carlo simulations rather cumbersome. Fortunately the probability distribution for the number of output electrons from my two models of the multiplication register can be calculated directly in a rapid and relatively straightforward manner.

We will start by discussing a single gain stage described by one of the models from Chapter 4.2.3. As the models are linear, taking the probability distribution describing the output when only one electron is input to the gain stage, and convolving this distribution with itself results in the probability distribution for the output electrons when two electrons are input. For model 1 we must convolve Equation 4.2 with itself:

$$P_{2e}(n) = P_{1e}(n) \otimes P_{1e}(n) \quad (4.22)$$

where $P_{2e}(n)$ is the probability distribution for the total number of output electrons given two input electrons, $P_{1e}(n)$ is the distribution for one input electron taken from Equation 4.2 and \otimes represents convolution of the probability distributions.

As $P_{1e}(n)$ and $P_{2e}(n)$ are only defined for discrete n , this convolution can be described in terms of the discrete Fourier transform of $P_{1e}(n)$:

$$P_{2e}(n) = \text{DFT} \left[\text{DFT}[P_{1e}(n)]^2 \right] \quad (4.23)$$

where $\text{DFT}[\dots]$ indicates a discrete Fourier transform, and $\text{DFT}[\dots]^2$ indicates that the individual Fourier components are squared. Numerically the discrete Fourier transforms can be performed using a Fast Fourier Transform algorithm. To limit the calculation time the probability distribution must be truncated at large n . As long as the truncation occurs at a sufficiently large value of n (with $n \gg 2\mu + \sqrt{2\mu}$) there is little loss of accuracy.

For m input electrons entering the gain stage the probability distribution for n , the number of output electrons, is given by:

$$P(m, n) = \text{DFT} [\text{DFT}[P_{1e}(n)]^m] \quad (4.24)$$

For a gain stage described in terms of the probability distribution $P_{1e}(n)$ for one input electron, this equation fully describes the operation of the gain stage for any number of input electrons.

The model can be extended by adding another gain stage, situated immediately before

the one we have just described. If one electron enters the new, additional gain stage, the probability distribution for the output electrons from the new stage can be calculated as before. Each possible outcome of this stage is dealt with separately and fed into the model for the next gain stage (based on Equation 4.24). The outcomes are weighted by the appropriate probabilities and summed to give the probability distribution for the total number of output electrons from the combined two-gain-stage system for one input electron.

The probability distribution for one electron entering the two-gain-stage system can be convolved with itself to give the probability distributions for m input electrons, in the same way as for Equations 4.22 to 4.24.

The process can be repeated to convert a two-gain-stage system into a three-gain-stage system, and so on for an arbitrary number of gain stages. To minimise the computation time, it is best to work entirely in the discrete Fourier domain, and only return to the probability domain at the end of the calculations.

A multiplication register where each gain stage was defined by model 2 was also simulated using the same approach. The same convolution procedure can be applied to any linear model of one individual gain stage in order to provide a model for a multi-stage multiplication register.

4.2.7 Results from numerical simulations

A short C program was written by the author to calculate the output electron probability distributions for multiplication registers with stages described by either model 1 or by model 2. The software could simulate a wide range of register gains with a variable number of gain stages. Simulations of multiplication registers which had similar numbers of stages to the registers in existing L3Vision CCDs typically took a few seconds on a year 2000 vintage PC. Two example curves produced by this software were included in Mackay *et al.* (2001).

A small number of Monte Carlo simulations were undertaken to verify the accuracy of the software – to obtain statistically useful results these typically required between one thousand and one million times as much computation time as the convolution software (depending on the simulation parameters). The results were consistent with the probability calculations within the statistical accuracy of the Monte Carlo results.

Results using model 1 for the gain stages

Simulations of the CCD65 L3Vision device with 591 gain stages were first undertaken using model 1 for the individual gain stages (where the additional impact ionisation electrons

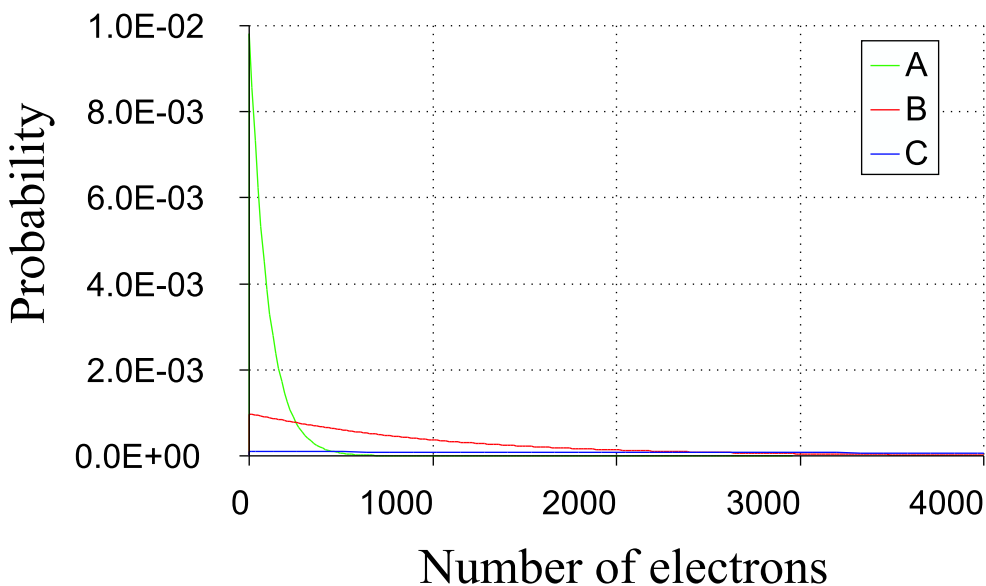


Figure 4.2: The probability distribution for the number of output electrons from a multiplication register of 591 stages with a single electron input and total register gains of 100, 1000 and 10000 (curves **A**, **B** and **C** respectively). All three probability curves fall to zero for the case of less than one output electron. For these simulations model 1 was used for the individual gain stages, where additional electrons are selected from a Poisson distribution. The same data are plotted on a logarithmic scale in Figure 4.3.

were chosen from a Poisson distribution). In the simulations the same value of the gain μ was used for each of the 591 stages. The total gain of the multiplication register was thus given by μ^{591} . The three simulations used three different values of μ chosen to give total multiplication register gains $g = \mu^{591}$ of $g = 100$, $g = 1000$ and $g = 10000$. The probability distributions for the output electrons in these three simulations are shown in Figure 4.2.

The probability distributions for the output electrons are well approximated by decaying exponential curves for large values of n . This is highlighted in Figure 4.3a where the curves are plotted on a logarithmic scale. The probability curves appear as straight lines over a wide range of n in the plot. For very large values of n the probability reaches the computational accuracy of the software corresponding to a value of $\sim 10^{-16}$, and beyond this point the probability calculations are dominated by noise. Figure 4.3b shows an expanded view of the probability distributions for small n . Exponential curves were least-squares fitted to the probability curves for the large n region, and these are extrapolated as dashed curves in this plot. For small values of n ($n \ll \mu$) the probability curve begins to fall very slightly below the best fit exponential before dropping rapidly to zero for $n = 0$.

Figure 4.4 shows similar plots for a 591 stage register with overall gain $g = 1000$ with different numbers of input electrons. The general shape of the curves was not strongly dependent on the number of gain stages s as long as s was large.

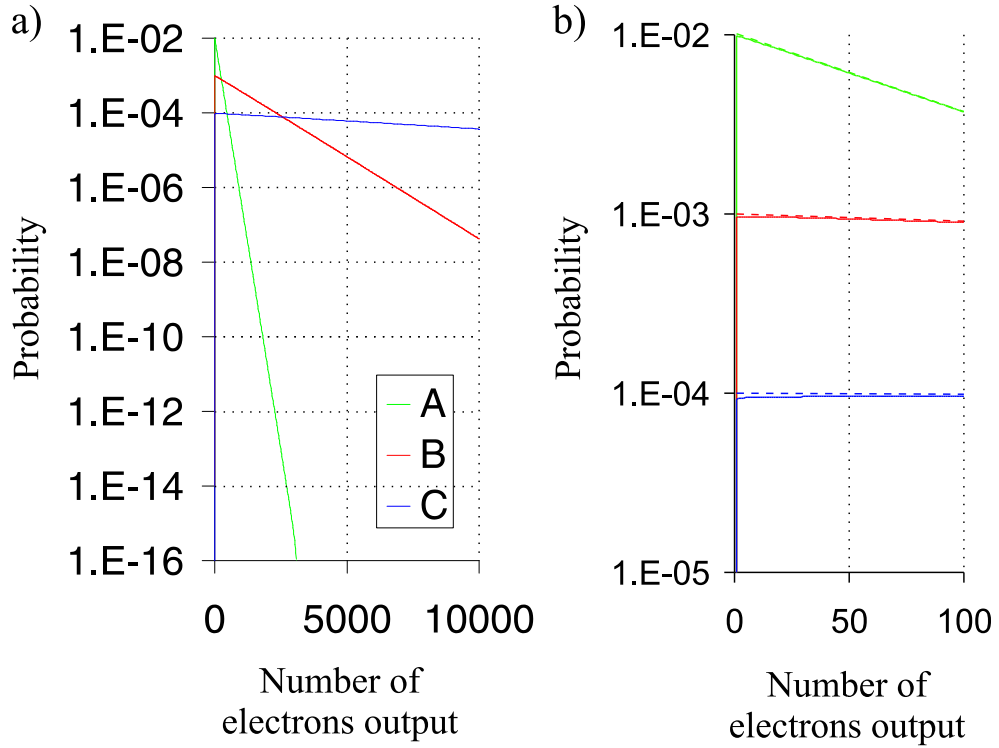


Figure 4.3: The probability distributions from Figure 4.2 plotted on a logarithmic scale. A multiplication register of 591 stages was simulated with a single electron input and total register gains of 100, 1000 and 10000 (curves **A**, **B** and **C** respectively). Model 1 was used for the individual gain stages, where additional electrons are selected from a Poisson distribution. Panel **b**) shows an enlargement of one portion of the plot in panel **a**). The curves in panel **a**) were well fitted with exponential functions for the case of large numbers of output electrons, and these fits have been extrapolated as dashed lines in panel **b**).

Based upon the exponential fits in Figure 4.3, we can say that the probability distributions for the number of output electrons produced when one input electron enters an electron multiplying CCD with a large number of gain stages can be approximated by the function:

$$P(n) \begin{cases} = \left(\exp\left(\frac{1}{g - \frac{1}{2}}\right) - 1 \right) \exp\left(\frac{-n}{g - \frac{1}{2}}\right) & \text{if } n \geq 1 \\ = 0 & \text{otherwise} \end{cases} \quad (4.25)$$

where n is an integer describing the number of output electrons and g is the overall gain of the multiplication register.

If we approximate Equation 4.25 as a continuous function and convolve it with itself we get an approximation for the probability distribution given two input electrons:

$$P(n) \begin{cases} = \left(\exp\left(\frac{1}{g - \frac{1}{2}}\right) - 1 \right)^2 (n - 1) \exp\left(\frac{-n}{g - \frac{1}{2}}\right) & \text{if } n \geq 2 \\ = 0 & \text{otherwise} \end{cases} \quad (4.26)$$

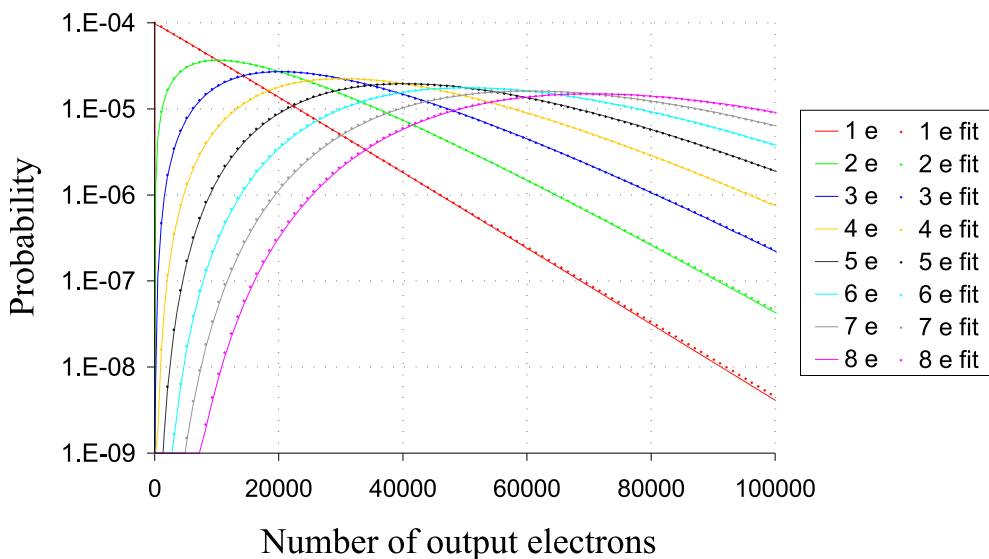


Figure 4.4: The probability distribution for the number of output electrons from a multiplication register of 591 stages with different numbers of input electrons. The discrete points on the graph show selected values from the numerical fit described by Equation 4.27, as discussed in the text.

With further convolutions, and taking approximations for the case of large gain g and a large number m of input electrons, I obtained the following model for the probability distribution for the output electrons:

$$P(n, m) \begin{cases} = \frac{(n - m + 1)^{m-1}}{(m - 1)! (g - 1 + \frac{1}{m})^m} \exp\left(-\frac{n - m + 1}{g - 1 + \frac{1}{m}}\right) & \text{if } n \geq m \\ = 0 & \text{otherwise} \end{cases} \quad (4.27)$$

where n is the number of output electrons. Individual data points calculated using this equation are included in Figure 4.4 alongside the appropriate probability curves calculated numerically for model 1. The approximation described by Equation 4.27 does not differ substantially from the numerically calculated curves even for one or two input electrons (although slightly better approximations for one and two input electrons are given by Equations 4.25 and 4.26 respectively).

Results using model 2

Figure 4.5 shows the probability distribution for the output electrons when the gain stages are described by model 2 (where electrons entering the gain stage can generate at most one electron by impact ionisation in that gain stage). The general shape of the curves is very similar to those produced by model 1 (see Figure 4.3 for comparison). With model 2 the curves fall away to zero slightly more quickly for small values of n . The approximations described by Equations 4.25 to 4.27 are also good descriptions for the output probability

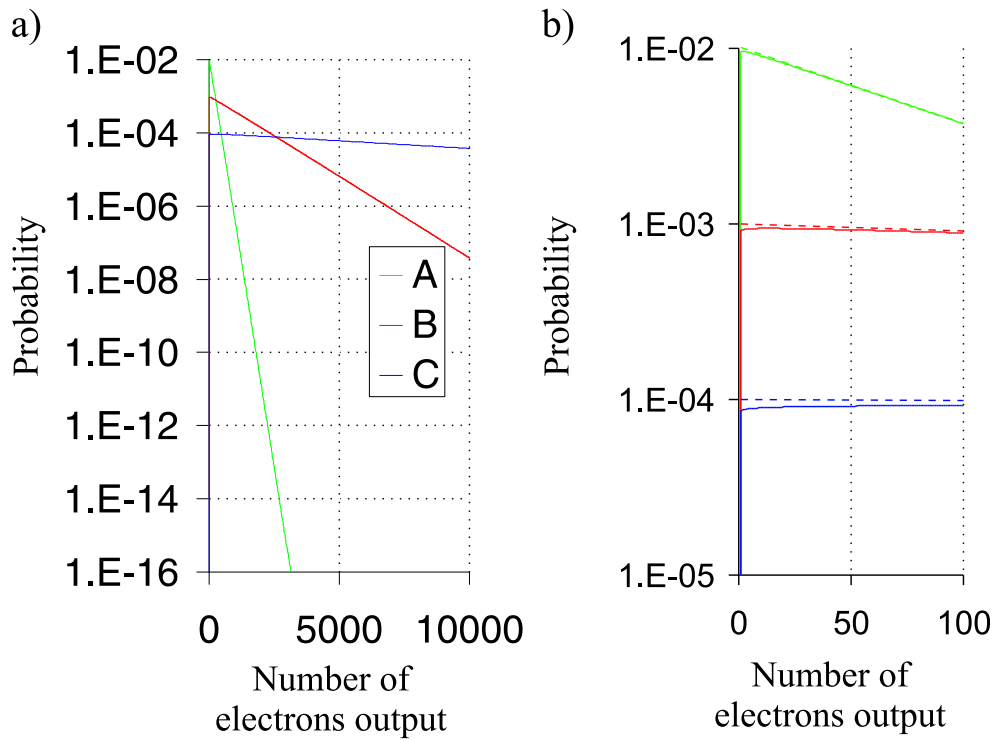


Figure 4.5: The probability distribution for the number of output electrons from a multiplication register of 591 stages using model 2 for the gain stages with a single electron input to the register. With this model each electron input to one gain stage is only allowed to take part in one impact ionisation process within that stage. Curves **A**, **B** and **C** correspond to simulations with total gains of 100, 1000 and 10000. Panel **b)** shows an enlargement of one portion of the plot in panel **a)**. The curves in panel **a)** were well fitted with exponential functions for the case of large numbers of output electrons, and these fits have been extrapolated as dashed lines in panel **b)**.

distributions with this model for the gain stages.

It is perhaps not surprising that the probability distributions for the output electrons with the two different gain stage models considered here are so similar, given that it is the discretisation of the signal into individual electrons which dominates the signal-to-noise performance of the register, and not the internal properties of the individual gain stages. Even if the gain stages of a real multiplication register differ slightly from either of the models described above, it seems likely that Equation 4.25 will provide a good approximation to the distribution of output electrons given one input electron.

Photon counting performance

In order to operate the electron multiplying CCDs as photon counting devices the gain must be sufficiently high that the output signal produced by one photon can usually be distinguished from the readout noise of the CCD. If the readout noise has an RMS σ_{read} ,

and we choose to treat all signals greater than $5\sigma_{read}$ as a detected photo-electron, the fraction f of electrons which are correctly discriminated from the noise will be given by a summation over Equation 4.25:

$$f = \left(\exp\left(\frac{1}{g - \frac{1}{2}}\right) - 1 \right) \sum_{i=5\sigma}^{\infty} \exp\left(\frac{-i}{g - \frac{1}{2}}\right) \quad (4.28)$$

$$= \exp\left(\frac{1 - 5\sigma}{g - \frac{1}{2}}\right) \quad (4.29)$$

where $5\sigma \geq 1e^-$ and $g \gg 1$.

Under suitable operating conditions individual photo-electrons can be detected efficiently above the noise – for example with a readout noise of $\sigma = 50e^-$ and a gain of $g = 5000$ the fraction of photo-electrons detected would be $f = 0.95$. The effective quantum efficiency of the device would be equal to the quantum efficiency for photo-electron generation in the sensor array multiplied by this factor. If the readout noise was Gaussian distributed, the number of photon events attributable to the readout noise would be 3×10^{-7} per pixel read out – lower than the sky background count rate in most astronomical applications.

As with other photon counting systems, the performance of these devices is limited at high light levels by coincidence losses. The electron multiplying CCDs do not suffer from many of the problems which plague conventional photon-counting systems, such as a loss of sensitivity after detection of a photon in the vicinity of the photon event (except within the pixel and frame concerned). Basden *et al.* (2003) have shown that at light levels where photon counting becomes limited by coincidence losses, the signal-to-noise for optical flux measurements can be improved by applying a thresholding scheme to the output of the CCD.

4.3 CCD measurements

A camera was specifically designed by Craig Mackay to house electron-multiplying CCDs. Both CCD65s and CCD87s from the E2V L3Vision family were used in the camera, both in laboratory tests and at the NOT. The CCDs used were front-illuminated, frame-transfer devices. The physical characteristics of these detectors is summarised in Table 4.1. The detector being used was cooled in a liquid nitrogen dewar to $-130\text{ }C$ in order to minimise the dark current. Figure 4.6 shows a CCD65 in the camera dewar. The CCD was read out by an Astrocum 4100 controller modified to provide a variable high voltage clock signal for the multiplication register of the CCD.

Detector	Pixel dimensions	Number of light sensitive pixels	Image area
CCD65	$20 \times 30 \mu\text{m}$	524×288	$10.5 \times 8.6 \text{ mm}$
CCD87	$16 \times 16 \mu\text{m}$	512×512	$8.2 \times 8.2 \text{ mm}$

Table 4.1: The properties of two E2V CCDs which were investigated, the CCD65 and the CCD87. Both of the detectors used were front illuminated, frame transfer devices.

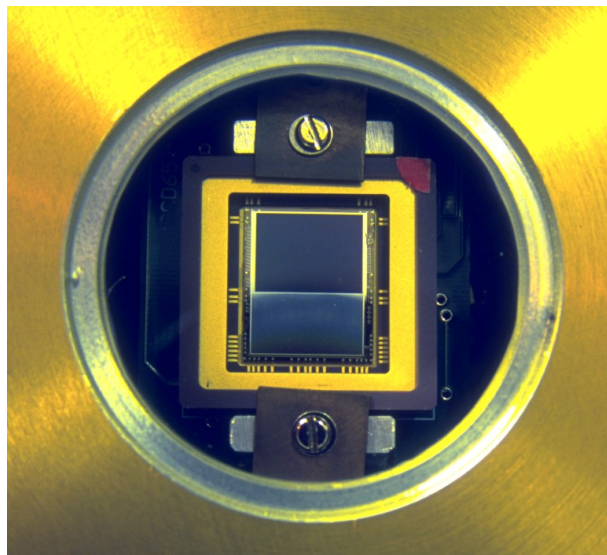


Figure 4.6: The CCD65 detector in the camera dewar. The mask covering the store area of the CCD can be seen on the lower half of the detector. The imaging area is in the upper part of the CCD.

4.3.1 Example data from observations at the NOT

In order to provide an example of the camera performance achieved during observing runs at the NOT, I have included a small amount of data from the observing run in June 2003 in this Chapter.

Figure 4.7 shows a small region of one short exposure taken while the camera was attached to the NOT on 2003 June 29. Long exposure imaging of the field displayed here showed that it did not contain any bright sources, so the detected flux is known to be much less than one photo-electron per pixel in this short exposure.

A small number of pixels in the short exposure show signal levels which are significantly higher than the typical noise in the image. It is likely that a photo-electron (or dark current electron) was generated in most of these pixels. The pixels with high signal levels found in several thousand short exposures such as this were found to be correlated with the locations of faint sources in the field, suggesting that they do indeed correspond to

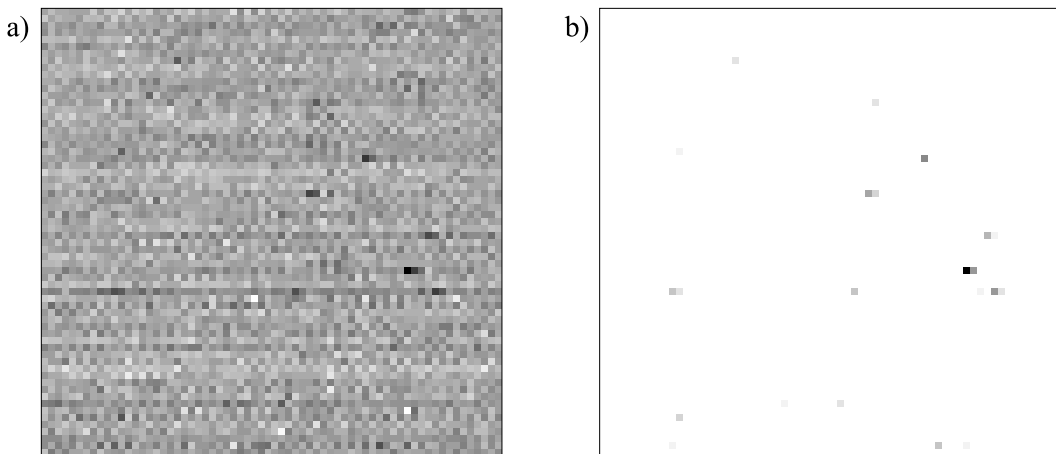


Figure 4.7: **a)** Part of a short exposure image taken at very low light level displayed as a negative image. **b)** The same negative image plotted with a greyscale having twice the contrast. Pixels with low signal levels have saturated to white with this greyscale.

photon events.

Figure 4.8 shows a histogram of the Digital Numbers (DNs) output from the camera in 5000 exposures similar to the one shown in Figure 4.7 (and including the exposure shown). The peak of the histogram can be relatively well fit by a Gaussian distribution, as shown in Figure 4.8a. The centre of this Gaussian distribution corresponds to the mean signal when no photons are detected in a pixel. The width of the Gaussian corresponds to the RMS readout noise. A least-squares fit to the data gave a value of 2799.9 *DN* for the centre of the Gaussian. The fitted Gaussian dropped to $1/e$ of the peak value 5.81 *DN* from the centre, implying an RMS readout noise of 5.81 *DN*. If each *DN* corresponds to *a* electrons leaving the multiplication register, the RMS readout noise *R* will be:

$$R = 5.81a \text{ electrons} \quad (4.30)$$

Figure 4.8b shows the same measurement data plotted on a logarithmic scale. The frequency distribution is well fit by an exponentially decaying function for high *DNs* (more than $5R$ from the centre of the Gaussian) as would be expected given the presence of photo-electrons in some of the pixels. The best fit exponential had a decay constant of -0.156 per *DN*. The gain of the multiplication register can be calculated from Equation 4.25 as:

$$g = \frac{a}{0.156} + \frac{1}{2} \quad (4.31)$$

Applying Equation 4.29 to the parameters given by Equations 4.30 and 4.31 allows us to

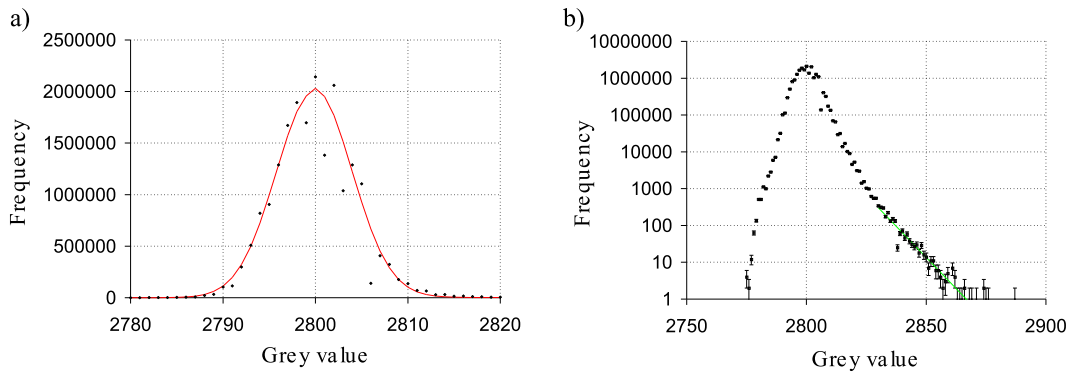


Figure 4.8: **a)** Histogram of the DNs measured by the CCD camera in 5000 exposures similar to that shown in Figure 4.7. A Gaussian has been least-squares fitted to the data. **b)** The same histogram plotted on a logarithmic scale. An exponentially decaying function has been fit to the data for high DNs .

calculate the efficiency f for counting photo-electrons:

$$f = \exp\left(\frac{0.156(1 - 5 \times 5.81a)}{a}\right) \quad (4.32)$$

$$= \exp\left(\frac{0.156}{a} - 4.52\right) \quad (4.33)$$

For $a \gg 0.156$ this gives an efficiency for photo-electron detection of:

$$f \simeq \exp(-4.52) \quad (4.34)$$

$$= 0.011 \quad (4.35)$$

which is far too low to be of practical use. a was expected to be approximately 100 based on the electronic setup of the camera).

The reason for the poor photon counting performance is highlighted if the RMS readout noise is expressed in terms of the mean input signal provided by one photo-electron (i.e. if the RMS readout noise is expressed in units of photo-electrons). This is achieved if Equation 4.30 is divided by Equation 4.31:

$$R = \frac{5.81a}{a/0.156 + 1/2} \text{ photo-electrons} \quad (4.36)$$

As $a \gg 0.156$ we can approximate this as:

$$R = 5.81 \times 0.156 \text{ photo-electrons} \quad (4.37)$$

$$= 0.906 \text{ photo-electrons} \quad (4.38)$$

Although the RMS readout noise is less than the mean signal from a photo-electron, it is too large to accurately distinguish most photon events from the readout noise.

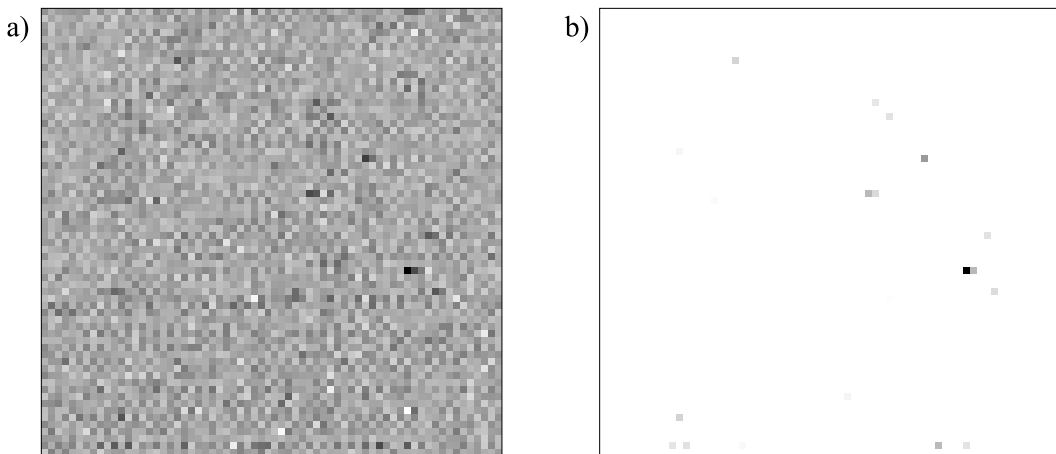


Figure 4.9: **a)** The same short exposure image as Figure 4.7 but with row to row variations suppressed as described in the text. **b)** The same negative image as shown in **a)** but plotted with a greyscale having twice the contrast. Pixels with low signal levels have saturated to white with this greyscale.

It should be noted that a readout noise of 0.9 photo-electrons at 3.5 MHz pixel rates represents a very substantial improvement over the read noise of 50—60 electrons for the camera used in the observations described in Chapter 3. State-of-the-art conventional CCDs can typically only achieve 10—100 electrons read noise at these pixel rates (Jerram *et al.* 2001).

A large part of the RMS noise in the example short exposure shown in Figure 4.7 is in the form of variations from one horizontal row of the image to the next. If these fluctuations are subtracted then the RMS noise is reduced. In order to do this it was necessary to get a measure of the typical *DNs* in each individual row of the image which was not strongly biased by the few pixels containing photo-electrons. A histogram was made of the *DNs* in each row of the image. The lowest 75% of *DNs* from the row were then averaged to provide a value slightly lower than the mean for *DNs* in the row, but not significantly biased by the small number of pixels containing photo-electrons. This mean value was then subtracted from all the pixels in the row. The image which resulted after this procedure was applied to each row in Figure 4.7 is shown in Figures 4.9a and 4.9b.

This process was applied to the full dataset of 5000 frames. The RMS readout noise calculated from the histogram of the *DNs* was reduced to $R = 4.95a$ electrons, where a is the number of electrons per *DN* as before. If the threshold for detection of a photo-electron is set at 5 times this RMS noise level, the efficiency of counting photo-electrons comes to just over 2%. Although this represents a substantial improvement over the case where row to row fluctuations are not subtracted, it will still give poorer signal-to-noise for imaging than would be obtained by treating the measured *DNs* like an analogue signal.

These results appear to be typical of the data I have analysed from the L3Vision camera at the NOT. It is clear that the photon counting approach would not have been successful

with this observational data, so I will treat the *DNs* output from the camera in an analogue fashion like the output from a conventional CCD camera in the remainder of this thesis. On later nights of the observing run in 2003 a higher camera gain setting was used, but there has been insufficient time to analyse that data for inclusion in this thesis.

4.3.2 Charge transfer efficiency problems with the camera

Many of the observations undertaken using L3Vision detectors at the NOT were affected by charge transfer efficiency problems in the detector (Tubbs *et al.* 2002). This problem occurs if photo-electrons in the image and store areas of the CCD do not always move to an adjacent pixel when they are supposed to (i.e. if there is a small probability that any given electron will be left behind in a transfer). Electrons which are left behind in one or more of the transfers on the CCD are registered as if they had come from a different pixel in the imaging array, causing images taken with the CCD to be shifted in position and image scale, and to appear blurred.

The problems with charge transfer efficiency were found to vary strongly with the voltage settings in the camera and other environmental effects. I will briefly discuss the effect of poor charge transfer efficiency on laboratory measurements before analysing any of the data taken at the telescope. The charge transfer efficiency was found to be substantially better in recent experiments using the CCD87 than had been found with the CCD65, but there has not been time to include a quantitative assessment of these results here.

Measurements of charge transfer efficiency at low signal levels

Measurements made with the camera at the NOT indicated that the charge transfer efficiency problems were limited to extremely low signal levels (less than one detected photon per pixel per frame). This strong non-linearity in the camera performance with the light level would make deconvolution of the affected images very difficult. A set of laboratory measurements was undertaken by Craig Mackay to investigate the charge transfer efficiency of the camera in detail at these low light levels in order to assist in the interpretation of our astronomical images.

Short exposure images were taken of a camera “test card” transparency using standard slide-copying optics, with a CCD65 detector in the camera. The voltage settings on the camera were such that the charge transfer efficiency deviated significantly from unity at low signal levels. At high signal levels the images of the test card showed a high degree of fine structure, ideal for charge transfer efficiency measurements.

Datasets of 1000 images each were taken operating the CCD65 at high multiplication register gain with exposure times of 60 ms and 1 s. In the test card images these light levels corresponded to 0.05—0.5 photons per pixel per frame and 0.9—9.0 photons per pixel per

frame respectively. Ten exposures of 60 s were also taken with no multiplication register gain to provide an accurate representation of the test card at high signal level. There was no evidence for charge transfer efficiency problems in these long exposure images.

The raw images did not show any visual evidence for poor charge transfer efficiency, but the signal level was too low in the individual 60 ms exposures to make an accurate assessment. Software was written by the author to combine the short exposures and deconvolve the resulting images in order to make a quantitative assessment of the charge transfer efficiency.

The 60 ms exposures were co-added to increase the signal-to-noise, as were the 1 s and 60 s exposures. The summed images from the 60 ms and 1 s exposures were then deconvolved using the summed image from the long exposures in order to give a “PSF” which described the charge transfer efficiency problems at low light levels. The fraction of the signal residing a given number of pixels from the origin of this PSF corresponds to the fraction of electrons which have been displaced by this distance due to charge transfer efficiency problems. In order to control the noise in the deconvolution process, a 2-D version of the Nahman-Guillaume one parameter filter was used (Nahman & Guillaume 1981). The filter parameter was adjusted until there was good dynamic range between the central peak of the PSF and the noise floor in the wings. In order to confirm that the filter was not adversely affecting the shape of the PSF, different long exposure images were deconvolved in the same way, providing a strongly peaked response at the origin which dropped to the noise floor within two pixels of the origin.

Figure 4.10 shows the result of deconvolving a section of the summed image from the 1 s exposures. The PSF shows a strong peak at the origin corresponding to those electrons which were transferred with good charge transfer efficiency. Weak tails extend both to the right and upwards, indicating that some of the photo-electrons are experiencing much poorer charge transfer efficiency for either horizontal or vertical transfers. With the shorter exposures (having fewer photons per pixel), the strong peak at the origin disappears, and the tails to the right and in the upwards direction are broadened and strongly enhanced to form a single peak offset from the origin, as shown by Figure 4.11.

A PSF was calculated in this way for different regions of the test card image using the 60 ms exposures. The horizontal offset and vertical offset of the peak in the PSF was found to depend linearly on the horizontal position and vertical position respectively in the image. This is consistent with charge transfer efficiency problems in the image and store areas of the CCD, as electrons which are generated further from the readout register must undergo a larger number of transfers.

Figure 4.12 shows a plot of the horizontal offset in the PSF peak against the horizontal (“ x ”) position of the region used for the calculations. The data points are fit by a line which crosses the x -axis at an x value of -201 . This implies that a significant fraction of the charge transfer efficiency loss is occurring after the signal has left the image and store areas of the CCD, and is presumably occurring in the multiplication register. The bulk

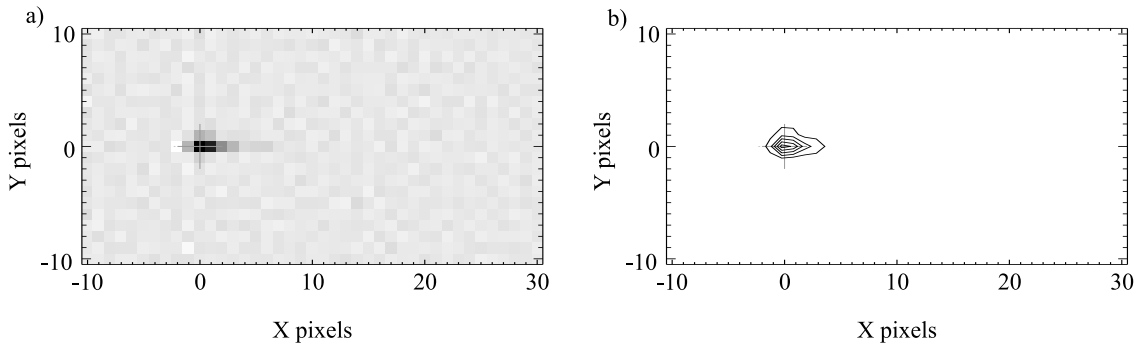


Figure 4.10: A PSF describing the charge transfer efficiency for 1 s exposures at low light level – see main text for details. A section near centre of test card image was used for this measurement.

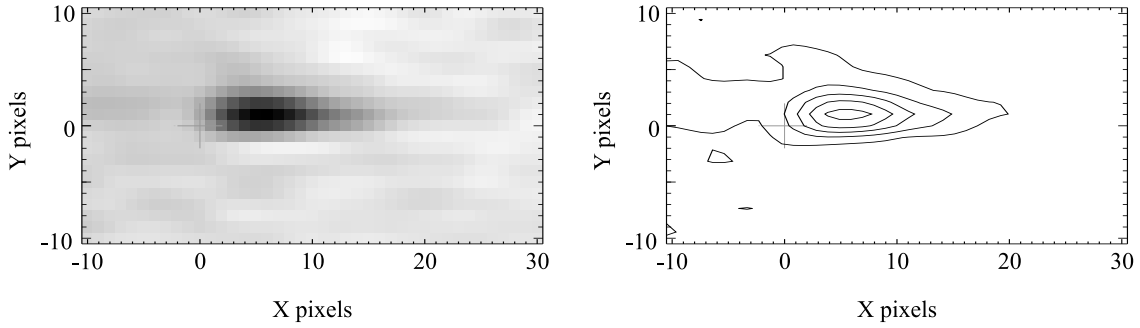


Figure 4.11: A PSF describing the charge transfer efficiency for 60 ms exposures at low light level. The same section of the test card was used as for Figure 4.10.

of the charge transfer efficiency losses do seem to occur in horizontal (serial) transfers in the store area of the CCD, however. The gradient of the line in Figure 4.12 indicates that electrons are being “left behind” in 1.4% of the serial transfers in the store area of the CCD for these measurements.

A cross section through the PSF calculated for a region centred on $x = 128$ pixels is shown in Figure 4.13. The curve is similar in shape to the binomial distribution which would be expected if it was the result of 329 transfers attempts, each having a 1.4% chance of failing to transfer the electron.

The charge transfer efficiency was found to be strongly dependent on the (variable) operating voltages and environmental conditions of the camera. It was possible to get very good charge transfer efficiency in the laboratory with the CCD87 by selecting appropriate operating conditions. The operating voltages used during observations at the NOT are not precisely known, and for this reason it will not be possible to predict the charge transfer efficiency which was present for observations at the NOT.

The experimental measurements and calculations of charge transfer efficiency at low signal

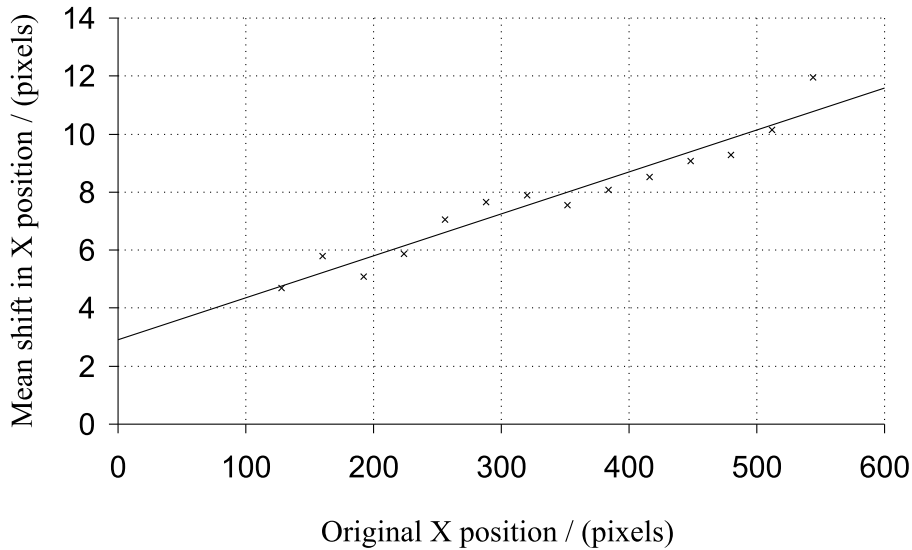


Figure 4.12: Charge transfer efficiency for 60 ms exposures at low light level. The offset in the position of the image plotted on the vertical axis indicates the number of failed charge transfers. The position of the test card region used is proportional to the total number of serial transfers in the store area of the CCD required to transfer the photo-electrons to the multiplication register. The horizontal offset of the line would correspond to 201 additional pixel transfers.

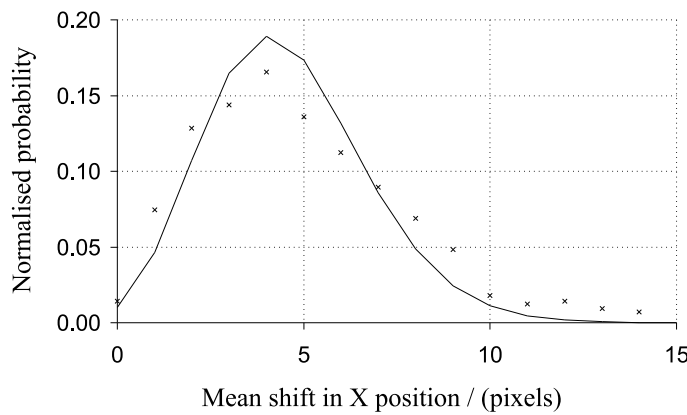


Figure 4.13: Charge transfer efficiency for 60 ms exposures at low light level. A square region of the test card image was selected for this analysis. The region was centred 128 pixels from the edge of the CCD in the horizontal (serial transfer) direction. The data shown in Figure 4.12 indicate that the offset in position for this region of the test card image was consistent with a 1.4% CTE loss in 329 transfers. The binomial distribution obtained for 329 transfers with probability of 1.4% for missing a transfer is shown.

level are currently relatively time consuming, and require an image with suitably fine structure to be projected on to the CCD in a stable experimental setup. It would be extremely beneficial if an automated approach to this analysis could be developed which could be performed when the camera was at an astronomical telescope, so that the charge transfer efficiency could be maximised before astronomical observations began.

4.4 Conclusions

The electron multiplying CCDs developed by E2V Technologies represent a major advance in high frame-rate, low light-level imaging (also presumably those developed by Texas Instruments, although at present there is less practical experience with these devices in the Institute of Astronomy). Numerical simulations indicate that these devices could be operated as a two-dimensional array of photon counting detectors with high quantum efficiencies. At high light levels where coincidence losses become significant, the output can be treated in an analogue fashion just like a conventional CCD. This flexibility gives the devices enormous dynamic range, ideal for the Lucky Exposures method. Bright reference stars could be recorded without the limitation of coincidence losses, while in another part of the field individual photons from a faint object could be counted individually with high Quantum efficiency.

Observational data taken using electron-multiplying CCDs in a custom-built camera was found to be generally consistent with a simple theoretical model for the electron-multiplying CCD architecture. There was evidence for poor charge transfer efficiency at low signal level under some operating conditions and this may impact some of the astronomical observations. The statistical properties of some sample data taken from an observing run suggest that the best approach to analysing the data presented in the following chapter is to treat the output of the CCD like an analogue signal.

Chapter 5

Observations with a low noise CCD at the NOT

5.1 Introduction

The observations described in Chapter 3 were of relatively bright stars using a conventional high frame-rate CCD camera. The readout noise present at these high frame rates would have led to poor signal-to-noise ratios for observations of faint sources using this camera.

In Chapter 4, I introduced the characteristics of the new L3Vision CCDs developed by E2V Technologies. The high signal-to-noise performance of these devices at high frame rates and low signal levels should make them ideally suited to the Lucky Exposures method. In this chapter I introduce some preliminary results from observations using L3Vision CCDs at the NOT. Many of these results were also published in Tubbs *et al.* (2002). These observations indicate that the method has enormous potential for a wide variety of future astronomical programs using low noise cameras. I develop an approach for obtaining high quality Lucky Exposures images from data with low signal-to-noise. The techniques introduced here will be of use in future astronomical programs utilising the Lucky Exposures method.

Observations were carried out using an L3Vision CCD in July 2001, July 2002 and June-July 2003 at the NOT. The limiting magnitude of reference star and isoplanatic angle are investigated in this chapter, and from these the sky coverage of the technique is calculated. A number of high resolution images of globular cluster cores and close binaries are presented, providing a taster of potential future astronomical results. This chapter includes a brief discussion of the astrometric and photometric precision which can be obtained from Lucky Exposures images.

5.2 Aims

The principle aim of these additional observing runs was to establish the applicability of the Lucky Exposures method to general astronomical programs when using low-noise imaging detectors.

As discussed in Chapter 1.3, the range of faint astronomical targets to which the technique can be applied depends on the likelihood of finding a suitably bright reference star sufficiently close to the astronomical target, and on the limiting magnitude for the target which can be reached in a reasonable amount of observing time.

The likelihood of finding a suitable reference star depends on three principle factors:

1. the isoplanatic angle (the maximum separation angle on the sky between the reference star and a source of interest for which high image quality can be obtained);
2. the limiting magnitude of reference star which can give useful measurements of the Strehl ratio and position of the brightest speckle; and
3. the density of stars on the sky which are sufficiently bright to act as reference stars.

The observational data presented in this chapter address points 1 and 2 directly; galactic star counts from the literature are used to address point 3.

A further issue which can be explored is the astrometric potential of the method. The image quality which can be obtained in the vicinity of a reference star using the Lucky Exposures method was discussed in detail in Chapter 3.5.1. The compact stellar cores in images produced by the Lucky Exposures method should allow accurate stellar positions to be determined. The performance will be very competitive, particularly in crowded fields where other speckle imaging techniques give relatively poor performance. The high Strehl ratios for the selected exposures give high dynamic range as starlight from bright objects contributes less flux to surrounding parts of the field of view, allowing accurate astrometry on nearby faint objects. In this chapter I will undertake a simple experiment intended to assess the suitability of Lucky Exposures imaging for astrometry.

In order to obtain images with the highest possible Strehl ratios and signal-to-noise ratios, I will investigate Fourier filters which are designed to suppress the noise in the short exposure images. The performance of these filters will then be assessed using observational data.

5.3 Observations

John Baldwin, Graham Cox, Craig Mackay and the author undertook three observing runs together using L3Vision CCDs at the NOT (in the summers of 2001, 2002 and 2003). A

Start date	CCD	No. of pixels	f/ratio used	Pixel scale mas	No. useful nights
2001/07/05	CCD65	624×288	60	27×40	1.5
2002/07/25	CCD65	624×288	64	25×37	1.0
2003/06/27	CCD87	512×512	32	40×40	7.0

Table 5.1: Log of observing runs at the NOT involving L3Vision CCDs. For many of the individual observations only a small region of the CCD was read out.

CCD65 detector (with 624×528 pixels, each $20 \times 30 \mu\text{m}$) was used for the first two runs, and a CCD87 (with 512×512 pixels, each $16 \times 16 \mu\text{m}$) was used for the 2003 run. Both devices were front-illuminated frame-transfer CCDs. A brief log of these three observing runs is shown in Table 5.1. For each run a single lens achromat was used to convert the f/11 beam at the Cassegrain focus to a suitable image scale for the CCD detector. A diverging lens achromat was used before the focus for the first two runs, while a converging lens was used after the focus for the third run, providing a re-imaged aperture plane within the instrument. Circular aperture stops could be placed in this re-imaged aperture plane if required.

For each of the runs the camera was shipped from Cambridge along with a supporting frame for fitting at the Cassegrain focus of the NOT. The optics and mechanics of the instrument were designed by John Baldwin, Craig Mackay and Donald Wilson. The frame used for the run in 2003 can be seen during assembly in Figure 5.1. The metal plate being attached on the left-hand side of the instrument is the mechanical interface to the telescope, while the camera dewar can be seen on the right-hand side of the frame.

In order to measure the isoplanatic angle it was necessary to undertake simultaneous imaging observations of widely separated stars. The limited dimensions of the L3Vision CCDs did not give a sufficiently wide field of view for this, given the requirements on pixel sampling with the Lucky Exposures technique, so a special optical arrangement was designed by John Baldwin to superimpose two fields of view on the detector. This allowed stars separated by up to 30 arcseconds to be observed simultaneously. A sketch of the optical layout used for observations in July 2001 and July 2002 is shown in Figure 5.2. The light path to the detector was folded into a “Z” shape. The second fold mirror actually consisted of two flat mirrors butted together at a slight angle, allowing two patches of sky (typically $\sim 20 \text{ arcseconds}$ apart) to be superimposed on the detector. In the figure, rays from two points on the sky which are superimposed on the detector are shown in red and blue. The second light path to the detector was blocked for observations of crowded fields to prevent confusion and to reduce the sky background contribution.

For the observing run in June/July 2003, a converging lens achromat was used after the Cassegrain focus as shown in Figure 5.3, providing a re-imaged aperture plane. The light path after this lens was folded in a similar way to the observations in 2001 and 2002, and also allowed two fields on the sky to be superimposed.

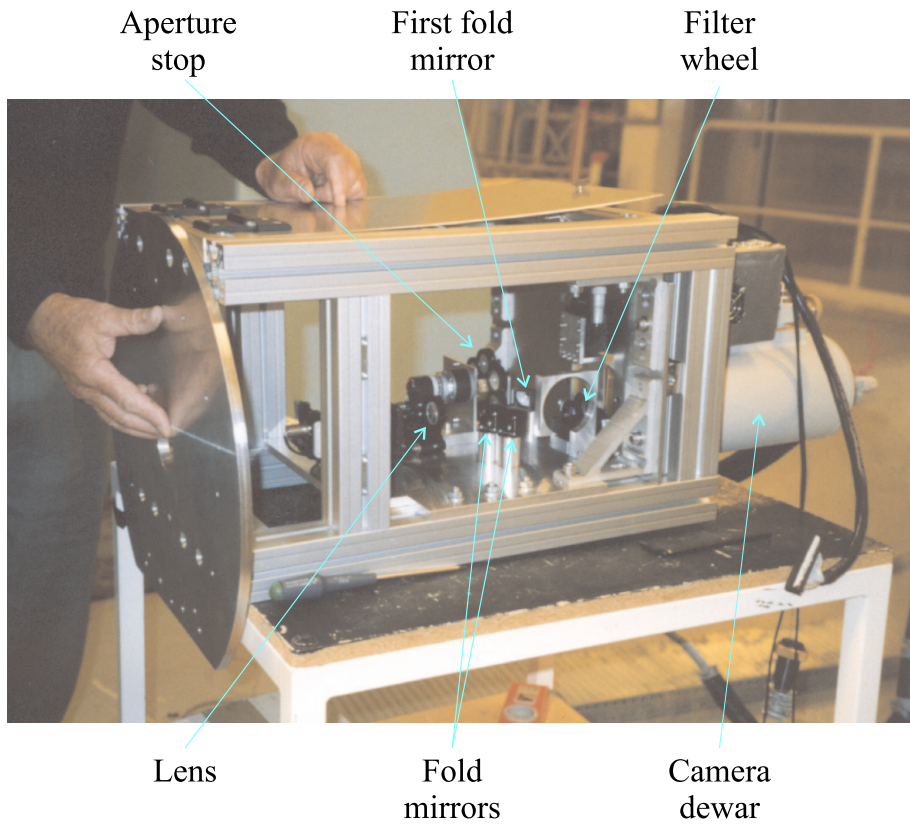


Figure 5.1: Assembling the “Luckycam” instrument at the NOT in 2003. During observations, starlight enters through the central hole in the circular plate being attached to the left-hand side.

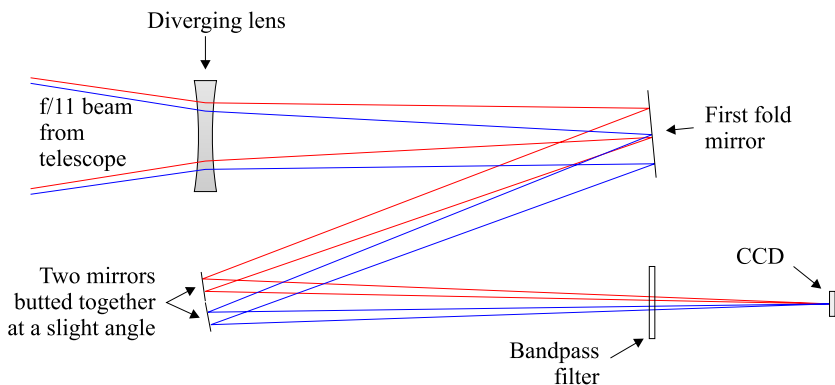


Figure 5.2: Schematic diagram indicating the general layout of the optics for the observing runs in July 2001 and July 2002. A diverging lens achromat was positioned before the Cassegrain image plane of the NOT increasing the $f/$ ratio of the beam. The light path was then folded into a “Z” shape. The first fold mirror was flat, while the second fold mirror consisted of two flat mirrors butted together at a slight angle so as to superimpose the images of two nearby patches of sky on the detector. In the figure, rays from two different points on the sky are indicated in red and blue. Bandpass filters were positioned just in front of the CCD. The diagram is not to scale.

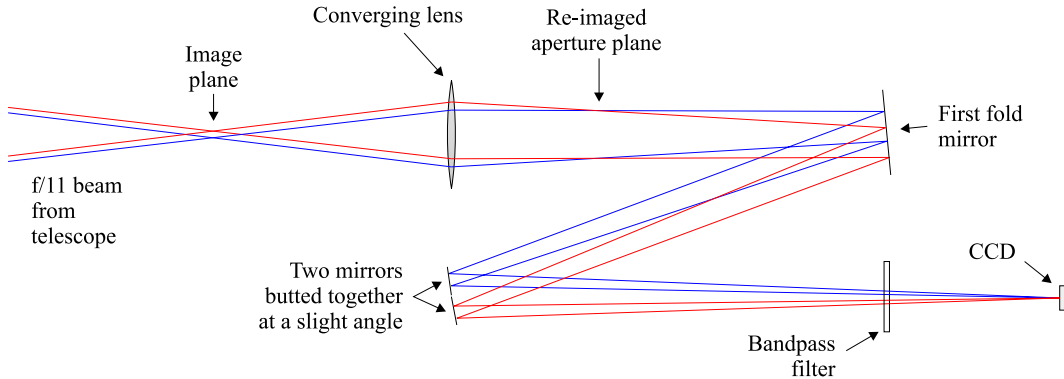


Figure 5.3: Schematic diagram indicating the general layout of the optics for the observing run in June/July 2003. After passing through the Cassegrain image plane of the NOT, the light was re-focussed by a converging lens achromat. A variable aperture stop followed in the re-imaged telescope aperture plane labelled in the figure. As in Figure 5.2 the light path was then folded into a “Z” shape. The first fold mirror was flat, while the second fold mirror consisted of two flat mirrors butted together at a slight angle so as to superimpose the images of two nearby patches of sky on the detector. In the figure, rays from two different points on the sky are indicated in red and blue. Bandpass filters were positioned just in front of the CCD. The diagram is not to scale.

The instrument design in 2003 allowed the telescope aperture to be stopped down in the re-imaged aperture plane using a remotely controlled mechanical system. Filter changes were performed manually during the night using a rotating filter wheel. Figure 5.4 shows the fully assembled “LuckyCam” instrument mounted at the Cassegrain focus of the NOT.

The camera used was one designed by Craig Mackay to run L3Vision detectors. The CCD was held in a liquid nitrogen dewar which was cooled to between 120 K and 140 K to minimise the dark current. An Astrocam 4100 controller was used to read out the CCD, with additional electronics providing the high voltage clock signal for the multiplication register. The CCDs were read out at frame rates between 10 Hz and 150 Hz, using sub-array readout where necessary to reduce the readout time.

5.3.1 Filters and bandpasses

In this chapter I will analyse observational data taken through two different filters, the I-band filter from the HiRac instrument at the NOT, and a 780 nm long pass filter (called *HiRac I* and 780 nm edge respectively). The bandpass of the HiRac I filter is approximately top-hat shaped with a centre wavelength of 810 nm and a width of 125 nm. The long wavelength limit was set by the sensitivity curve of the front-illuminated CCD for observations using the 780 edge filter. Figure 5.5 shows simple models for the responses of the filters (based on the data available from the manufacturers). Also shown are estimates

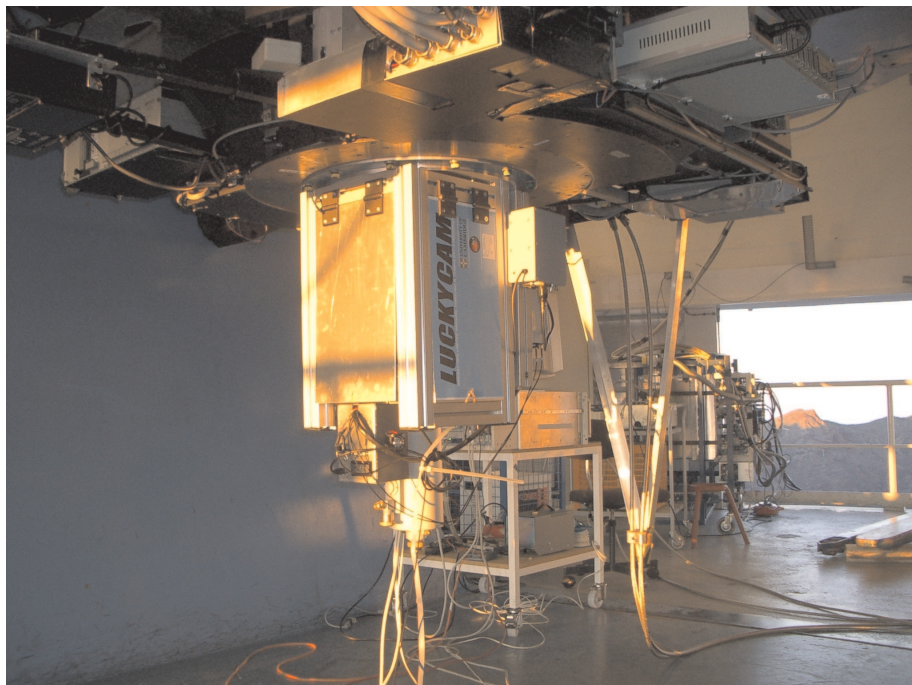


Figure 5.4: The camera and optics assembly attached to the Cassegrain focus of the NOT – Photograph by Craig Mackay

of the combined photon-detection efficiency of the telescope, filter and instrument based on estimates of the quantum efficiency of the front-illuminated CCD, the reflection coefficients for the dewar window and lens, and the reflectivity of the telescope and instrument mirrors.

5.3.2 Observations in July 2001

Observations were undertaken at the NOT on the nights of 2001 July 25–26 using a CCD65 detector. On the first night of observing the camera showed very poor charge transfer efficiency. On the second night the CCD was heated electrically inside the liquid nitrogen dewar and the charge transfer efficiency appeared to improve. The results presented in this thesis are restricted to data taken on the second night of observing. Table 5.2 lists the targets observed on the second night. Some runs where the target saturated the detector or drifted out of the field have been excluded. All the runs on this night were taken through the HiRac I-band filter with the bandpass shown in Figure 5.5. Some of the short exposure images were affected by one or more white spots which may have resulted from trace amounts of radioactive material in the instrument hardware.

For all the observations except those of 61 Cygnii, the multiplication register was clocked with a high voltage providing a substantial gain in the signal level.

In order to investigate the size of the isoplanatic patch which prevails at the times of the

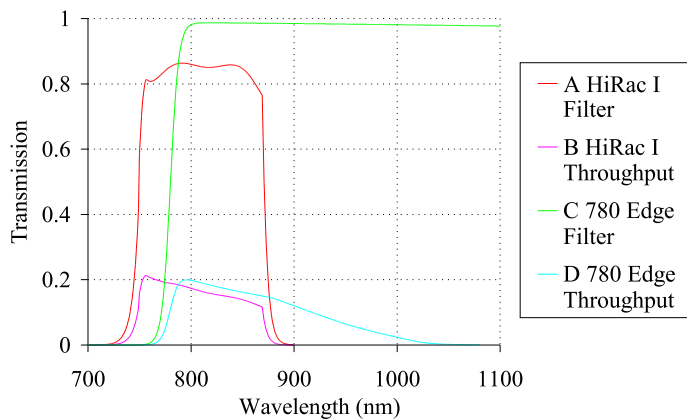


Figure 5.5: Bandpasses for two filters used at the NOT. All the observational results presented in this chapter were taken through one of these two filters. Curve **A** shows the approximate response for the HiRac I filter, and curve **C** shows the estimated bandpass for the 780 nm edge filter. These curves are based on data provided by the manufacturers. Also shown are the combined responses of these filters with the estimated quantum efficiency of the front-illuminated CCD, the estimated mirror reflectivities and estimates for reflection coefficients of the dewar window and lens. These are labelled **B** and **D** for the HiRac I and 780 nm edge filters respectively.

Target	Object type	Number of exposures	Image size (pixels)
CCDM J17339+1747	Binary star	14000	256 × 256 and 160 × 160
HD161796	Planetary nebula progenitor	18000	160 × 160
NGC 6543	Planetary nebula progenitor	2000	512 × 64
^a M13 field 1	Globular cluster	3000	624 × 288
^a M13 field 2	Globular cluster	6000	624 × 288
M56	Globular cluster	3000	624 × 288
M15 field 1	Globular cluster	2000	624 × 288
M15 field 2	Globular cluster	4000	624 × 288
HD 203991	Binary star	12000	128 × 128
61 Cygni	Binary star	15000	624 × 128 and 624 × 64
8 Lacertae	Binary star	12000	128 × 128

^a CCD electrical heating disconnected.

Table 5.2: Observations on 2001 July 6. Some runs where the detector was saturated or the target drifted out of the field have been excluded. For some of the targets several runs were taken with different image sizes. All the observations were taken using the HiRac I filter centred at 810 nm. The bandpass of this filter is plotted in Figure 5.5.

Target	Object type	Number of exposures	Image size (pixels)
Gliese 569	Multiple brown dwarf	21000	288 × 288
NGC7008	Planetary nebula progenitor	8000	288 × 288
WR 140	Wolf Rayet binary system	8000	288 × 288

Table 5.3: Observations on 2002 July 25 through the HiRac I filter at the NOT.

best exposures, observations of binary stars with a range of separations were undertaken. As the dimensions of the CCD65 detector corresponded to 14×11 *as* on the sky, two of these binaries did not fit within the CCD field of view. In order to observe these targets, an optical arrangement was employed whereby two fields on the sky were superimposed on the detector (as discussed in Figure 5.1). The centres of the two fields which could be superimposed were separated by approximately 21 *as*, allowing the 22 *as* binary 8 Lacertae to be observed in a 128×128 pixel sub-array of the CCD. A long 624 pixel strip across the CCD was used for observations of the 30 *as* binary 61 Cygni. All the observations were taken within two hours of each other and at relatively small zenith angles, so as to minimise the changes in seeing from one observation to the next.

A number of relatively crowded fields in globular clusters were observed in order to determine the limiting magnitude of reference star for exposure selection and image re-centring. Different stars in the field of view were picked as the reference, in order to find the faintest star for which high resolution images could be obtained. The fields chosen had previously been surveyed by the Hubble Space Telescope, and stellar magnitudes were available for some of the stars. These fields were also useful for testing the astrometric performance, as the relative positions of a large number of stars could be compared between different runs.

5.3.3 Observations in July 2002

On the nights of 2002 July 25–27 little data was obtained largely due to the poor atmospheric conditions on La Palma. High winds and dust forced us to close the dome shortly after twilight on the first night. Severe dust extinction and a gradual decline in the seeing hindered observations on the second and third nights. Table 5.3 lists the targets observed through very severe dust extinction on the first night before we were forced to close the dome.

There was less dust extinction on the second night, but the seeing gradually deteriorated from 0.5 *as* to 1.2 *as*. The charge transfer efficiency of the camera appeared to be poorer for some of the runs on this night. The targets observed are listed in Table 5.4. The optical filters used on the second night provided a range of different bandpasses between 600 nm and 1 μm . Table 5.5 lists the general properties of the filters used. The bandpasses of two

Target	Object type	Filter	Number of exposures	Image size (pixels)
CVS 97A	Gravitational lens	HiRac I	20000	624 × 288
M13	Globular cluster core	HiRac I	10000	624 × 288
M15	Globular cluster core	HiRac I	12000	624 × 288
M15	Globular cluster core*	HiRac I	4000	624 × 288
M15	Globular cluster core*	Coherent R	4000	624 × 288
M15	Globular cluster core	Coherent R	4000	624 × 288
M15	Globular cluster mosaic	HiRac I	12000	624 × 288
NGC7469	Active Galactic Nucleus	HiRac I	4000	624 × 288
NGC7469	Active Galactic Nucleus	780 nm edge	10000	624 × 288
M32	Galactic Nucleus	780 nm edge	4000	624 × 288
ADS 15828	Binary	HiRac I	7000	624 × 122
ADS 191	Binary	HiRac I	4000	624 × 122
8 Lacertae	Binary	HiRac I	4000	624 × 288

Table 5.4: Principle observations on 2002 July 26. Runs where the detector was saturated or the target drifted out of the field have been excluded. The seeing conditions gradually deteriorated, reaching 1—1.2 as for the last few runs.

Filter name	Centroid of observing band	Filter description
Coherent R	650 nm	Top hat filter with 72 nm FWHM
HiRac I	810 nm	Top hat filter with 125 nm FWHM
780 edge	~ 860 nm	Long-pass filter (long wavelength cutoff set by limit of the CCD detector)

Table 5.5: Filters used for the observations in 2001 and 2002.

of the filters used are also shown in Figure 5.5.

On the third night (2002 July 27) the seeing typically ranged from 1.5 as to 2.3 as , and little useful data was obtained.

5.3.4 Observations in June-July 2003

Better conditions prevailed on the nights of 2003 June 27 to July 4, with the seeing better than 1 as most of the time and occasionally as good as 0.4 as . Observational results from data taken of M13 on 2003 June 29 will be presented in this chapter. The 780 nm edge filter was used for this run of 8000 frames, each of 552 × 104 pixels. A substantial amount of other data from a wide range of targets exists from the observations in June-July 2003, and for reference these are listed in Appendix B.

The square pixels of the CCD87 array used in 2003 allowed larger areas of the sky to be observed without compromising the frame rate or pixel sampling used for the observations. The observations presented here from 2003 were taken through a 780 nm long-pass filter, with the long wavelength cut-off for the bandpass determined by the sensitivity curve for the CCD87 detector (see Figure 5.5).

5.4 Data reduction

Data from the L3Vision CCDs were analysed using a similar approach to that described in Chapter 3. However, a stronger emphasis was put on minimising sources of noise in order to extend the Lucky Exposures method to the faintest possible targets.

The observations in 2001 and 2002 were taken using a CCD65 detector with $20 \times 30\text{ }\mu\text{m}$ pixels. In order to obtain output images with square pixels and the correct aspect ratio, the sinc-resampling process applied to the short exposures was modified (panels **c**) and **f**) of Figure 3.13). In the modified scheme the images were resampled to have 4 times as many pixels in the horizontal direction and 6 times as many pixels in the vertical direction. The observations in 2003 were performed using a CCD87 detector with square pixels, so the images were resampled to have 4 times as many pixels in both directions.

For many of the observations (particularly those near the centres of globular star clusters) it was necessary to select one star from a crowded field to act as a reference. In order to select light from the reference in each case, a rectangular region around the star was selected in the long-exposure average image (the image formed by summing all of the individual exposures without re-centring). This region was always chosen to include most of the flux from the reference star, but to exclude light from other nearby stars. The same region of each of the individual short exposures was then used in the calculation of the Strehl ratios and positions of the brightest speckles (as indicated in panels **b**)—**d**) of the flow chart in Figure 3.13).

Nieto & Thouvenot (1991) discuss the artificial sharpening (or “over-resolution”) of the reference star image brought about by exposure selection and image re-centring at low signal-to-noise ratios. This results from coherent addition of noise in the re-centred exposures. An extreme example of this would be provided by a truly photon-counting detector used to image a field where there is never more than one photon per short exposure in the whole field of view. The exposures with a single photon in would be re-centred based upon the location of the photon, providing a δ -function at the re-centring position regardless of the real sky brightness distribution.

For the data presented here, where many photons are received from the reference star in each exposure and the signal-to-noise ratio is determined by readout noise, the image quality obtained for other stars in the field in the final Lucky Exposures image can provide

Application	Description	Filter used
1	The measurement of the Strehl ratio and position of the brightest speckle in each of the short exposures	Diffraction-limited modulation transfer function
2	For the production of a high signal-to-noise image from the re-centred selected exposures	Modified Hanning window

Table 5.6: The two applications of Fourier filtering in the revised data-reduction scheme.

a reliable measure of the imaging PSF, as long as the readout noise is not distributed in a pattern which is coherent across the imaging area of the detector.

5.4.1 Fourier filtering

For all three observing runs at the NOT the pixel sampling used was sufficient to record Fourier spatial frequencies higher than the telescope diffraction limit of $\frac{d}{\lambda}$ in certain orientations with respect to the pixel array. As the photon shot noise and multiplication register noise are stochastic they contribute equally at all spatial frequencies. The spatial frequencies beyond the diffraction limit of the telescope will contain no signal from the astronomical source but as much photon shot noise and multiplication register noise as are found in lower spatial frequencies. By suppressing spatial frequencies beyond $\frac{d}{\lambda}$ in the data it is thus possible to obtain an improvement in the overall signal-to-noise ratio of the images. This will lead directly to an improvement in the limiting magnitude of reference star which can be used, and in the limiting magnitude of faint source which can be detected in the field.

The readout noise from the analogue camera electronics is distributed at a range of spatial frequencies within the images. A significant fraction of this noise appears at spatial frequencies beyond the telescope diffraction limit, and this component of the readout noise is also reduced if high spatial frequencies are suppressed.

There are two clear applications for Fourier filtering in my approach to the data reduction, as listed in Table 5.6.

In the first application we want to find bright speckles in the noisy short exposure images. A very effective approach is to search for the peak cross-correlation between the short exposure image and a diffraction-limited telescope PSF. This cross-correlation process is equivalent to multiplying the images by the modulation transfer function of the diffraction-limited telescope in the Fourier domain (effectively convolving the image with a diffraction-limited telescope PSF). In order to minimise the additional computation required, this was

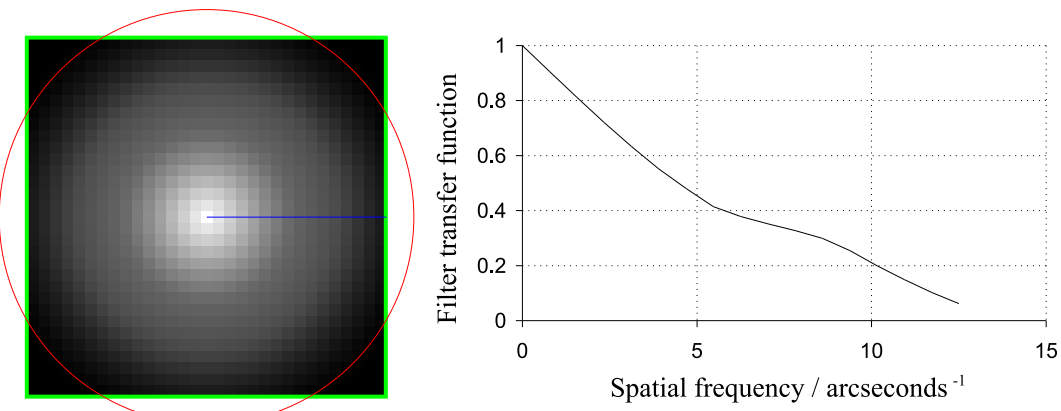


Figure 5.6: The modulation transfer function for a diffraction-limited telescope (this modulation transfer function corresponds to the amplitude of the Fourier transform of the diffraction-limited PSF shown in Figures 3.8b–d). On the left is a greyscale plot of the modulation transfer function for the simple model of the NOT aperture shown in Figure 3.4, with white corresponding to unity and black corresponding to zero in the function. The red circle has a radius of $\frac{d}{\lambda}$ corresponding to the diffraction-limit of the telescope aperture at a wavelength of $\lambda = 0.86 \mu m$. The green box corresponds to the Nyquist limit of the CCD pixel array for $40 \times 40 mas$ pixels – no Fourier components were recorded beyond this limit. The origin of the spatial frequency domain is at the centre. A horizontal cross-section along the blue line is shown on the right.

implemented during the sinc-resampling process, which is also performed in the Fourier domain. The model for the modulation transfer function which I used was calculated from the autocorrelation of the simple model of the NOT aperture described by Figure 3.4, and I have included a graphical description of the transfer function in Figure 5.6. I used the same geometrical approach for calculating this function as was used for the autocorrelation of two circles in Appendix A (see Equation A.15).

After the filtering and resampling have been completed, the peak in the resampled image corresponds to the most likely location of the brightest speckle. The height of the peak provides a measure of the flux in the brightest speckle, and hence the Strehl ratio. The measured Strehl ratio and position would then be used to select and re-centre the sinc-resampled (but unfiltered) exposures. In the high signal-to-noise regime the peak flux in the filtered short exposures was related to the peak flux in the original exposure by a non-linear, monotonically increasing function. The non-linearity of this function does not introduce complications, however, as the measurements made on the filtered images are simply used to sort the exposures according to their quality, and then to re-centre the selected exposures. Strehl ratios quoted in the text are based on measurements of the brightest pixel in the final Lucky Exposures image.

In the second application of filtering described in Table 5.6, only spatial Fourier components beyond $\frac{d}{\lambda}$ can be suppressed without blurring the astronomical image. However, the

dynamic range of sinc-resampled images is limited by Gibb's phenomena, which can be suppressed only if the spatial Fourier components of the image are smoothly reduced to zero below the Nyquist cutoff spatial frequency of the CCD pixel array. A two dimensional Fourier filter was developed based on the Hanning window which attempted to suppress both the noise and Gibb's phenomena whilst minimising the blurring of the image. The filter function was flat-topped but dropped smoothly to zero before reaching the Nyquist frequency in all orientations, and also dropped smoothly to zero at spatial frequencies beyond $\frac{d}{\lambda}$ in orientations where $\frac{d}{\lambda}$ was lower than the Nyquist frequency (λ was taken as the centroid of the observing band). A greyscale representation of the filter and cross-section are shown in Figure 5.7. The value of this filter function F_N can be defined in polar coordinates as follows:

$$F_N(r, \theta) = \begin{cases} 1 & \text{if } r \leq r_c(\theta) \\ \cos^2\left(\frac{\pi(r-r_c(\theta))}{2w}\right) & \text{if } r_c(\theta) < r < r_c(\theta) + w \\ 0 & \text{if } r \geq r_c(\theta) + w \end{cases} \quad (5.1)$$

where $r_c(\theta)$ was the spatial frequency beyond which Fourier components should be suppressed, w was the width of region over which the filter function dropped smoothly to zero and θ and r describe a polar coordinate system with the origin at zero spatial frequency. The cut-off spatial frequency $r_c(\theta)$ is defined in terms of θ because the filter must drop to zero sooner in some orientations due to the Nyquist sampling of the detector (following the rules described earlier and as shown in Figure 5.7). A width w corresponding to one-fifth of the Nyquist sampling frequency was used for the analyses presented here. For observing runs using CCDs with pixels which were not square, the Nyquist sampling frequency of the CCD was different in the horizontal and vertical directions, and the filter function used was modified appropriately obeying the same rules.

The two applications of spatial filtering mentioned above were incorporated into my approach to the data reduction relatively straightforwardly. In both applications the filtering was implemented in the Fourier domain at the same time as the sinc-resampling of the relevant images. A modified version of the data reduction flow chart of Figure 3.13 incorporating the filtering is shown in Figure 5.8.

5.4.2 Performance of the Fourier filtering

In order to assess the performance of the noise filtering for faint reference stars, it will be necessary to introduce some observational data from the NOT obtained using an L3Vision detector. I will use a single run of 3000 frames of a field near the centre of the globular cluster M13 taken on the night of 2003 July 2. The long exposure average image of the field (obtained by summing all the frames without re-centring) can be seen in Figure 5.9. These observations were taken with a bandpass centred at 860 nm with a frame rate of 50 Hz.

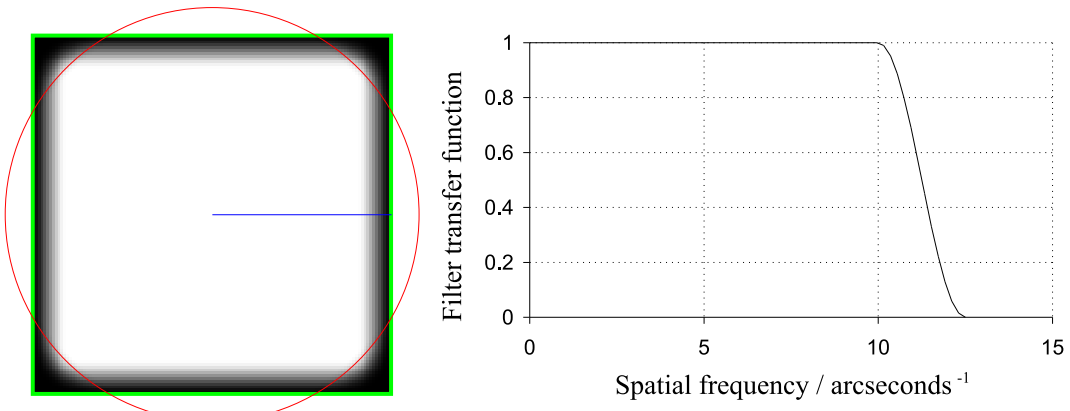


Figure 5.7: Filter function used to suppress noise. The function is based on a Hanning window but has a flat top. A linear greyscale plot is shown on the left with white corresponding to unity and black corresponding to zero. The function dropped smoothly to zero before reaching the Nyquist frequency for the CCD pixel array in all orientations. The Nyquist frequency is indicated by the green box. The function also dropped smoothly to zero at spatial frequencies beyond the diffraction limit of $\frac{d}{\lambda}$ in orientations where this was lower than the Nyquist frequency. Spatial frequencies of $\frac{d}{\lambda}$ are indicated in the plot by the red circle. A horizontal cross-section along the blue line is shown on the right.

The faint star circled in the average image was used as a reference for selecting and re-centring the short exposures. Stars H and W with magnitudes of $I = 11.6$ and $I = 12.5$ from Cohen *et al.* (1997) have been labelled in the image. In order to assess the improvement in the performance of the Strehl selection and re-centring obtained by Fourier filtering the short exposures using the diffraction-limited transfer function shown in Figure 5.6, analysis of this dataset was repeated a number of times both with and without the filtering process. Figure 5.10a shows the image obtained when the Strehl ratio and position of the brightest speckle is calculated from the brightest pixel in the image of this star in the sinc-resampled short exposures (with no filtering applied). The exposures with the highest 1% of Strehl ratios were selected and re-centred to produce the image shown in the figure. The sharpness of the point source found at the location of the reference star is artificial – it results from the coherent addition of noise in the original short exposures brought about by the selection and re-centring process as discussed in Chapter 5.4. The images of the other stars in the field are clearly more compact than in the average image of Figure 5.9, indicating that the re-centring process is performing well.

Figure 5.10b shows the image obtained when the short exposure images are filtered using the function described in Figure 5.6 before the Strehl ratio and location of the brightest speckle are calculated. The original raw exposures were selected and re-centred based on this data in the same way as for Figure 5.10a. The general characteristics of the image are similar to Figure 5.10a, and the reference star is again artificially sharp. The other stars in the field are slightly more compact in Figure 5.10b with a smaller halo surrounding

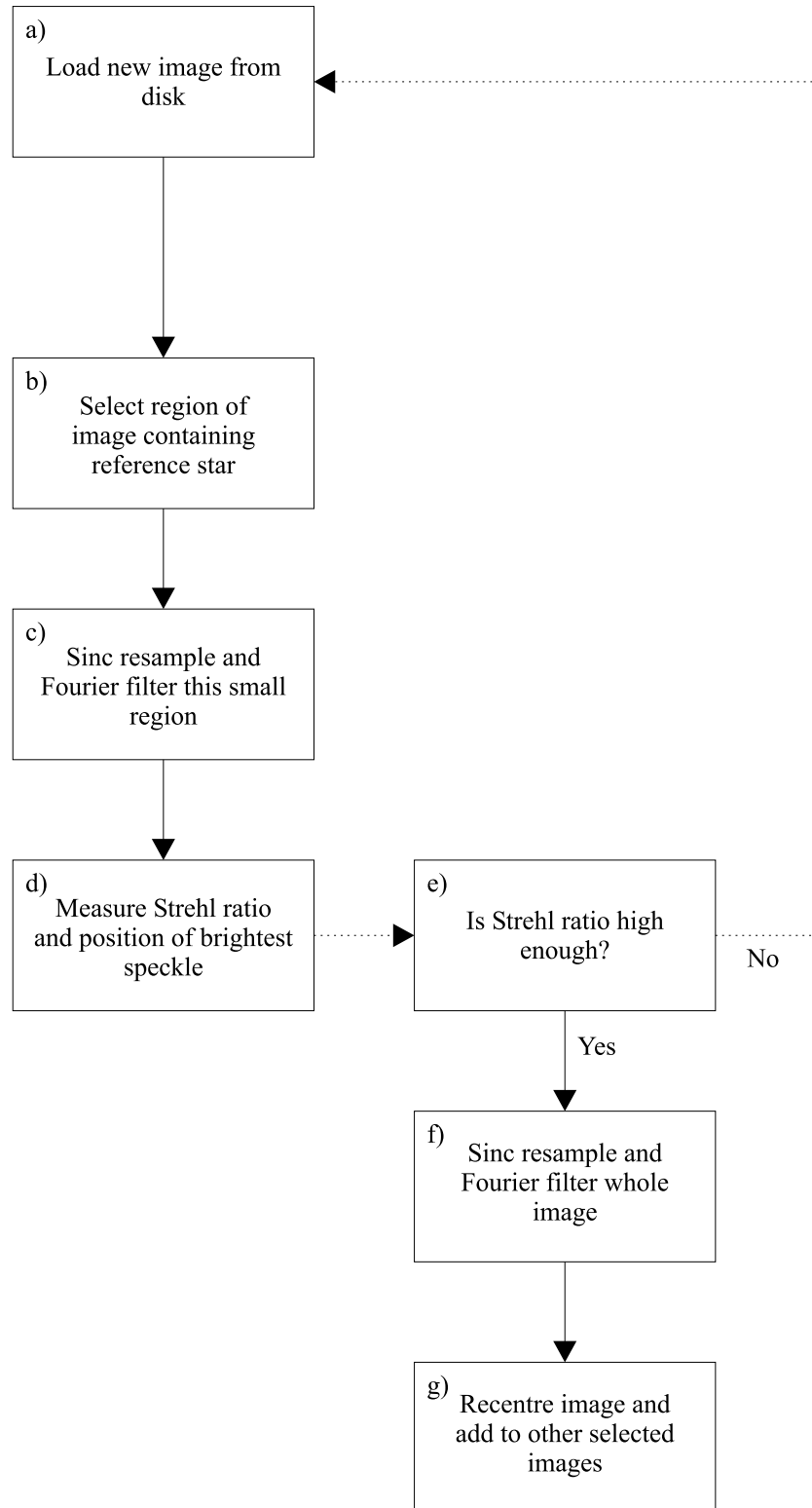


Figure 5.8: Flow chart describing the data reduction method.

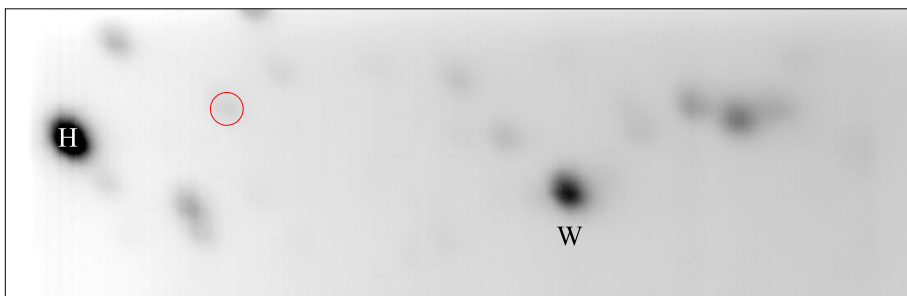


Figure 5.9: Long exposure image of M13 generated by summing the exposures in one run. Stars *H* and *W* from Cohen *et al.* (1997) are labelled. The reference star used in tests of Fourier filtering is circled. North is to right.

them. It is clear that the filtering process has improved the image quality.

Figures 5.10c and 5.10d show the results without filtering and with filtering respectively, using all of the short exposures in the run. The smoothness of the halos around the stars makes the improvement in image quality provided by the filtering less apparent for the comparison of these two images than for the case of the selected exposures. The FWHM of stars towards the left-hand side of the field is reduced from 400×280 mas without filtering to 300×260 mas with the filtering, however.

In order to test the performance of the second application of Fourier filtering (the application of the noise filter shown in Figure 5.7 to the selected exposures) I repeated the analysis of Figure 5.10b without filtering the selected exposures when they were re-centred and co-added. The effect of the noise filtering on the final image quality is shown Figure 5.11. This shows an enlargement of part of Figure 5.10b around the left-hand bright star in panel **a**) using the noise filter, and the result of the same analysis performed without using the noise filter on the selected exposures in **b**). There is no evidence for blurring of the filtered image, and the highest spatial frequency components in the noise have been suppressed in comparison with Figure 5.11b.

The results of the two approaches to Fourier filtering appeared successful, so these filtering procedures were used in the data reduction presented in the remainder of this chapter (except where specifically stated otherwise in the text).

5.5 Results

5.5.1 Results of exposure selection

Observations undertaken using a CCD65 detector on the night of 2001 July 6 are listed in Table 5.2. All the data were taken through the HiRac I-band filter based at the NOT. The observational data was reduced using the approach described by the flow diagram of

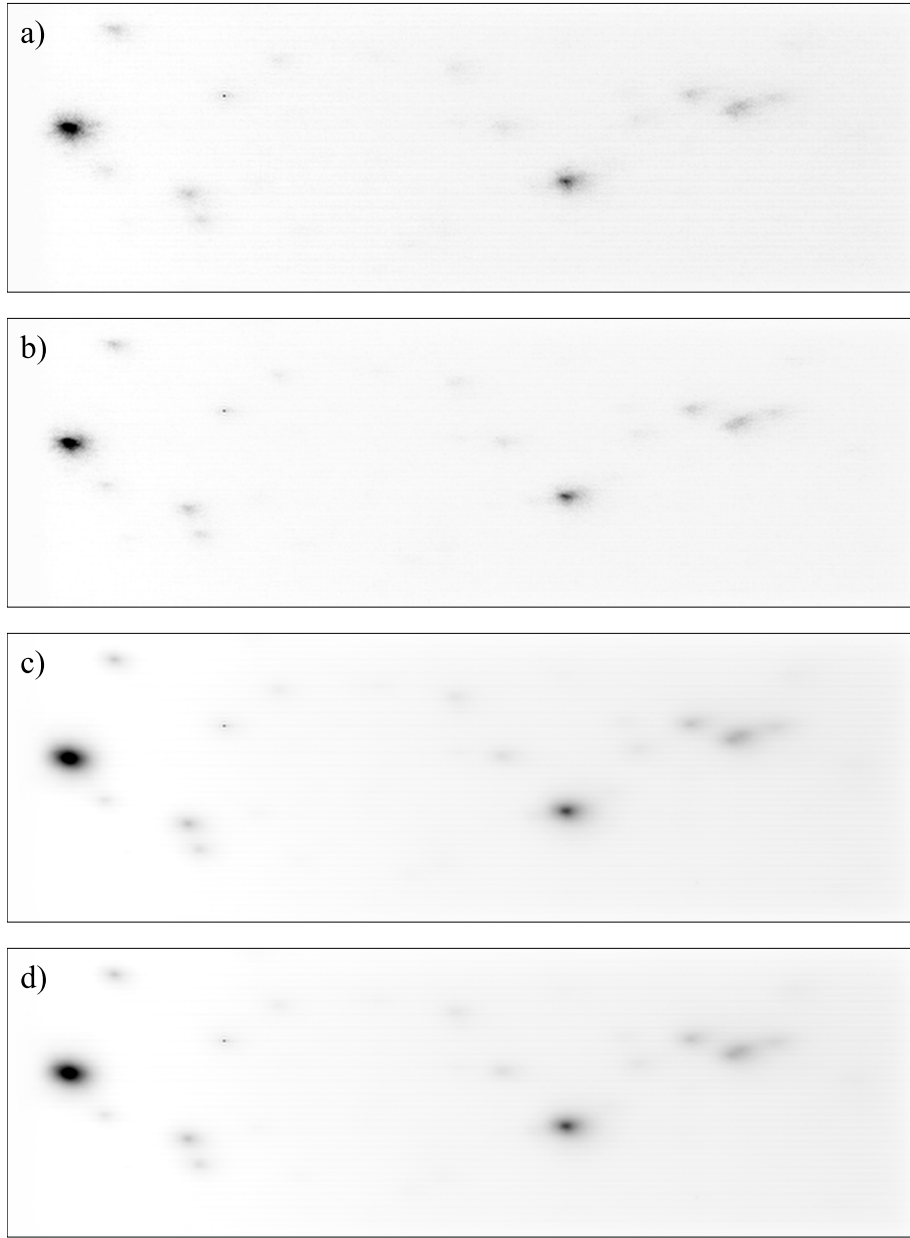


Figure 5.10: Four images of M13 generated using the same 3000 frames. The reference star used for image selection and re-centring is circled in Figure 5.9. For panel **a)** the short exposures were not filtered to suppress the noise before the Strehl ratio and position of the brightest speckle were calculated in the reference star image. The best 1% of exposures were selected to produce the image. Panel **b)** shows the result when the filter described in Figure 5.6 is used to suppress the noise before calculating the Strehl ratio and position of the brightest speckle for the reference star. The best 1% of exposures were selected. Panel **c)** shows the result of re-centring and co-adding *all* the exposures without the filtering. Panel **d)** shows the result when the filtering is used. The typical FWHM for stars on the left-hand side of these images are: **a)** 300×200 mas; **b)** 280×180 mas; **c)** 400×280 mas; and **d)** 300×260 mas.

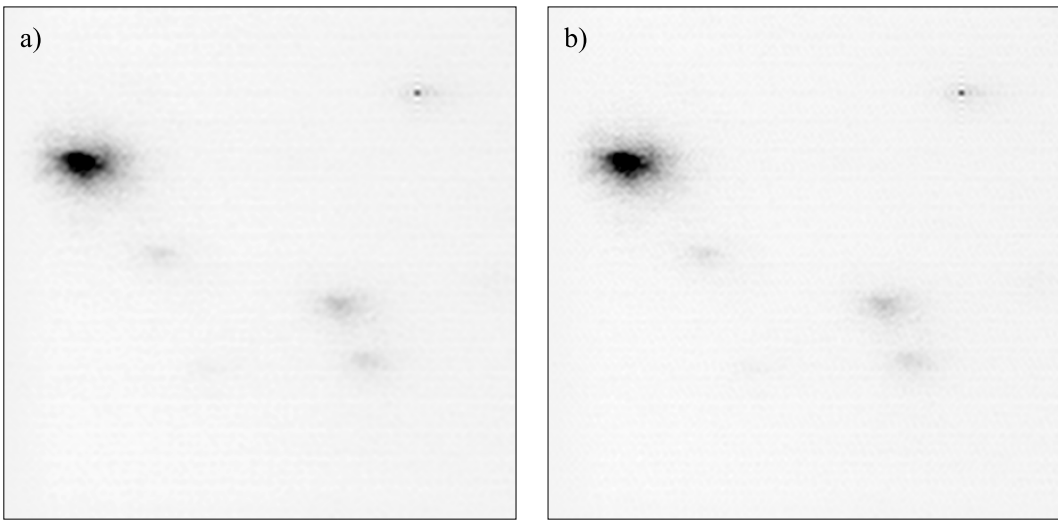


Figure 5.11: Panel **a)** shows the region of Figure 5.10b around the left-hand bright star. In producing this image the final selected exposures were Fourier filtered in order to suppress noise. Panel **b)** shows the image obtained without the noise filtering.

Figure 5.8.

An example image generated by applying the Lucky Exposures method to 110 s of data taken on M15 (*field 1*) on 2001 July 26 is shown in Figure 5.12. The $I = 13$ star which was used as the reference for selection of the best 1% of exposures and for exposure re-centring has been circled in the figure. The full frame of the CCD was read out in these observations. With the 3.4 MHz pixel rate of the CCD controller the frame rate for these observations was limited to 18 Hz , allowing image motion to slightly blur the exposures. Despite this, other stars in the field have FWHM as small as 160 mas , a substantial improvement over 500 mas for the seeing limited image shown in Figure 5.13. There was no evidence for gradual drift in the stellar positions during this run, indicative of telescope tracking errors which would blur the seeing-limited image.

As only 1% of the observing time was used for the image shown in Figure 5.12, the signal-to-noise ratio for detection of a star is expected to be lower than for the average image in Figure 5.13. If we assume that the images are sky-background limited, we can estimate the fractional decrease in signal-to-noise ratio relatively straightforwardly. We need to take into account the change in the size and shape of the PSF, but the image FWHM provides a good estimate for this effect. A good estimate for the fractional change f in signal-to-noise ratio for detection of a star of flux S will be:

$$f = \frac{St_{le}}{\sqrt{Bt_{le}d_{le}^2}} \times \frac{\sqrt{Bt_c d_c^2}}{St_c} \quad (5.2)$$

where t_{le} is the total observing time in the Lucky Exposures, d_{le} is the diameter of the PSF

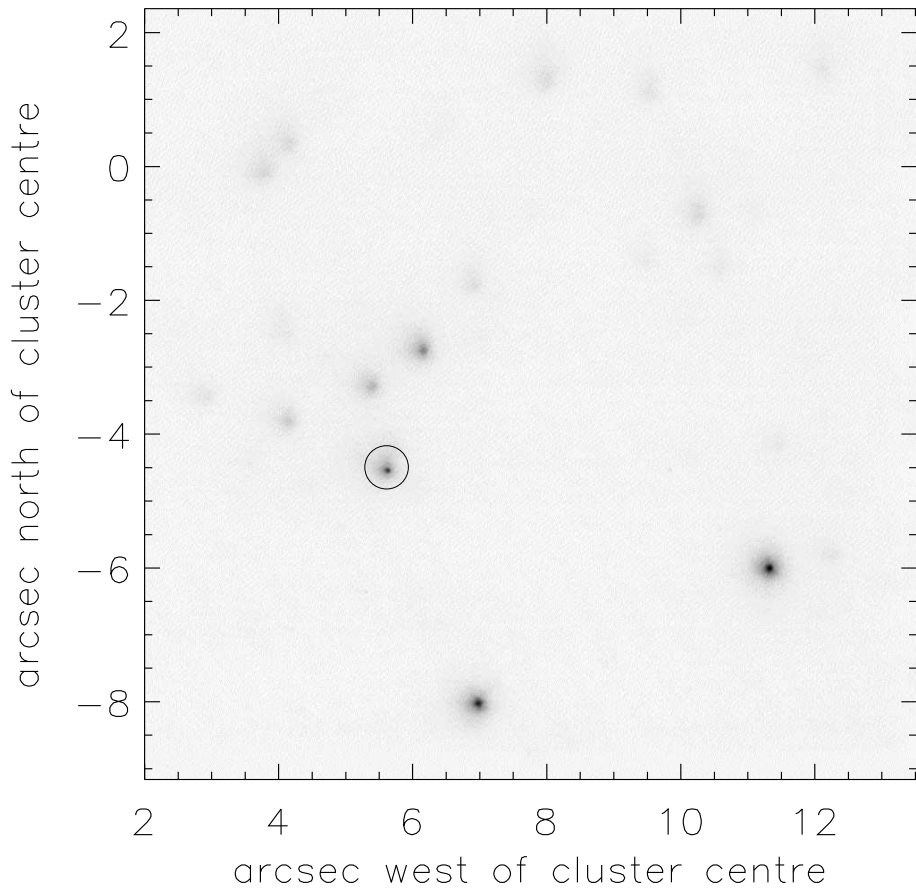


Figure 5.12: Selected exposures from 110 s of data on M15. The $I = 13.1$ reference star used for calculating the Strehl ratio and for re-centring the short exposures has been circled.

for Lucky Exposures observations in as , t_c is the total observing time for the conventional (long exposure) image, d_c is the diameter of the PSF for the conventional observation in as , and B is the sky background flux per as^2 . For the data presented in Figures 5.12 and 5.13, the fractional decrease in signal-to-noise ratio for using the Lucky Exposures method is:

$$f = 0.31 \quad (5.3)$$

In practice an astronomer must weigh this decrease in signal-to-noise against the benefits of higher image resolution.

5.5.2 Isoplanatic angle

In order to investigate the size of the isoplanatic patch, observations of binary stars with a range of separations were also undertaken on 2001 July 26. All of the stars used were bright enough that the “over resolution” effect described in Chapter 5.4 due to the selection of noise features is expected to be small. The seeing conditions were good for all the observations (seeing FWHM $\sim 0.5\ as$), and frame rates greater than 70 Hz were used for

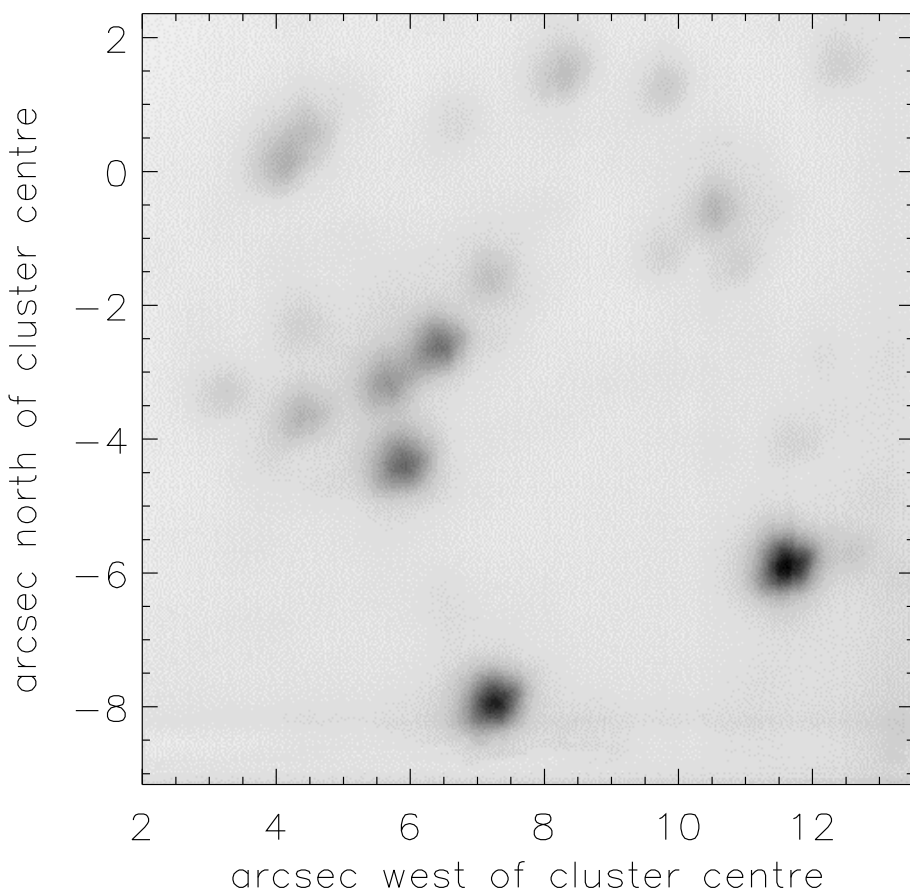


Figure 5.13: Seeing limited image generated by adding all the exposures from one run on M15 without re-centring them.

the data presented here.

For each observation, one of the binary components was used as a reference star, and the image FWHM and Strehl ratio of the other component was measured in the final Lucky Exposures image. Figure 5.14 shows the fractional reduction in Strehl ratio (i.e. the companion star Strehl ratio divided by the reference star Strehl ratio) for the binary stars HD 203991, 8 Lacertae and 61 Cygnii with separations of 0.6, 22 and 30 *as* respectively.

As in Chapter 3.5.6 I will define the isoplanatic angle θ_e as that at which the Strehl ratio falls to $\frac{1}{e}$ of the value obtained close to the reference star. A model for the anisoplanatism is required in order to calculate the size of the isoplanatic patch from measurements such as these. For both the best fit Gaussian model (shown in Figure 5.14) and for a fit of the form of Equation 2.20 a value of 30 *as* is obtained.

The 30 *as* separation for 61 Cygnii was close to the measured θ_e , and it is of interest to look at the image quality obtained on this star. The Lucky Exposures image on one component generated using the other binary component to select and re-centre the best 1% of exposures is displayed alongside the seeing-limited average image in Figure 5.15. The FWHM of 130 *mas* obtained for the Lucky Exposures image represents a substantial

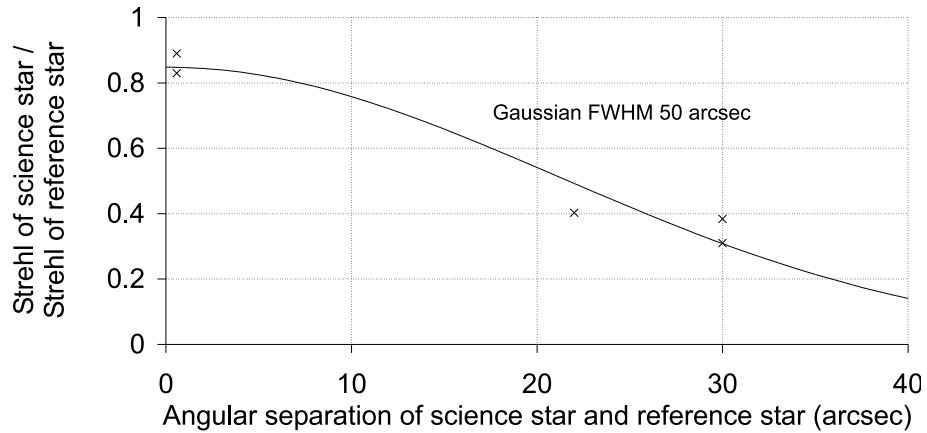


Figure 5.14: The Strehl ratio of each science object divided by the Strehl ratio for the corresponding reference star is plotted against the angular separation between science object and reference star.

improvement over the FWHM of 450 mas for the seeing-limited image. The halo around the core of the Lucky Exposures image is very compact, and it is clear that this PSF would provide good quality high resolution imaging. Any differential motion between the images of the two stars must have been extremely small. The FWHM of the companion star in the Lucky Exposures image increases to 230 mas when the best 10% of exposures are selected using the reference star. For a shift-and-add image using all of the exposures the FWHM of the companion star is 300 mas.

An isoplanatic angle of 30 as is impressively large for observations at I-band. Previous authors have predicted much smaller values of isoplanatic angle, both for speckle imaging and non-conjugate adaptive optics (typically 2–15 as – see e.g. Vernin & Muñoz-Tuñón (1994); Roddier *et al.* (1982a, 1990); Marks *et al.* (1999)). Observations at other wavelengths can be scaled to give a corresponding value for I-band using the dependence of r_0 on wavelength given in Equation 2.9.

On several nights in June and July 2003 high frame-rate observations of the globular clusters M13 and M15 were obtained covering fields which were 20 as across. It is hoped that these datasets will provide a set of isoplanatic angle measurements which can be used to determine whether the result obtained in 2001 is unusual or typical of the summer seeing conditions at the NOT. Initial results from these observations look very promising, but detailed analyses will not be presented here.

5.5.3 Limiting magnitude of reference star

In order to assess the performance with fainter reference stars, a field in the globular cluster M13 was observed with stars having a wide range of different magnitudes on 2001 July 26. The observations are listed as *M13 field 2* in Table 5.2. A Lucky Exposures

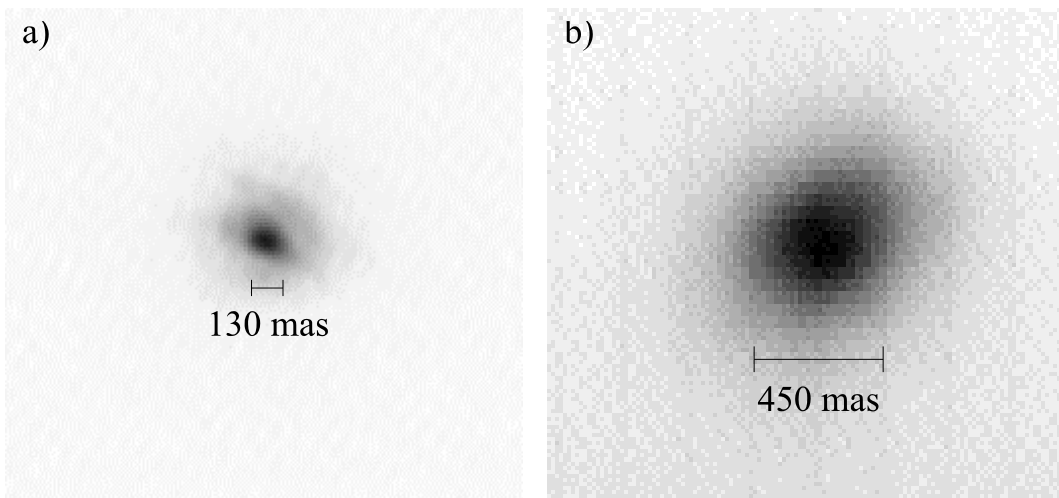


Figure 5.15: Panel **a)**) shows the image quality obtained 30 *as* from a reference star using the best 1% of exposures. One component of the binary 61 Cygni was used as the reference star for exposure selection and re-centring. The other component of the 30 *as* binary is shown here. The image FWHM of 130 *mas* represents a very substantial improvement over the FWHM of 450 *mas* for the seeing-limited image shown in **b)**). This image was generated from the same data, but without selecting or re-centring the exposures based on the reference star.

image of the field using 1% of the 6000 exposures with this telescope pointing is shown in Figure 5.16a. The $I = 12.7$ star labelled *Z* in the image was used as the reference for image selection and re-centring in this case. The frame rate used for these observations was 18 *Hz*, giving a total integration time on the sky of 330 *s*. Star *A* from Cohen *et al.* (1997) is labelled in the figure. This star was saturated in the best short exposures, and has hence been omitted from further analyses. The stellar image FWHM of ~ 100 *mas* are very competitive with other imaging techniques. The image shows faint asymmetrical horizontal tails around the fainter stars, which may be evidence of poor charge transfer efficiency (vertical tails are also visible in the cross-sections of Figure 5.16b). The electrical heating was not connected at the time these runs were taken, so it is plausible that the charge transfer efficiency might have been poorer here than during other runs on the same night. Despite this effect, the stellar cores throughout the image are extremely compact.

The analysis of this data was repeated using a range of different stars in the field as the reference for exposure selection and re-centring. The Lucky Exposures method was found to work very successfully with relatively faint reference stars. First the $I = 13.8$ star labelled *X* in Figure 5.16 was used as a reference for selecting the best 1% of exposures and re-centring them. A section of the resulting image (the region around the star labelled *Z* in Figure 5.16) is shown in Figure 5.17a. Note that neither of the two stars visible in this figure was used as the reference in this case (star *X* was used) and yet the stellar cores are extremely sharp. The Strehl ratio for the stars in this image was measured as 0.13. Figure 5.17b shows a similar image generated using an $I = 15.9$ reference star. The

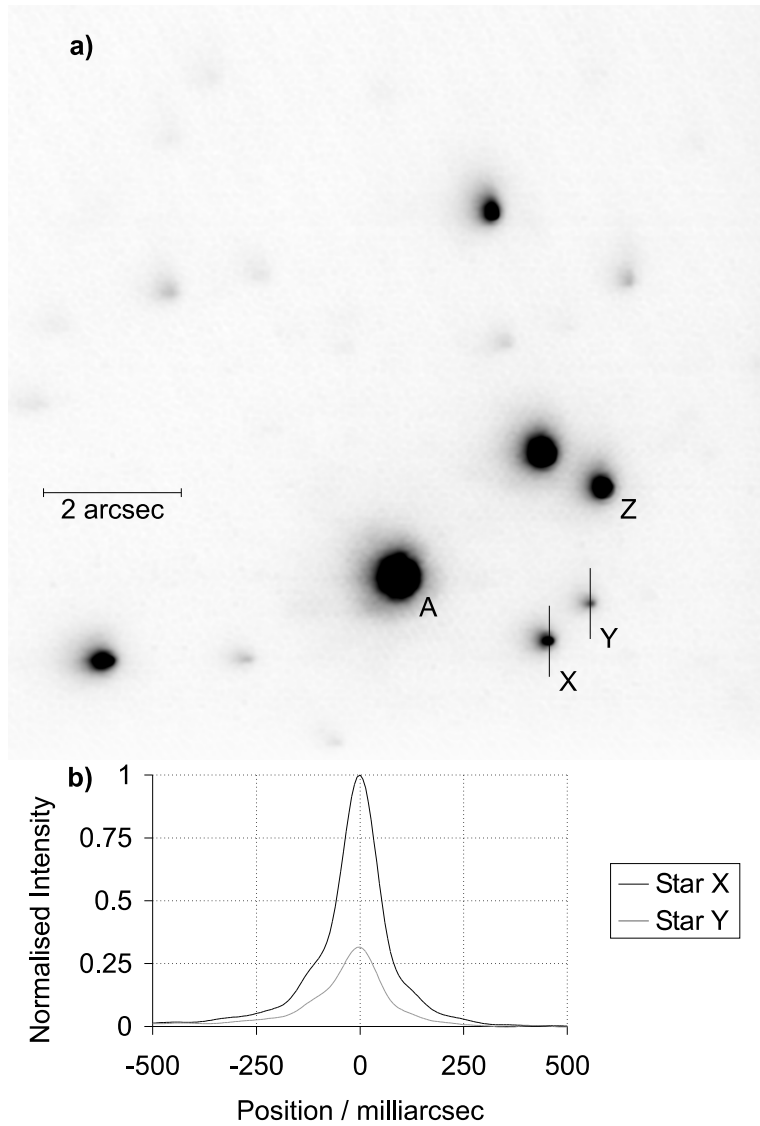


Figure 5.16: The best 1% of exposures of M13 were selected and re-centred to produce the near diffraction-limited image shown in a). Star A from Cohen *et al.* (1997) has been labelled. The $I = 12.7$ star Z was the reference star used for image selection. Panel b) shows cross-sections through stars X and Y along the lines indicated in panel a).

Strehl ratio of 0.065 still represents a substantial improvement over the Strehl ratio of 0.019 for the averaged (long exposure) image shown in Figure 5.17c. The image FWHM of 180 mas for Figure 5.17b would be extremely valuable for many astrophysical programs, and represents an enormous improvement over the 570×390 mas for the long exposure image. The asymmetry in the long exposure image might be the result of telescope tracking errors, as M13 was close to the zenith. The position of the brightest speckle in the image of a reference star shows jumps in the horizontal direction, as can be seen in Figure 5.18.

Figure 5.19 shows plots of the variation in the Strehl ratio and FWHM of nearby stars when a range of different stars are used as the reference for image selection and for the shifting and adding process. 1% of the exposures were selected in the analyses used to generate these plots, and the Strehl ratios and FWHM were calculated using nearby stars in order to minimise the effects of anisoplanatism. Figure 5.19a shows the decline in Strehl ratio with increasingly faint reference star magnitude. The Strehl ratio of the Lucky Exposures image remains substantially higher than the seeing-limited value of 0.019 even for reference stars as faint as $I = 16$. Figure 5.19b shows the image FWHM obtained using the same reference stars. An image FWHM of 100 mas can be achieved using reference stars as faint as $I = 14$, and there is a substantial improvement over the FWHM for the seeing-limited image of 570×390 mas even for $I = 15.9$ reference stars.

The faint limiting magnitude for the Lucky Exposures method stems partly from the high signal-to-noise ratio for measurements of the brightest speckle in those exposures having the highest Strehl ratios. This is highlighted in Figure 5.20, which shows surface plots of two frames taken from a run on the $I = 10$ star CCDM J17339+1747B on 2001 July 26 (listed in Table 5.2). Figure 5.20a shows an exposure with a high Strehl ratio (0.21). The location and Strehl ratio of the brightest speckle in this image can be measured with a high signal-to-noise ratio. Good results would be obtained if exposures such as this were re-centred based on the location of the brightest speckle. In contrast, Figure 5.20b shows a typical exposure with poorer Strehl ratio. The brightest speckle has a peak flux which is barely above the noise level, and the errors in determining the location of the brightest speckle will be substantially higher in this case. If a large fraction of the exposures are selected and re-centred, these errors would lead to poorer image quality for other objects in the field around the reference star. Conversely, if only those exposures with high Strehl ratios are used, we would expect the re-centring errors to be smaller. Combined with the higher intrinsic Strehl ratios in the selected exposures, these should lead to much higher image resolution for objects in the field.

The Lucky Exposures image quality obtained from the run on CCDM J17339+1747AB is summarised in Figure 5.21. The lower right $I = 10$ star was the one shown in Figure 5.20, and this star was used as the reference for exposure selection and re-centring. Figure 5.21a shows the image obtained by selecting and re-centring the best 1% of exposures based on the brightest pixel in the filtered exposures in the usual way. Figure 5.21b shows the result obtained if the brightest pixel in the raw short exposures is used without Fourier filtering

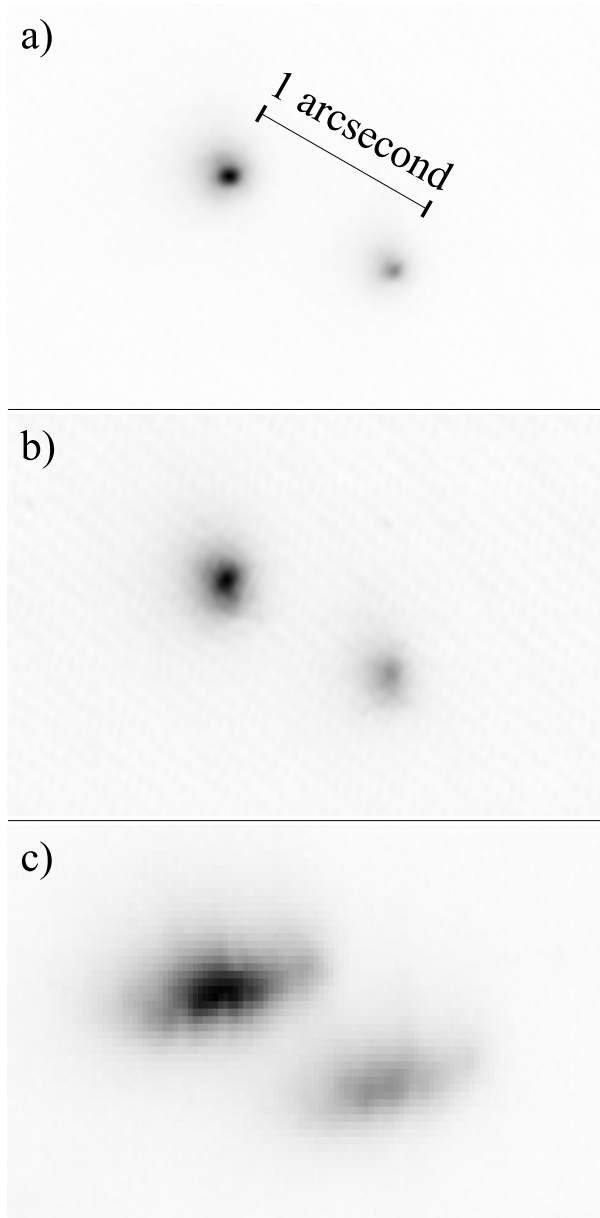


Figure 5.17: **a)**—**c)** Image resolution for a field in M13 with different reference stars.

- a)** The result of image selection, shifting and adding using an $I = 13.8$ reference star $2.5 \text{ } as$ away from the centre of the field shown. The stellar cores in this image have FWHM of 100 mas and Strehl ratios of 0.13.
- b)** Image selection, shifting and adding using an $I = 15.9$ reference star $2.9 \text{ } as$ away. The stellar FWHM in the image are 180 mas and the Strehl ratios are 0.065.
- c)** Conventional image of the same field produced by summing together 1000 of the raw frames without shifting to compensate for image motion. The FWHM of the stars are $570 \times 390 \text{ mas}$ with a Strehl ratio of 0.019.

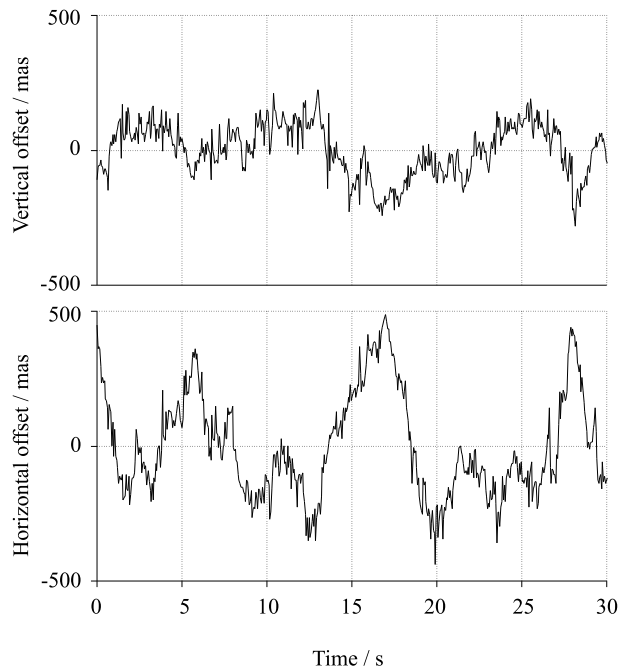


Figure 5.18: The position of the brightest speckle measured in the image of star Z in our exposures (see Figure 5.16) as a function of time. The upper plot shows the vertical offset from the mean position for the brightest speckle, and the lower plot shows the horizontal offset.

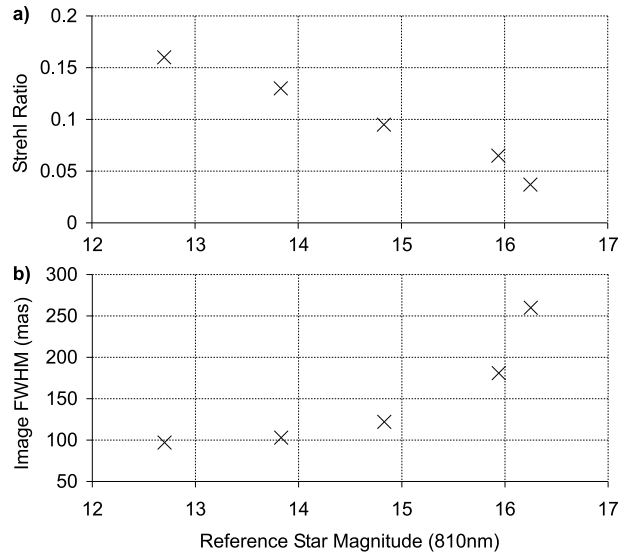


Figure 5.19: a), b) Image resolution for a range of different reference stars in M13.

- a) Average values for the Strehl ratios of bright stars within a few arcseconds of the reference star, for a range of reference star magnitudes.
- b) Image FWHM in milliarcseconds for bright stars within a few arcseconds of the reference star, for a range of reference star magnitudes.

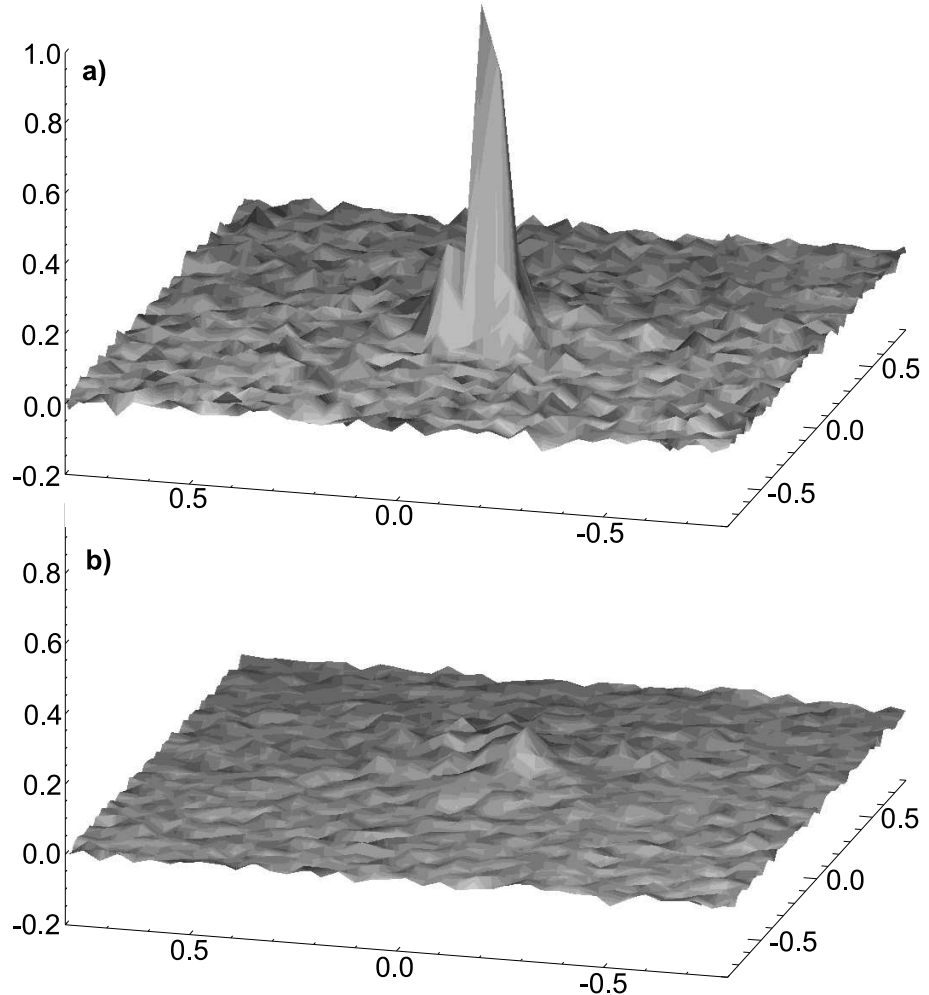


Figure 5.20: **a), b)** Surface plots of intensity in two example exposures taken from a run on the faint star CCDM J17339+1747B. The exposures had a duration of 9.7 ms.

- a) The single best 9.7 ms exposure from the first run the $I \simeq 10$ star CCDM J17339+1747B, with a Strehl ratio of 0.21. In selected exposures such as this the signal to noise is very high.
- b) The exposure of CCDM J17339+1747B with the modal Strehl ratio of 0.05.

using the function shown in Figure 5.6 for calculations of the Strehl ratio and position of the brightest speckle. The halo around the bright star is clearly less compact in this image. Figures 5.21c and 5.21d show images generated in the same way but using all of the exposures. The re-centring process was based on the position of the brightest pixel in the raw exposures for the fainter star at the lower right for Figures 5.21d. Despite the relatively low signal-to-noise ratio apparent in Figure 5.20, the re-centring process has reduced the image FWHM to 120 mas from 0.5 as achieved without re-centring. Good image quality is obtained at this signal-to-noise even without filtering out the noise.

Using the flux calibration for an $A0$ V star in Cox (2000) and the predicted throughput of the telescope, instrument, filter and CCD quantum efficiency shown Figure 5.5 I calculated the number of detected photons expected from a $I = 15.9$ reference star in a single 55 ms exposure. The total transmission under curve **B** corresponds to an equivalent bandpass of 23 nm with 100% transmission. Using a value of $6.1 \times 10^{-15} W m^{-2} nm^{-1}$ for the flux from an $I = 15.9$ at 810 nm wavelength this would imply a rate of 1.2×10^5 detected photons per second. In a 55 ms exposure we would thus expect about 5900 photons. If the Strehl ratio in a good exposure is 0.2, 20% of this flux will fall in one bright speckle (corresponding to about 1200 photons). Taking the simplified model for the signal-to-noise ratio with L3Vision CCDs described by Equation 4.20, we expect a signal-to-noise ratio of about 24 on such a speckle.

5.5.4 Assessment of image quality

In order to measure the stability of the image scale and PSF across the field and make a rudimentary assessment of the performance of Lucky Exposures images in astrometric measurements, the observations used for Figure 5.16a were re-analysed.

The 60 best exposures from the same dataset on M13 used in Chapter 5.5.3 were separated into two groups of 30. The exposures in these two groups were observed during two separate time windows, so the atmospheric effects should be uncorrelated for the two datasets. The exposures in each group were shifted and added together to give two independent images of the field in M13. I used the same approach to accurately measure the positions of the stars in these two images as was used for measuring the location of the brightest speckles in individual short exposures – the two images were filtered using the modulation transfer function of a diffraction-limited telescope (shown in Figure 5.6) and resampled, and the peak pixel in the resulting stellar images was taken as the position of each star. The relative star positions calculated for the two independent datasets were compared and found to agree within 6 mas for eight of the brightest stars, without accounting for changes in plate scale or orientation. The stellar magnitudes agreed within 0.02. Clearly for astronomically useful measurements the optical distortions in the instrument would need to be accurately determined, and any shift in the stellar positions due to limited charge transfer efficiency would also have to be characterised. Given good in-

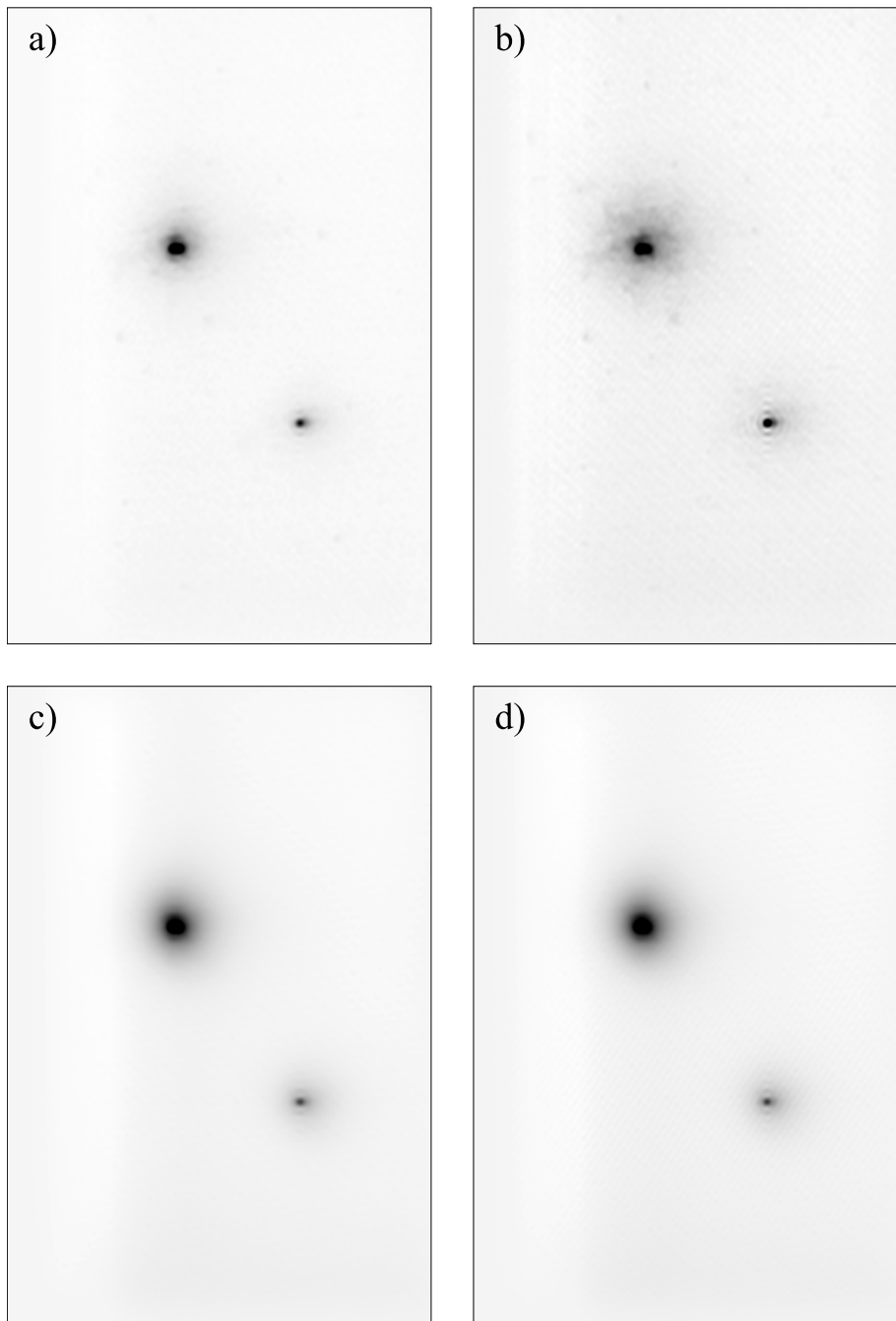


Figure 5.21: Results of exposure selection on CCDM J17339+1747AB. For **a)**, the best 1% of exposures were selected using the standard approach. **b)** shows the result without the use of Fourier filtering to suppress noise in the exposure selection step. **c)** and **d)** are the same as **a)** and **b)** but using all of the exposures.

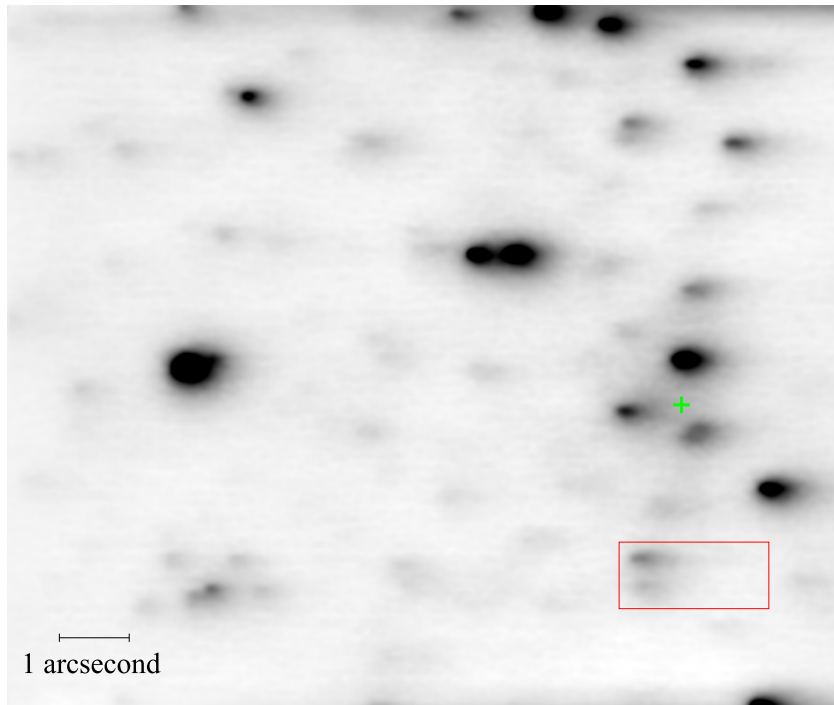


Figure 5.22: Lucky Exposures image from the core of M15. The region in the red box is enlarged in Figure 5.23a.

strument characterisation, the accuracy of the astrometry and photometry would improve substantially with increased observing time, potentially allowing accurate measurements of globular cluster velocity dispersions and photometric variability studies.

Some of the Lucky Exposures images generated from data taken using L3Vision CCDs were found to show evidence for smearing at low signal levels in the direction of CCD serial transfers. The dependency of the smearing effect on both the position in the image and on the signal level gave weight to the hypothesis that problems with charge transfer efficiency might be to blame. In order to investigate the smearing effect in more detail I chose an image of M15 which was quite badly affected, taken from our observing run in July 2002 through the 810 nm HiRac I filter at the NOT. Figure 5.22 shows a region around the core of M15. The cluster centre is marked by a green cross toward the right-hand side (as determined by Guhathakurta *et al.* (1996)). The image has been contrast stretched to highlight some of the fainter stars. Most of the stars show some evidence of horizontal smearing, particular the fainter stars toward the right-hand edge. Cross-sections through two stars toward the lower right-hand corner of the image are shown in Figure 5.23. The horizontal cross-section along line C shows a long tail to the right of the stellar centroid, reminiscent of the charge distributions measured in the laboratory under conditions of poor transfer efficiency (one of these distributions was shown in Figure 4.13).

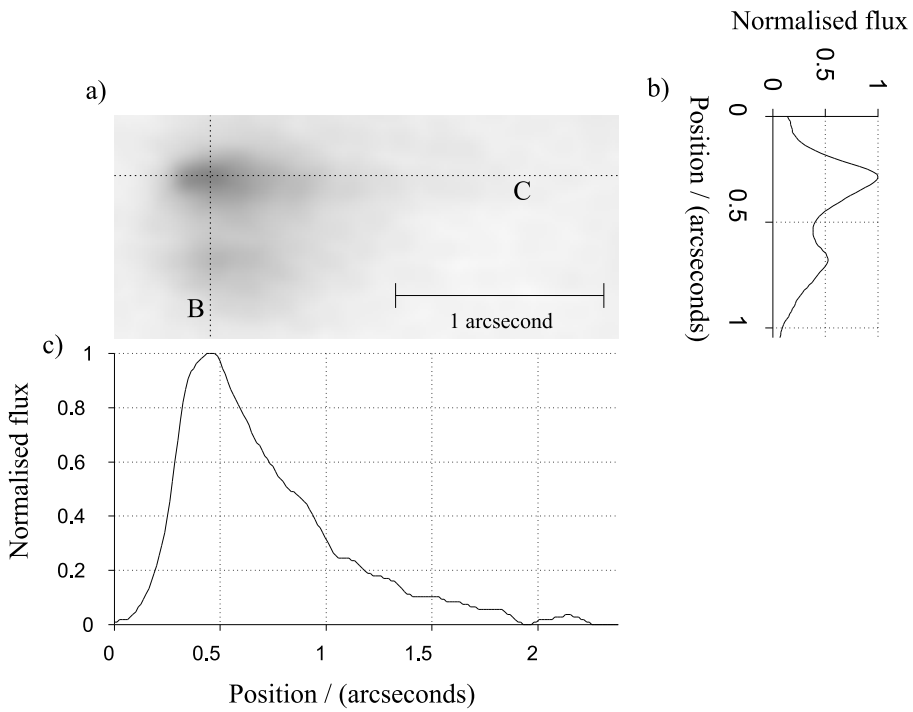


Figure 5.23: Selected exposures from the core of M15. Cross sections through the image are shown in panels **b)** and **c)** along the dotted lines in **a)**.

5.5.5 Dynamic range

Figure 5.24 shows an example image generated by selecting the best 5% of exposures out of 8000 taken at 50 Hz on M13 on the night of 2003 June 29. The observations were taken through the 780 nm edge filter, with the long-wavelength cutoff determined by the sensitivity limit of the CCD (as illustrated in Figure 5.5). The $I = 11.6$ star at the bottom of the image was used as a reference. The high dynamic range in this image is apparent when the image contrast is stretched one hundred fold, as demonstrated in Figure 5.25. Stars as faint as $I = 18$ can be clearly detected above the noise. Stars H and W from Cohen *et al.* (1997) have been labelled in the image. The stars toward the top of the image have asymmetrical tails around them. The image FWHM range from 180×110 mas for stars at the bottom of the image to 400×220 mas for stars at the top. In order to confirm that this blurring did not result from anisoplanatism, the data analysis was repeated using star W as the reference instead of star H .

Figure 5.26a shows the image of star W when star H was the reference (this is a section of the image shown in Figures 5.24 and 5.25). The asymmetry in the stellar image is very clear in this enlargement. The image of star H when star W was the reference is shown in Figure 5.26b. There is much less evidence for asymmetry in this second image (with the same angular separation of the target from the reference star) suggesting that the smearing is not a result of anisoplanatism. It appears to simply depend on the distance from the readout register of the CCD, and is consistent with poor charge transfer efficiency

Figure 5.24: The best 5% of exposures of M13 from 30 June 2003 were selected, shifted and added to produce this image with a linear greyscale. North is toward the top of the image.



Figure 5.25: Same image as for Figure 5.24 but with the greyscale contrast stretched linearly 100 times.

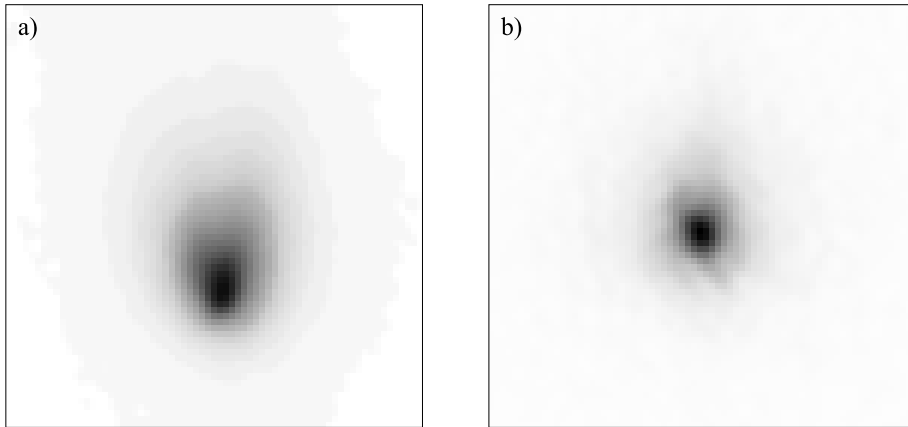


Figure 5.26: The asymmetrical smearing of stellar images toward the top of Figures 5.24 and 5.25 is highlighted by the enlargement of star W shown in panel **a)**. When star W was used as the reference, the image of star H did not show this asymmetry, as shown in panel **b)**. This implies that the blurring is an instrumental effect and not the result of anisoplanatism.

on the CCD (as discussed in Chapter 4.3.2). The orientation of the Figure is such that the direction of serial transfers on the CCD is downwards in the images.

The dynamic range of Lucky Exposures is highlighted in a more quantitative manner by Figure 5.27. This data on Gliese 569 was taken at a frame rate of 30 Hz on 2002 July 25 (as listed in Table 5.3). At the 810 nm observing wavelength the magnitude difference is 8, and yet the faint companion is easily detected with little light contamination from the primary 5 *as* away. The data were taken through high Saharan dust extinction, and there is insufficient signal-to-noise to separate the binary components.

5.6 Sky coverage

The applicability of the Lucky Exposures method to faint astronomical targets depends on the limiting magnitude of reference star which can be used, and the size of the isoplanatic patch over which the technique will work. The results presented in Figure 5.19 indicate that reference stars as faint of $I = 15.9$ can be used successfully for Lucky Exposures imaging. The results obtained on other nights (see e.g. Figure 5.12 and Chapter 5.5.5) were broadly consistent with these results from July 2001. Measurements of binaries presented in Figure 5.14 indicate that the technique works well up to 30 *as* from the reference star. These observations were taken on one night, and it has not been possible to confirm whether or not this isoplanatic angle is typical of the summer seeing conditions at the NOT.

From the limiting magnitude and isoplanatic angle measurements it is possible to calculate the fraction of the night sky which is close enough to a suitably bright reference star.

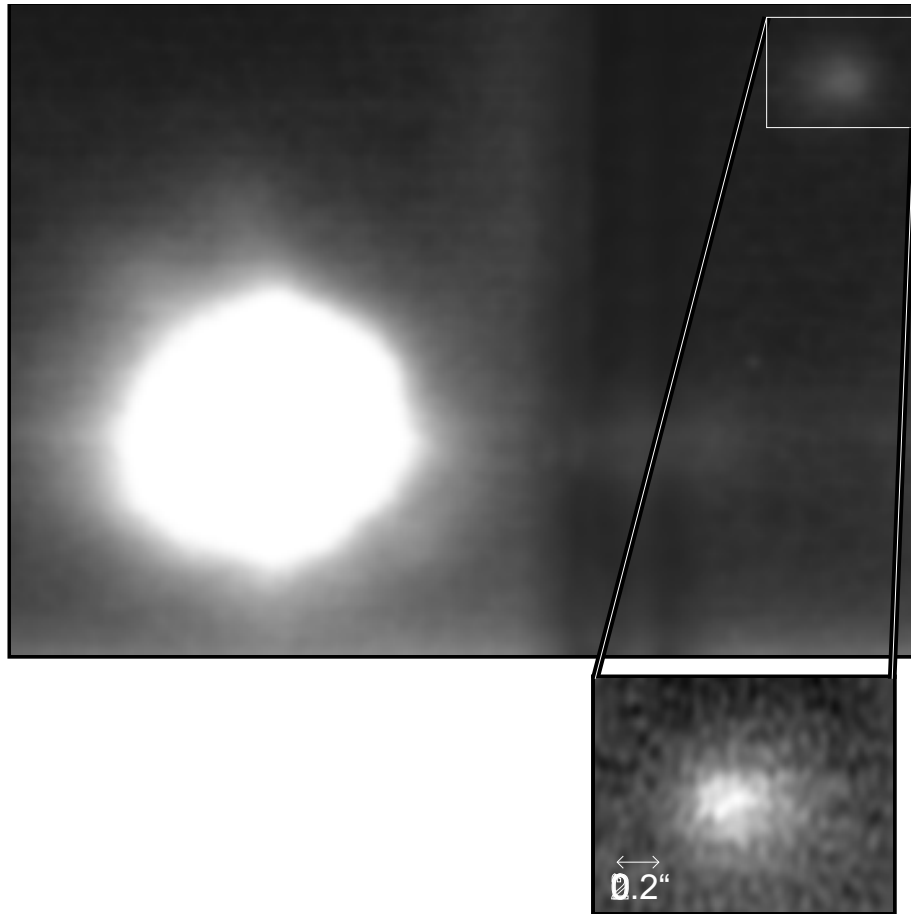


Figure 5.27: The best 4% of exposures of the multiple star system Gliese 569. The primary star has a magnitude of $I = 10$. The $I = 18$ object on the right is thought to be a brown dwarf triple system (Kenworthy *et al.* 2001). The images were selected from 10 minutes of observing time at the NOT, on a night with high Saharan dust extinction at the observatory.

Cox (2000); Bahcall & Soneira (1984) indicate that the mean density of stars brighter than $I = 15.9$ is about 1300 stars per square degree. Based on their models for the distribution of stars in galactic coordinates, the fraction of the night sky within range of a suitable reference star ranges from 10% near the South Galactic pole to 25% at $b = 30$. In the galactic plane the probability can be much higher, particularly toward the galactic centre. This represents a very substantial improvement over the case of I-band natural guide star adaptive optics, where the sky coverage is typically less than 0.1% for high resolution imaging. High resolution astronomical observations using I-band adaptive optics are limited predominantly to searches for faint companions around bright nearby stars. The small isoplanatic patch and bright reference stars mean that deep imaging observations often suffer from problems with scattered light from the reference star. In contrast, the Lucky Exposures method should be applicable to a much wider range of galactic and extra-galactic observing programs.

5.7 Conclusions

In this chapter Fourier filters were developed in order to suppress the noise in the short exposure images. These improved the image FWHM which could be obtained using faint reference stars, and helped to slightly suppress the noise in the final Lucky Exposures images.

The images obtained by applying the Lucky Exposures method to data taken with the low noise CCDs were generally of high quality. It is clear that the Lucky Exposures method can provide a substantial improvement in resolution over conventional imaging.

Measurements of the isoplanatic angle on the night of 2001 July 26 showed it to be $\sim 30\text{ as}$. This is substantially higher than the typical value achieved for I-band adaptive optics. Analysis of further observations will be required in order to determine whether this result is representative of the summer seeing conditions at the NOT.

The Lucky Exposures method was found to work successfully using reference stars as faint as $I = 15.9$. This magnitude limit is expected to be further increased with the use of back-illuminated CCDs and an anti-reflection coated dewar window.

Based on the limiting magnitude for the Lucky Exposures method, the isoplanatic angle measured on the night of 2001 July 26, and star counts from the literature we would expect the sky coverage for the Lucky Exposures technique to be about 25% at I-band. This is substantially better than that achieved with natural guide star adaptive optics at this wavelength.

Analysis of data taken on M13 suggest that accurate astrometry will be possible in crowded fields if the plate scale and image distortions can be suitably determined and if the charge transfer efficiency of the detector is good. Some of the data presented shows evidence of

problems with charge transfer efficiency, and it will be important to address this for future observing runs.

Chapter 6

Conclusions

In this chapter I hope to bring together the results presented within previous chapters, and to draw general conclusions about the advantages and disadvantages of the Lucky Exposures method. It is clear that the Lucky Exposures approach has great potential for a number of astronomical programs. A substantial amount of observational data from 2003 is yet to be processed, and hopefully this will provide a number of important science results.

The selection of short exposures based on measurements of the Strehl ratio using reference stars in the image has been demonstrated as a technique that can provide high resolution I-band images at a 2.56 *m* telescope. The high Strehl ratios, small FWHM and good dynamic range offered by the technique would be very valuable in a number of astronomical imaging programs. The true imaging capability and faint limiting magnitude of reference stars for Lucky Exposures can provide significant advantages over other high frame rate imaging techniques. I will list here a few of the key conclusions which have been listed at the end of individual chapters.

Sky coverage

Observations at the NOT in July 2001 indicated that the isoplanatic angle for observations using the Lucky Exposures method was 30 *as*. This represents a substantial improvement over the typical values expected for I-band adaptive optics. Images with FWHM as small as 130 *as* were obtained at this separation from a reference star. Observations in May 2000 were suggestive of a smaller isoplanatic angle at that time. Future analysis of data taken at the NOT in 2003 may give a better indication of the typical range of isoplanatic angles at the NOT site.

Observations of M13 in July 2001 indicate that good image quality can be obtained using reference stars as faint as $I = 15.9$. Observations analysed using faint reference stars from

June 2003 had image quality which was consistent with that obtained in July 2001 using reference stars of similar magnitude.

The limiting magnitude and isoplanatic angle, combined with models for galactic star counts at I-band indicate that approximately 25% of the night sky should be within range of a suitable reference star for the Lucky Exposures method.

Image quality

Using bright reference stars, the Lucky Exposures method can provide I-band images of exceptional quality from a telescope of 2.56 m diameter under good seeing conditions. The measured Strehl ratios are consistent with those predicted by numerical simulations. The images of close binaries showed very good agreement between the stars, while there was evidence for some anisoplanatism in wider binaries. Spatial autocorrelations of ζ Boötis indicate that the re-centring of short exposure images works most effectively when the short exposure Strehl ratios are high. The image resolution obtained using the Lucky Exposures method decreases gradually when the fraction of exposures is increased.

Observations of M13 indicate that high precision relative astrometry should be possible in crowded fields given good charge transfer efficiency and a suitable understanding of the plate scale and relevant aberrations.

Results from simulation

Previous theoretical studies have indicated that the timescales and isoplanatic angles relevant to speckle imaging may be larger than those for non-conjugate adaptive optics at many astronomical observatories. Numerical simulations presented here were broadly consistent with these predictions.

High Strehl ratio images would be expected from the Lucky Exposures technique even if there are aberrations in the telescope mirror, as the method will tend to select exposures at times when the atmosphere is counter-acting the mirror aberrations. Structure on the mirror surfaces which is on very different scales to the dominant atmospheric perturbations is much less likely to be corrected in this way.

Sinc-resampling of the short exposures can significantly improve the estimation of the Strehl ratio and position of the brightest speckle. In low signal-to-noise data, Fourier filtering can be used to improve the performance of the exposure selection and re-centring, and reduce the noise in the final reconstructed image.

Timescale measurements

The atmospheric coherence time for speckle imaging at I-band was found to be approximately 65 ms at the NOT in May 2000. The excellent image quality obtained using frame rates as low as 18 Hz in 2001 is consistent with this. The oscillation of the NOT telescope was found to cause slight blurring of exposures having duration longer than ten milliseconds.

L3Vision CCD performance

Theoretical modelling of L3Vision CCDs from E2V Technologies indicate that these devices have the potential to act as an image plane photon-counting array. The distribution of output electrons can be modelled numerically for any given flux of detected photons.

Experimental measurements of L3Vision CCDs in our camera both at the NOT and in the laboratory indicate that short exposures are often affected by charge transfer efficiency problems at low signal levels.

Future prospects

There are a number of modifications to the Lucky Exposures method as presented here which would make it applicable to a wider range of astronomical observations. In crowded fields, the image quality could be monitored using a number of reference stars across the field, allowing exposures to be selected on the basis of isoplanatic angle as well as overall image quality. By combining data from several different reference stars, the signal-to-noise ratio for Strehl ratio measurements could also be improved.

The Lucky Exposures method is not restricted to single-wavelength detectors – light from a science target could be directed into a spectrograph with an Integral Field Unit (IFU) while the light from a reference star was monitored on a conventional imaging detector in order to select moments of high image quality. Array detectors with spectroscopic sensitivity such as Superconducting Tunnel Junction (STJ) devices could also be used to provide spectral information. If the reference star is faint, a broader bandpass could be used for the reference star than for the observations of the science target.

The dependence of r_0 on observing wavelength described in Equation 2.9 implies that the Lucky Exposures method should work well on much larger telescopes if longer observing wavelengths are used. An 8 m telescope observing at K-band would have the same number of r_0 across its diameter as a 2.5 m telescope observing at 800 nm wavelength, and a similar probability of Lucky Exposures would be expected. Current low noise infra-red cameras can typically only be read at low frame rates, so further camera and detector development might be required to make such an instrument viable. Observations could also be

performed at shorter wavelengths using smaller telescopes, although this would probably require faster camera readout rates and possibly an atmospheric dispersion corrector.

In order to improve the resolution attainable with the Lucky Exposures technique, non-circular apertures could also be exploited. If a large (diameter greater than $7r_0$) telescope were broken up into a series of slit apertures, the probability of obtaining good atmospheric conditions over one of these slits would be higher than for the telescope aperture as a whole. By repeating observations with a range of different slit position angles, high resolution data could be obtained in all orientations from an astronomical target.

Alternatively, a low-order adaptive optics system designed for long wavelength imaging might provide a substantial improvement to the probability of obtaining Lucky Exposures at short wavelengths on a large telescope, as it would eliminate the large scale structure in the atmospheric phase perturbations. This could allow high resolution imaging from large telescopes without the need for high-order adaptive optics correction (which usually requires a bright reference star).

Summary

It is clear that the Lucky Exposures method has great potential for many astronomical programs. The higher sky coverage of the Lucky Exposures method at I-band as compared to that for natural guide star adaptive optics means that this method can be applied to a much wider range of astronomical targets. If a large isoplanatic patch is frequently available during Lucky Exposures observations, it will be possible to image large fields at high resolution.

A substantial quantity of observational data taken in 2003 is waiting to be analysed. The wide range of astronomically interesting targets promise many exciting astronomical results. The dataset will also be very valuable in characterising the atmospheric conditions at the NOT over a more statistically significant period.

The development of instrumentation for Lucky Exposures is ongoing in the Institute of Astronomy, and the staff at the NOT and associated institutes have expressed a keen interest in becoming involved with this work. With a bit of Luck, this program will eventually lead to a permanent exposure selection instrument available to the whole astronomical community.

Appendix A

Simplified approximation to a single Taylor screen atmosphere

To begin with I will look at some basic imaging properties of the simple single-lens telescope shown in Figure A.1. Point p in the figure is within the image plane of the telescope. The contribution to the optical flux at this point can be determined by first selecting a plane X which is perpendicular to the line of sight from p (joining the point p and the centre of the lens in Figure A.1). The integral of the complex wavefunction across the plane X determines the contribution to the wavefunction amplitude at point p . The photon flux is proportional to the square of this amplitude.

Figure A.2 shows the same situation as Figure A.1, but the incoming wavefronts have been perturbed by the atmosphere. The phase fluctuations will affect the integral of the wavefunction over plane X altering the measured intensity at point p .

For the case of a single wind-blown Taylor screen, the phase perturbations introduced by the atmosphere will be translated laterally across the telescope aperture by the wind with no change in the structure of these perturbations. The modulus of the integral of the wavefunction over the plane X is not directly affected by the lateral motion of the phase fluctuations, but the motion of the screen introduces new phase perturbations at the upwind side of the aperture and removes phase perturbations at the downwind side. This can be seen clearly if the outline of the telescope aperture is projected along the line of sight from p onto the Taylor screen, as shown by the solid circle in Figure A.3. After time has elapsed and the wind-blown Taylor screen has moved a distance ρ , the outline of telescope aperture will be projected onto the dotted circle. Area B is common to both timepoints and will contribute equally to the amplitude of the wavefunction at point p in the image plane, but the contribution from area A will be lost, and a new contribution from area C will be included at the later timepoint. In reality, the atmospheric phase in areas C and A will remain correlated to that in area B over a region extending approximately r_0 from the boundary of area B , but for the particular case of large diameter apertures this only

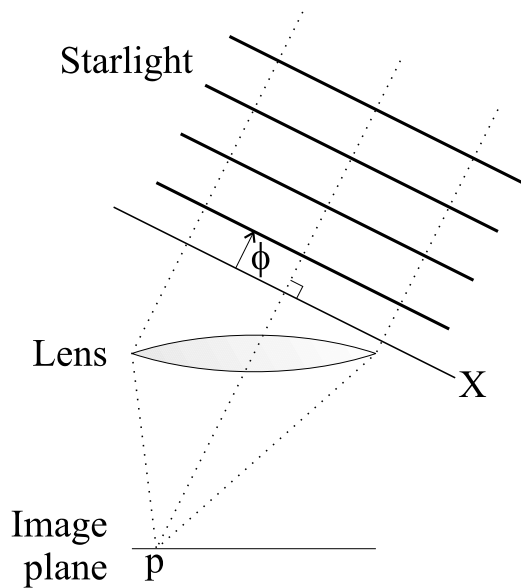


Figure A.1: Plane waves are focussed by a single-lens telescope onto a point p in the image plane. Plane X is perpendicular to the direction of propagation of the light focussed onto point p . The optical flux at point p can be determined by integrating the optical wavefunction across plane X , and squaring the amplitude of the result. The phase of the wavefunction ϕ at plane X is represented schematically in the figure by the distance to the nearest wavefront peak.

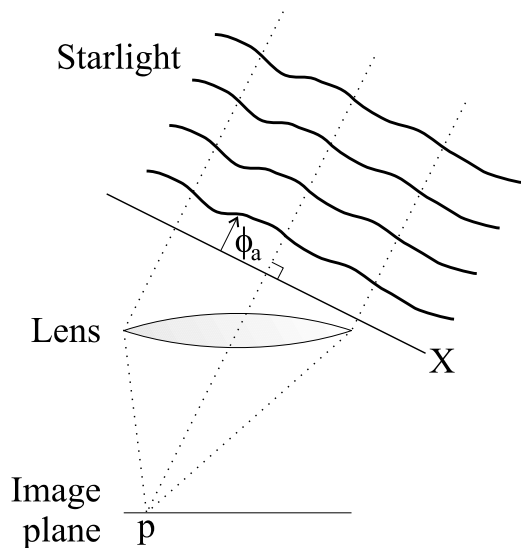


Figure A.2: The planar wavefronts of Figure A.1 are replaced by atmospherically perturbed wavefronts. The magnitude of the integral across plane X will be reduced due to the phase perturbations in the wavefunction, reducing the optical flux measured at point p .

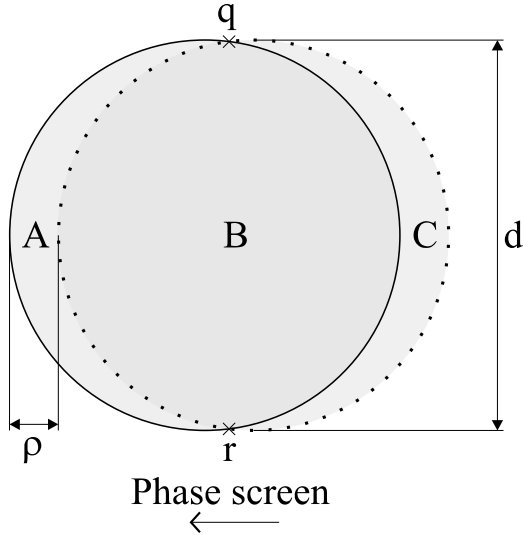


Figure A.3: For observations at the zenith, the solid circle represents the original projection of the telescope aperture onto the Taylor screen, while the dotted circle represents the same projection after the Taylor screen has been blown a distance ρ by the wind. d is the diameter of the telescope primary. For observations away from the zenith, projection effects will slightly elongate the circles.

has a small effect on our calculations and will be neglected in this simple approximation.

We can write the contributions ψ_A , ψ_B and ψ_C to the wavefunction at point p from areas A , B and C respectively as:

$$\psi_A = \chi_A e^{i\phi_A} \quad (\text{A.1})$$

$$\psi_B = \chi_B e^{i\phi_B} \quad (\text{A.2})$$

$$\psi_C = \chi_C e^{i\phi_C} \quad (\text{A.3})$$

where χ_A , χ_B and χ_C describe the amplitudes and ϕ_A , ϕ_B and ϕ_C the phases of these contributions. If the linear dimensions of areas A , B and C in Figure A.3 are much larger than r_0 , then the phases ϕ_A , ϕ_B and ϕ_C will not be correlated with each other, as the structure function of Equation 1.3 indicates that the typical phase variation between points separated by distances much greater r_0 will be many cycles in magnitude.

If the linear dimensions of areas A , B and C are much larger than r_0 then the ensemble average amplitudes $\langle \chi_A \rangle$, $\langle \chi_B \rangle$ and $\langle \chi_C \rangle$ will be proportional to the square root of the areas of A , B and C respectively. This can most clearly be seen if we imagine utilising a telescope whose aperture has the same size and shape as one of these three regions. The atmospheric seeing will generate an image with a FWHM of approximately λ/r_0 regardless of the aperture size and shape (as long as the aperture is much larger than r_0), with an average intensity proportional to the area of the aperture.

As the phases ϕ_A , ϕ_B and ϕ_C are not correlated with each other, if the light from more than

one of these regions is combined then the ensemble averages of the relevant amplitudes must be added in quadrature to give the total amplitude. It is useful to consider three ensemble average intensities $\langle I_A \rangle$, $\langle I_B \rangle$ and $\langle I_C \rangle$ which describe the contributions from the areas A , B and C as follows:

$$\langle I_A \rangle = \langle |\psi_A|^2 \rangle \quad (\text{A.4})$$

$$\langle I_B \rangle = \langle |\psi_B|^2 \rangle \quad (\text{A.5})$$

$$\langle I_C \rangle = \langle |\psi_C|^2 \rangle \quad (\text{A.6})$$

As we have assumed that the wavefunctions ψ_A , ψ_B and ψ_C are not correlated (not coherent), the ensemble average intensities $\langle I_A \rangle$, $\langle I_B \rangle$ and $\langle I_C \rangle$ can be summed linearly. As the areas of A and C are equal, the corresponding ensemble average intensities will be equal:

$$\langle I_A \rangle = \langle I_C \rangle \quad (\text{A.7})$$

We are interested in the intensity I_{AB} produced at the first timepoint when light from areas A and B is combined:

$$I_{AB} = |\psi_A + \psi_B|^2 \quad (\text{A.8})$$

and the intensity I_{BC} from areas B and C , corresponding to a time when the Taylor screen has moved by a distance ρ in Figure A.3:

$$I_{BC} = |\psi_B + \psi_C|^2 \quad (\text{A.9})$$

The ensemble average of both of these intensities is simply the sum of the relevant ensemble average intensities for the constituent components:

$$\langle I_{AB} \rangle = \langle I_A \rangle + \langle I_B \rangle \quad (\text{A.10})$$

$$\langle I_{BC} \rangle = \langle I_B \rangle + \langle I_C \rangle \quad (\text{A.11})$$

As the total area of each of the circles in Figure A.3 is independent of ρ , the combined intensities $\langle I_{AB} \rangle$ and $\langle I_{BC} \rangle$ will be independent of the offset ρ .

The value of $\langle I_B \rangle$ is directly dependent on ρ . For non-zero values of $\langle I_B \rangle$, the fluctuations in the instantaneous intensities I_{AB} and I_{BC} will be correlated, as both intensities include a contribution from ψ_B . Conversely, if the value of $\langle I_B \rangle$ were zero then the contribution ψ_B would be zero, and fluctuations in I_{AB} and I_{BC} would be completely uncorrelated. We are interested in determining the size of the contribution $\langle I_B \rangle$ for which the correlation between fluctuations in I_{AB} and I_{BC} has dropped by a factor of $1/e$. As the wavefront components ψ_A , ψ_B and ψ_C are uncorrelated Rayleigh distributions, this will be true when

the ensemble average intensity $\langle I_B \rangle$ from area B contributes $1/\sqrt{e}$ of the total intensity:

$$\langle I_B \rangle = \frac{I_{AB}}{\sqrt{e}} \quad (\text{A.12})$$

The intensity $\langle I_B \rangle$ will obey Equation A.12 when areas A and B are related as follows:

$$B = \frac{A + B}{\sqrt{e}} \quad (\text{A.13})$$

If the telescope aperture is described by a function $\chi_t(\mathbf{r})$ such as the example case in Equation 1.7, then area of overlap B between two offset apertures comes directly from the autocorrelation of this function $R_\chi(\rho)$:

$$R_\chi(\rho) \equiv \int_{-\infty}^{\infty} \chi_t(r + \rho) \chi_t^*(r) dr \quad (\text{A.14})$$

It is useful to note that this remains true regardless of the shape of the telescope aperture described by $\chi_t(\mathbf{r})$.

For the simple case presented in Figure A.3 of a filled circular aperture of diameter d , the area of overlap B can be calculated geometrically. The line joining q and r in Figure A.3 is a chord to both the dotted and filled circles. B is constructed from two symmetric regions either side of this chord, each having an area:

$$\frac{B}{2} = \frac{d^2}{4} \arccos\left(\frac{\rho}{d}\right) - \frac{\rho}{4} \sqrt{d^2 - \rho^2} \quad (\text{A.15})$$

The separation at which the area of B is reduced by a factor of $1/\sqrt{e}$ was evaluated numerically as $\rho_e = 0.31d$ for a telescope of diameter d , giving a coherence timescale:

$$\tau_e = \frac{0.31d}{|\mathbf{v}|} \quad (\text{A.16})$$

for a constant wind velocity \mathbf{v} .

Appendix B

Observation log for June-July 2003 observations at the NOT

A substantial amount of observational data from a wide range of targets was obtained at the NOT on the nights of 2003 June 27 to 2003 July 4. The optical filters used for these observing runs provided a range of different bandpasses between 600 nm and 1 μ m. Table B.1 lists the general properties of these filters. The runs are summarised in Tables B.2 to B.9 for the benefit future researchers. For many of the runs the aperture diameter was stopped down in a re-imaged pupil plane. The aperture diameter was usually chosen to match $7r_0$ at the observing wavelength, although experiments with different apertures sizes were performed for a few of the runs.

Filter name	Centroid of observing band	Filter description
Coherent R	650 nm	Top hat filter with 72 nm FWHM
H α	656 nm	Filter with 11 nm FWHM
HiRac I	810 nm	Top hat filter with 125 nm FWHM
715 edge	\sim 820 nm	Long-pass filter (long wavelength cutoff set by limit of the CCD detector)
780 edge and HiRac I	\sim 830 nm	Filter pair gives bandpass with 90 nm FWHM
780 edge	\sim 860 nm	Long-pass filter (long wavelength cutoff set by limit of the CCD detector)
850 edge and HiRac I	860 nm	Filter pair gives bandpass with 20 nm FWHM
850 edge	\sim 890 nm	Long-pass filter (long wavelength cutoff set by limit of the CCD detector)

Table B.1: Filters used in observations at the NOT

Target	Object type	Filter	Aperture diameter	Image size (pixels)
100 Herculis	Binary	HiRac I	1.89 <i>m</i>	552 × 104
BD +193457C	Binary	HiRac I	1.89 <i>m</i>	552 × 176
M13 core	Globular cluster	HiRac I	1.89 <i>m</i>	552 × 176
M13 core	Globular cluster	HiRac I	1.32 <i>m</i>	552 × 176
CVS 97A	Gravitational lens	HiRac I	1.89 <i>m</i>	552 × 176
PNG 0456	Planetary nebula progenitor	HiRac I	1.89 <i>m</i>	552 × 176
M15 core	Globular cluster	HiRac I	1.89 <i>m</i>	552 × 264
M15 core	Globular cluster	HiRac I	1.89 <i>m</i>	552 × 528
M15 core	Globular cluster	HiRac I	1.32 <i>m</i>	552 × 528
Neptune and Triton	Solar system	HiRac I	1.32 <i>m</i>	552 × 528
Neptune and Triton	Solar system	HiRac I	2.56 <i>m</i>	552 × 528
BD +064730	Star	HiRac I	2.56 <i>m</i>	552 × 528
BD +064730	Star	850 edge	2.56 <i>m</i>	552 × 528
BD +064730	Star	780 edge	2.56 <i>m</i>	552 × 528
BD +064730	Star	715 edge	2.56 <i>m</i>	552 × 528
BD +064730	Star	H α	2.56 <i>m</i>	552 × 528
BD +064730	Star	Coherent R	2.56 <i>m</i>	552 × 528

Table B.2: Log of observations on night of 2003 June 27 at the NOT.

Target	Object type	Filter	Aperture diameter	Image size (pixels)
Gliese 569	Multiple brown dwarf	HiRac I	2.56 <i>m</i>	552 × 104
3C 294	Active galactic nucleus	HiRac I	2.56 <i>m</i>	552 × 104
M13 core	Globular cluster	780 edge	2.56 <i>m</i>	552 × 528
M13 core	Globular cluster	780 edge	2.56 <i>m</i>	552 × 104
M13 core	Globular cluster	780 edge	2.56 <i>m</i>	552 × 176
M13 core	Globular cluster	850 edge	2.56 <i>m</i>	552 × 176
100 Herculis	Binary	850 edge and HiRac I	2.56 <i>m</i>	552 × 80
UU Sagittae	Eclipsing binary	780 edge	2.56 <i>m</i>	552 × 176
SN2002hh	Supernova	780 edge	2.56 <i>m</i>	552 × 528
WR 140	Wolf Rayet binary system	850 edge and HiRac I	2.56 <i>m</i>	552 × 104
NGC7469	Active galactic nucleus	780 edge	2.56 <i>m</i>	552 × 176

Table B.3: Log of observations on night of 2003 June 28 at the NOT.

Target	Object type	Filter	Aperture diameter	Image size (pixels)
NGC 5548	Active galactic nucleus	780 edge	2.56 m	552 × 176
M13 core	Globular cluster	780 edge	2.56 m	552 × 104 ^a
M13 mosaic	Globular cluster	780 edge	2.56 m	552 × 528
100 Herculis	binary	850 edge and HiRac I	2.56 m	184 × 104
V536 Aquilae	Variable star	780 edge	2.56 m	552 × 104
WR 140	Wolf Rayet binary system	850 edge and HiRac I	2.56 m	112 × 104
M15 core	Globular cluster	780 edge	2.56 m	552 × 528
M15 core	Globular cluster	780 edge	2.56 m	552 × 176

^aObservational results from this run are presented in Chapter 5.5.5

Table B.4: Log of observations on night of 2003 June 29 at the NOT.

Target	Object type	Filter	Aperture diameter	Image size (pixels)
100 Herculis	Globular cluster	HiRac I	2.56 m	184 × 104 ^b
100 Herculis	Globular cluster	HiRac I	2.08 m	184 × 104 ^b
100 Herculis	Globular cluster	HiRac I	1.70 m	184 × 104 ^b
M13 core	Globular cluster	780 edge	2.56 m	552 × 176 ^b
V 653 Ophiuchii	T-Tauri star	780 edge	2.56 m	552 × 528 ^b
V 653 Ophiuchii	T-Tauri star	850 edge	2.56 m	552 × 528 ^b
V 536 Aquilae	Variable star	780 edge	2.56 m	552 × 176 ^b
SN2002hh	Supernova	780 edge	2.56 m	552 × 296
NGC 7008	Planetary nebula progenitor	780 edge	2.56 m	184 × 176
NGC 7008	Planetary nebula progenitor	Coherent R	2.08 m	184 × 176
M15 core	Globular cluster	780 edge	2.56 m	552 × 528
M15 core	Globular cluster	780 edge	1.89 m	552 × 528
M15 core	Globular cluster	780 edge	1.32 m	552 × 528
M15 core	Globular cluster	780 edge	2.56 m	552 × 176
M15 core	Globular cluster	780 edge	1.89 m	552 × 176
M15 core	Globular cluster	780 edge	1.32 m	552 × 176

^bObserving through patchy cloud

Table B.5: Log of observations on night of 2003 June 30 at the NOT.

Target	Object type	Filter	Aperture diameter	Image size (pixels)
NGC 4151	Active galactic nucleus	780 edge	2.56 m	552 × 176
NGC 4151	Active galactic nucleus	Coherent R	2.56 m	552 × 176
CVS 97A	Gravitational lens	780 edge	2.56 m	552 × 176
Target for P. Hewitt	Galaxy core	780 edge	2.56 m	552 × 176 ^b
M13 core	Globular cluster	780 edge	2.56 m	552 × 176
100 Herculis	binary	850 edge and HiRac I	2.56 m	184 × 104
Neptune and star	Solar system	780 edge	2.56 m	184 × 528
Neptune and star	Solar system	780 edge	2.08 m	184 × 528
Neptune and star	Solar system	780 edge	1.89 m	184 × 528
WR 140	Wolf Rayet binary system	780 edge and HiRac I	1.89 m	552 × 176
M15 core	Globular cluster	780 edge	2.56 m	552 × 528
M15 mosaic	Globular cluster	780 edge	2.08 m	552 × 528
M15 core	Globular cluster	780 edge	2.08 m	552 × 176

^bObserving through patchy cloud

Table B.6: Log of observations on night of 2003 July 1 at the NOT.

Target	Object type	Filter	Aperture diameter	Image size (pixels)
NGC 4151	Active galactic nucleus	780 edge	2.56 m	552 × 176
Gliese 569	Multiple brown dwarf	HiRac I	2.56 m	280 × 104
Q1518+58	Active galactic nucleus	780 edge	2.56 m	552 × 176
M13 core	Globular cluster	780 edge	2.56 m	552 × 176
M13 core	Globular cluster	780 edge	1.32 m	552 × 176
M13 core	Globular cluster	Coherent R	1.32 m	552 × 176
100 Herculis	binary	850 edge and HiRac I	2.56 m	184 × 104
WR 124	Wolf Rayet star	780 edge	2.56 m	552 × 176
WR 124	Wolf Rayet star	H α	2.56 m	552 × 176
UU Sagittae	Observations during eclipse of binary component	780 edge	2.56 m	552 × 176
M15 core	Globular cluster	780 edge	2.56 m	552 × 176

Table B.7: Log of observations on night of 2003 July 2 at the NOT.

Target	Object type	Filter	Aperture diameter	Image size (pixels)
Gliese 569	Multiple brown dwarf	780 edge	various	280×104
Gliese 623	Multiple brown dwarf	780 edge	$2.56 m$	552×176
Gliese 623	Multiple brown dwarf	780 edge	$2.56 m$	280×104
Mars and star	Solar system	850 edge	$2.56 m$	552×528
Mars and star	Solar system	Coherent R	$2.56 m$	552×528

Table B.8: Log of observations on night of 2003 July 3 at the NOT. The seeing was generally poor ($1\text{-}3$ arcseconds), and little useful data was obtained.

Target	Object type	Filter	Aperture diameter	Image size (pixels)
M13 field	Globular cluster	780 edge	various	552×528
M13 field	Globular cluster	780 edge	various	552×176
M13 core	Globular cluster	780 edge	$2.56 m$	552×176
Gliese 623	Multiple brown dwarf	780 edge	$1.89 m$	112×104
100 Herculis	binary	850 edge and HiRac I	various	184×104
WR 124	Wolf Rayet star	780 edge and HiRac I	$2.56 m$	552×176
WR 124	Wolf Rayet star	Coherent R	$2.56 m$	552×176
Mars	Solar system	850 edge	$2.56 m$	552×528
M15 mosaic	Globular cluster	780 edge	$1.70 m$	552×528

Table B.9: Log of observations on night of 2003 July 4 at the NOT.

Bibliography

- AIME, C., RICORT, G., KADIRI, S., & MARTIN, F. 1981. Temporal autocorrelation functions of solar speckle patterns. *Optics Communications*, **39**(Nov.), 287–292.
- AIME, C., BORGINO, J., MARTIN, F., PETROV, R., & RICORT, G. 1986. Contribution to the space-time study of stellar speckle patterns. *Optical Society of America, Journal, A: Optics and Image Science*, **3**(July), 1001–1009.
- ALLER, L. H., APPENZELLER, I., BASCHEK, B., DUERBECK, H. W., HERCZEG, T., LAMLA, E., MEYER-HOFMEISTER, E., SCHMIDT-KALER, T., SCHOLZ, M., SEGGEWISS, W., SEITTER, W. C., & WEIDEMANN, V. (eds). 1982. *Landolt-Börnstein: Numerical Data and Functional Relationships in Science and Technology - Group VI (Astronomy and Astrophysics)*, Vol. 2b (*Stars and Star Clusters*), Schaifers & Voigt, Eds., Chapter 4.2.
- ANDERSEN, M. I., & SØRENSEN, A. N. 1996 (Feb.). *Image quality at the Nordic Optical Telescope*. IJAF Report 2. Copenhagen University Observatory, Denmark.
- AVILA, R., VERNIN, J., & MASCIADRI, E. 1997. Whole atmospheric-turbulence profiling with generalized scidar. *Applied Optics*, **36**(Oct.), 7898–7905.
- BAHCALL, J. N., & SONEIRA, R. M. 1984. Comparisons of a standard galaxy model with stellar observations in five fields. *Astrophysical Journal Supplement Series*, **55**(May), 67–99.
- BALDWIN, J. E., HANIFF, C. A., MACKAY, C. D., & WARNER, P. J. 1986. Closure phase in high-resolution optical imaging. *Nature*, **320**(Apr.), 595–597.
- BALDWIN, J. E., BECKETT, M. G., BOYSEN, R. C., BURNS, D., BUSCHER, D. F., COX, G. C., HANIFF, C. A., MACKAY, C. D., NIGHTINGALE, N. S., ROGERS, J., SCHEUER, P. A. G., SCOTT, T. R., TUTHILL, P. G., WARNER, P. J., WILSON, D. M. A., & WILSON, R. W. 1996. The first images from an optical aperture synthesis array: mapping of Capella with COAST at two epochs. *Astronomy and Astrophysics*, **306**(Feb.), L13+.
- BALDWIN, J. E., TUBBS, R. N., COX, G. C., MACKAY, C. D., WILSON, R. W., & ANDERSEN, M. I. 2001. Diffraction-limited 800 nm imaging with the 2.56 m Nordic Optical Telescope. *Astronomy and Astrophysics*, **368**(Mar.), L1–L4.

- BARNABY, D., SPILLAR, E., CHRISTOU, J. C., & DRUMMOND, J. D. 2000. Measurements of Binary Stars with the Starfire Optical Range Adaptive Optics Systems. *Astronomical Journal*, **119**(Jan.), 378–389.
- BASDEN, A. G., HANIFF, C. A., & MACKAY, C. D. 2003. Photon counting strategies with low light level CCDs. *Monthly Notices of the Royal Astronomical Society*, **345**(Nov.), 985–991.
- BATCHELOR, G. K., & TOWNSEND, A. A. 1949 (May). The nature of turbulent motion at large wave-numbers. *Pages 238–255 of: Proceedings of the Royal Society of London A*, 199.
- BURNS, D., BALDWIN, J. E., BOYSEN, R. C., HANIFF, C. A., LAWSON, P. R., MACKAY, C. D., ROGERS, J., SCOTT, T. R., WARNER, P. J., WILSON, D. M. A., & YOUNG, J. S. 1997. The surface structure and limb-darkening profile of Betelgeuse. *Monthly Notices of the Royal Astronomical Society*, **290**(Sept.), L11–L16.
- BURT, D., & BELL, R. 1998. CCD imagers with multiplication register. *European Patent Application Bulletin*, **39**(Sept.), EP 0 866 501 A1.
- BUSCHER, D. F., & HANIFF, C. A. 1993. Diffraction-limited imaging with partially redundant masks: II. Optical imaging of faint sources. *Optical Society of America Journal*, **10**(Sept.), 1882–1894.
- BUSCHER, D. F., ARMSTRONG, J. T., HUMMEL, C. A., QUIRRENBACH, A., MOZURKEWICH, D., JOHNSTON, K. J., DENISON, C. S., COLAVITA, M. M., & SHAO, M. 1995. Interferometric seeing measurements on Mt. Wilson: power spectra and outer scales. *Applied Optics*, **34**(Feb.), 1081–1096.
- CACCIA, J. L., AZOUI, M., & VERNIN, J. 1987. Wind and C_N -squared profiling by single-star scintillation analysis. *Applied Optics*, **26**(Apr.), 1288–1294.
- CHELLI, A. 1987. Comparison Between Image Plane Phase Reconstruction Methods in Optical Interferometry. *Revista Mexicana de Astronomia y Astrofisica*, **14**(May), 751+.
- CHRISTOU, J. C. 1991. Image quality, tip-tilt correction, and shift-and-add infrared imaging. *Publications of the Astronomical Society of the Pacific*, **103**(Sept.), 1040–1048.
- COHEN, R. L., GUHATHAKURTA, P., YANNY, B., SCHNEIDER, D. P., & BAHCALL, J. N. 1997. Globular Cluster Photometry with the Hubble Space Telescope.VI.WF/PC-I Observations of the Stellar Populations in the Core of M13 (NGC 6205). *Astronomical Journal*, **113**(Feb.), 669–681.
- COLAVITA, M. M., SHAO, M., & STAELIN, D. H. 1987. Atmospheric phase measurements with the Mark III stellar interferometer. *Applied Optics*, **26**(Oct.), 4106–4112.

- CONAN, J., ROUSSET, G., & MADEC, P. 1995. Wave-front temporal spectra in high-resolution imaging through turbulence. *Optical Society of America Journal*, **12**(July), 1559–1570.
- COULMAN, C. E., VERNIN, J., COQUEUGNIOT, Y., & CACCIA, J.-L. 1988. Outer scale of turbulence appropriate to modeling refractive-index structure profiles. *Applied Optics*, **27**(Jan.), 155+.
- COX, A. N. 2000. *Allen's Astrophysical Quantities*. New York: Springer-Verlag.
- CRAMPTON, D., MCCLURE, R. D., FLETCHER, J. M., & HUTCHINGS, J. B. 1989. A search for closely spaced gravitational lenses. *Astronomical Journal*, **98**(Oct.), 1188–1194.
- DAINTY, J. C., HENNINGS, D. R., & ODONNELL, K. A. 1981. Space-time correlation of stellar speckle patterns. *Optical Society of America, Journal*, **71**(Apr.), 490–492.
- DANTOWITZ, R. F. 1998. Sharper Images Through Video. *Sky and Telescope*, **96**(Aug.), 48.
- DANTOWITZ, R. F., TEARE, S. W., & KOZUBAL, M. J. 2000. Ground-based High-Resolution Imaging of Mercury. *Astronomical Journal*, **119**(May), 2455–2457.
- DAVIS, J., & NORTH, J. R. 2001. Binary Star Observations in Selected Instants of Good Seeing. *Publications of the Astronomical Society of Australia*, **18**, 281–286.
- DAVIS, J., LAWSON, P. R., BOOTH, A. J., TANGO, W. J., & THORVALDSON, E. D. 1995. Atmospheric path variations for baselines up to 80m measured with the Sydney University Stellar Interferometer. *Monthly Notices of the Royal Astronomical Society*, **273**(Apr.), L53–L58.
- ENGLANDER, A., SLATKINE, M., KAROUBI, R., & BENSIMON, D. 1983. Probabilistic diffraction limited imaging through turbulence. *Optical Engineering*, **22**(Feb.), 145–148.
- FRIED, D. L. 1965. Statistics of a Geometric Representation of Wavefront Distortion. *Optical Society of America Journal*, **55**, 1427–1435.
- FRIED, D. L. 1978. Probability of getting a lucky short-exposure image through turbulence. *Optical Society of America Journal*, **68**(Dec.), 1651–1658.
- FRISCH, U., SULEM, P., & NELKIN, M. 1978. A simple dynamical model of intermittent fully developed turbulence. *Journal of Fluid Mechanics*, **87**, 719–736.
- GRAVES, J. E., NORTHCOTT, M. J., RODDIER, F. J., RODDIER, C. A., & CLOSE, L. M. 1998 (Sept.). First light for Hokupa'a: 36-element curvature AO system at UH. *Pages 34–43 of: SPIE Proceedings, Vol. 3353, Adaptive Optical System Technologies, D. Bonaccini, R. Tyson; Eds.*

- GUHATHAKURTA, P., YANNY, B., SCHNEIDER, D. P., & BAHCALL, J. N. 1996. Globular Cluster Photometry With the Hubble Space Telescope. V. WFPC Study of M15's Central density Cusp. *Astronomical Journal*, **111**(Jan.), 267+.
- HANIFF, C. A., & BUSCHER, D. F. 1992. Diffraction-limited imaging with partially redundant masks. I. Infrared imaging of bright objects. *Optical Society of America Journal*, **9**(Feb.), 203–218.
- HANIFF, C. A., MACKAY, C. D., TITTERINGTON, D. J., SIVIA, D., & BALDWIN, J. E. 1987. The first images from optical aperture synthesis. *Nature*, **328**(Aug.), 694–696.
- HANIFF, C. A., BUSCHER, D. F., CHRISTOU, J. C., & RIDGWAY, S. T. 1989. Synthetic aperture imaging at infrared wavelengths. *Monthly Notices of the Royal Astronomical Society*, **241**(Nov.), 51P–56PP.
- HARDY, J. W. 1998. *Adaptive optics for astronomical telescopes*. New York: Oxford University Press.
- HARRIS, E. J., ROYLE, G. J., SPENCER, R. D., SPENCER, S., & SUSKE, W. 2000. Evaluation of a Novel CCD Camera for Dose Reduction in Digital Radiography. *Proceedings of the IEEE Nuclear Science Symposium and Medical Imaging Conference*, Lyons, Sept.
- HECQUET, J., & COUPINOT, G. 1985. A gain in resolution by the superposition of selected recentered short exposures. *Journal of Optics*, **16**(Feb.), 21–26.
- HYNECEK, J., & NISHIWAKI, T. 2002 (July). Recent progress toward single photon detection using charge multiplying CCD image sensors. *Pages 7–12 of: Proc. 16th World Multiconference on Systems and Cybernetics, SCI2002/ISAS2002*, No. 2.
- ISHIMARU, A. 1978. *Wave propagation and scattering in random media, Vol. 2: Multiple scattering, turbulence, rough surfaces and remote sensing*. New York ; London: Academic Press.
- JERRAM, P., POOL, P. J., BELL, R., BURT, D. J., BOWRING, S., SPENCER, S., HAZELWOOD, M., MOODY, I., CATLETT, N., & HEYES, P. S. 2001 (May). The LLCCD: low-light imaging without the need for an intensifier. *Pages 178–186 of: SPIE Proceedings, Vol. 4306, Sensors and Camera Systems II*, M. Blouke et al Eds.
- KARO, D. P., & SCHNEIDERMAN, A. M. 1978. Speckle interferometry at finite spectral bandwidths and exposure times (E). *Optical Society of America Journal*, **68**, 480–+.
- KARR, T. J. 1991. Temporal response of atmospheric turbulence compensation. *Applied Optics*, **30**(Feb.), 363+.
- KEEN, J. W. 1999 (Dec.). *Personal communication – algorithm for generating Kolmogorov turbulence developed by Dave Buscher and modified by James Keen*.

- KENWORTHY, M., HOFMANN, K., CLOSE, L., HINZ, P., MAMAJEK, E., SCHERTL, D., WEIGELT, G., ANGEL, R., BALEGA, Y. Y., HINZ, J., & RIEKE, G. 2001. Gliese 569B: A Young Multiple Brown Dwarf System? *Astrophysical Journal Letters*, **554**(June), L67–LL70.
- KIM, Y., & JAGGARD, D. L. 1988. Band-limited fractal model of atmospheric refractivity fluctuation. *Optical Society of America Journal*, **5**(Apr.), 475–480.
- KOLMOGOROV, A. N. 1941a. Dissipation of energy in the locally isotropic turbulence. *Comptes rendus (Doklady) de l'Académie des Sciences de l'U.R.S.S.*, **32**, 16–18.
- KOLMOGOROV, A. N. 1941b. The local structure of turbulence in incompressible viscous fluid for very large Reynold's numbers. *Comptes rendus (Doklady) de l'Académie des Sciences de l'U.R.S.S.*, **30**, 301–305.
- KUO, A. Y.-S., & CORRSIN, S. 1972. *Journal of Fluid Mechanicis*, **56**, 447.
- LABEYRIE, A. 1970. Attainment of Diffraction Limited Resolution in Large Telescopes by Fourier Analysing Speckle Patterns in Star Images. *Astronomy and Astrophysics*, **6**(May), 85+.
- LELIEVRE, G., NIETO, J.-L., THOUVENOT, E., SALMON, D., & LLEBARIA, A. 1988. Very high resolution imaging using sub-pupil apertures, recentering and selection of short exposures. *Astronomy and Astrophysics*, **200**(July), 301–311.
- LINFIELD, R. P., COLAVITA, M. M., & LANE, B. F. 2001. Atmospheric Turbulence Measurements with the Palomar Testbed Interferometer. *Astrophysical Journal*, **554**(June), 505–513.
- LOHMANN, A. W., & WEIGELT, G. P. 1979. Astronomical speckle interferometry; measurements of isoplanicity and of temporal correlation. *Optik*, **53**(Aug.), 167–180.
- LOPEZ, B., & SARAZIN, M. 1993. The ESO atmospheric temporal coherence monitor dedicated to high angular resolution imaging. *Astronomy and Astrophysics*, **276**(Sept.), 320+.
- MACKAY, C. D., TUBBS, R. N., BELL, R., BURT, D. J., JERRAM, P., & MOODY, I. 2001 (May). Subelectron read noise at MHz pixel rates. *Pages 289–298 of: SPIE Proceedings, Vol. 4306, Sensors and Camera Systems II, M. M. Blouke et al Eds.*
- MANDELBROT, B. B. 1974. Intermittent turbulence in self-similar cascades: divergence of high moments and dimension of the carrier. *Journal of Fluid Mechanicis*, **62**, 331–358.
- MARKS, R. D., VERNIN, J., AZOUI, M., MANIGAULT, J. F., & CLEVELIN, C. 1999. Measurement of optical seeing on the high antarctic plateau. *Astronomy and Astrophysics Supplement Series*, **134**(Jan.), 161–172.

- MARTIN, F., CONAN, R., TOKOVININ, A., ZIAD, A., TRINQUET, H., BORGNO, J., AGABI, A., & SARAZIN, M. 2000. Optical parameters relevant for High Angular Resolution at Paranal from GSM instrument and surface layer contribution. *Astronomy and Astrophysics Supplement Series*, **144**(May), 39–44.
- MCALISTER, H. A., HARTKOPF, W. I., SOWELL, J. R., DOMBROWSKI, E. G., & FRANZ, O. G. 1989. ICCD speckle observations of binary stars. IV – Measurements during 1986–1988 from the Kitt Peak 4 M telescope. *Astronomical Journal*, **97**(Feb.), 510–531.
- MONNIER, J. D. 2003. Optical interferometry in astronomy. *Reports of Progress in Physics*, **66**(May), 789–857.
- MUÑOZ-TUÑÓN, C., VERNIN, J., & VARELA, A. M. 1997. Night-time image quality at Roque de los Muchachos Observatory. *Astronomy and Astrophysics Supplement Series*, **125**(Oct.), 183–193.
- NAHMAN, N. S., & GUILLAUME, M. E. 1981. Deconvolution of time domain waveforms in the presence of noise. *NBS Technical Note*, **1047**(Oct.), 1–122.
- NIETO, J.-L., & THOUVENOT, E. 1991. Recentring and selection of short-exposure images with photon-counting detectors. I – Reliability tests. *Astronomy and Astrophysics*, **241**(Jan.), 663–672.
- NIETO, J.-L., LLEBARIA, A., & DI SEREGO ALIGHIERI, S. 1987. Photon-counting detectors in time-resolved imaging mode – Image recentring and selection algorithms. *Astronomy and Astrophysics*, **178**(May), 301–306.
- NIETO, J.-L., ROQUES, S., LLEBARIA, A., VANDERRIEST, C., LELIEVRE, G., DI SEREGO ALIGHIERI, S., MACCHETTO, F. D., & PERRYMAN, M. A. C. 1988. High-resolution imaging of the double QSO 2345 + 007 – Evidence for subcomponents. *Astrophysical Journal*, **325**(Feb.), 644–650.
- NIETO, J.-L., AURIERE, M., SEBAG, J., ARNAUD, J., LELIEVRE, G., BLAZIT, A., FOY, R., BONALDO, S., & THOUVENOT, E. 1990. The optical counterpart of the X-ray binary in the globular cluster NGC 6712. *Astronomy and Astrophysics*, **239**(Nov.), 155–162.
- NIGHTINGALE, N. S., & BUSCHER, D. F. 1991. Interferometric seeing measurements at the La Palma Observatory. *Monthly Notices of the Royal Astronomical Society*, **251**(July), 155–166.
- NOLL, R. J. 1976. Zernike polynomials and atmospheric turbulence. *Optical Society of America Journal*, **66**(Mar.), 207–211.
- O'BYRNE, J. W. 1988. Seeing measurements using a shearing interferometer. *Publications of the Astronomical Society of the Pacific*, **100**(Sept.), 1169–1177.

- PARRY, G., WALKER, J. G., & SCADDAN, R. J. 1979. Statistics of stellar speckle patterns and pupil plane scintillation. *Optica Acta*, **26**(Oct.), 563.
- POGSON, N. 1856. Magnitudes of Thirty-six of the Minor Planets for the first day of each month of the year 1857. *Monthly Notices of the Royal Astronomical Society*, **17**(Nov.), 12–15.
- RACINE, R. 1996. Temporal Fluctuations of Atmospheric Seeing. *Publications of the Astronomical Society of the Pacific*, **108**(Apr.), 372+.
- RAGAZZONI, R., & FARINATO, J. 1999. Sensitivity of a pyramidal Wave Front sensor in closed loop Adaptive Optics. *Astronomy and Astrophysics*, **350**(Oct.), L23–L26.
- ROBBINS, M. S., & HADWEN, B. J. 2003. The noise performance of electron multiplying charge coupled devices. *IEEE Transactions on Electron Devices*, **50**(May), 1227–1232.
- RODDIER, F. 1981. The effects of atmospheric turbulence in optical astronomy. *Pages 281–376 of: Progress in optics. Volume 19. Amsterdam, North-Holland Publishing Co.*
- RODDIER, F. 1988. Interferometric imaging in optical astronomy. *Physics Reports*, **170**, 99–166.
- RODDIER, F., GILLI, J. M., & LUND, G. 1982a. On the origin of speckle boiling and its effects in stellar speckle interferometry. *Journal of Optics*, **13**(Oct.), 263–271.
- RODDIER, F., GILLI, J. M., & VERNIN, J. 1982b. On the isoplanatic patch size in stellar speckle interferometry. *Journal of Optics*, **13**(Mar.), 63–70.
- RODDIER, F., COWIE, L., GRAVES, J. E., SONGAILA, A., & MCKENNA, D. 1990 (July). Seeing at Mauna Kea - A joint UH-UN-NOAO-CFHT study. *Pages 485–491 of: SPIE Proceedings, Vol. 1236, Advanced technology at optical telescopes IV Part 1.*
- RODDIER, F., NORTHCOTT, M. J., GRAVES, J. E., MCKENNA, D. L., & RODDIER, D. 1993. One-dimensional spectra of turbulence-induced Zernike aberrations: time-delay and isoplanicity error in partial adaptive compensation. *Optical Society of America Journal*, **10**(May), 957–965.
- SAINT-JACQUES, D., & BALDWIN, J. E. 2000 (July). Taylor's hypothesis: good for nuts. *Pages 951–962 of: SPIE Proceedings, Vol. 4006, Interferometry in Optical Astronomy, P. Lena; A. Quirrenbach; Eds.*
- SAINT-JACQUES, D., COX, G. C., BALDWIN, J. E., MACKAY, C. D., WALDRAM, E. M., & WILSON, R. W. 1997. The JOSE atmospheric seeing monitor at the William Herschel Telescope. *Monthly Notices of the Royal Astronomical Society*, **290**(Sept.), 66–74.
- SCADDAN, R. J., & WALKER, J. G. 1978. Statistics of stellar speckle patterns. *Applied Optics*, **17**(Dec.), 3779–3784.

- SIGGIA, E. D. 1978. Model of intermittency in three-dimensional turbulence. *Physical Review A*, **17**(Mar.), 1166–1176.
- SØRENSEN, A. N. 2002 (Feb.). *Personal communication – the measured shape of aberrations in the NOT optics*.
- STREHL, K. 1895. Aplanatische und fehlerhafte Abbildung im Fernrohr. *Zeitschrift für Instrumentenkunde*, **15**(Oct.), 362–370.
- STREHL, K. 1902. Ueber Luftsclieren und Zonenfehler. *Zeitschrift für Instrumentenkunde*, **22**(July), 213–217.
- TATARSKI, V. I. 1961. *Wave Propagation in a Turbulent Medium*. McGraw-Hill.
- TAYLOR, G. I. 1938 (Feb.). The spectrum of turbulence. *Pages 476–490 of: Proceedings of the Royal Society of London A*, **164**.
- TUBBS, R. N., BALDWIN, J. E., MACKAY, C. D., & COX, G. C. 2002. Diffraction-limited CCD imaging with faint reference stars. *Astronomy and Astrophysics*, **387**(May), L21–L24.
- TUTHILL, P. G., MONNIER, J. D., DANCHI, W. C., WISHNOW, E. H., & HANIFF, C. A. 2000. Michelson Interferometry with the Keck I Telescope. *Publications of the Astronomical Society of the Pacific*, **112**(Apr.), 555–565.
- VERNIN, J., & MUÑOZ-TUÑÓN, C. 1994. Optical seeing at La Palma Observatory. 2: Intensive site testing campaign at the Nordic Optical Telescope. *Astronomy and Astrophysics*, **284**(Apr.), 311–318.
- VERNIN, J., & MUÑOZ-TUÑÓN, C. 1998. The temporal behaviour of seeing. *New Astronomy Review*, **42**(Nov.), 451–454.
- VERNIN, J., & RODDIER, F. 1973. Experimental determination of two-dimensional spatiotemporal power spectra of stellar light scintillation. Evidence for a multilayer structure of the air turbulence in the upper troposphere. *Journal of the Optical Society of America*, **63**(Mar.), 270–273.
- VERNIN, J., CACCIA, J.-L., WEIGELT, G., & MUELLER, M. 1991. Speckle lifetime and isoplanicity determinations – Direct measurements and derivation from turbulence and wind profiles. *Astronomy and Astrophysics*, **243**(Mar.), 553–558.
- WILSON, R. W. 2002. SLODAR: measuring optical turbulence altitude with a Shack-Hartmann wavefront sensor. *Monthly Notices of the Royal Astronomical Society*, **337**(Nov.), 103–108.
- WILSON, R. W. 2003 (July). *Personal communication – results from the ING seeing monitor at Roque de los Muchachos Observatory*.

- WILSON, R. W., & SAUNTER, C. 2003 (Feb.). Turbulence profiler and seeing monitor for laser guide star adaptive optics. *Pages 466–472 of: SPIE Proceedings, Vol. 4839, Adaptive Optical System Technologies II, P. Wizinowich and D. Bonaccini Eds.*
- WILSON, R. W., O'MAHONY, N., PACKHAM, C., & AZZARO, M. 1999. The seeing at the William Herschel Telescope. *Monthly Notices of the Royal Astronomical Society*, **309**(Oct.), 379–387.
- YOUNG, J. S., BALDWIN, J. E., BOYSEN, R. C., HANIFF, C. A., LAWSON, P. R., MACKAY, C. D., PEARSON, D., ROGERS, J., ST.-JACQUES, D., WARNER, P. J., WILSON, D. M. A., & WILSON, R. W. 2000. New views of Betelgeuse: multi-wavelength surface imaging and implications for models of hotspot generation. *Monthly Notices of the Royal Astronomical Society*, **315**(July), 635–645.
- YOUNG, J. S., BALDWIN, J. E., BASDEN, A. G., BHARMAL, N. A., BUSCHER, D. F., GEORGE, A. V., HANIFF, C. A., KEEN, J. W., O'DONOVAN, B., PEARSON, D., THORSTEINSSON, H., THUREAU, N. D., TUBBS, R. N., & WARNER, P. J. 2003 (Feb.). Astrophysical results from COAST. *Pages 369–378 of: SPIE Proceedings, Vol. 4838, Interferometry for Optical Astronomy II, W. Traub Eds.*
- ZIAD, A., BORNINO, J., MARTIN, F., & AGABI, A. 1994. Experimental estimation of the spatial-coherence outer scale from a wavefront statistical analysis. *Astronomy and Astrophysics*, **282**(Feb.), 1021–1033.